DGK Deutsche Geodätische Kommission
der Bayerischen Akademie der Wissenschaften

Reihe C | Dissertationen | Heft Nr. 711

Majid Naeimi

Inversion of satellite gravity data using spherical radial base functions

München 2013

Verlag der Bayerischen Akademie der Wissenschaften
in Kommission beim Verlag C. H. Beck

ISSN 0065-5325 ISBN 978-3-7696-5123-2

Diese Arbeit ist gleichzeitig veröffentlicht in:
Wissenschaftliche Arbeiten der Fachrichtung Geodäsie und Geoinformatik der Leibniz Universität Hannover
ISSN 0174-1454, Nr. 309, Hannover 2013

Deutsche Geodätische Kommission
der Bayerischen Akademie der Wissenschaften

Reihe C | Dissertationen | Heft Nr. 711

Inversion of satellite gravity data using spherical radial base functions

Von der Fakultät für Bauingenieurwesen und Geodäsie
der Gottfried Wilhelm Leibniz Universität Hannover
zur Erlangung des Grades
Doktor-Ingenieur (Dr.-Ing.)
genehmigte Dissertation

von

M.Sc. Majid Naeimi

München 2013

Verlag der Bayerischen Akademie der Wissenschaften
in Kommission bei der C. H. Beck'schen Verlagsbuchhandlung München

ISSN 0065-5325 ISBN 978-3-7696-5123-2

Diese Arbeit ist gleichzeitig veröffentlicht in:
Wissenschaftliche Arbeiten der Fachrichtung Geodäsie und Geoinformatik der Leibniz Universität Hannover
ISSN 0174-1454, Nr. 309, Hannover 2013

Adresse der Deutschen Geodätischen Kommission:

Deutsche Geodätische Kommission

Alfons-Goppel-Straße 11 ● D – 80 539 München

Telefon +49 – 89 – 23 031 1113 ● Telefax +49 – 89 – 23 031 - 1283 / - 1100

e-mail hornik@dgfi.badw.de ● http://www.dgk.badw.de

Prüfungskommission

Referent:	Prof. Dr.-Ing. Jakob Flury
Korreferenten:	Prof. Dr.-Ing. Michael Schmidt
	PD Dr. Gerhard Heinzel
	Prof. Dr.-Ing. Ingo Neumann

Tag der mündlichen Prüfung: 23.08.2013

ISSN 0065-5325 ISBN 978-3-7696-5123-2

Summary

The regional gravity field modelling based on satellite data in spherical radial base functions (SRBF) is investigated in this thesis. The SRBF have been recently used for the regional representation of the Earth's gravity field as an alternative to the global spherical harmonic analysis. The use of SRBF for the regional gravity field modelling requires several choices to be made. The shape of the SRBF and their positions, the treatment of boundary effects and the use of a prior gravity field model to reduce the long wavelengths can be mentioned as different choices which have to be made. There is a wide variety of options for these choices which make it almost impossible to define a unique and standard way for regional gravity field modelling. Moreover, no matter how these choices are made, the resulting observation equations are strictly inconsistent and the associated design and normal matrices are strongly ill-posed. The solution must be then obtained by means of a proper regularization method. The main objective of this thesis is the development of new methods for the regularization of regional gravity field solutions based on satellite data.

In the first three chapters of the thesis, the basic concepts of the satellite gravimetry and gradiometry are given briefly. Several mathematical models for the functional link between satellite observations and the gravitational potential are addressed. Furthermore, the mathematical expressions of the global gravity field modelling using spherical harmonics and SRBF are given. It will be numerically shown that these two groups of base functions provide the same accuracy for the representation of gravity field on the global scale. The spatial pattern of the estimated scaling coefficients on the global scale (for the SRBF) gives a perspective about the expected 'geometry' of the coefficients (as unknown parameters) in the regional modelling. Such perspective can be then used as prior knowledge about the unknown parameters.

In Chapter 4, the mathematical description of global gravity field modelling using SRBF, is extended to regional solutions. We classify different choices for the model setup to seven groups. These groups are investigated in detail and our approach to define the choices is proposed.

In Chapter 5, the issue of regularization of discrete ill-posed problems will be investigated generally. We describe the mathematical description of the ill-posed problems in general. In addition, some 'diagnostic' tools to determine the extent of the 'ill-posedness' will be introduced. The Tikhonov regularization and the singular value decomposition, as powerful tools for the treatment of ill-posed problems, are explained further. Several techniques for the choice of (Tikhonov) regularization parameter such as the variance component estimation (VCE), the generalized cross validation (GCV) and the L-curve method are considered. Based on the space-localization properties of the SRBF, we introduce our proposed method, called the parameter-signal correlation (PSC), for the choice of regularization parameter. Since the regularization parameter should be chosen from an extremely large set of numbers, we also propose two methods to obtain an initial and realistic value for the regularization parameter. These methods significantly reduce the computation costs and lead to a very fast convergence. The connection between the regularization and the shape of SRBF will also be explained which simplifies the choice of the shape functions.

Finally, the regional gravity field modelling will be numerically investigated in several test areas. We chose three test regions according to their geographical locations as well as their signal contents. These regions are: Scandinavia, Central Africa and South America along the Andes. In addition, we considered two types of satellite observations: simulated GRACE-type data corrupted with coloured noise and real GOCE gravity gradients. Therefore the numerical considerations are divided into two steps. In the first step, the simulated GRACE data are considered. A global gravity field solution using spherical harmonics up to degree and order 120, as well as several regional solutions, are determined based on the same simulated satellite data. For the regional solutions, the VCE, GCV, L-curve and the proposed PSC methods have been used as the regularization

parameter choice methods. The results are then compared to the input model to quantify the quality of different solutions. In all solutions, our PSC method gives the most promising results with the least geoid RMS on the Earth's surface. It also gives better results when the regional solutions are compared to the global spherical harmonic solution in the corresponding regions. The north-south GRACE stripes are remarkably reduced as the result of PSC regularization. In the second step, we employed real GOCE observations for regional modelling. Two months of calibrated V_{zz} components are used. The solutions are compared to the global gravity field model EGM2008 as well as the recent combined model GOCO03s. Again, the performance of four different regularization approaches are compared in the test areas. The PSC method gives the least geoid RMS compared to other approaches which shows the success of the proposed method. Moreover, the solutions show a considerable improvement compared to the global model EGM2008. The deviations between the regional solutions and the model GOCO03s, are also in the range of accumulated geoid errors of the recent global models. This indicates that even a short period of GOCE observations can provide promising results in medium and short wavelengths of the Earth's gravity field. In addition, this provides evidence that the regional gravity field determination based on satellite data provides satisfactory results if the solution is properly regularized.

Zusammenfassung

In der vorliegenden Arbeit wird ein Ansatz zur regionalen Schwerefeldmodellierung mit sphärischen radialen Basisfunktionen (SRBF) untersucht. Sphärische radiale Basisfunktionen werden seit wenigen Jahren für die regionale Darstellung des Erdschwerefeldes genutzt und stellen eine Alternative zur globalen sphärisch-harmonischen Analyse dar. Beim Einsatz radialer Basisfunktionen für die regionale Schwerefeldmodellierung sind verschiedene Entscheidungen zu treffen. Es seien beispielhaft die Wahl der Form der sphärischen radialen Basisfunktion und deren Position, die Behandlung von Randeffekten sowie die Verwendung eines bereits existierenden Schwerefeldmodells zur Reduktion langwelliger Schwerefeldanteile genannt. Die Vielfalt an denkbaren Optionen (für diese Entscheidungen) macht es beinahe unmöglich, ein Standardverfahren für die regionale Schwerefeldmodellierung zu definieren. Darüber hinaus sind unabhängig von den getroffenen Entscheidungen die sich ergebenden Beobachtungsgleichungen streng inkonsistent, was zu einem schlecht gestellten inversen Problem führt. Die Lösung muss dann mit Hilfe eines geeigneten Regularisierungsverfahrens erreicht werden. Das Hauptziel dieser Arbeit ist die Entwicklung neuer Methoden zur Regularisierung regionaler Schwerefeldlösungen basierend auf Satellitendaten.

In den ersten drei Kapiteln, werden in Kürze die grundlegenden Konzepte der Satellitengravimetrie und Satellitengradiometrie erläutert und mehrere mathematische Modelle für die funktionalen Zusammenhänge zwischen Satellitenbeobachtungen und Gravitationspotential dargestellt. Ferner werden die mathematischen Modelle der globalen Schwerefeldmodellierung sowohl in Form sphärisch-harmonischer als auch sphärisch-radialer Basisfunktionen beschrieben. Es wird numerisch belegt, dass diese beiden Gruppen von Basisfunktionen für die Darstellung von Schwerefeldmodellen auf einer globalen Skala die gleichen Genauigkeiten aufweisen. Das räumliche Muster der geschätzten Skalierungskoeffizienten (für die sphärischen radialen Basisfunktionen) auf einer globalen Skala gibt Aufschluss über die zu erwartende Geometrie der Koeffizienten (als unbekannte Parameter) in der regionalen Modellierung. Aus derartigen Betrachtungen können Vorabinformationen über die unbekannten Parameter abgeleitet werden.

In Kapitel 4 wird die mathematische Beschreibung globaler Schwerefeldmodellierung unter Einsatz von SRBF auf regionale Lösungen erweitert. Es erfolgt eine Klassifizierung verschiedener Optionen des Modells in bis zu sieben Gruppen. Diese Gruppen werden detailliert untersucht und es wird ein Ansatz für die Wahl der Optionen vorgeschlagen.

Kapital 5 stellt den Hauptteil der Arbeit dar und geht allgemein auf das Thema der Regularisierung von diskreten schlecht gestellten Problemen und deren mathematische Beschreibung ein. Es wird ein Diagnose-Tool vorgestellt, welches die Bestimmung des Ausmaßes eines schlecht gestellten Problems ermöglicht. Ergänzend werden die Tikhonov Regularisierung und Singulärwertzerlegung als zwei leistungsfähige Verfahren zur Behandlung schlecht gestellter Probleme erläutert. Es werden verschiedene Techniken für die Wahl des (Tikhonov) Regularisierungsparameter betrachtet, wie etwa die Varianzkomponentenschätzung (VCE), die generalisierte Kreuzvalidierung (GCV) und die L-curve Methode.

Basierend auf den raum-lokalisierenden Eigenschaften der sphärischen radialen Basisfunktionen wird die im Rahmen dieser Arbeit vorgeschlagene Methode, die sogenannte Parameter-Signal Korrelation (PSC), zur Wahl der Regularisierungsparameter vorgestellt. Da die Regularisierungsparameter aus einer extrem großen Menge an Zahlen gewählt werden sollten, werden ebenfalls zwei Methoden vorgeschlagen, um einen initialen und einen realistischen Wert für die Regularisierungsparameter zu erhalten. Diese Methoden tragen zu einer deutlichen Verringerung der Rechenzeit sowie zu einer sehr schnellen Konvergenz bei. Die Verbindung zwischen der Regularisierung und der Form der sphärischen radialen Basisfunktion wird ebenfalls erläutert, wodurch die Wahl der Formfunktion vereinfacht wird. Schließlich wird die

regionale Schwerefeldmodellierung in mehreren Testgebieten numerisch untersucht. Die Auswahl fiel auf drei Testgebiete, die anhand ihrer geografischen Lage sowie ihres Signalgehalts ausgewählt wurden. Die Gebiete sind Skandinavien, Zentralafrika und Südamerika entlang der Anden. Als zwei Arten von Satellitenbeobachtungen werden simulierte GRACE-Daten mit farbigem Rauschen und reale GOCE Gravitationsgradienten genutzt. Die numerischen Betrachtungen werden in zwei Schritte unterteilt. Im ersten Schritt werden die simulierten GRACE-Daten berücksichtigt. Daraus wird eine globale Schwerefeldlösung in Form von sphärisch-harmonischen Koeffizienten bis Grad und Ordnung 120 sowie mehrere regionale Lösungen auf Basis derselben Satellitendaten bestimmt. Für die regionalen Lösungen werden für die Wahl der Regularisierungsparameter die VCE, GCV, L-curve und die vorgeschlagene PSC Methode verwendet.

Die Ergebnisse werden dann mit dem Eingangsmodell verglichen, um die Qualität verschiedener Lösungen zu quantifizieren. In allen Lösungen liefert das PSC Verfahren die vielversprechendsten Ergebnisse mit dem geringsten Geoid RMS Fehler auf der Erdoberfläche. Das Verfahren führt ebenfalls zu den besten Ergebnissen, wenn die regionalen Lösungen in den entsprechenden Gebieten mit den globalen sphärisch-harmonischen Lösungen verglichen werden. Die GRACE Streifen in Nord-Süd-Richtung werden als ein Resultat der PSC Regularisierung erheblich reduziert. Im zweiten Schritt werden reale GOCE Beobachtungen in Form von zwei Monaten kalibrierter Vzz Tensorkomponenten für die regionale Modellierung genutzt. Die Ergebnisse werden einerseits mit dem globalen Schwerefeldmodell EGM2008 sowie dem rein satellitenbasieren Kombinationsmodell GOCO03s verglichen. Erneut werden in den Testgebieten die Ergebnisse der vier Regularisierungsansätze miteinander verglichen. Die PSC Methode liefert den geringsten Geoid RMS im Verglich zu den anderen Ansätzen, was die Überlegenheit der vorgeschlagenen Methode unterstreicht. Darüber hinaus zeigt die Lösung eine erhebliche Verbesserung gegenüber dem globalen Modell EGM2008. Die Abweichungen zwischen den regionalen Lösungen und dem Modell GOCO03s liegen im Bereich der akkumulierten Geoidfehlergradvarianzen der neuesten globalen Modelle. Dies deutet darauf hin, dass bereits ein kurzer Zeitraum von GOCE Beobachtungen vielversprechende Ergebnisse im Bereich mittlerer und kurzer Wellenlängen des Erdschwererfeldes liefern kann. Außerdem stellt dies auch den Beweis dar, dass eine regionale Schwerefeldbestimmung auf Basis von Satellitendaten zufriedenstellende Ergebnisse liefert, wenn die Lösung geeignet regularisiert wird.

Abbreviations

CHAMP	CHAllenging Mini-satellite Payload
CuP	Cubic Polynomials
GCV	Generalized Cross Validation
GFZ	GeoForschungsZentrum (German Research Centre for Geosciences)
GOCE	Gravity and steady-state Ocean Circulation Explorer
GPS	Global Positioning System
GRACE	Gravity Recovery And Climate Experiment
GRF	Gradiometer Reference Frame
KBR	k-Band Ranging
LEO	Low Earth Orbiter
LNOF	Local North Oriented Frame
PSC	Parameter-Signal-Correlation
RMS	Root Mean Square
SGG	Satellite Gravity Gradiometry
SH	Spherical Harmonics
SRBF	Spherical Radial Base Function
SST	Satellite-to-Satellite Tracking
SST-hl	Satellite-to-Satellite tracking, high-low
SST-ll	Satellite-to-Satellite tracking, low-low
SVD	Singular Value Decomposition
VCE	Variance Component Estimation

Contents

1 Introduction **1**
1.1 Problem statement and thesis objectives . . . 3
1.2 Thesis outlines . . . 4
1.3 Preliminaries . . . 4
1.3.1 Units and constants . . . 4
1.3.2 Components of the Earth's gravity field . . . 5
1.3.3 Functionals and observables of the Earth's gravity field . . . 5

2 Gravity field from satellite data **7**
2.1 Precise orbit determination . . . 9
2.2 Gravity field from SST data . . . 9
2.2.1 Variational approach . . . 11
2.2.2 Short arc approach . . . 11
2.2.3 Acceleration approach . . . 12
2.2.4 Energy balance approach . . . 13
2.3 Gravity field from SGG data . . . 15
2.3.1 Gravity gradiometry . . . 16
2.3.2 From the GOCE observation frame to the Earth fixed frame . . . 16
2.4 Evolution of global gravity field models and state-of-the-art . . . 18
2.5 Follow-on missions . . . 19

3 Global gravity field modelling **23**
3.1 Spherical harmonics (SH) . . . 24
3.1.1 Mathematical description of SH . . . 24
3.1.2 Expansion of the gravitational potential into SH . . . 27
3.1.3 Estimation of spherical harmonic coefficients using least-squares adjustment . . . 29
3.1.4 Disadvantages of spherical harmonics . . . 31
3.2 Spherical radial base functions (SRBF): A first look . . . 32
3.2.1 Mathematical description of SRBF . . . 33
3.2.2 Relation to spherical harmonics . . . 35
3.3 SH versus SRBF in satellite gravimetry: numerical aspects on the global scale . . . 35
3.3.1 Simulated input data and noise . . . 36
3.3.2 Global gravity field solutions . . . 37

4 Regional gravity field modelling using SRBF **41**
4.1 From global to regional scale . . . 41
4.2 Model setup using SRBF . . . 43
4.2.1 Shape of the SRBF . . . 44
4.2.2 Maximum degree of expansion . . . 48
4.2.3 Removal of the long wavelengths . . . 49
4.2.4 Position of the SRBF . . . 50
4.2.5 Extension of the data zone . . . 53
4.2.6 Extension of the grid zone . . . 54
4.2.7 Inversion process . . . 55

5 Regularization of regional gravity field solutions 57
5.1 Gravity field modelling: an inverse problem . . . 57
5.2 Diagnosis of ill-posedness in inverse problems . . . 59
5.2.1 Condition number . . . 60
5.2.2 Singular value decomposition . . . 60
5.2.3 Discrete Picard condition . . . 63
5.3 Ill-posedness of gravity field determination . . . 63
5.4 Regularization of ill-posed problems . . . 64
5.4.1 Truncated singular value decomposition . . . 65
5.4.2 Tikhonov regularization . . . 66
5.4.3 Tikhonov regularization in terms of SVD . . . 68
5.5 The choice of the regularization parameter . . . 71
5.5.1 Generalized cross validation . . . 71
5.5.2 Variance component estimation . . . 73
5.5.3 L-curve analysis . . . 74
5.6 Signal-adaptive parameter choice: The parameter-signal correlation (PSC) . . . 75
5.7 Initial value for the regularization parameter . . . 78
5.7.1 Initial guess based on the size of the region . . . 79
5.7.2 Initial guess based on the condition number . . . 80
5.8 Different types of SRBF and their impact on the regularization . . . 81
5.9 Assessment of regional solutions . . . 83
5.9.1 Statistical assessment . . . 83
5.9.2 External validation . . . 84
5.9.3 Model-dependent evidences . . . 84

6 Numerical results 85
6.1 Specifications of regional solutions . . . 85
6.1.1 Test regions . . . 85
6.1.2 Type of SRBF . . . 86
6.1.3 Type of grid points . . . 86
6.2 Regional gravity field modelling based on GRACE-type simulation . . . 87
6.2.1 Simulated data and noise . . . 87
6.2.2 Regional solutions in Central Africa . . . 88
6.2.3 Regional solutions in Scandinavia . . . 95
6.2.4 Regional solutions in South America . . . 99
6.3 Regional gravity field modelling based on GOCE gravity gradients . . . 104
6.3.1 GOCE data and functional model . . . 104
6.3.2 Setting up the regional models . . . 106
6.3.3 Regional solutions based on GOCE data . . . 106
6.3.4 Summary of regional solutions based on real GOCE data . . . 117

7 Summary and conclusions 119

List of Figures

1.1 The approximate value of the global gravity . . . 1
1.2 The value of gravity . . . 2
1.3 The long term gravity changes on the global scale . . . 2

2.1 The Earth's gravity field from different satellite techniques . . . 8
2.2 Concept of SST high-low and SST low-low . . . 10
2.3 Coordinate systems used for GOCE data processing . . . 17
2.4 Satellite missions and spatial resolution . . . 20
2.5 Error degree amplitudes in terms of geoid heights . . . 21
2.6 Cumulative geoid errors for several global models . . . 22

3.1 Normalized spherical harmonics of degree 4 . . . 25
3.2 Uncertainty principle in space and frequency . . . 32
3.3 SRBF of different resolution . . . 34
3.4 Geoid heights computed from geopotential model GOCO03s up to $N_{max} = 70$ . . . 36
3.5 geoid error degree amplitude of the global model . . . 38
3.6 Geoid differences between the global model GOCO03s and the computed model using SH . . . 39
3.7 Similarity of the geoid heights and the estimated coefficients . . . 40
3.8 Cross-correlation function for the estimated scaling coefficients α_k and the geoid heights . . . 40

4.1 Gravity field modelling on global and regional scales . . . 41
4.2 Model zone, data zone and grid zone . . . 43
4.3 The Shannon kernel . . . 45
4.4 The Blackman kernel . . . 46
4.5 The CuP kernel . . . 47
4.6 The spline kernel . . . 48
4.7 Distance between adjacent SRBF on the Reuter grid . . . 52
4.8 Two Reuter grids with different point densities . . . 52
4.9 The Reuter and Fibonacci grids . . . 53
4.10 The extension of the grid and data zones with respect to the model zone . . . 54

5.1 The forward and inverse problems . . . 57
5.2 The operator $\mathbf{A}$ and its mapping from function space to the observation space . . . 58
5.3 Two coordinate systems to describe one object . . . 62
5.4 Singular values of the normal matrices on global and regional scales . . . 64
5.5 Non-regularized and regularized coefficients . . . 68
5.6 Singular values, regularization and filter factors . . . 70
5.7 The generalized cross validation function . . . 72
5.8 The L-curve and its curvature . . . 74
5.9 The PSC function . . . 77
5.10 The geoid difference for the models EGM2008 and EGM1996 used for the PSC method . . . 78
5.11 The search band for the choice of regularization parameter . . . 79
5.12 The sequence of matrix operations to obtain the solution from the observation vector . . . 83

6.1 Test areas for regional gravity field modelling . . . 86
6.2 Simulation scenario used to assess the performance of regional gravity field modelling . . . 87

6.3 The geoid differences between the estimated global model using SH and the model GOCO03s 88
6.4 geoid and geoid differences in Central Africa 89
6.5 The model zone ,the data zone and the grid zone in Central Africa 90
6.6 The coefficients obtained from the PSC regularization approach in Central Africa 92
6.7 The geoid differences between the model GOCO03s and regional solutions in Central Africa (Reuter) 93
6.8 The geoid differences between the model GOCO03s and regional solutions in Central Africa (Fibonacci) 94
6.9 Geoid and geoid differences in Scandinavia 95
6.10 The model zone, the data zone and the grid zone for regional modelling in Scandinavia 96
6.11 The geoid differences between the model GOCO03s and the regional solutions in Scandinavia 97
6.12 The coefficients obtained from the PSC regularization approach in Scandinavia 98
6.13 Geoid and geoid differences in the are of Andes 99
6.14 The model, data and grid zones for regional modelling in the Andes 100
6.15 The estimated coefficients obtained from the PSC regularization approach in South America . 101
6.16 The geoid differences between the model GOCO03s and the regional solutions in South America 102
6.17 The differences between regional solutions in Central Africa and the global model EGM2008 . 108
6.18 The differences between regional solutions in Central Africa and the global model GOCO03s . 109
6.19 The estimated coefficients and geoid heights in Central Africa 110
6.20 The differences between regional solutions in Scandinavia and the global model EGM2008 . . 112
6.21 The differences between regional solutions in Scandinavia and the global model GOCO03s . . 113
6.22 The estimated coefficients and geoid heights in Scandinavia 114
6.23 The differences between regional solutions in the Andes and the global model EGM2008 . . . 116
6.24 The differences between regional solutions in the Andes and the global model GOCO03s . . . 116
6.25 The estimated coefficients and geoid heights in the area of Andes 117

List of Tables

1.1 Table of constants 5

2.1 Several past and current dedicated satellite missions 7
2.2 Several geopotential models determined from 1999 until 2013 19

5.1 Different geopotential models used to compute dV_k for the PSC method 78

6.1 Specifications of the regional modelling in Central Africa 91
6.2 Summary of the regional solutions in Central Africa and their quality measures 93
6.3 Summary of the solutions in Central Africa and their quality measures 94
6.4 Specifications of the regional modelling in Scandinavia 96
6.5 Summary of the regional solutions in Scandinavia with their quality measures 97
6.6 Specifications of the regional modelling in South America along the Andes 100
6.7 Summary of the regional solutions in the Andes with their quality measures 102
6.8 Specifications of the regional modelling in Central Africa 107
6.9 Summary of the regional solutions in Central Africa and their quality measures 107
6.10 Specifications of the regional modelling in Scandinavia 111
6.11 Summary of the regional solutions in Scandinavia and their quality measures 111
6.12 Specifications of the regional modelling in the area of the Andes 115
6.13 Summary of the regional solutions in the area of Andes and their quality measures 115

1 Introduction

Gravity is the well-known force near the Earth's surface which directly influences many aspects of humankind's life. As a physical property of the Earth, the gravity is a function of mass distribution and mass redistribution. The Earth's geometry, on the other hand, is also dependent on the mass structure of the Earth. Therefore, gravity is a way to connect the geometry of the Earth to its physical properties and it plays an important role in the definition of the figure of the Earth. The approximate value of gravity acceleration, near the Earth's surface, is about $9.8\,\mathrm{m/s^2}$ which multiplied by the mass of particles, determines the force of gravity. Due to its dependency on the mass distribution (and redistribution), gravity varies in space and in time. Figure 1.1 illustrates the value of gravity near the Earth's surface.

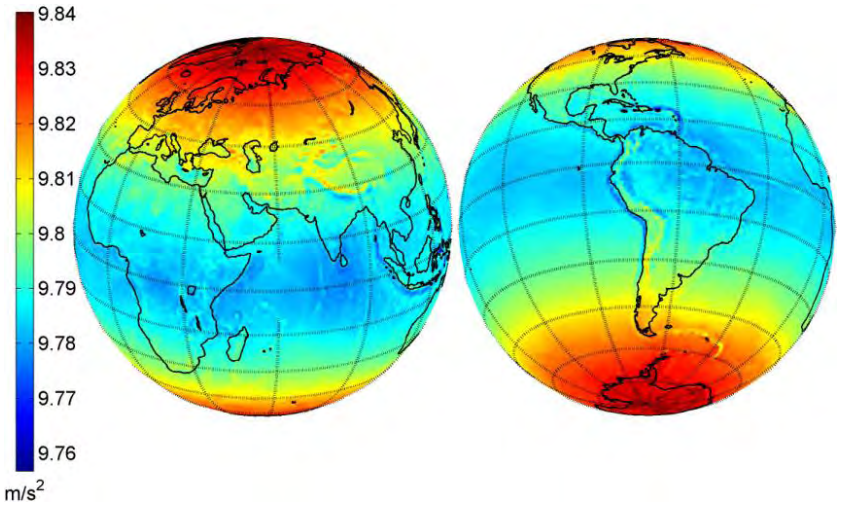

Figure 1.1: The approximate value of the gravity acceleration at the Earth's surface. The maximum values are in polar regions while the minima are in the equatorial area. For a better visualization the anomalies are exaggerated.

As it can be seen in figure 1.1, the global variations of the gravity range from about 9.75 to $9.85\,\mathrm{m/s^2}$ which is mainly due to the Earth's oblateness. This is the largest spatial variation on the Earth's surface. Spatial changes in smaller scales are due to regional and local properties of the Earth's mass structure and mass changes. This is symbolically shown in figure 1.2.
Temporal variations are caused by mass changes within the Earth system. Such mass changes can occur very slowly over long periods of time (such as geological changes) or very sudden such as changes caused by earthquakes and volcanic eruptions. Generally speaking, all phenomena, which are dependent on the mass structure of the Earth or its variations, affect the gravity of the Earth. Figure 1.3 shows the secular changes of the gravity on the global scale. The figure clearly shows that in some regions the gravity changes are considerably large. For instance, in Greenland and Antarctic the gravity is decreasing as a result of ice mass loss. In contrast, the gravity is increasing in Scandinavia due to the post glacial rebound in this region. Therefore the precise knowledge of the Earth's gravity field and its spatial and temporal variations is an important source of information in determining the mass dependence of geophysical phenomena.

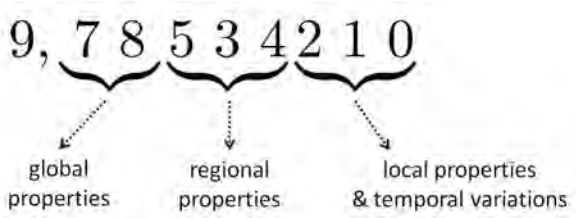

Figure 1.2: The value of gravity and its dependency on different spatial and temporal mass changes inside the Earth. The number 9 never changes near the Earth's surface. The first two or three decimal numbers (in the order of $10^{-2}\,\mathrm{m/s^2}$ change only on the global scale. The changes in the range of $10^{-5}\,\mathrm{m/s^2}$ are due to the heights in the continental scales. Finally the changes in the order of $10^{-8}\,\mathrm{m/s^2}$ are because of small scale changes in mass densities as well as temporal variations.

Hence, gravity observations are among the most fundamental data sets in geophysical and geodynamical studies from global to local scales. Geological phenomena such as volcanic activities, tectonic plates, land uplift and subsidence, interpreted as the mass movements in the Earth's interior, can be monitored using gravity observations. Hydrologists are also able to track water cycles in continents as well as water exchange between land and ocean using gravity data. Studying the annual cycle of the snow pack, post glacial rebound (PGR) and changes in sea-level are also possible using precise knowledge of the Earth's gravitational field.

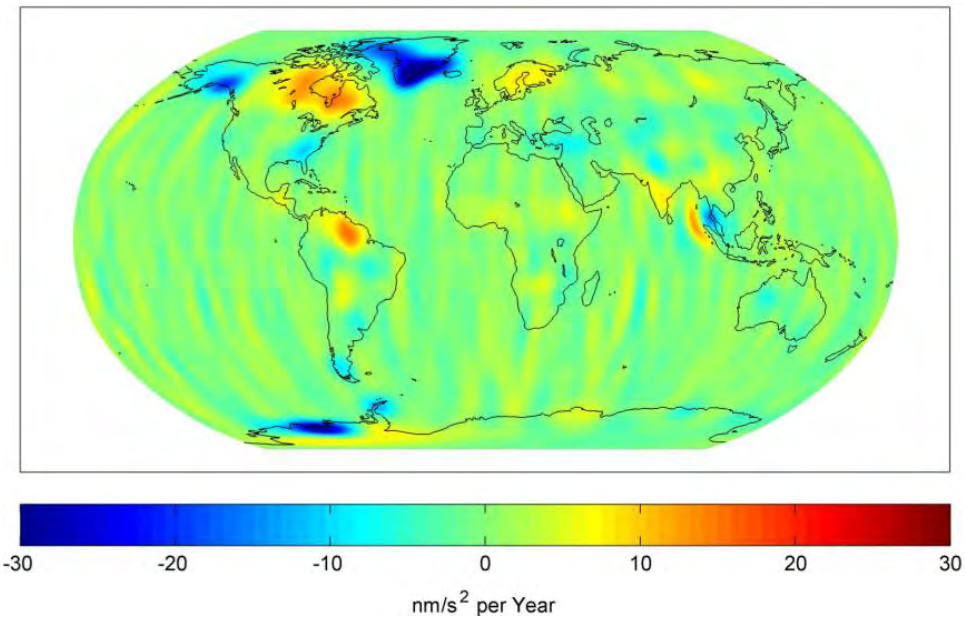

Figure 1.3: The long term gravity changes on the global scale. The results are based on the data from the GRACE mission. In Greenland and Antarctica, gravity is decreasing because of ice mass loss. The land uplift in Scandinavia and north America as the result of post glacial rebound, causes gravity increase. The figure shows the annual rate of gravity changes.

In addition, almost all geodetic observations are affected by the gravity field of the Earth which should be accounted for in data reduction steps (Vanicek and Krakiwsky, 1982). Accurate gravity field models are also necessary for the orbit determination in satellite missions. There is a huge number of examples which state that **the precise knowledge of the Earth's gravity field is essential in nearly all fields of the geosciences.**

1.1 Problem statement and thesis objectives

The modelling of the Earth's gravity field is an old issue in geodesy and geophysics. High resolution gravity field determination in the last decades was restricted to specific regions based on the available terrestrial gravimetric data. The global recovery of the gravity field has only been possible since satellites were launched in the 60's. However due to the lack of high precision and high sensitive sensors on board satellites, the recovery of global gravity fields was limited to the long wavelengths of the gravitational field.
Nowadays, thanks to the availability of a huge amount of data from current satellite missions, with highly sensitive sensors, the recovery of detailed gravity field on the global scale is possible down to the spatial scales of a few hundred kilometres. Since the year 2000, over 60 global gravity field models have been determined using **spherical harmonics** based on either the combination of terrestrial and satellite data or satellite data only (GFZ, 2013). Some of these models incorporate the same data sets but still have different characteristics. Such diversity of existing global gravity field models indicates that the optimum gravity field determination is a challenge and there is still room for further improvements. The main reason for the differences between existing global models is due to the application of various mathematical approaches used to set up the models. The mathematical approach includes the pre-processing of the data, the setup of the observation equations, the base functions used for the representation, the weighting strategy for the noisy data, the matter of the inversion and regularization and finally, the quality assessment of the solution.
Besides the global gravity field solutions, the issue of **regional gravity field determination** based on satellite data manifolds the variety of options for gravity field determination. As an advantage of regional modelling, the computational costs are significantly reduced, when the solution is confined to a region for a specific application. But the main focus of the regional gravity field modelling is to extract more information out of the data by passing the data through dedicated regional filters rather than global ones. This is possible by employing a set of **space-localizing** base functions to **zoom-in** on the target region. Gravity field modelling using space-localizing base functions has been investigated for several decades. The use of point masses as an alternative to spherical harmonics can be mentioned as one of the early attempts to use space-localizing base functions for the representation of the Earth's gravity field (Weightman, 1965). Least-squares collocation (Moritz, 1980) is another example of using space-localizing base function for regional gravity field modelling in which the auto-covariance function is used as the analysing base function.
In the last two decades, regional gravity field modelling has been investigated by many research groups. The reason is the availability of numerous and new sets of satellite-based observations. The mathematical investigations at University of Kaiserslautern to develop the concept of multi-scale modelling using spherical radial base functions (SRBF) and spherical wavelets (Freeden, 1999), the recent studies at University of Bonn to use harmonic splines (Eicker, 2008), the multi-scale approach of the DGFI in Munich (Schmidt *et al.*, 2007) and the current focus of several research studies at Universities of Delft (Wittwer, 2009) and Stuttgart (Antoni, 2012) indicate more interest and demands for this issue. A more comprehensive overview of the previous works in this field, will be given in section 4.2 where more details are addressed.
Despite the existence of several valuable research studies to determine the Earth's gravity field on the regional scales there is yet no standard and unique way to establish the regional modelling of the gravity using SRBF. The reason originates in the fact that there are many choices and options in the construction of regional gravity field models. Various types of space-localizing base functions, the position of the base functions, treatment of border distortions and the inversion of the resulting ill-posed model can be mentioned for instance. Almost in all previous works, the choices have been made using trial and error.
The goal of this PhD thesis is to develop a simple and efficient methodology for the regional gravity field determination. We try to provide a reasonable strategy to put various components of regional gravity field modelling together in a logical way. Thus, no extemporary choice shall be made in our methodology. The emphasis is put on the satellite data but the method can be generalized to other types of observations as well. In addition, we focus particularly on the inversion process where the solution must be obtained by means of a proper regularization method.

1.2 Thesis outlines

This PhD thesis is organized in seven chapters. In the remaining part of chapter 1, the basic definitions in the context of the Earth's gravity field are given. Section 2 is dedicated to the gravity field determination from satellite data. A brief history of the gravity satellite missions is given. The precise orbit determination as an important step in gravity field recovery will be shortly discussed. Moreover, several approaches for the functional link between GRACE-type SST (Satellite-to-Satellite Tracking) data and the gravitational potential are summarized. Furthermore, the functional model to determine the Earth's gravity field based on the GOCE gravity gradients as well as related problems will be considered. The section ends with the consideration of the state-of-the-art and current developments in global gravity field modelling based on satellite data.
The representation of the global gravity field on the Earth's surface will be investigated in chapter 3. First the mathematical description of spherical harmonics as well as SRBF are given in detail. The least-squares adjustment to determine the unknown coefficients will be addressed as well. As an alternative to spherical harmonics, the applicability of SRBF to represent the gravity field on the global scale is considered. Although it is not common to use the SRBF for the global modelling of the gravity field (due to its high computational burden compared to spherical harmonics), such practice gives an insight into the regularization of regional solutions using these base functions.
Section 4 addresses the regional modelling of the gravity using the SRBF. Due to the diversity of options for the regional setup, a collection of choices has to be made to end up with the observation equations. We discuss these choices and propose our methodology for the regional model setup.
Once the model is set up, the resulting observation equations are strongly inconsistent and the associated design and normal matrices are strongly ill-posed. A useful solution should be then obtained by means of a proper regularization method. This is a crucial issue in regional gravity field determination which must be taken into account considerately. The regularization procedure of the ill-posed problems will be generally investigated in chapter 5. The emphasis is put on the standard Tikhonov regularization where the choice of the regularization parameter is the key issue. We address several well-known approaches for the choice of the regularization parameter and discuss their characteristics. A new approach, called the parameter-signal-correlation (PSC), will be proposed for the choice of the regularization parameter. The PSC method is dedicated to the regularization of ill-posed problems where the SRBF serve as the analysing (base) functions.
In chapter 6, the performance of these regularization approaches will be studied in a comparison manner. To check the methods under different conditions, the regional solutions will be determined in several test areas and based on different types of satellite observations.
At the end, the summary and concluding remarks as well as further research directions in this field will be provided in chapter 7.

1.3 Preliminaries

1.3.1 Units and constants

There are mainly two units used for the gravity: $^{\mathrm{N}}/_{\mathrm{kg}}$ (Newton per kilogram) and $^{\mathrm{m}}/_{\mathrm{s}^2}$. The former is used in analysis systems where the gravity, as a force, interacts with other forces. The latter, $^{\mathrm{m}}/_{\mathrm{s}^2}$, is widely used in physics and geosciences, where gravity is considered as an acceleration. In geodesy and geophysics another unit, gal, is also used for more detailed considerations. $1\,\mathrm{gal}$ is equal to $1\,^{\mathrm{cm}}/_{\mathrm{s}^2}$ or $10^{-2}\,^{\mathrm{m}}/_{\mathrm{s}^2}$. For some applications mgal (milligal) and $\mu\mathrm{gal}$ (microgal) are used. The relations between these units are

$$1\,^{\mathrm{N}}/_{\mathrm{kg}} = 1\,^{\mathrm{m}}/_{\mathrm{s}^2} = 10^2\,\mathrm{gal} = 10^5\,\mathrm{mgal} = 10^8\,\mu\mathrm{gal}. \tag{1.1}$$

The unit used for the potential is $^{\mathrm{m}^2}/_{\mathrm{s}^2}$. The second derivatives of the gravitational potential or gravity gradients, have the dimension $^{1}/_{\mathrm{s}^2}$. Another unit used for the gravity gradients is Eötvös which is equal to $^{10^{-9}}/_{\mathrm{s}^2}$.
In the context of the Earth's gravity field modelling, several constants are used. These values might be slightly different in various standards and models. We use the numerical values given by the International Earth Rotation and Reference Systems Service (Petit and Luzum, 2010). Table 1 gives the value and the definition of these constants which will be used in this thesis.

Constant	definition	value	dimension
G	universal gravitational constant	6.67428×10^{-11}	$\mathrm{m}^3/\mathrm{kgs}^2$
GM	geocentric gravitational constant	$0.3986004418 \times 10^{15}$	$\mathrm{m}^3/\mathrm{s}^2$
a	semi major axis of rotational ellipsoid	6.3781366×6	m
ω_e	the Earth's angular velocity	7.29211×10^{-5}	rad/s

Table 1.1: The constants used in this thesis for gravity field determination. These values are given by the international Earth Rotation and Reference Systems Service.

1.3.2 Components of the Earth's gravity field

The gravity field of the Earth is composed of two parts:

- The gravitational part: this part is the consequence of all gravitational attractions within the Earth system including its atmosphere. Gravitational acceleration $\mathbf{g}^g$ at position *i* is a function of mass distribution and mass densities inside the Earth and is given by Newton's law of gravitation (e.g. Heiskanen and Moritz (1967)):

$$\mathbf{g}_i^g = GM \iiint_{\mathbb{V}} \frac{\rho(\mathbf{r})}{\|\mathbf{r} - \mathbf{r}_i\|^3}(\mathbf{r} - \mathbf{r}_i)d\mathbb{V} \tag{1.2}$$

  in which $\rho(\mathbf{r})$ is the density of the Earth as a function of the position vector $\mathbf{r}$ and $d\mathbb{V}$ is an infinitesimally small element of the volume of the Earth $\mathbb{V}$.

- The centrifugal part: this acceleration is caused by the Earth rotation and is computed using the Earth's angular velocity vector $\boldsymbol{\omega}_e$ and the distance $\mathbf{p}_i$ from the Earth rotation axis:

$$\mathbf{g}_i^c = \boldsymbol{\omega}_e \times (\boldsymbol{\omega}_e \times \mathbf{p}_i). \tag{1.3}$$

  The maximum value of the centrifugal acceleration is on the equator and is approximately equal to $3.4 \times 10^{-2}\ \mathrm{m}/\mathrm{s}^2$. There is consequently no centrifugal acceleration at poles since $\mathbf{p}_i = 0$.

The sum of these two accelerations is called the gravity $\mathbf{g}$:

$$\mathbf{g} = \mathbf{g}^g + \mathbf{g}^c. \tag{1.4}$$

In this thesis, the gravitational acceleration shall be considered. We use the terms gravitational acceleration and gravity alternatively but unless otherwise stated, we mean the gravitational acceleration part.

1.3.3 Functionals and observables of the Earth's gravity field

The vector of gravity is the gradient of a scalar field which is the **gravitational potential**. The gravitational potential is denoted by V and is defined as:

$$\nabla V = \mathbf{g} \tag{1.5}$$

in which $\nabla = \begin{bmatrix}\partial/\partial x & \partial/\partial y & \partial/\partial z\end{bmatrix}^T$ is the gradient operator in an arbitrary three dimensional coordinate system defined by the axes x, y and z. The main part of the gravitational potential can be described by the potential of a reference ellipsoid approximating the figure of the Earth. This reference field is called the normal potential and is denoted by U. The difference between the gravitational potential and the normal potential is the disturbing potential T:

$$T = V - U. \tag{1.6}$$

Similar to (1.5), the normal gravity is the gradient of the normal potential:

$$\nabla U = \boldsymbol{\gamma}. \tag{1.7}$$

The vectors of the normal gravity $\boldsymbol{\gamma}$ and the gravity $\mathbf{g}$ are different in their magnitude and their direction. The difference in the magnitude is called the **gravity anomaly** defined by:

$$\Delta g = g_P - \gamma_Q \tag{1.8}$$

where g_P is the (reduced) gravity at the point P on geoid and γ_Q denotes the normal gravity at point Q on the reference ellipsoid. See e.g. Hofmann and Moritz (2005) or Vanicek and Krakiwsky (1982). The directional difference between the gravity and the normal gravity is called the **deflection of the vertical** and has two components: the north-south component ξ, and the east-west component η defined by

$$\begin{cases} \xi = \Phi - \phi \\ \eta = (\Lambda - \lambda)\cos\phi \end{cases} \tag{1.9}$$

in which (Φ, Λ) are the astronomical latitude and longitude or astronomical coordinates and (ϕ, λ) are the geodetic latitude and longitude on the ellipsoid coordinates. See, e.g. Vanicek and Krakiwsky (1982) and Torge and Müller (2012) for the definition of astronomical and geodetic coordinates.
The distance between the points P and Q is the **geoid height** N. The geoid height or the geoid undulation can be obtained from the disturbing potential T and the normal gravity γ using:

$$N = \frac{T}{\gamma} \tag{1.10}$$

The second derivative of the gravitational potential, called the **gravity gradients**, are defined as follows:

$$\nabla^2 V = \nabla \mathbf{g}. \tag{1.11}$$

The gravity gradients consist of 9 components V_{ij} where $i = 1, 2, 3$ and $j = 1, 2, 3$ define the axes of the coordinate system in which the derivatives are taken. For more details on the definition of different functional of the gravitational potential as well as their interrelations see, e.g., Hofmann and Moritz (2005) or Torge and Müller (2012).
There are currently various observation techniques and instruments to measure the functionals of the gravitational potential. For example the absolute and relative values of gravity can be measured by absolute and relative gravimeters (Xu, 2010). The deflection of vertical can be obtained by the observations from zenith cameras and GPS coordinates (Hirt *et al.*, 2010). The geoid heights are derived based on the combination of GPS-levelling and gravimetric data (Torge and Müller, 2012). In addition, it is also possible to determine geoid heights over the oceans based on satellite altimetry data (Bosch, 2002, Lee-Lueng and Cazenave, 2000). Finally, gravity gradients are observed on ground using the torsion balances or from space using satellite gravity gradiometery. These observations are different in the sense that they contain different spectral content depending on the resolution and accuracy of the corresponding instrument. These functionals can be used to determine the gravitational potential as the mother function.
The direct measurement of the geopotential difference is theoretically possible based on the relativistic approach (Bjerhammer, 1975) using high precision clocks. The approach -where the gravitational redshift from clock reading at different places is observed- offers a new technique for the direct measurement of the potential differences in continental distances without satellite systems (Bjerhammer, 1985). The quality of this method is highly dependent on the precision of clocks. The research in this field is still ongoing to make use of modern measurement techniques for the determination of time and frequency using atomic clocks.

2 Gravity field from satellite data

According to equation (1.2), an accurate determination of the Earth's gravity field would be possible if sufficient information about the Earth's structure and mass densities were available. But due to the lack of such information, there is no exact analytical way to determine the gravity. The only way to obtain information about it, is to **measure** it. Gravity can be measured on the Earth's surface (terrestrial gravimetry), by an aircraft (airborne gravimetry) or from space using observations provided by the satellite missions (satellite gravimetry). Terrestrial gravimetry consists of point-wise observations using relative or absolute gravimeters which are of high accuracy and precision. The coverage of such data is often very poor, inhomogeneous and limited to some areas. In addition terrestrial gravimetry is very time consuming and expensive. Airborne gravimetry is an efficient way to provide accurate high-resolution gravity data on regional scales. With current airborne gravimetry systems the gravity can be obtained at a spatial resolution of $2\,\mathrm{km}$ with an accuracy of $1-2\,\mathrm{mgal}$ (Alberts, 2009).
Observing the Earth's gravity field from space has been possible since the early 1960's. A noteworthy feature of satellite techniques is the availability of homogeneous observations on the global scale which has not been possible before. In the last four decades, several low-Earth orbiting satellites have been launched and valuable satellite-based data are provided. Table 2.1 gives an overview of some selected past as well as the current satellite mission. Based on the data provide by these missions, many gravity models have been released in terms of spherical harmonic expansions of the Earth's gravitational potential. The quality of these models has been rapidly improved as the latest advanced sensors were employed in the missions.

Mission name	Year launched	Altitude (km)	Inclination (degrees)	Tracking method	Observation technique
GEOS-3	1975	820	115	SLR	Altimetry
GeoSAT	1985	800	108	SLR	Altimetry
Topex Poseidon	1992	1330	66	GPS/SLR	Altimetry
CHAMP	2000	450	87	GPS	SST-hl
GRACE	2002	500	89.5	GPS	SST-hl/ll
GOCE	2009	250	96	GPS	SST-hl and SGG
GRACE Follow on	2017 (planned)	500	89.5	GPS	SST-hl/ll

Table 2.1: Some of past and current dedicated satellite missions used for gravity field determination.

A new era of satellite gravimetry began in the year 2000 when the CHAllenging Minisatellite Payload (CHAMP) was placed into orbit. CHAMP mission was followed by the Gravity recovery and climate experiment (GRACE) in 2002 and Gravity field and steady-state Ocean Circulation Explorer (GOCE) in 2009. The GRACE twin satellites, for the first time, provide valuable information about the time variable components of the Earth's gravity field in long and medium wavelength. The innovative observation technique in the GRACE mission is the K-band ranging system which measures the range between two satellites with a micrometer accuracy (Tapley *et al.*, 2004). GOCE carries the first-ever gravity gradiometer in space and is about to supply an unprecedented level of accuracy in determining the gravity of the Earth. Follow-on gravity missions are now being designed and prepared to operate in a very near future with the idea of sensor integration and data combination (Hofmann and Moritz, 2005). Rummel *et al.* (2002) gives more details on the principle of

dedicated satellite missions and their aims.
There are mainly three observation techniques for the recovery of the Earth's gravity field from space: satellite altimetry, satellite-to-satellite tracking (SST) and satellite gravity gradiometry (SGG). With the satellite altimetry it is possible to measure the distance from the satellite to a reflecting surface using the radar (and laser) techniques to determine the sea level. The outcome of the satellite altimetry is the mean sea level which results in a good approximation of geoid heights in the oceans and seas. In addition, the sea level slope is a good approximation of the deflections of the vertical and sea surface curvature can be translated to the vertical gravity gradients. See Bosch (2002) for more details about satellite altimetry and its application in geodetic science.
Generally speaking, there are two important steps which should be specified in gravity field modelling from satellite data:

- An approach to set the link between satellite observables and the Earth's gravitational potential
- A method to represent the gravitational potential on the Earth's surface or above

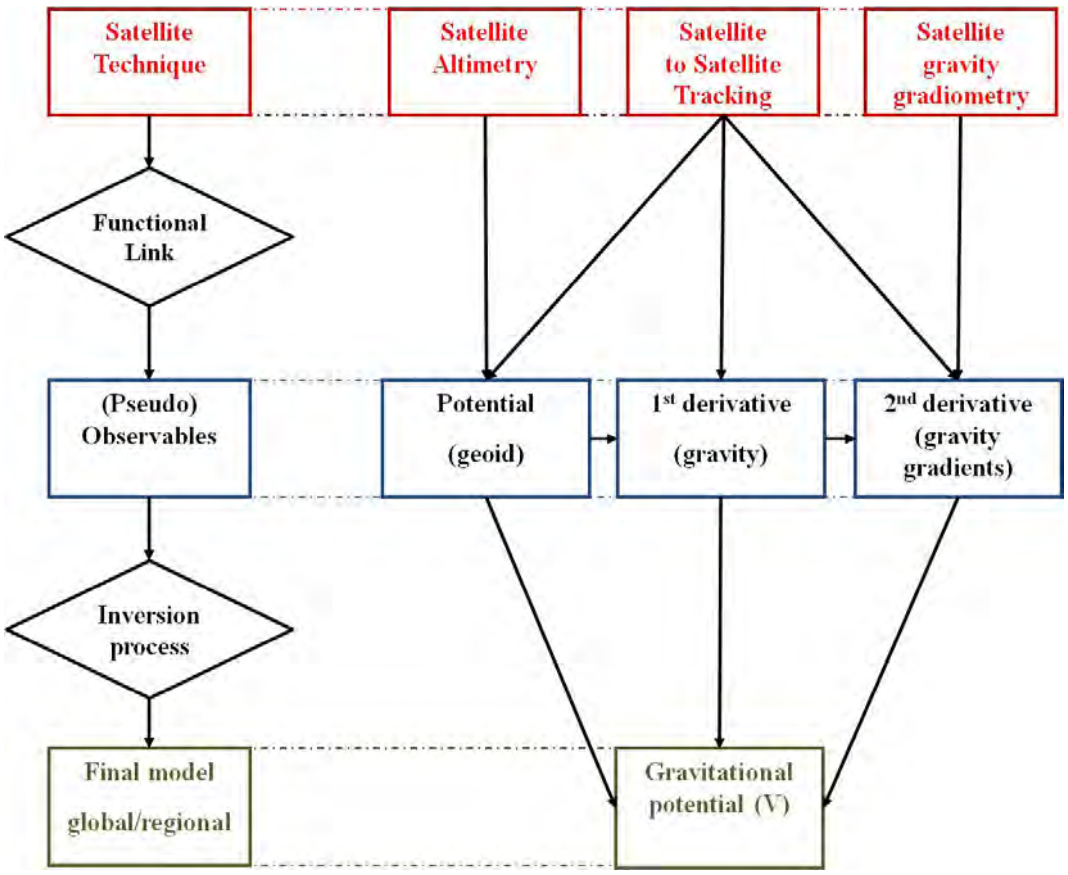

Figure 2.1: Recovery of the Earth's gravity field based on different satellite techniques. The observations from satellites are, first, mathematically linked to a functional of the Earth's gravitational potential. In the next step, the gravitational potential is determined in an inversion process using appropriate set of base functions.

Figure 2.1 displays different steps for the recovery of the gravity field from satellite data. In the first step, the observations from satellite missions should be linked to a functional of the Earth's gravity field. Then the gravity field shall be represented on the Earth's surface using a set of appropriate base functions. For this step, the Earth's gravity field parameters should be solved for by inverting a large system of equations which is often ill-posed.

In this chapter, several approaches for the functional link between satellite data and the gravity field will be considered. More details on the SST and SGG techniques are given which will be used, further, for global and regional gravity field modelling. The issue of inversion for the gravity field representation, which is the main focus of this PhD thesis, will be investigated in the next chapters.

2.1 Precise orbit determination

The position and velocity of the satellites play the central role in all techniques for the recovery of the Earth's gravity field from satellite data. One reason is that the orbit of the satellites, i.e. the positions and velocities, are affected by the Earth's gravitational field. Therefore, the precise determination of the satellite orbits is essential for gravity field modelling. In addition, the precise orbit data are necessary to locate in-orbit observations such as range and range rates from GRACE or SGG data from GOCE. Hence, one important step for gravity field modelling is to precisely determine the orbit of the satellite(s). There are several methods for precise orbit determination. Kinematic orbit determination, dynamic orbit determination and reduced dynamic orbit determination can be mentioned for instance. For more details concerning the precise orbit determination see for example Kang *et al.* (2006), Jäggi *et al.* (2007), Montenbruck and Gill (2000), Kroes (2006), Bisnath (2004) and Zaho (2004).
In gravity field determination based on satellite data, the position of Low Earth Orbiter (LEO) satellites can be assumed to be known. Therefore the precise orbits are determined beforehand and then gravity field parameters are estimated. This method is known as two-step approach. However, it is possible to improve the satellite orbit along with the gravity field parameters simultaneously. In this one-step approach the SST-hl (high-low) data from the GPS satellites as well as the SST-ll (low-low) data are employed to determine the orbit of the LEO satellite in addition to the Earth's gravity field parameters. In the one-step approach, the orbit of the GPS satellites are assumed to be precisely known and thus fixed. One can even try to improve the GPS orbit at the same time with the LEO orbit and the gravity field parameters. This integrated approached is proposed by Zhu *et al.* (2004). The idea was to use all available data from GPS, GRACE and CHAMP satellites as well as the ground-based GPS code and phase data for the simultaneous determination of GPS and LEO orbit as well as the gravity field parameters. They concluded that this approach improves the accuracy of the ephemerides for the GPS, GRACE and CHAMP satellites in addition to the geocenter variations and the gravity field parameters, compared to stepwise methods. The benefit of this approach is that the equation system to be solved for, gains stability from high satellites and sensitivity from low satellites.
In the context of this thesis, the positions and velocities of the LEO satellites are assumed to be fixed during gravity field modelling. No orbit determination is included here and only the Earth's gravity field parameters are to be estimated in a two-step approach.

2.2 Gravity field from SST data

Satellite-to-satellite tracking data or SST are among the most important satellite-based data sets which are sensitive to the medium and short wavelengths of the Earth's gravity field. According to Rummel *et al.* (1978), the advantageous characteristics of SST are:

- continuous tracking between satellites,
- possibility to maintain an ideal observation geometry and
- sensitivity to the medium and short wavelengths of the gravity field.

One can distinguish between SST-hl mode and SST-ll. The former technique, which was first proposed by Kaula (1966), includes position and velocities of one or more low Earth orbiting satellites which are continuously provided by satellites at high orbits (GPS satellites for instance). The CHAMP is using SST-hl for example. However this technique is not that different from conventional tracking of satellites from ground stations (Rummel et al. 1978) and hence it is not capable of recovering medium wavelengths of the gravity field. Wolff (1969) proposed the idea of low-low SST using a satellite pair, which is more sensitive to the medium

and short wavelengths of the gravity field. His idea became reality about thirty years later in March 2002 when the GRACE twin satellites were placed into the orbit. SST-ll consists of inter-satellite ranging products which are known as **range**, **range rates** and **range accelerations**. Gravity field recovery from GRACE observations combines both the SST-hl and SST-ll techniques to achieve a spatial resolution down to $400\,\mathrm{km}$ on the Earth's surface based on a month of data. Figure 2.2 displays the concept of SST in both high-low and low-low constellation.

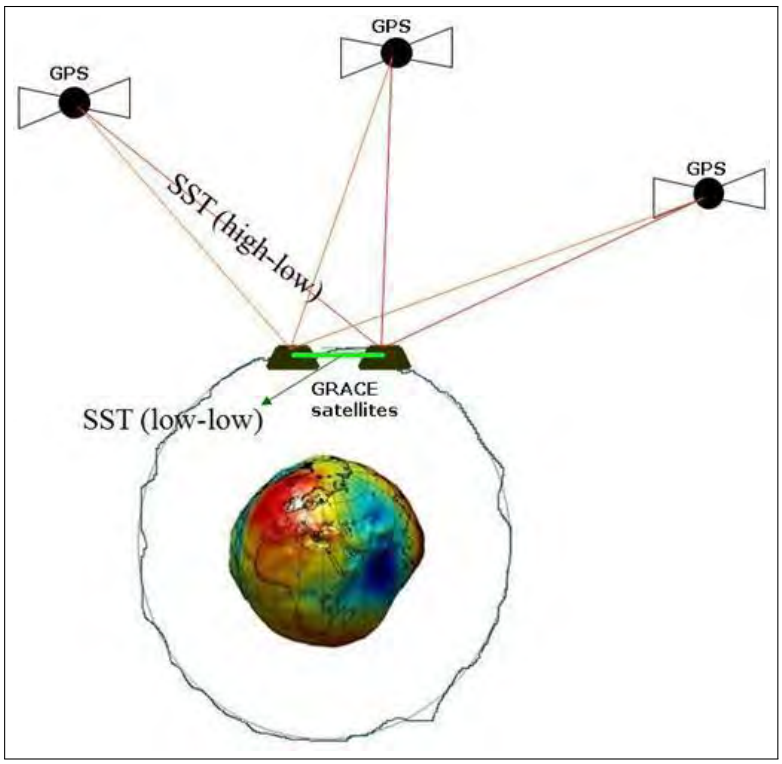

Figure 2.2: Concept of SST high-low and SST low-low applied in the GRACE mission.

An important step in gravity field modelling based on SST data is to set a link between these data and the gravitational potential. Two physical laws are usually used in satellite geodesy for this purpose:

- **Newton's law of motion**: Combining the Newton's second law of motion, ($\mathbf{f} = m\mathbf{g}$) with the Newton's universal law of gravitation yields

$$\ddot{\mathbf{r}} = \boldsymbol{\nabla} V. \tag{2.1}$$

  Therein $\ddot{\mathbf{r}}$ denotes the acceleration vector of the satellite and V is the gravitational potential of the Earth. Based on this law, there are roughly three approaches that are in use at present for the Earth's gravity field recovery: **the variational approach**, **the short arc approach** and **the acceleration approach**.

- **Energy conservation law**: In mechanics, conservation of energy is

$$C = E + V \tag{2.2}$$

  where E and V are the kinetic and potential energy, respectively. C denotes the total energy which is conserved over time. This law can be used in gravity field modelling as **the energy balance** approach.

In the following, these approaches are explained briefly with emphasis put on the energy balance approach which will be used further in our global and regional gravity field modelling.

2.2.1 Variational approach

The variational approach is the traditional method to determine gravity field parameters. It can be either a one-step approach or a two-step approach. According to Reigber (1989), the equation of motion has the form

$$\ddot{\mathbf{r}} = f(\mathbf{r}, \dot{\mathbf{r}}, \mathbf{p}) \tag{2.3}$$

which describes the acceleration of a satellite as a function of initial positions $\mathbf{r}$, velocities $\dot{\mathbf{r}}$ and a set of parameters $\mathbf{p}$ to which the accelerations are sensitive. The set $\mathbf{p}$ includes two types of parameters:

- Internal or arc-dependent parameters
  - state vector at each epoch,
  - drag and solar radiation pressure parameters.
- External or arc-independent parameters
  - gravity field parameters,
  - tidal parameters,
  - Earth rotation parameters.

The parameters $\mathbf{p}$ have to be estimated in an iterative process due to the non-linearity of the observation equation (2.3) with respect to the vector $\mathbf{p}$. The linearisation process is done through computing the partial derivatives of the acceleration vector $\ddot{\mathbf{r}}$ with respect to the unknown vector $\mathbf{p}$. See also Beutler *et al.* (2010) for more detailed description of the variational approach.

2.2.2 Short arc approach

The short arc approach is a variant of the variational approach explained in the previous section. The idea of using short arcs for gravity field recovery is to control accumulated effects of disturbing forces. Moreover, a kinematic orbit determination cannot provide continuous orbit data over a long period of time (i.e. more than a year). The reasons for that are gross errors and gaps in SST observations as well as orbit manoeuvres or other events (Mayer-Gürr *et al.*, 2005). Hence, it is logical to restrict the analysis to several short arcs. The short-arc approach is based on Newton's equation of motion which is formulated as a boundary value problem in the form of a Fredholm integral equation. For every short arc in the time period, the solution of equation (2.1) with boundary values $\mathbf{r}_A = \mathbf{r}(t_A)$ and $\mathbf{r}_B = \mathbf{r}(t_B)$ reads (Schneider, 1968);

$$\mathbf{r}(\tau) = (1-\tau)\mathbf{r}_A + \tau\mathbf{r}_B - t_{AB}^2 \int_{\tau'=0}^{1} K(\tau,\tau')\ddot{\mathbf{r}}(\tau')d\tau' \tag{2.4}$$

where τ is a normalized time variable at which the position vector is desired. τ is defined as

$$\tau = \frac{t - t_A}{t_{AB}}, \quad t_A \le t \le t_B, \tag{2.5}$$

and τ' is the integration variable for the given forces $\ddot{\mathbf{r}}$. The kernel $K(\tau,\tau')$ is

$$K(\tau,\tau') = \begin{cases} \tau(1-\tau'), & \tau \le \tau' \\ \tau'(1-\tau), & \tau' \le \tau \end{cases} . \tag{2.6}$$

In equation (2.4), the position vector $\mathbf{r}$ is used directly as the observation and no numerical differentiation is needed. The short-arc or the integral equation approach has been successfully used in a series of gravity field modelling from CHAMP kinematic orbit (Mayer-Gürr *et al.*, 2005), and GRACE K-Band Ranging (KBR) data (Mayer-Gürr, 2006).

2.2.3 Acceleration approach

The acceleration approach is a direct application of equation (2.1). The accelerations of the satellite at discrete points i are used as the observed values to determine gravity field parameters (Reubelt *et al.*, 2003). At each discrete point i, three observation equations can be written to set up the linear system of equations:

$$\boldsymbol{\nabla} V_i = \begin{bmatrix} V_x \\ V_y \\ V_z \end{bmatrix}_i = \begin{bmatrix} \dfrac{\partial V}{\partial x} \\ \dfrac{\partial V}{\partial y} \\ \dfrac{\partial V}{\partial z} \end{bmatrix}_i . \tag{2.7}$$

Since the output of the precise orbit determination is the position vector, the acceleration vector $\ddot{\mathbf{r}}$ should be derived by two times numerical differentiation of the position vector $\mathbf{r}$. The drawback of this approach is that numerical differentiation of noisy data results in noise amplification especially at higher frequencies. To overcome this problem some kind of regularization is necessary for high-resolution gravity field recovery. Besides, numerical differentiation includes fitting a polynomial of a certain degree defined at a set of epochs. Thus the derivative of this polynomial can be obtained analytically and consequently the velocity and acceleration vectors can be evaluated (Lio, 2008). In order to obtain a rather good approximation of accelerations at points i, high degree polynomials should be used. Reubelt *et al.* (2006) showed that the degree of this polynomial should be at least 8. This leads, however, to instabilities in the numerical differentiation process and tailored algorithms must be used. Lio (2008) used an average acceleration scheme for processing real CHAMP and GRACE kinematic orbits and concluded that satellite acceleration derived from kinematic orbits can be used for high quality Earth's gravity field modelling. The acceleration approach, in the case of GRACE KBR data has a slightly different formulation. It is sometimes called the difference acceleration approach since it deals with relative quantities. According to Rummel (1979), to derive the equation of difference acceleration approach for GRACE-type observations, one can start from the position vector between two satellites $\mathbf{r}_{AB}$

$$\mathbf{r}_{AB} = \mathbf{r}_B - \mathbf{r}_A, \tag{2.8}$$

where $\mathbf{r}_{AB}$ is the difference of position vector of the satellites in an Earth-fixed frame. The inner product of this vector with itself gives the square of the **range** ρ:

$$\rho^2 = \mathbf{r}_{AB} \cdot \mathbf{r}_{AB}. \tag{2.9}$$

Taking the first derivative of equation (2.9) yields

$$\rho\dot{\rho} = \mathbf{r}_{AB} \cdot \dot{\mathbf{r}}_{AB}. \tag{2.10}$$

$\dot{\rho}$ and $\dot{\mathbf{r}}_{AB}$ are **range-rate** and the velocity difference vector, respectively. Equation (2.10) can be rewritten as

$$\dot{\rho} = \frac{\mathbf{r}_{AB}}{\rho} \cdot \dot{\mathbf{r}}_{AB}. \tag{2.11}$$

Therein $\dfrac{\mathbf{r}_{AB}}{\rho}$ is the orthonormal line of sight vector or briefly, hereafter, LOS vector:

$$\mathbf{e}_{LOS} = \frac{\mathbf{r}_{AB}}{\rho}. \tag{2.12}$$

Substituting (2.12) into (2.11) and taking its time derivative results in the **range-acceleration** $\ddot{\rho}$:

$$\ddot{\rho} = \dot{\mathbf{e}}_{LOS} \cdot \dot{\mathbf{r}}_{AB} + \mathbf{e}_{LOS} \cdot \ddot{\mathbf{r}}_{AB} \tag{2.13}$$

where $\ddot{r}_{AB}$ is the acceleration difference between the two satellites. Rearranging (2.13) and replacing $\ddot{\mathbf{r}}_{AB}$ by $\boldsymbol{\nabla} V_{AB}$ gives the final equation of the (difference) acceleration approach:

$$\mathbf{e}_{LOS} \cdot \boldsymbol{\nabla} V_{AB} = \ddot{\rho} + \frac{\dot{\rho}^2}{\rho} - \frac{|\dot{\mathbf{r}}_{AB}|^2}{\rho} \tag{2.14}$$

where $|.|$ denotes the lengths of a vector. Equation (2.14) indicates that the projection of the acceleration difference of the satellite pair onto the LOS vector can be linked to the inter satellite data products range, range-rates and range-acceleration.
The left hand side of this equation contains the gravity field parameters to be estimated (depending on the type of representation) and the observables are on the right hand side. The range rate $\dot{\rho}$ and the range accelerations $\ddot{\rho}$, are derived by numerical differentiation of the biased range and the range rate $\dot{\rho}$ respectively. Therefore these quantities are affected by the disadvantages of the numerical differentiation (noise amplification by differentiating). The range ρ and velocity difference $\dot{r}_{AB}$ are numerically derived from GPS data and therefore their accuracy does not match the accuracy of $\dot{\rho}$. Thus equation (2.14) without any modification cannot be suitable for high quality gravity field recovery from GRACE data. Lio (2008) presented two modified variants of the acceleration approach; 3-point range-rate combination (3RRC) and 3-point range combination (3RC) approach to reduce the role of GPS-derived quantities in the modelling. The idea of the 3RRC approach is to compute radial components of velocity differences from KBR data and thus to reduce the impact of GPS data on the overall error budget. In the 3RC approach the velocity term is totally removed from the observation equation. Hashemi *et al.* (2012) used the 3RC approach to determine the static part of the Earth's gravitational potential based on the combination of GRACE and GOCE data.

2.2.4 Energy balance approach

As stated before, the energy balance approach is based on the physical law of energy conservation. Based on equation (2.2) one can assume that the potential energy of a satellite (with negative sign[1]) is equal to the sum of kinetic energy and a constant (total energy of the closed system) in an ideal case, where no other forces act on the satellite:

$$V = E + C. \tag{2.15}$$

The kinetic energy of a satellite is given by:

$$E = \frac{1}{2}\|\dot{\mathbf{r}}\|^2 \tag{2.16}$$

which is the energy per unit mass. Equation (2.15) cannot describe the motion of a satellite in its orbit. The first reason is the Earth rotation which causes the potential field to be rotational for the satellite. This means the rotation of the potential field should also be considered in (2.15). Moreover, there are other forces (rather than the gravitational force) which are considered as dissipating energy in the system. According to Jekeli (1999), the exact relationship of the energy conservation law in an inertial frame for a satellite is given by

$$V = \frac{1}{2}\|\dot{\mathbf{r}}\|^2 + \int_0^t \frac{\partial V}{\partial t} dt - \sum_k \int_0^t \mathbf{F}_k . \dot{\mathbf{r}}_k dt + C. \tag{2.17}$$

[1]The term potential has different definition in physics and geodesy. In physics, potential is a feature of particle and is the work necessary to bring a particle from its initial state to its current position. In geodesy, potential is a feature of the field and is proportional to the work necessary to bring a particle from infinity to its current position. Therefore potential in geodesy appears with negative sign compared to physics literature.

Therein the second term on the right hand side is the time variation of the potential due to Earth rotation in the inertial frame which is integrated along the orbit within the time period $[0\ \ t]$. The third term is the dissipating energy which is the sum of the known k non-gravitational forces. The potential rotation term can also be written as (Jekeli, 1999)

$$\int_0^t \frac{\partial V}{\partial t} dt = -\omega_e(x\dot{y} - y\dot{x}) \tag{2.18}$$

with ω_e being the Earth's angular velocity. x and y are the Cartesian coordinates and $\dot{x}$ and $\dot{y}$ are their first derivatives i.e the velocities. Therefore equation (2.17) can be rewritten as

$$V = \frac{1}{2}\|\dot{\mathbf{r}}\|^2 - \omega_e(x\dot{y} - y\dot{x}) - \sum_k \int_0^t \mathbf{F}_k \dot{\mathbf{r}}_k dt + C. \tag{2.19}$$

This relation is valid in an inertial reference frame with a rotating Earth. The representation of the gravitational field is desired in an Earth fixed frame with rotating coordinate system. In Earth fixed frame the '**rotation potential**' should be considered instead of '**potential rotation**'. These names are proposed by Jekeli (1999) to distinguish between potential in inertial and Earth fixed frames. For the rotation potential in an Earth fixed frame one can write

$$Z_{rot} = \frac{1}{2}(\omega_e \times \mathbf{r})^2 \tag{2.20}$$

or

$$Z_{rot} = \frac{1}{2}\omega_e^2(x^2 + y^2). \tag{2.21}$$

(2.19) in an Earth fixed frame reads:

$$V = \frac{1}{2}\|\dot{\mathbf{r}}\|^2 - \frac{1}{2}\omega_e^2(x^2 + y^2) - \sum_k \int_0^t \mathbf{F}_k \dot{\mathbf{r}}_k dt + C. \tag{2.22}$$

It should be noted that all components in (2.19) and (2.22) must be used with respect to inertial frame and Earth fixed frame, respectively.
These equations are applicable for one satellite such as CHAMP or GOCE. For GRACE observations with the KBR link, the equation can also be written for two satellites, i.e. potential differences between satellites A and B. Writing equation (2.19) for the potential differences yields

$$\begin{aligned} V_{AB} = \frac{1}{2}\|\dot{\mathbf{r}}_B\|^2 - \frac{1}{2}\|\dot{\mathbf{r}}_A\|^2 - \omega_e(x_B\dot{y}_B - y_B\dot{x}_B - x_A\dot{y}_A + y_A\dot{x}_A) \\ - \sum_k \int_0^t (\mathbf{F}_{Bk}\dot{\mathbf{r}}_{Bk} - \mathbf{F}_{Ak}\dot{\mathbf{r}}_{Ak}) dt + C_{AB}. \end{aligned} \tag{2.23}$$

The difference of kinetic energy between two satellites can be rewritten in terms of KBR products:

$$E_{AB} = \frac{1}{2}\|\dot{\mathbf{r}}_B\|^2 - \frac{1}{2}\|\dot{\mathbf{r}}_A\|^2 = \frac{1}{2}(\dot{\mathbf{r}}_A + \dot{\mathbf{r}}_B)^T \dot{\mathbf{r}}_{AB}. \tag{2.24}$$

Taking the first derivative of (2.12)

$$\dot{\mathbf{r}}_{AB} = \dot{\rho}\mathbf{e}_{LOS} + \rho\dot{\mathbf{e}}_{LOS} \tag{2.25}$$

and applying this to (2.24) results in

$$E_{AB} = \frac{1}{2}(\dot{\mathbf{r}}_A + \dot{\mathbf{r}}_B)^T(\dot{\rho}\mathbf{e}_{LOS} + \rho\dot{\mathbf{e}}_{LOS}). \tag{2.26}$$

Inserting this equation in (2.23) yields:

$$\begin{aligned} V_{AB} = \frac{1}{2}(\dot{\mathbf{r}}_A + \dot{\mathbf{r}}_B)^T(\dot{\rho}\mathbf{e}_{LOS} + \rho\dot{\mathbf{e}}_{LOS}) - \omega_e(x_B\dot{y}_B - y_B\dot{x}_B + x_A\dot{y}_A - y_A\dot{x}_A) \\ - \sum_k \int_0^t (\mathbf{F}_{Bk}\dot{\mathbf{r}}_{Bk} - \mathbf{F}_{Ak}\dot{\mathbf{r}}_{Ak})dt + C_{AB}, \end{aligned} \tag{2.27}$$

which relates the KBR data to the potential difference between the GRACE satellites along their orbit. The energy constant C_{AB} can either be computed using a prior model or estimated along with gravity field parameters as an additional unknown parameter. The term for dissipating energy can be neglected when dealing with simulated data. Therefore we exclude this term in our analyses. An advantage of the energy balance or energy integral approach is that it is linear with respect to the Earth's gravitational parameters (similar to the acceleration approach). There is no need for an iterative procedure compared to variational approach. It is numerically more efficient than the variational approach provided that precise kinematic orbit is available. This approach has been used to determine several gravits field models; TUM-1s and TUM-2s from CHAMP data (Gerlach *et al.*, 2003). Han *et al.* (2002, 2005, 2006) used this approach to model gravity field based on CHAMP and GRACE data.
It should also be mentioned that the energy balance approach is affected by the accuracy of the velocity vector which is derived numerically from the GPS data. As a result of numerical differentiation, the noise of the velocity will be amplified proportional to the frequency. Hence, the resulting correlated noise should be handled properly in the inversion process (e.g. by frequency dependent weighting). See Han *et al.* (2006) for more details on this issue.

2.3 Gravity field from SGG data

The goal of gravimetry, as explained before, is to determine the Earth gravitational potential based on the data provided by gravimeters. Gravimeters measure the first derivative of the gravitational potential, i.e. $\boldsymbol{\nabla}V$. Similar to gravimetry, the goal of gradiometry is also the accurate determination of the Earth gravitational potential. The measured data in gradiometry are the second derivatives of the gravitational potential which are called gravity gradients. The gravity gradients can be observed on the Earth's surface using the Torsion Balance which was invented by Roland von Eötvös at the beginning of 20^{th} century. He obtained, with his instrument, the precision of $10^{-9}/\mathrm{s}^2$ or $1\,\mathrm{E}$[1].
The idea of measuring gravity gradients using satellites or SGG is more than 50 years old. However, there was no realization of SGG until the launch of GOCE in 2009. According to the GOCE mission objectives (Gruber *et al.*, 2010) the goal is to achieve an accuracy of $1\,\mathrm{mgal}$ for gravity anomalies or $1-2\,\mathrm{cm}$ of geoid heights at a spatial resolution of $100\,\mathrm{km}$ based on observed gravity gradients on board the GOCE satellite. For more details on the concepts and principles of the GOCE (Rummel *et al.*, 2012). In this section, the principle of gravity field modelling based on GOCE gradiometry is briefly explained to the extent which fulfils the purpose of this thesis.

[1]The CGS unit for gravitational gradient is named Eötvös in his honour.

2.3.1 Gravity gradiometry

Equation (2.7) describes the first derivative of the gravitational potential V. Since the observations in gravity gradiometry are the second order derivatives of the gravitational potential, one needs to apply the gradient operator to equation (2.7) which yields:

$$\mathbf{V}_{jk} = \begin{bmatrix} \frac{\partial^2 V}{\partial x^2} & \frac{\partial^2 V}{\partial x \partial y} & \frac{\partial^2 V}{\partial x \partial z} \\ \frac{\partial^2 V}{\partial y \partial x} & \frac{\partial^2 V}{\partial y^2} & \frac{\partial^2 V}{\partial y \partial z} \\ \frac{\partial^2 V}{\partial z \partial x} & \frac{\partial^2 V}{\partial z \partial y} & \frac{\partial^2 V}{\partial z^2} \end{bmatrix} = \begin{bmatrix} V_{xx} & V_{xy} & V_{xz} \\ V_{yx} & V_{yy} & V_{yz} \\ V_{zx} & V_{zy} & V_{zz} \end{bmatrix} . \tag{2.28}$$

The 3×3 matrix $\mathbf{V}_{jk}$ is called the **gradient tensor** (also gravity tensor) which is a symmetric matrix. This implies that:

$$\begin{cases} V_{xy} = V_{yx} \\ V_{xz} = V_{zx} \\ V_{zy} = V_{yz}. \end{cases} \tag{2.29}$$

In addition, since the gravitational potential is a harmonic function outside the Earth, it fulfils the **Laplace's equation**

$$\Delta V = V_{xx} + V_{yy} + V_{zz} = 0. \tag{2.30}$$

According to equations (2.29) and (2.30), only five out of nine components of the gradient tensor are linearly independent. Equation (2.28) is the basic equation of gravity gradiometry. The components of the gradient tensor are observables and the gravity field parameters (e.g. spherical harmonic coefficients) are to be estimated based on these measurements. This makes the the determination of gravity field based on gravity gradients a straightforward problem provided that the components of the gradient tensor are really measured in the corresponding Earth fixed frame where the representation of V is desired. In contrast, the direct measurement of gravity gradients in an Earth-fixed frame is not easily possible, especially on board an Earth orbiting satellite. Therefore, some coordinate transformations are necessary in order to use (2.28).

2.3.2 From the GOCE observation frame to the Earth fixed frame

Figure 2.3 illustrates the observation frame on board the GOCE satellite. Six accelerometers are placed along three axes of a local coordinate system which is called **Gradiometer Reference Frame** or in brief **GRF**.

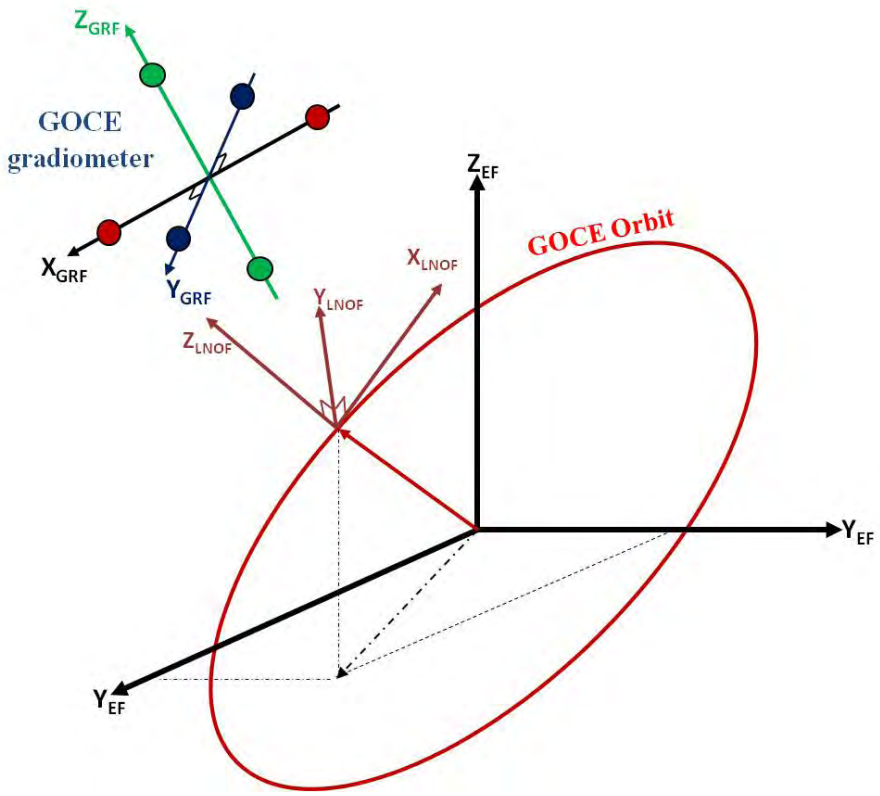

Figure 2.3: Different coordinate systems used in connection with GOCE data. The GOCE measurements are obtained in the GRF on board GOCE satellite. The representation of the gravity field is desired in geocentric Earth-fixed frame or EF. The LNOF is a coordinate system which is used to connect the observations to the gravity field parameters.

To convert gravity gradients from GRF to the Earth fixed frame, another interim frame is used in GOCE standards known as the **Local North Oriented Frame** or **LNOF**. LNOF is defined as follows:

- The origin is located at the nominal satellite center of mass with spherical coordinate (r, ϕ, λ).
- The Z axis is defined as the vector from the geocenter to the origin of LNOF pointing outwards.
- Y is parallel to the normal vector to the plane of the geocentric meridian of the satellite center of mass, pointing westward. The direction of the Y axis makes the LNOF a right-handed frame.
- The X axis points the geodetic north pole and is parallel to the normal vector to the plane defined by Y and Z.

Figure 2.3 shows LNOF in connection with GRF and the Earth fixed frame (EF). See also (Gruber *et al.*, 2010) for the definition of different frames used for GOCE data processing. To convert the gravity gradients from GRF to LNOF the following relation is used:

$$\mathbf{V}_{jk}^{LNOF} = \hat{\mathbf{R}}^T \mathbf{V}_{jk}^{GRF} \hat{\mathbf{R}} \tag{2.31}$$

where $\mathbf{V}_{jk}^{GRF}$ and $\mathbf{V}_{jk}^{LNOF}$ are gradient tensors in GRF and LNOF, respectively. The rotation matrix $\hat{\mathbf{R}}$ is a 3×3 orthonormal matrix where

$$\hat{\mathbf{R}}^T = \hat{\mathbf{R}}^{-1} \tag{2.32}$$

which implies

$$\hat{\mathbf{R}}^T\hat{\mathbf{R}} = \hat{\mathbf{R}}\hat{\mathbf{R}}^T = \mathbf{I} \tag{2.33}$$

and consequently

$$\mathbf{V}_{jk}^{GRF} = \hat{\mathbf{R}}\mathbf{V}_{jk}^{LNOF}\hat{\mathbf{R}}^T. \tag{2.34}$$

The rotation matrices $\hat{\mathbf{R}}$ are unique for each observation point along the GOCE orbit. The last step will be to establish the relation between gradients in the LNOF and the Earth-fixed frame. It can be shown that the gravity gradients in the LNOF can be written in terms of the gravity gradients in the Earth-fixed frame as (Koop, 1993)

$$\begin{cases} V_{xx}^{LNOF}(r,\phi,\lambda) = \dfrac{1}{r}V_r(r,\phi,\lambda) + \dfrac{1}{r^2}V_{\phi\phi}(r,\phi,\lambda) \\ V_{xy}^{LNOF}(r,\phi,\lambda) = V_{yx}^{LNOF}(r,\phi,\lambda) = \dfrac{1}{r^2\cos\phi}(-\tan\phi V_\lambda(r,\phi,\lambda) - V_{\phi\lambda}(r,\phi,\lambda)) \\ V_{xz}^{LNOF}(r,\phi,\lambda) = V_{zx}^{LNOF}(r,\phi,\lambda) = -\dfrac{1}{r^2}V_\phi(r,\phi,\lambda) + \dfrac{1}{r}V_{r\phi}(r,\phi,\lambda) \\ V_{yy}^{LNOF}(r,\phi,\lambda) = \dfrac{1}{r}V_r(r,\phi,\lambda) - \dfrac{1}{r^2}\tan\phi V_\phi(r,\phi,\lambda) + \dfrac{1}{r^2\cos^2\phi}V_{\lambda\lambda}(r,\phi,\lambda) \\ V_{yz}^{LNOF}(r,\phi,\lambda) = V_{zy}^{LNOF}(r,\phi,\lambda) = \dfrac{1}{r\cos\phi}[\dfrac{1}{r}V_\lambda(r,\phi,\lambda) - V_{r\lambda}(r,\phi,\lambda)] \\ V_{zz}^{LNOF}(r,\phi,\lambda) = V_{rr}(r,\phi,\lambda) \end{cases} \tag{2.35}$$

in which the first and second derivatives of the potential are expressed in terms of curve-linear spherical coordinates. The evaluation of V_r, V_ϕ and V_λ as well as V_{rr}, $V_{r\phi}$, $V_{\phi\phi}$, $V_{\phi\lambda}$ and $V_{\lambda\lambda}$ depends on the type of base functions used to represent the gravitational potential V. For the evaluation of these derivatives using spherical harmonics, see, e.g., Ditmar and Klees (2002) or Koop (1993). In Chapter 6, we determine the first and second derivatives of the gravitational potential using the SRBF.

2.4 Evolution of global gravity field models and state-of-the-art

A rather complete list of the global gravity field solutions is provided by GFZ (2013). Over 130 global solutions have been determined since 1966 up to the present time. The accuracy and resolution of these models have been rapidly improving due to the availability of precise and advanced observation techniques. Before the launch of the CHAMP mission in 2000, the global models (based on satellite data) were limited to the low frequencies of the Earth's gravity field. Figure 2.4 illustrates the contribution of the current satellite missions to the improvement of the gravity field determination in frequency and space domains. Moreover, to see the impact of current satellite missions on the resolution and quality of the Earth's gravity field, we compare several global models which are determined based on the available satellite data of their time. Table 2.2 gives the details of these models. The error degree amplitude of these global models are shown in figure 2.5 in terms of geoid heights. In addition, the cumulative geoid errors of these models are shown in figure 2.6.
The oldest model which is considered here is the model GRIM5S1 (Biancale *et al.*, 2000) which was published in 1999. The model has been determined based on the available tracking data of 21 satellites with different orbit altitude and inclination. The error amplitudes are rapidly increasing as the harmonic degrees beyond 10 are included. The geoid error is about 15 cm at its highest resolution. A remarkable improvement at low frequencies ($n < 50$) was achieved after the launch of the CHAMP mission. The launch of the GRACE in 2002, brought a step forward in the determination of global gravity field in long and medium wave lengths. Compared to CHAMP models, GRACE data could improve the quality of gravity field determination, up to two orders of magnitude. This improvement was achieved based on a month of GRACE data only. The error amplitude was

geo-potential model	data used	N_{max}	year
GRIM5S1	orbit of 21 satellites	99	1999
EIGEN-CHAMP03S	CHAMP	140	2004
GFZ monthly	GRACE	120	2007
ITG-Grace2010s	GRACE	180	2010
GOCO03S	GOCE and GRACE	250	2012
TIM-R4	GOCE	250	2013
ITG-Goce02	GOCE	240	2013

Table 2.2: Some selected geopotential models determined from 1999 until 2013 based on the state-of-the-art observation techniques. The second column shows the data used to determine the gravity field model. See GFZ (2013) for more details about these models.

further reduced as more GRACE data were included in the modelling of the static gravity field. Since March 2009, GOCE observations increased the resolution and quality of the higher degrees of the Earth's gravity field. GOCE cannot compete with the accuracy of the medium long wavelengths determined by GRACE. GRACE and GOCE are now considered as the complementary missions. Thus combining GRACE and GOCE observations is currently the state-of-the-art for high resolution gravity field modelling based on satellite data only. See also Pail *et al.* (2013) for more details on the recent developments and accuracies of the global geo-potential models.

2.5 Follow-on missions

The geodetic satellite missions have provided a large amount of valuable observations for the geoscientific community. Due to the availability of such data many geophysical phenomena are better understood in the last decade. Investigations are still ongoing to improve the quality of satellite data to extract more and more information out of available data. Apart from that, there is no doubt about the necessity of launching new satellite missions to keep acquiring useful data from space. The GRACE follow-on is to be launched in 2017 to continue monitoring changes of the Earth's gravitational potential. It is a rebuild of GRACE with the possibility to test the inter-satellite laser ranging technique to increase the precision of SST-ll data (Sheard *et al.*, 2012). Moreover, there are several research studies carried out to design and propose new concepts for future satellite missions. See Flury and Rummel (2005) and Panet *et al.* (2012) for more technical discussion and details.

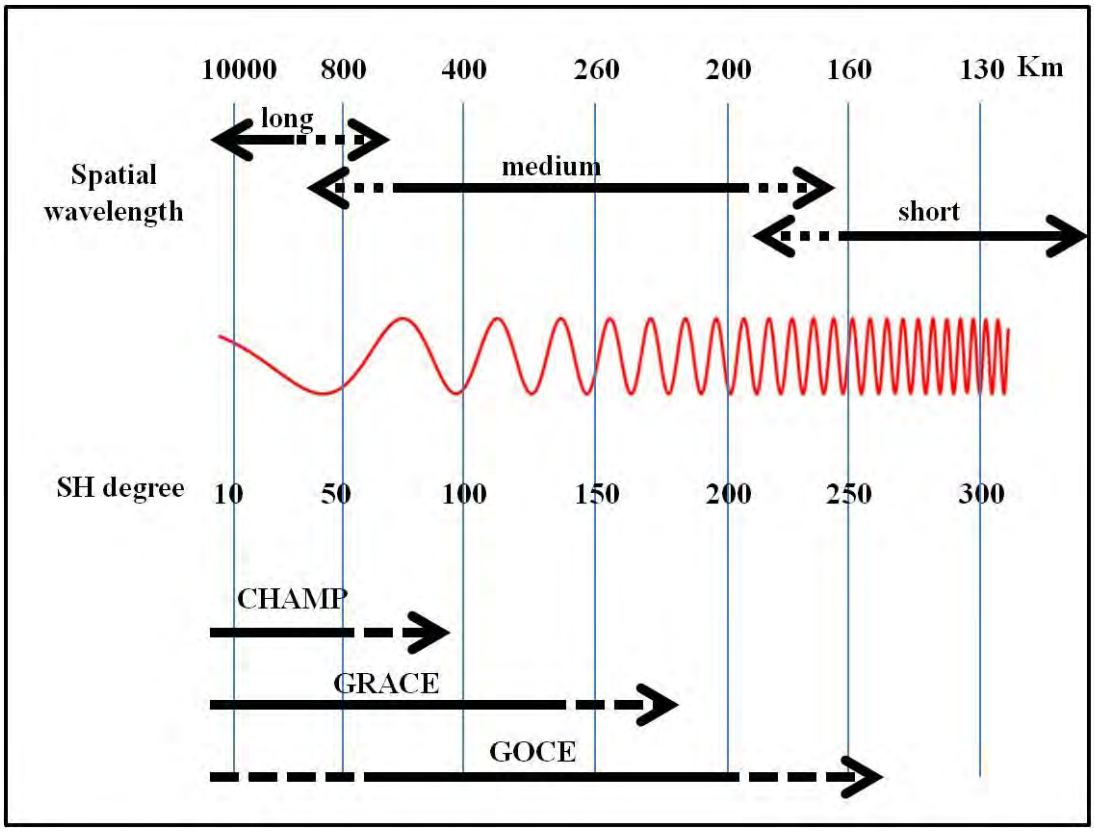

Figure 2.4: The contribution of current satellite missions to the improvement of the short, medium and the long wavelengths of the gravity field. The frequency and spatial resolution shown here are just rough estimations. The dotted lines indicate the uncertainty for the definition of borders between long, medium and short wavelengths as well as the exact resolution of the satellite missions.

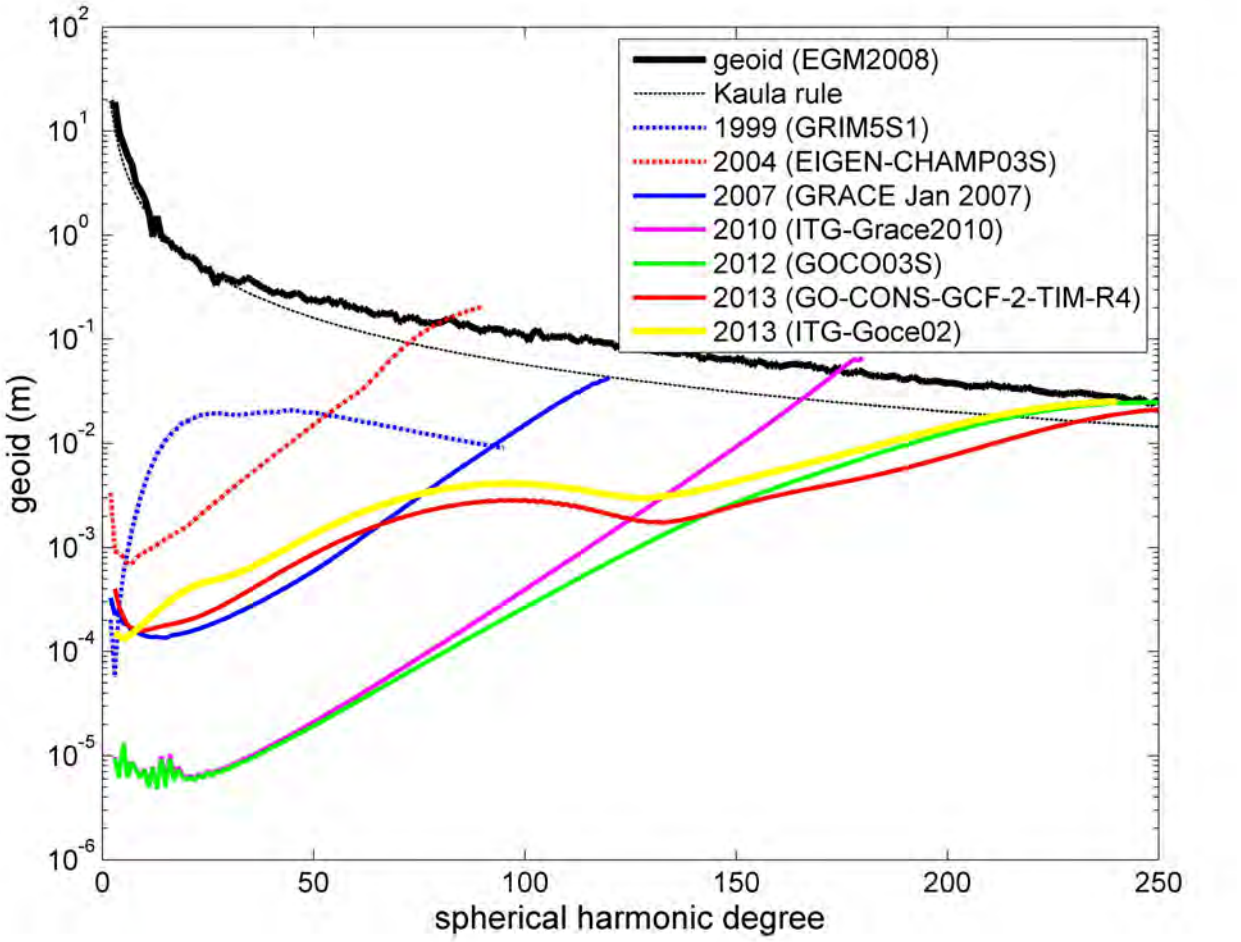

Figure 2.5: Error degree amplitudes in terms of geoid heights. The results are based on several global models from 1999 until 2013. All models are satellite-only solutions. The solutions are improved with the new observations from satellite data. As it can be seen from 1999 until 2013 the accuracy of global models is improved at least two orders of magnitude. In addition the resolution is also increased from about $n = 25$ in 1999 up to $n = 220$ in 2013. For the Kaula rule see Section 3.1.2

.

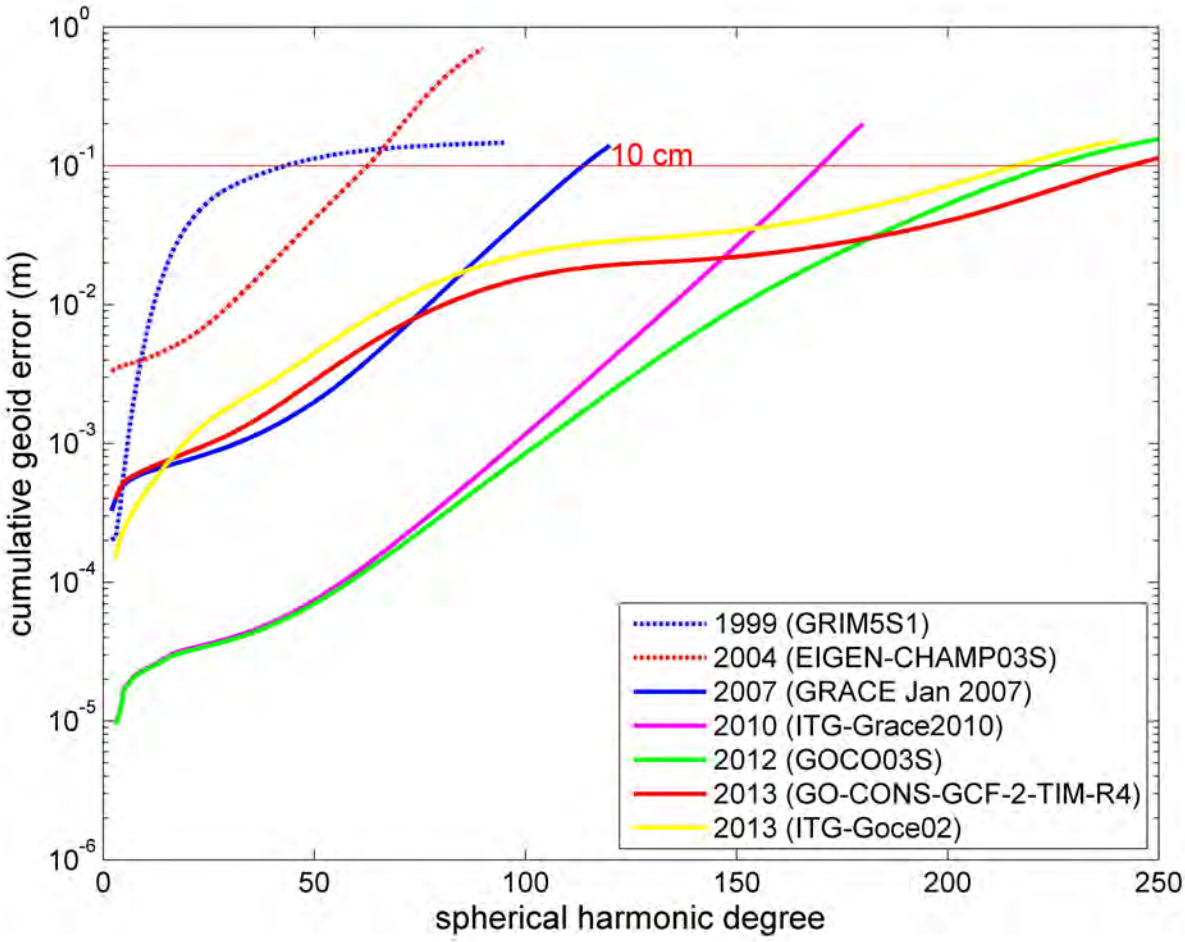

Figure 2.6: The cumulative geoid errors for several global models in the last decade. The current accumulated geoid error is about $14\,\mathrm{cm}$ for GRACE-only models up to degree 120 and $11\,\mathrm{cm}$ for GOCE-only solutions up to degree 250.

3 Global gravity field modelling

In the previous chapter, we discussed the general form of different approaches for the connection between gravitational potential V and a set of SST-hl and/or SST-ll observations. These approaches provide (directly or indirectly) the information about the gravitational potential or its derivatives at satellite altitude. For example the energy balance approach supplies the gravitational potential (or potential differences between satellites in the case of GRACE) along the orbit. The difference acceleration approach gives acceleration differences along the orbit which are projected onto line of sight vector. After setting the functional link between the data and the potential field, the goal of gravity field modelling is to construct the potential field on the Earth's surface or above it using an analytical continuous function which represents the feature of the gravitational potential.
The mathematical description of this problem can be expressed as follows:
Let Ω be a sphere with radius R and (ϕ, λ) the geographical latitude and longitude respectively. We define $\mathbf{r}$ to be the position vector of a point on or above Ω, as:

$$\mathbf{r} = r[\cos\phi\cos\lambda \quad \cos\phi\sin\lambda \quad \sin\phi]^T, \quad |\mathbf{r}| = r \geq R. \tag{3.1}$$

The potential values (or its functional) v_i, are given at discrete observation points $\mathbf{r}_i$, the goal is to find a function f such that:

$$f(\mathbf{r}_i) = v_i + e_i \quad , \quad i = 1, 2, ..., I \tag{3.2}$$

where e_i denotes the errors in the observations. Since the gravitational potential is a harmonic function (Moritz 1980), f must also be a harmonic function to represent the characteristics of the field. In an ideal case, the function f should represent the error-free values v_i and reveal the features of the potential field with no uncertainty. In reality f shall be approximated using a set of known functions, called **the base functions**, and their corresponding coefficients.
Polynomials are among the most important and interesting approximating functions in numerical analysis and modelling. Polynomial approximation is an old subject in mathematics and there are numerous theorems describing the properties of these functions. Perhaps the most important theorem for polynomial approximation is the theorem of Weierstrass (Moritz and Sünkel 1978). It states that every continuous function f can be uniformly approximated by a polynomial with arbitrary accuracy. This polynomial approximation can be written as

$$f(\mathbf{r}_i) = \sum_{k=0}^{K} \alpha_k B_k(\mathbf{r}_i) \tag{3.3}$$

which means the function f is approximated by a linear combination of K base functions B_k and corresponding coefficients α_k. Putting equations (3.2) and (3.3) together, one can write the generic form of gravity field modelling based on observed values v_i:

$$\sum_{k=0}^{K} \alpha_k B_k(\mathbf{r}_i) = v_i + e_i \quad , \quad i = 1, 2, ..., I. \tag{3.4}$$

Based on this equation, gravity field modelling is, in practice, the determination of unknown coefficients α_k, associated with the known base functions B_k. There are some other alternative terms for gravity field modelling, in the literature: **Gravity field analysis**, **gravity field determination**, **gravity field inversion** or sometimes, **gravity field parametrization** can be mentioned for instance.

The interpretation of the coefficients α_k and the information they contain, is directly dependent on the choice of the base functions B_k. For example, if the base functions are defined as harmonic functions, the scaling coefficients α_k are their corresponding amplitude and reveal the spectral properties. Therefore the proper choice of the base function, is an important step for gravity field modelling. In the following, we describe the spherical harmonics (SH), which are the most commonly used functions for the approximation on the sphere and in particular for gravity field modelling. Later in this chapter, we discuss the advantages and disadvantages of SH and introduce other alternatives. Among other alternatives we put emphasis on the SRBF which will be considered in the next chapter.

3.1 Spherical harmonics (SH)

The well-known base functions (polynomials) used for gravity field modelling, are the spherical harmonics. These functions are a great tool for global applications due to their global support. They are characterized by the nice feature of orthogonality and the numerical implementation of them is straightforward. Spherical harmonics have different applications in various disciplines and therefore are seen from different perspectives. In approximation theory, spherical harmonics are the basis for harmonic homogeneous polynomials of a certain degree on the sphere (Freeden *et al.*, 1998, Müller, 1966). Spherical harmonics are also used in physics and quantum mechanics as the eigenfunctions of angular momentum operators (Edmonds, 1957). In potential theory, spherical harmonics can be seen as the solution of the Laplace equation (Heiskanen and Moritz, 1967) and are also considered as the eigenfunctions of the Laplace operator. Moreover, they can be interpreted as the generalization of the Fourier transform to the spherical coordinates and therefore share important properties with ordinary Fourier series in one or more dimensions (Colombo, 1981).

3.1.1 Mathematical description of SH

A square integrable function f, defined on the sphere Ω, can be approximated using a series of trigonometric functions $\bar{P}_{nm}(\sin\phi)\ \cos m\lambda$ and $\bar{P}_{nm}(\sin\phi)\ \sin m\lambda$:

$$f(\phi,\lambda)=\sum_{n=0}^{\infty}\sum_{m=0}^{n}(\bar{a}_{nm}\cos m\lambda+\bar{b}_{nm}\sin m\lambda)\bar{P}_{nm}(\sin\phi) \tag{3.5}$$

with ϕ and λ being the surface spherical coordinates on the unit sphere. $\bar{a}_{nm}$ and $\bar{b}_{nm}$ are the normalized spherical harmonic coefficients of degree n and order m. These coefficients are also called the Stokes coefficients in the literature. The fully normalized associated Legendre functions $\bar{P}_{nm}$ are a solution of Legendre's differential equation (Heiskanen and Moritz, 1967). These functions have also explicit relation to the m^{th} derivative of the Legendre polynomials P_n of degree n

$$P_{nm}(\sin\phi)=(\cos\phi)^m\frac{d^m}{(d\sin\phi)^m}P_n(\sin\phi) \tag{3.6}$$

where $P_{nm}(\sin\phi)$ are the non-normalized Legendre functions.
The functions $\bar{P}_{nm}(\sin\phi)\ \cos m\lambda$ and $\bar{P}_{nm}(\sin\phi)\ \sin m\lambda$ are the spherical harmonic base functions, employed to approximate the function f. In the literature and text books, spherical harmonics are usually denoted by $\bar{Y}^c_{nm}(\phi,\lambda)$ and $\bar{Y}^s_{nm}(\phi,\lambda)$ as:

$$\begin{cases}\bar{Y}^c_{nm}(\phi,\lambda)=\bar{P}_{nm}(\sin\phi)\ \cos m\lambda\\ \bar{Y}^s_{nm}(\phi,\lambda)=\bar{P}_{nm}(\sin\phi)\ \sin m\lambda\end{cases}. \tag{3.7}$$

Figure 3.1 illustrates the normalized spherical harmonics of degree 4. The approximation procedure of the function f is in fact to measure, how much the known functions $\bar{Y}^c_{nm}$ and $\bar{Y}^s_{nm}$ are similar to the unknown function f. The tool for this '*similarity measurement*' is the inner product, or the metric of the space. The inner

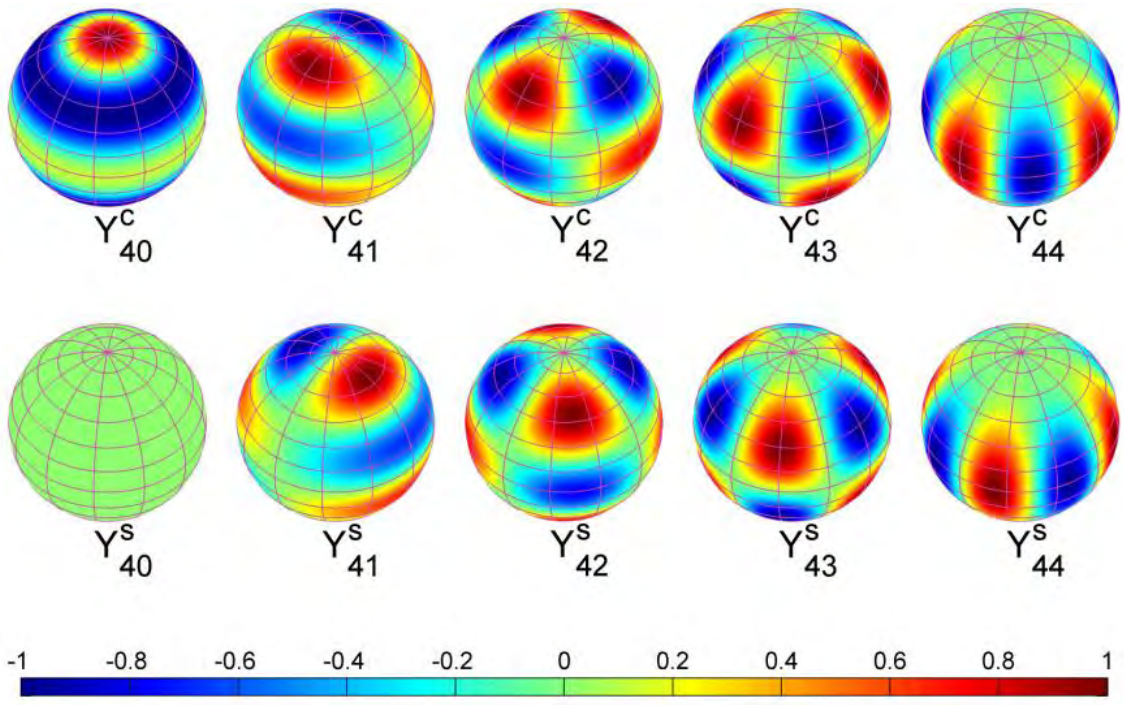

Figure 3.1: Normalized spherical harmonics of degree 4

product is defined as a result of the square integrability condition. Square integrability implies that the integral of f^2 should be bounded. In mathematical form, the function f is said to be square integrable if

$$\iint_{\Omega} f(\phi,\lambda)^2 d\Omega < \infty. \tag{3.8}$$

Therein, $d\Omega = \sin\phi d\phi d\lambda$ is the surface element on the sphere. Thus f belongs to the space of all square integrable functions denoted by $L_2(\Omega)$. Using the square integrability condition (3.8), the inner product of the functions f and g is defined as:

$$< f, g >= \iint_{\Omega} f(\phi,\lambda) g(\phi,\lambda) d\Omega \tag{3.9}$$

which is bounded by definition. The norm[1] of f is also measured by the inner product:

$$\|f\| = \sqrt{< f, f >} = \sqrt{\iint_{\Omega} f(\phi,\lambda)^2 d\Omega}. \tag{3.10}$$

The interesting feature of spherical harmonics is their orthogonality relations which can be described by

$$\begin{cases} \iint_{\Omega} \bar{Y}^c_{nm}(\phi,\lambda)\bar{Y}^c_{pq}(\phi,\lambda)d\Omega = 0 & \text{if } n \neq p \text{ or } m \neq q \text{ or both} \\ \iint_{\Omega} \bar{Y}^s_{nm}(\phi,\lambda)\bar{Y}^s_{pq}(\phi,\lambda)d\Omega = 0 & \text{if } n \neq p \text{ or } m \neq q \text{ or both} \\ \iint_{\Omega} \bar{Y}^c_{nm}(\phi,\lambda)\bar{Y}^s_{pq}(\phi,\lambda)d\Omega = 0 & \text{always} \end{cases} \tag{3.11}$$

[1]The term 'norm' used in this thesis, refers to the L^2 norm.

which means every spherical harmonic function is orthogonal to other spherical harmonics. Finally, the inner product of two similar $\bar{Y}^c_{nm}(\phi,\lambda)$ or $\bar{Y}^s_{nm}(\phi,\lambda)$ yields:

$$\iint_{\Omega} \bar{Y}^c_{nm}(\phi,\lambda)\bar{Y}^c_{nm}(\phi,\lambda)d\Omega = \iint_{\Omega} \bar{Y}^s_{nm}(\phi,\lambda)\bar{Y}^s_{nm}(\phi,\lambda)d\Omega = 1. \tag{3.12}$$

According to the orthogonality relations, if the function f is expanded into a series of spherical harmonics, as in equation (3.5), the coefficients $\bar{a}_{nm}$ and $\bar{b}_{nm}$ can be independently computed using the inner product:

$$\begin{cases} \bar{a}_{nm} =< f, \bar{Y}^c_{nm}(\phi,\lambda) >= \iint_{\Omega} f(\phi,\lambda)\bar{Y}^c_{nm}(\phi,\lambda)d\Omega \\ \bar{b}_{nm} =< f, \bar{Y}^s_{nm}(\phi,\lambda) >= \iint_{\Omega} f(\phi,\lambda)\bar{Y}^s_{nm}(\phi,\lambda)d\Omega \end{cases} \tag{3.13}$$

which expresses that the coefficient $\bar{a}_{nm}$ and $\bar{b}_{nm}$ are the averages of the inner products of the function f and the corresponding approximating functions $\bar{Y}^c_{nm}(\phi,\lambda)$ and $\bar{Y}^s_{nm}(\phi,\lambda)$. Equations (3.5) and (3.13) are also called spherical harmonic synthesis and spherical harmonic analysis, respectively. In analogy to the Fourier transform, the power spectrum of the function f is defined by the set of all degree variances σ^2_n:

$$\sigma^2_n = \sum_{m=0}^{n} (\bar{a}^2_{nm} + \bar{b}^2_{nm}). \tag{3.14}$$

Another important property of spherical harmonics is the Parseval's relation (Colombo, 1981, Kreyszig, 1978):

$$\|f\|^2 = \iint_{\Omega} f(\phi,\lambda)^2 d\Omega = \sum_{n=0}^{\infty} \sigma^2_n \tag{3.15}$$

that states the norm of the function f and the norm of its spherical harmonic expansion are the same. Parseval's relation also indicates that the set of spherical harmonic functions $\bar{Y}^c_{nm}(\phi,\lambda)$ and $\bar{Y}^s_{nm}(\phi,\lambda)$ constitutes a complete orthogonal set on the sphere. It should also be mentioned that the set of all square integrable functions on the sphere in addition to the metric defined by inner product, construct a Hilbert space. Among all square integrable functions in this space, spherical harmonics are unique and carry nice properties such as orthogonality and totality (Kreyszig, 1978).
Another property of spherical harmonics is the addition theorem, which is a result of the orthogonality of these base functions. The addition theorem reads:

$$(2n+1)P_n(\cos\psi) = \sum_{m=-n}^{n} \bar{Y}_{nm}(\phi_i,\lambda_i)\bar{Y}_{nm}(\phi_k,\lambda_k) \tag{3.16}$$

where $\cos\psi$ is the spherical distance between two points i and k on the sphere and is given by:

$$\cos\psi = \sin\phi_i \sin\phi_k + \cos\phi_i \cos\phi_k \cos(\lambda_i - \lambda_k). \tag{3.17}$$

This relation will be further used for the definition of SRBF in the next chapters.
The orthogonality of spherical harmonics, in addition to the fact that they form a complete set of functions on the sphere are the main reasons that they are widely used for approximation and modelling on the sphere. Moreover, the solid spherical harmonics:

$$\begin{cases} \frac{1}{r^{n+1}}\bar{Y}^c_{nm}(\phi,\lambda) \\ \frac{1}{r^{n+1}}\bar{Y}^s_{nm}(\phi,\lambda) \end{cases} \tag{3.18}$$

and

$$\begin{cases} r^n \bar{Y}^c_{nm}(\phi, \lambda) \\ r^n \bar{Y}^s_{nm}(\phi, \lambda) \end{cases} \tag{3.19}$$

also satisfy Laplace equation (Hofmann and Moritz, 2005) and have all properties of the surface spherical harmonics. The exterior solid spherical harmonics (3.19) are valid outside the unit sphere while the interior ones hold inside the unit sphere. Hence, the exterior solid spherical harmonics are appropriate functions to analyse the geopotential data observed above the surface of the sphere (i.e. satellite-based observations). Both types of surface spherical harmonics and solid spherical harmonics are usually referred to as spherical harmonics. In the following, we also use the generic term spherical harmonics for simplicity but keeping in mind that the exterior solid spherical harmonics are meant. More complete mathematical descriptions and characteristics of spherical harmonics can be found in numerous text books and papers, e.g. Colombo (1981), Heiskanen and Moritz (1967), Moritz (1980), Vanicek and Krakiwsky (1982).

3.1.2 Expansion of the gravitational potential into SH

The equations in Section 3.1.1 are valid for all square integrable functions on the unit sphere with radius $R = 1$. These relations can be generalized for spheres with arbitrary radii. For the expansion of the gravitational potential outside the Earth, it is common to use the exterior solid spherical harmonics (3.18) defined on the sphere with radius R. The radius R is usually equal to the radius of a sphere which circumscribes the Earth and its topography (Hofmann and Moritz, 2005) and is known as the Brillouin sphere (Vanicek and Krakiwsky, 1982).
The gravitational potential V outside the Brillouin sphere can be expanded into a series of (exterior) solid spherical harmonics:

$$V(r, \phi, \lambda) = \frac{GM}{R} \sum_{n=0}^{\infty} (\frac{R}{r})^{n+1} \sum_{m=0}^{n} (\bar{c}_{nm} \cos m\lambda + \bar{s}_{nm} \sin m\lambda) \bar{P}_{nm}(\sin \phi) \tag{3.20}$$

wherein $r > R$ is the distance between evaluation point and the center of the Earth, $\bar{c}_{nm}$ and $\bar{s}_{nm}$ are the corresponding Stokes coefficients. $\bar{c}_{nm}$ and $\bar{s}_{nm}$ are the scaled version of $\bar{a}_{nm}$ and $\bar{b}_{nm}$ in equations (3.5) and (3.13) such that

$$\begin{cases} \bar{c}_{nm} = \dfrac{R^{-n}}{GM} \bar{a}_{nm} \\ \\ \bar{s}_{nm} = \dfrac{R^{-n}}{GM} \bar{b}_{nm} \end{cases} . \tag{3.21}$$

These coefficients can be determined using (solid) spherical harmonic analysis relations:

$$\begin{cases} \bar{c}_{nm} = \iint\limits_{d\Omega} V(r, \phi, \lambda) (\dfrac{R}{r})^{n+1} \bar{Y}^c_{nm}(\phi, \lambda) d\Omega \\ \bar{s}_{nm} = \iint\limits_{d\Omega} V(r, \phi, \lambda) (\dfrac{R}{r})^{n+1} \bar{Y}^s_{nm}(\phi, \lambda) d\Omega \end{cases} . \tag{3.22}$$

Similar to (3.14), the degree variances for the gravitational potential can be derived from spherical harmonic coefficients:

$$\sigma_n^2 = \sum_{m=0}^{n} (\bar{c}_{nm}^2 + \bar{s}_{nm}^2) \tag{3.23}$$

and accordingly the degree standard deviations:

$$\sigma_n = \sqrt{\sum_{m=0}^{n} (\bar{c}_{nm}^2 + \bar{s}_{nm}^2)} \tag{3.24}$$

which show the energy content of each specific spherical harmonic degree. A rough rule to obtain the degree variances σ_n^2 without using the coefficients $\bar{c}_{nm}$ and $\bar{s}_{nm}$ is obtained from the autocovariance analysis of gravimetry (Kaula, 1966):

$$\sigma_n^2 \approx \frac{160 \times 10^{-12}}{n^3}. \tag{3.25}$$

Using (3.23) and (3.24) one can write

$$\sigma_n(\bar{c}_{nm}, \bar{s}_{nm}) = \sqrt{\frac{160 \times 10^{-12}}{(2n+1)n^3}} \tag{3.26}$$

which is known as Kaula's rule of thumb. Kaula's rule of thumb is considered as the a priori information about the coefficients $\bar{c}_{nm}$ and $\bar{s}_{nm}$ and is widely used for the **regularization** of global gravity field modelling using spherical harmonics. Equation (3.20) is sometimes written as

$$V(r, \phi, \lambda) = \frac{GM}{R} \sum_{n=0}^{\infty} (\frac{R}{r})^{n+1} \sum_{m=-n}^{n} \bar{C}_{nm} \bar{Y}_{nm}(\phi, \lambda) \tag{3.27}$$

in which $\bar{C}_{nm} = \bar{c}_{nm}$ and $\bar{Y}_{nm} = \bar{Y}_{nm}^c$ for $m \geq 0$ and also $\bar{C}_{nm} = \bar{s}_{nm}$ and $\bar{Y}_{nm} = \bar{Y}_{nm}^s$ for $m < 0$. The coefficients $\bar{C}_{nm}$ can be determined by:

$$\bar{C}_{nm} = \iint_{d\Omega} (\frac{R}{r})^{n+1} V(r, \phi, \lambda) \bar{Y}_{nm}(\phi, \lambda) d\Omega. \tag{3.28}$$

This alternative representation will be further used in section 3.2 for the relation between spherical harmonics and kernel functions.
Concerning spherical harmonic analysis using equations (3.22) some remarks should be made:

- Equations (3.22) and (3.13) are important because they show the orthogonality of spherical harmonics. Nevertheless, the evaluation of Stokes's coefficients $\bar{c}_{nm}$ and $\bar{s}_{nm}$ is not possible using (3.22) since the gravitational potential V is not continuously available. Instead, a set of noisy v_i at discrete locations (r_i,ϕ_i,λ_i) is measured. Therefore, (3.22) can be rewritten in discrete form for numerical implementations:

$$\begin{cases} \bar{c}_{nm} = \sum_{\Delta\phi} \sum_{\Delta\lambda} V(r_i, \phi_i, \lambda_i) \frac{1}{r_i^{n+1}} \bar{Y}_{nm}^c(\phi_i, \lambda_i) \Delta\Omega \\ \bar{s}_{nm} = \sum_{\Delta\phi} \sum_{\Delta\lambda} V(r_i, \phi_i, \lambda_i) \frac{1}{r_i^{n+1}} \bar{Y}_{nm}^s(\phi_i, \lambda_i) \Delta\Omega \end{cases}. \tag{3.29}$$

  The same argument holds for spherical harmonic synthesis using equation (3.20). The gravitational potential V can be evaluated at discrete points i using given coefficients $\bar{c}_{nm}$ and $\bar{s}_{nm}$:

$$V(r_i, \phi_i, \lambda_i) = \frac{GM}{R} \sum_{n=0}^{N_{max}} (\frac{R}{r_i})^{n+1} \sum_{m=0}^{n} (\bar{c}_{nm} \cos m\lambda_i + \bar{s}_{nm} \sin m\lambda_i) \bar{P}_{nm}(\sin \phi_i). \tag{3.30}$$

  The maximum degree N_{max} used in the expansion is chosen based on the measured data and the resolution of the desired model. To be more specific, N_{max} is chosen because all coefficients with $n > N_{max}$ are zero or their values are neglected. In this case the function V is said to be band-limited.

- The orthogonality of spherical harmonics is always preserved if these functions are continuously available. In practice these functions are sampled at discrete points i where observations are available. Therefore the orthogonality relations (3.11) do not hold in discrete form and consequently the Stokes coefficients cannot be simply determined using (3.22) or (3.29) without a proper quadrature method. If data are given on a special grid where the circles of latitude are located at zeros of $P_n(\sin\phi)$, equations (3.29) are applicable using special quadratures weights (Colombo, 1981). This specific grid is known as the Gauss grid and the corresponding quadratures method is Gaussian quadratures (Payne, 1971). Although it is possible to generate or interpolate data on a Gaussian grid, such methods are applicable for data on the surface of the sphere. For satellite measurements at orbit altitude it is not possible to apply this technique. Hence the Stokes coefficients cannot be determined using (3.29) and consequently should be calculated using alternative methods.

3.1.3 Estimation of spherical harmonic coefficients using least-squares adjustment

The coefficients α_k (here $\bar{c}_{nm}$ and $\bar{s}_{nm}$), can also be estimated using the method of least-squares (Colombo, 1981, Koch, 1999, Vanicek and Krakiwsky, 1982). Least-squares is a method to determine the unknown coefficients α_k with the assumption that the error norm $\|\mathbf{e}\|$ is minimum. The least-squares adjustment procedure for determining the geopotential based on observed values v_i on or above the surface can be expressed in matrix notation. Substituting equation (3.30) in (3.2) yields:

$$\frac{GM}{R}\sum_{n=0}^{N_{max}}(\frac{R}{r_i})^{n+1}\sum_{m=0}^{n}(\bar{c}_{nm}\cos m\lambda_i+\bar{s}_{nm}\sin m\lambda_i)\bar{P}_{nm}(\sin\phi_i)=v_i+e_i \tag{3.31}$$

This equation results in a liner system with I equations (observations) and $K=(N_{max}+1)^2$ unknowns to be estimated. In matrix notation, (3.31) can be written as

$$\mathbf{l}+\mathbf{e}=\mathbf{A}\mathbf{x}. \tag{3.32}$$

$\mathbf{l}=[v_1,v_2,...,v_I]^T$ and $\mathbf{e}=[e_1,e_2,...,e_I]^T$ are the observation and error vectors, respectively. The design matrix $\mathbf{A}_{I\times K}$ describes the model and is a linear operator which projects the elements of the space of unknowns onto the observation space. The column vectors of $\mathbf{A}$ are the base functions of the approximation problem. For spherical harmonic analysis, the base functions or the column vectors of $\mathbf{A}$ are the spherical harmonics:

$$\mathbf{A}=\begin{bmatrix}\dfrac{\partial V(\mathbf{r})}{\partial\bar{c}_{nm}} & \dfrac{\partial V(\mathbf{r})}{\partial\bar{s}_{nm}}\end{bmatrix} \tag{3.33}$$

with

$$\begin{cases}\dfrac{\partial V(\mathbf{r})}{\partial\bar{c}_{nm}}=\dfrac{GM}{R}(\dfrac{R}{r})^{n+1}\cos m\lambda\bar{P}_{nm}(\sin\phi)\\[2ex]\dfrac{\partial V(\mathbf{r})}{\partial\bar{s}_{nm}}=\dfrac{GM}{R}(\dfrac{R}{r})^{n+1}\sin m\lambda\bar{P}_{nm}(\sin\phi)\end{cases} \tag{3.34}$$

and the vector $\mathbf{x}$ contains the unknown coefficients $\bar{c}_{nm}$ and $\bar{s}_{nm}$. The least-squares solution $\hat{\mathbf{x}}$, is obtained under the minimum error norm condition:

$$\min\ \|\mathbf{A}\mathbf{x}-\mathbf{l}\|^2_{\mathbf{P}_l} \tag{3.35}$$

and is given by (Koch, 1999)

$$\hat{\mathbf{x}} = \mathbf{N}^{-1}\mathbf{y} \tag{3.36}$$

if $\mathbf{N}^{-1}$ exists. The elements of equation (3.36) are

$$\begin{cases} \mathbf{N} = \mathbf{A}^T\mathbf{P}_l\mathbf{A} \\ \\ \mathbf{y} = \mathbf{A}^T\mathbf{P}_l\mathbf{l}. \end{cases} \tag{3.37}$$

$\mathbf{P}_l$ is the positive definite weight matrix and is inversely proportional to the covariance matrix of observations $\mathbf{C}_l$:

$$\mathbf{C}_l \propto \mathbf{P}_l^{-1}. \tag{3.38}$$

Introducing the variance factor σ_0^2, the weight matrix $\mathbf{P}_l$ can be related to $\mathbf{C}_l$:

$$\mathbf{C}_l = \sigma_0^2\mathbf{P}_l^{-1} \tag{3.39}$$

which is the stochastic part of the observation equation (3.32). The solution obtained from the least-squares approach has several nice properties such as unbiasedness, best and unique approximation and minimum error. The latter is valid only for the normally distributed errors. More details about the method of least-squares adjustment can be found for example in Koch (1999), Moritz and Sünkel (1978), Vanicek and Krakiwsky (1982).
To assess the quality of estimated parameters using least-squares method, one can derive the covariance matrix $\mathbf{C}_{\hat{\mathbf{x}}}$

$$\mathbf{C}_{\hat{\mathbf{x}}} = \sigma_0^2\mathbf{N}^{-1}. \tag{3.40}$$

The variance factor σ_0^2 is not known in the beginning of the least-squares adjustment and is usually set equal to 1. However a measure of this value can be determined after estimating the unknown coefficients using the following equation (Koch, 1999, Vanicek and Krakiwsky, 1982):

$$\hat{\sigma}_0^2 = \frac{\hat{\mathbf{e}}^T\mathbf{P}_l\hat{\mathbf{e}}}{I-K} \tag{3.41}$$

where $\hat{\mathbf{e}} = \mathbf{A}\hat{\mathbf{x}} - \mathbf{l}$ is the estimated vector of residuals and $I - K$ is the **degree of freedom** or the redundancy of the least-squares adjustment. Using the a posteriori variance factor $\hat{\sigma}_0^2$ the estimated covariance matrix of $\hat{\mathbf{x}}$ will be:

$$\hat{\mathbf{C}}_{\hat{\mathbf{x}}} = \hat{\sigma}_0^2\mathbf{N}^{-1}. \tag{3.42}$$

The diagonal elements of $\hat{\mathbf{C}}_{\hat{\mathbf{x}}}$ are variances of the estimated spherical harmonic coefficients. Denoting these variances by $\hat{\sigma}^2_{c_{nm}}$ and $\hat{\sigma}^2_{s_{nm}}$, the error degree amplitudes are computed as

$$d\sigma_n = \sqrt{\sum_{m=0}^{n}(\hat{\sigma}^2_{c_{nm}} + \hat{\sigma}^2_{s_{nm}})} \tag{3.43}$$

which together with the degree variances (3.23) are used to assess the quality of gravity field models as they reveal the energy and error contained in each degree. Typical plots of degree variances and error degree amplitudes are shown in figure 2.5.

3.1.4 Disadvantages of spherical harmonics

Spherical harmonic analysis (and synthesis) is straightforward. It is indeed the best analysis tool for globally (homogeneous) distributed data on the sphere. Optimal spectral localization is possible and interpretation and assessment of the model in terms of degree and error degree amplitude is rather easy. In contrast to these advantages, there are also some drawbacks when dealing with spherical harmonics:

- Geopotential models are often used to investigate a particular phenomenon over a certain region (e.g. ice mass loss in Greenland, water storage in river basins, land uplift in Scandinavia, etc.). In general, spherical harmonic analysis and the same global Stokes coefficients are used for all these applications. The global solution using spherical harmonics is equivalent to applying a global filter to the data. This may lead to over-filtering of the data in some regions. For some applications it is desired to zoom-in into a specific region and extract as much signal as possible out of the data. For this purpose, spherical harmonics are not the best choices and regionally adapted base functions should be used.

- Obtaining the solution over a region decreases remarkably the cost of computations compared to global spherical harmonic solutions. The number of observations and unknown parameters included in the model setup and consequently the cost of computations will be dramatically reduced. This is especially demanded for the current and future satellite missions such as GOCE and GRACE follow-on missions where the expected resolutions of the models are rather high. For example, to obtain a global solution based on GOCE data up to degree and order $n = 250$, one needs to deal with an observation equation with over 63000 parameters to be estimated. A regional model with the same resolution can be achieved for a region as big as Central Africa with about 6000 unknown parameters where the same or even better accuracy is expected (see section 6.3.3).

- Due to the globally averaging feature of spherical harmonics, observation errors will propagate globally. If, especially, errors are limited to a certain region (e.g. ocean tide models, atmospheric effects) all coefficients and thus the whole global model will be affected (Lemoine *et al.*, 2007).

- Another obvious disadvantage of using spherical harmonics is that these global base functions need global data distribution as well. As we discussed in (3.3.2), spherical harmonic functions are sampled at discrete points where data are available. Since these functions are almost non-zero everywhere on the sphere, data should also be available everywhere on the sphere for proper sampling. As a result of this all spherical harmonic coefficients depend on all data over the sphere and any change in data (even in a small region) would require the re-computation of all coefficients.

- If global data are not homogeneously available, one expects to extract more details (the higher frequencies) out of the data in those regions where a denser distribution is provided. According to the Nyquist-Shannon sampling theorem (Steven, 1997) the highest frequency, which could be modelled from a given discrete data set, is twice the sampling interval or one-half of the sampling frequency. If the data sampling rate is not constant, it is difficult to define the highest frequency (spherical harmonic degree) for the analysis. This happens always in gravity field modelling since a completely homogeneous data distribution is never available. It is however possible to include higher spherical harmonic degrees based on the region with the densest data coverage. Though, this is unnecessary for other regions and one may desire to model the field using more optimal alternative ways. Choosing low degree spherical harmonics leads to smoothing the signal in regions with denser data and aliasing problems for the spectrum.

- A very common case in gravity field modelling is to deal with heterogeneous observations such as combining terrestrial gravity data and satellite-based observations. The heterogeneous data are not homogeneously distributed and the matter of highest frequency explained above is an issue again. Even if heterogeneous data are homogeneously available, such data sets contain different frequency content so that spherical harmonic analysis is not appropriate. Thus dense terrestrial data are better modelled using localizing base functions.

In principle other base functions can also be used to represent the gravitational potential on the surface of the sphere. One approach is to use the so called 'mascons' which refer to mass concentrations. Mascons

can be localized in both space and frequency domains and are appropriate for regional gravity field modelling (Lemoine *et al.*, 2007). Another alternative to spherical harmonics are the SRBF. The SRBF have been recently used in many research studies to model the gravity field of the Earth on regional scales. The SRBF will be considered briefly in the following section. In chapter 4, more details about the SRBF will be given for the regional gravity field modelling.

3.2 Spherical radial base functions (SRBF): A first look

In section 3.1.4, we discussed several disadvantages of spherical harmonics for gravity field modelling. Most of these drawbacks originate in the fact, that the spherical harmonics are ideal frequency-localizing base functions and have no measure of space-localization. The reason is, that the recovery of the spectral properties of the field needs a sort of base functions with global support in the field domain. To overcome the problems mentioned in 3.1.4, one needs to use base functions which have space-localizing features. In other words, such base functions should have compact support, that is, the base functions are non-zero in a certain sub-domain and zero elsewhere. The ideal space-localizing functions are the well-known Dirac functions. The Dirac function is zero everywhere except at zero and hence has a strict compact support (the support is $\{0\}$). Having ideal space-localizing property, the Dirac function has no frequency-localization instead. A perfect space-localization cannot be achieved simultaneously with a perfect frequency-localization. This issue is known as the *'uncertainty principle'* which states, that it is impossible to know exactly where (or when) a certain frequency occurs. See for example Neumann (1968), Freeden *et al.* (1998) and Keller (2004). Spherical harmonics (Fourier Transform) and Dirac functions describe two edges of signal analysis in the frequency and space (time) domain. While the former needs infinite frequencies to reconstruct a non band-limited signal, the latter needs infinite Dirac functions to model a continuous signal.

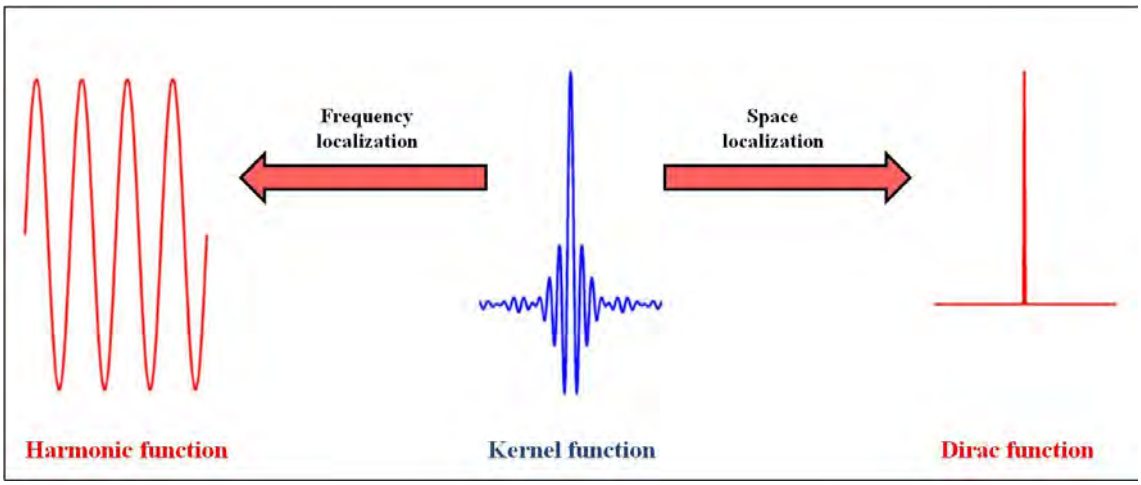

Figure 3.2: Uncertainty principle in space and frequency. Spherical harmonics with ideal frequency localization and Dirac functions with ideal space localizations are two extreme edges in signal processing. Kernel functions are a good compromise in between. See also Freeden (1999).

A good compromise between ideal frequency-localization (SH) and ideal space-localization (Dirac) are *kernel functions* as illustrated in figure 3.2. The kernel functions are used for pattern analysis or pattern recognition in many applications. Souza and César (2010) list several kernel functions and basic definitions for different applications. In the following, we use SRBF as kernel function which provide a balance between frequency and space localization. These functions are appropriate alternatives to spherical harmonics especially if the gravity field is to be determined on regional scales.

3.2.1 Mathematical description of SRBF

To explain the gravity field representation using SRBF, we consider the same setup as in previous section, given by equations (3.1) through (3.4). For spherical harmonic analysis and synthesis, we used spherical harmonics B_k and the coefficients α_k will be the Stokes coefficients $\bar{c}_{nm}$ and $\bar{s}_{nm}$ accordingly. The same settings hold for gravity field analysis and synthesis using SRBF; B_k are SRBF and α_k will be the corresponding *scaling coefficients*.
If we plug equation (3.28) into (3.27)

$$V(r_i,\phi_i,\lambda_i)=\sum_{n=0}^{\infty}(\frac{R}{r_i})^{n+1}\sum_{m=-n}^{n}\iint_{\Omega}V(r_k,\phi_k,\lambda_k)\bar{Y}_{nm}(\phi_k,\lambda_k)\bar{Y}_{nm}(\phi_i,\lambda_i)d\Omega, \tag{3.44}$$

rearranging the order of summation and integration yields

$$V(r_i,\phi_i,\lambda_i)=\iint_{\Omega}V(r_k,\phi_k,\lambda_k)\sum_{n=0}^{\infty}(\frac{R}{r_i})^{n+1}\underbrace{\sum_{m=-n}^{n}\bar{Y}_{nm}(\phi_k,\lambda_k)\bar{Y}_{nm}(\phi_i,\lambda_i)}_{\text{Addition theorem}}\,d\Omega. \tag{3.45}$$

Using the addition theorem given by equation (3.16), one can write

$$V(r_i,\phi_i,\lambda_i)=\iint_{\Omega}V(r_k,\phi_k,\lambda_k)\underbrace{\sum_{n=0}^{\infty}(\frac{R}{r_i})^{n+1}(2n+1)P_n(\cos\psi)}_{\text{Reproducing kernel function}=H(\mathbf{r}_k,\mathbf{r}_i)}\,d\Omega. \tag{3.46}$$

Introducing the *reproducing kernel function* $H(\mathbf{r}_k,\mathbf{r}_i)$, as defined in (3.46), results in

$$V(r_i,\phi_i,\lambda_i)=\iint_{\Omega}V(r_k,\phi_k,\lambda_k)H(\mathbf{r}_k,\mathbf{r}_i)d\Omega, \tag{3.47}$$

which shows the reproducing property of $H(\mathbf{r}_k,\mathbf{r}_i)$; if $\mathbf{r}_k=\mathbf{r}_i$ then the integration of V and H on the right hand side of (3.47), reproduces V. According to (3.9) the right hand side of (3.47) can be replaced by the inner product

$$V(r_i,\phi_i,\lambda_i)=<V(r_k,\phi_k,\lambda_k),H(\mathbf{r}_k,\mathbf{r}_i)>. \tag{3.48}$$

Schmidt *et al.* (2007) showed that this inner product can be replaced by a series expansion in terms of SRBF $B(\mathbf{r_i},\mathbf{r_k})$

$$V(r_i,\phi_i,\lambda_i)=<V(r_k,\phi_k,\lambda_k),H(\mathbf{r}_k,\mathbf{r}_i)>=\frac{GM}{R}\sum_{k=1}^{\infty}\alpha_k B(\mathbf{r}_i,\mathbf{r}_k). \tag{3.49}$$

A SRBF at position $\mathbf{r}_k$ on the surface of the sphere Ω_R, is defined as:

$$B(\mathbf{r}_i,\mathbf{r}_k)=\sum_{n=0}^{\infty}(\frac{R}{r_i})^{n+1}(2n+1)b_nP_n(\cos\psi) \tag{3.50}$$

where b_n are the so-called shape coefficients or the Legendre coefficients and will be discussed later. The Legendre polynomials $P_n(\cos\psi)$ are the function of spherical distance, $\cos\psi$, which is given by equation (3.17). In the special case where $b_n=1$ the SRBF will be the reproducing kernel H.

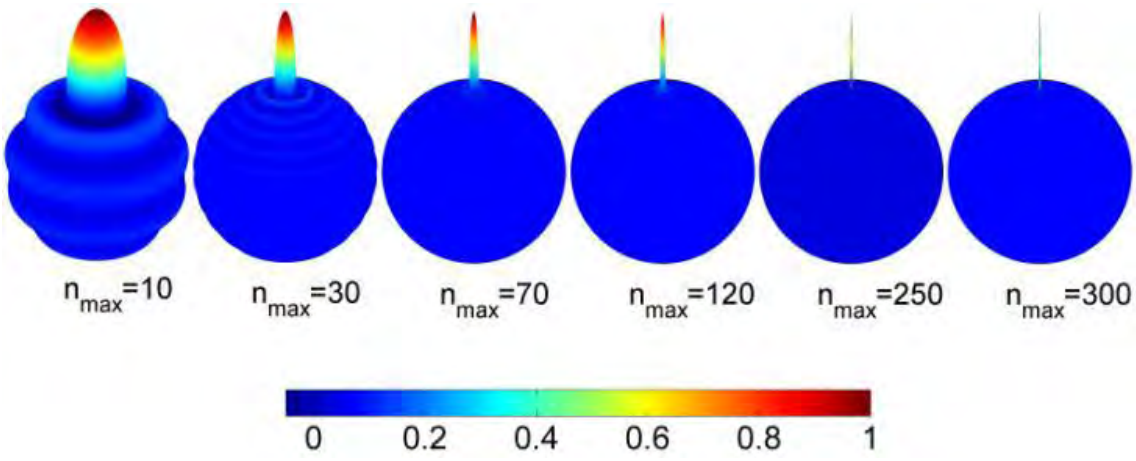

Figure 3.3: Normalized SRBF of different resolution. As the maximum degree of expansion increases, the base functions get narrower. This means the high frequency content can be examined with narrow base functions while wider base functions are only suitable for the investigation of lower frequencies. The SRBF should be located at certain positions. See more details in Section 4.2.4.

Equation (3.49) together with (3.50) yields:

$$V(r_i, \phi_i, \lambda_i) = \frac{GM}{R} \sum_{k=1}^{\infty} \alpha_k \sum_{n=0}^{\infty} (\frac{R}{r_i})^{n+1} (2n+1) b_n P_n(\cos\psi), \tag{3.51}$$

which is analogous to (3.20). The equivalence of (3.51) and (3.20) indicates that SH and SRBF are two basis which span the same function space. This is similar to use two different *coordinate system*s to describe the elements of a space. Therefore, in an ideal global case, expansion of the gravitational potential V into a set of spherical harmonics or SRBF lead to the same results from mathematical point of view.
The main feature of SRBF is, that they are dependent on the spherical distance between the data points and the location of the base functions. The value of a radial base function is maximum at its centre while it oscillates and decreases in far zones. Figure 3.3 shows six SRBF of different resolution. The resolution is measured by the maximum degree of expansion in (3.51). As it is obvious from this figure, the higher the resolution is, the narrower the base function will be. This means, the finer structures of the gravitational potential (higher frequencies) can be recovered only by narrower base functions.
According to (3.50), SRBF have global oscillations and do not have strict compact support for an ideal space localization. Nevertheless, the oscillations are rather small in far zones, so that they can be neglected. Therefore when analysing the gravitational potential using SRBF $B(\mathbf{r}_i, \mathbf{r}_k)$, the corresponding scaling coefficients α_k are predominantly determined by the observations around the centre of B. In chapter 5 we use this feature for the recovery of the regional gravity field and introduce a new condition for the regularization process.
Equation (3.51) describes the synthesis of the gravitational potential using SRBF (forward modelling) which is similar to spherical harmonic synthesis given by equation (3.30). The gravity field analysis using SRBF (i.e. determining scaling coefficients α_k) can be performed by means of spherical convolution integrals. Details of such numerical integration can be found in Freeden *et al.* (1998), Freeden (1999) or Schmidt *et al.* (2007). Evaluation of scaling coefficients using discrete convolution integrals has the advantage that there is no need to solve an inverse problem which is very often ill-posed. This is of great importance especially in regional modelling. Nevertheless, similar to the arguments given in section 3.1.2, the drawback is that the numerical integration by means of quadrature rules is limited to the surface of the sphere. This is due to the lack of appropriate cubature rules for the data above this surface (Schmidt *et al.*, 2007). See Fengler *et al.* (2005) for more details of numerical integration methods for data outside the sphere Ω_R.
Another alternative to determine the scaling coefficients α_k is least-squares adjustment as explained in (3.1.3). The least-squares estimation of the coefficients α_k is mainly similar to the estimation of spherical harmonic

coefficients given by equations (3.31) through (3.42) in section (3.1.3). To evaluate α_k using least-squares method, equation (3.31) should be rewritten in terms of SRBF for band limited observations v_i:

$$\frac{GM}{R}\sum_{k=1}^{K}\alpha_k\sum_{n=0}^{N_{max}}(\frac{R}{r_i})^{n+1}(2n+1)b_nP_n(\cos\psi)=v_i+e_i, \tag{3.52}$$

where the upper bounds of the summations are restricted to K and N_{max} in numerical computations. The design matrix $\mathbf{A}$ will be:

$$\mathbf{A}=\left[\frac{\partial V(\mathbf{r})}{\partial\alpha_1}\quad\ldots\quad\frac{\partial V(\mathbf{r})}{\partial\alpha_k}\right], \tag{3.53}$$

with

$$\frac{\partial V(\mathbf{r})}{\partial\alpha_k}=\frac{GM}{R}\sum_{n=0}^{N_{max}}(\frac{R}{\mathbf{r}})^{n+1}(2n+1)b_nP_n(\cos\psi). \tag{3.54}$$

Once the design matrix is computed, the least-squares estimation of the scaling coefficients and their covariance matrix are obtained using (3.36) and (3.42) respectively. In the next section, we describe the procedure of gravity field analysis using SRBF in more detail. To finish this section, it should be mentioned that the least-squares process given in section 3.1.3 is applicable in the case that the observations are potential values (e.g. potential values derived from CHAMP or GRACE data). For other types of observations such as potential differences dV and line-of-sight accelerometry from the GRACE mission or gravity gradiometry from GOCE the equations have to be written in terms of first or second order derivatives of the gravitational potential accordingly. See chapter 2 for more details on the observation equations related to various satellite data.

3.2.2 Relation to spherical harmonics

For the relation between spherical harmonics and SRBF, we make use of the addition theorem given by (3.16) and put it in equation (3.51)

$$V(r_i,\phi_i,\lambda_i)=\frac{GM}{R}\sum_{n=0}^{N_{max}}(\frac{R}{r_i})^{n+1}\sum_{m=-n}^{n}\bar{Y}_{nm}(\phi_i,\lambda_i)\sum_{k=1}^{K}\alpha_kb_n\bar{Y}_{nm}(\phi_k,\lambda_k). \tag{3.55}$$

Comparing equations (3.55) and (3.27), one can write a closed relation between the Stokes coefficients $\bar{C}_{nm}$ and the scaling coefficients α_k:

$$\bar{C}_{nm}=\sum_{k=1}^{K}\alpha_kb_n\bar{Y}_{nm}(\phi_k,\lambda_k). \tag{3.56}$$

This equation shows that spherical harmonic coefficients can be directly computed from the scaling coefficients. The reverse is not directly possible since it is an under determined inverse problem. Equation (3.56) has applications when the scaling coefficients α_k are to be assessed or to be compared to spherical harmonic solutions.

3.3 SH versus SRBF in satellite gravimetry: numerical aspects on the global scale

In this section, we consider the numerical implementation of gravity field analysis on the global scale using SRBF. The global gravity field will be determined using SRBF with maximum degree $N_{max}=70$. The

analysis is based on simulated potential differences along a GRACE-type orbit, no real data will be considered here. The reason is, that the focus is on the characteristics of the modelling rather than the field itself. Yet to be consistent to a good extent, with real data processing, a realistic noise level is also added to the simulated potential differences along the GRACE orbit. Furthermore, based on these simulated data, the global gravity field will be determined using spherical harmonics up to degree and order 70, so that it resembles the first model derived from SRBF. Different aspects of these two analysis methods such as their design and normal matrices, singular values, condition numbers and the estimated coefficients will be compared. It should be mentioned that global gravity field modelling using SRBF is not common in practice due to its rather high computational burden, compared to traditional spherical harmonic analysis. Nevertheless, it gives valuable insight into regional modelling using SRBF particularly for regularization purposes and this is to be illustrated in this section. Figure 3.4 shows geoid heights computed using the geopotential model GOCO03s (Mayer-Gürr, 2012) up to degree and order 70. In the following considerations, this gravity field model (in terms of geoid heights) will be considered as the true field to be reconstructed using spherical harmonics and SRBF.

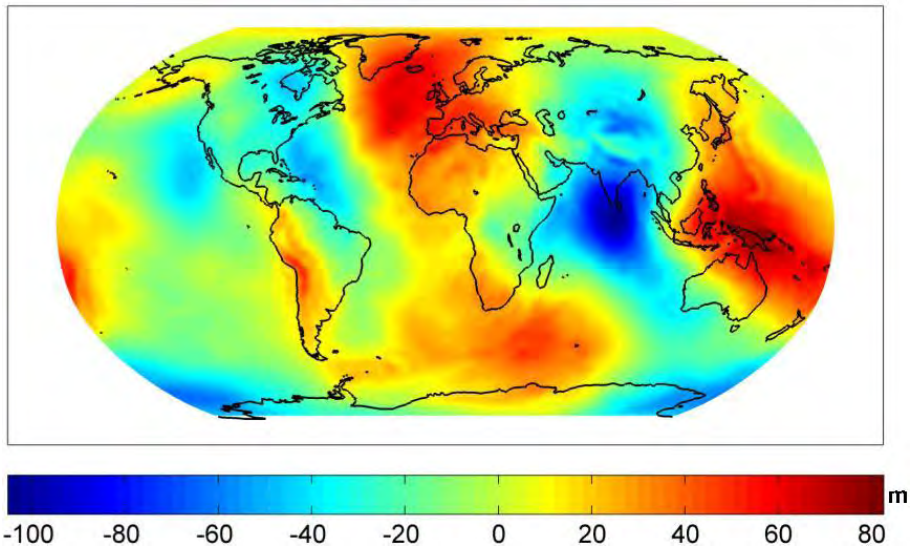

Figure 3.4: Geoid heights computed from geopotential model GOCO03s. The highest degree and order included in this expansion is 70. The unit is meter.

3.3.1 Simulated input data and noise

The input data are synthesized potential differences along a GRACE-type orbit. The synthesis is only based on the geopotential model GOCO03s and no force model, i.e. tides and atmospheric effects, are applied. The highest degree used in the synthesis is $n = 70$. The data cover a time period of 30 days with sampling interval of 5 seconds. Thus the total number of samples along the orbit is 518400 data points. To include observation noise in the modelling, a realization of random noise (white noise) is generated with a realistic standard deviation as follows: According to Jekeli (1999), the potential difference V_{AB} between two GRACE satellites can be well approximated by

$$V_{AB} \approx \|\dot{\mathbf{r}}_A\|\dot{\rho}, \tag{3.57}$$

which is a good approximate for pre-analysis purposes. $\dot{\mathbf{r}}_A$ and $\dot{\rho}$ are the velocity vector of the first satellite and the range rate, respectively. We postulate the error for $\dot{\mathbf{r}}_A$ and $\dot{\rho}$ to be in the order of $10^{-4}\,\mathrm{m/s}$ and $10^{-7}\,\mathrm{m/s}$, respectively (Case *et al.*, 2010, Tapley *et al.*, 2004). Applying the error propagation law to equation (3.57), a realistic noise level for the potential differences along the orbit will be approximately in the order of $10^{-3}\,\mathrm{m^2/s^2}$. Han *et al.* (2003) also used the same level of noise for their analysis based on simulated data. To avoid being too optimistic about the noise level, we assume the noise level to be two times larger i.e. $2 \times 10^{-3}\,\mathrm{m^2/s^2}$. Since the observation noise is not usually white, the white noise is then used to generate coloured noise by introducing correlation between adjacent observations. The coloured noise is generated using the following relations

$$\begin{aligned} c_0 &= w_0 \\ c_1 &= \beta c_0 + \sqrt{1-\beta^2} w_1 \\ &\vdots \\ c_{i+1} &= \beta c_i + \sqrt{1-\beta^2} w_{i+1}, \end{aligned} \tag{3.58}$$

where c_i denotes the coloured noise based on a realization of the white noise w_i. The parameter $0 \leq \beta \leq 1$ determines the correlation between adjacent observations which in our simulation, is $\beta = 0.9$. This model for coloured noise is proposed by Grafarend and Vanicek (1980) for the weight estimation in levelling networks and is also used by Austen and Grafarend (2004) for the recovery of the gravitational field from simulated GRACE data. Hence, the noisy observations are obtained by adding the coloured noise c_i to the synthesized potential differences V_{AB}.
The result of closed-loop simulation indicate that the imposed noise is realistic and fits to the current accuracy of GRACE monthly solutions (c.f. figure 3.5).

3.3.2 Global gravity field solutions

The observation equations for both spherical harmonics and SRBF should be written for the potential differences V_{AB}. According to equation (3.32), the general model in matrix form reads

$$\mathbf{l} + \mathbf{e} = \mathbf{A}_{sh}\mathbf{x}_{sh} = \mathbf{A}_{srbf}\mathbf{x}_{srbf}, \tag{3.59}$$

where $\mathbf{A}_{sh}$ and $\mathbf{x}_{sh}$ are the design matrix and vector of unknown Stokes's coefficients for spherical harmonic analysis. $\mathbf{A}_{srbf}$ and $\mathbf{x}_{srbf}$ are the design matrix and vector of scaling coefficients related to SRBF. The observation vector $\mathbf{l} = [v_1\ v_2\ ...v_I]^T_{AB}$ consists of potential differences along the GRACE orbit.

Solution 1: Spherical harmonics

The design matrix for spherical harmonics, based on the potential differences, is set up using (3.33) as the difference between satellites A and B. Since the maximum degree and order included in the series expansion is 70, the total number of unknowns will be $(70+1)^2 = 5041$. Three coefficients, c_{10}, c_{11} and s_{11}, are set to zero as the coordinate system is assumed to coincide with the Earth's center of mass (Hofmann and Moritz, 2005). Therefore the number of unknowns will be decreased to 5038. Together with 518400 observations, the size of $\mathbf{A}_{sh}$ and the corresponding normal matrix $\mathbf{N}_{sh} = \mathbf{A}^T_{sh}\mathbf{A}_{sh}$ will be 518400×5038 and 5038×5038, respectively.
The unknown coefficients $\bar{c}_{nm}$ and $\bar{s}_{nm}$ are determined using equation (3.36) and their corresponding standard deviations will be estimated using (3.42). To evaluate global spherical harmonic models, it is common to illustrate degree standard deviations σ_n and error degree standard deviations $d\sigma_n$ which show the signal and error contained in each specific frequency (spherical harmonic degree). For this, we computed σ_n using (3.23) and $d\sigma_n$ using (3.43) which are shown in figure 3.5. In addition, the degree standard deviation using Kaula's rule of thumb, given by equation (3.26), was also computed and displayed in this figure. A considerably good agreement can be seen between degree standard deviations derived from the model and Kaula's rule of thumb.
To estimate errors in simulation scenarios, it is possible to compute the differences between estimated spherical harmonic coefficients and coefficients given in the input model (here GOCO03s). These so called empirical errors can be used to assess the quality of computations as well as simulation:

$$\begin{cases} [dc_{nm}]^{emp} = [\bar{c}_{nm}]^{model} - [c_{nm}]^{goco03s} \\ [ds_{nm}]^{emp} = [\bar{s}_{nm}]^{model} - [s_{nm}]^{goco03s} \end{cases} \tag{3.60}$$

Figure 3.5 also shows the empirical errors computed from (3.60).

The estimated errors are two orders of magnitude larger than the GOCO03s errors. This is however expected because only one month of simulated data is used to compute this model. Therefore the errors should be compared to the errors of monthly GRACE solutions which are based on the same period. A good agreement can be seen between the errors of a GRACE monthly solution and our computations. This agreement is an indication, that the noise level added to the potential differences along the orbit is realistic.

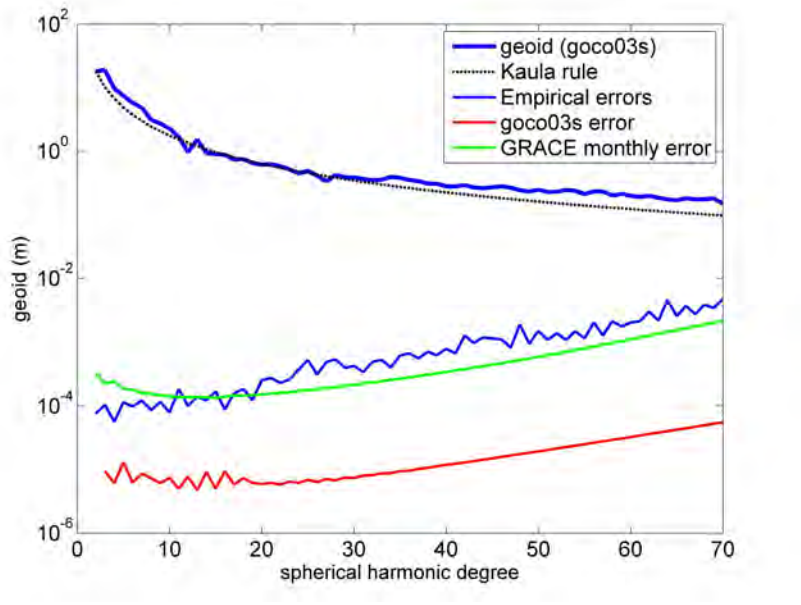

Figure 3.5: The results obtained from global modelling using a spherical harmonic analysis based on simulated potential difference along the GRACE orbit; geoid degree standard deviations of the computed model (thick-blue), degree standard deviations using Kaula's rule of thumb (dotted-black), estimated errors given in the model GOCO03s (red), empirical errors of the computed model (thin-blue) according to input model GOCO03s and errors of GRACE monthly solutions.

Based on the estimated coefficients $\bar{c}_{nm}$ and $\bar{s}_{nm}$, the geoid heights on the Earth's surface can be computed and compared to the GOCO03s geoid. Figure 3.6 shows the geoid difference between the GOCO03s geoid as shown in 3.4 and the geoid from the estimated model.

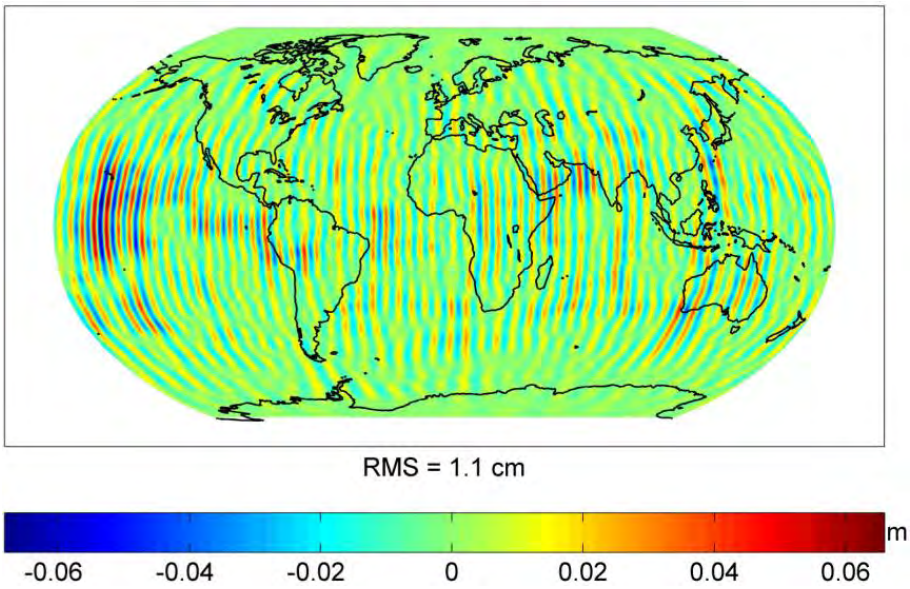

Figure 3.6: The result of the closed-loop simulation in terms of geoid differences between the global model GOCO03s and the computed model using spherical harmonics. The differences are in cm level with a global RMS of about $1\,\mathrm{cm}$.

As it can be seen, the geoid differences are in cm level with largest deviations near the equator. This is due to the less dense sampling of GRACE-like orbit around the equator. The rms value of the geoid differences is about $1\,\mathrm{cm}$ with minimum and maximum values of $-7\,\mathrm{cm}$ and $7\,\mathrm{cm}$ respectively.

Solution 2: Spherical radial base functions

The design matrix $\mathbf{A}_{srbf}$ will be set up using (3.53) and (3.54) as the potential difference between two GRACE satellites.
The maximum degree of expansion in equation (3.52) is set equal to 70, ($N_{max} = 70$), to obtain an equivalent solution to the spherical harmonic case. The Legendre coefficients b_n are set equal to 1 since no smoothing is desired on the global scale. The base functions are distributed on a Reuter grid corresponding to maximum degree 70 (the Reuter grid is defined in section 4.2.4). The number of base functions used in this analysis are 6207 corresponding to the number of points on the Reuter grid. Thus, the size of $\mathbf{A}_{srbf}$ and $\mathbf{N}_{srbf}$ are 518400×6207 and 6207×6207, respectively. Estimation of the unknown scaling coefficients α_k on the global scale is not as straightforward as the Stokes coefficients. The reason roots in the fact that spherical harmonic functions are (theoretically) orthonormal base functions and therefore are independent. This implies that the normal matrix $\mathbf{N}_{sh}$ is of full column rank and its inverse in (3.36) can be computed without any difficulty. This does not hold for $\mathbf{N}_{srbf}$ due to the dependency of column vectors. The normal matrix $\mathbf{N}_{srbf}$ belongs to the class of rank-deficient matrices with dependent columns (and rows). This rank-deficiency has nothing to do with the observation vector and can be resolved using spectral decomposition of $\mathbf{N}_{srbf}$ or the so called singular value decomposition (SVD)[1]. Figure 5.4 shows the singular values of $\mathbf{N}_{srbf}$ and $\mathbf{N}_{sh}$. As it can be seen, 5038 singular values of $\mathbf{N}_{sh}$ as well as the first 5038 singular values of $\mathbf{N}_{srbf}$ decay very slowly. There is a sudden jump between the 5038^{th} and 5039^{th} singular values of $\mathbf{N}_{srbf}$. This gap is an indication for the rank-deficiency of the normal matrix associated with SRBF. This means only 5038 base functions among 6027 base functions used on the global scale are linearly independent which is equal to the number of spherical harmonics. This can be considered as a numerical proof that **the spherical harmonics and the SRBF span the same function space.**
The solution, i.e. the scaling coefficients α_k, are estimated using the truncated SVD method by taking the first 5038 singular values of $\mathbf{N}_{srbf}$ into account (c.f. section 5.4.1) . Using the estimated coefficients, the geoid

[1] See 5.2.2 for more details about the singular value decomposition.

heights are synthesized and compared to the GOCO03s geoid. The geoid differences are the same as those obtained from SH shown in figure 3.6 (to the numerical precision of the used computer).
Figure 3.7 (right) shows the spatial pattern of the estimated coefficients on the corresponding Reuter grid points. The left panel displays the synthesized geoid using the scaling coefficients α_k at the same locations. Evidently, the scaling coefficients and the geoid heights reveal the same spatial pattern. In other words, the estimated scaling coefficients look like the geoid or disturbing potential. (compare these two figures also to figure 3.4. The reason is the space-localizing feature of the SRBF. According to figure 3.3, the energy of these base functions are concentrated on their centre (the nodes of the grid). Therefore it is expected that the scaling coefficients are highly affected by the data around their location.

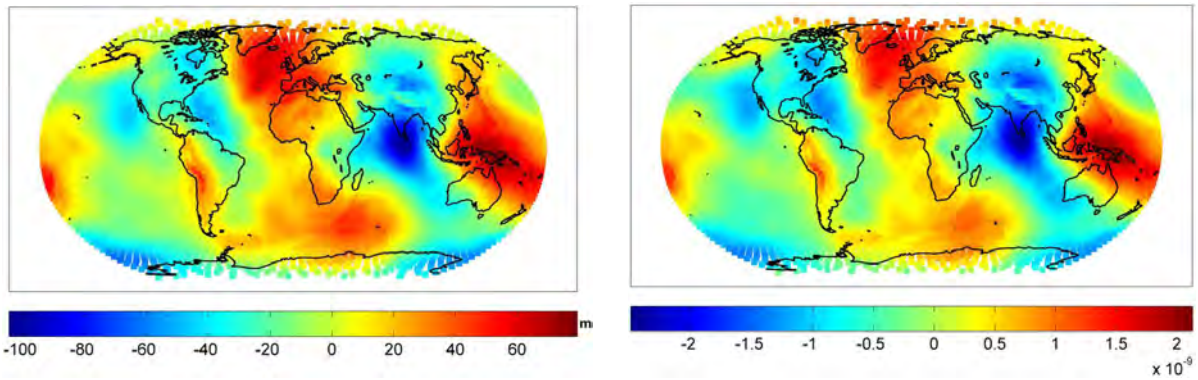

Figure 3.7: **Left**: The geoid heights computed on the Reuter grid using the estimated scaling coefficients. **Right**: The value of the estimated scaling coefficients α_k (dimensionless) for each point on the Reuter grid. According to the space-localizing property of the SRBF, the scaling coefficients represent the general shape of the geoid. This nice feature can be used as prior information for regularization purposes. See Chapter 5.

To measure the similarity of the scaling coefficients α_k and the geoid heights N_k at locations (ϕ_k, λ_k), we computed the cross correlation function using these two signals. The maximum correlation is achieved at zero lag as expected which amounts to 0.986. The cross correlation function is displayed in figure 3.8. We discuss this feature with more detail in Section 5.6, where we make use of it as prior knowledge about the unknown coefficients α_k.

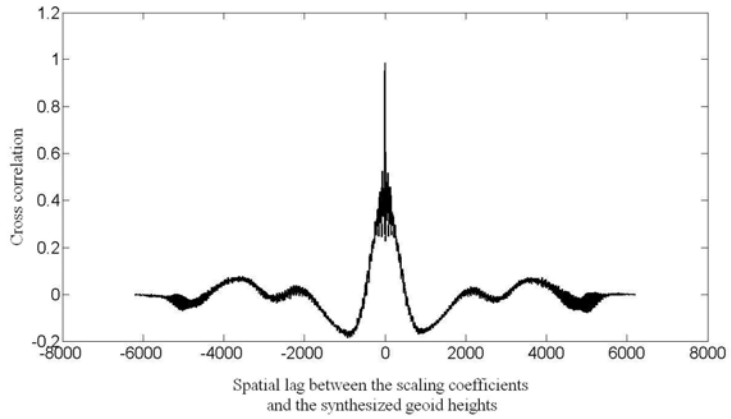

Figure 3.8: The cross-correlation function for the estimated scaling coefficients α_k and the geoid heights synthesized at the same locations. The maximum correlation is about 0.986 at zero lag of the cross-correlation function. The horizontal axis shows the lag of the cross-correlation function.

4 Regional gravity field modelling using SRBF

In the previous chapter, we considered the representation of the Earth's gravity field using spherical harmonics and the drawbacks of using these global base functions were discussed. SRBF in their general form were explained. For spherical harmonic analysis, the only parameter which should be chosen, is the highest degree and order included in series expansion, i.e. N_{max} in equation (3.31). The maximum degree is selected based on the expected frequency content of the input signal or observations. For example the expected maximum degree of the GRACE monthly solutions is about 120 or for the case of the GOCE static field it is roughly 250. Once this maximum degree is selected, the design matrix can be set up using (3.33) and (3.34) and the solution will be obtained. This also holds for global gravity field analysis using SRBF. The reproducing kernel defined by equation (3.46) is a good choice (and comparable to SH) for global modelling using SRBF and, similar to SH, only the maximum degree should be chosen. While the mathematical expressions, for global and regional gravity field modelling using SRBF are rather similar, the numerical implementation differs significantly.
This chapter addresses the use of band-limited SRBF for regional gravity field modelling. The emphasis is put on satellite-based observations. These base functions are mainly suitable for regional gravity field modelling and might be considered as complementary approaches to spherical harmonics.

4.1 From global to regional scale

The fundamental difference between the global and regional gravity field modelling using SRBF is, that the base functions and observations cover only a specific part of the sphere $\tilde{\Omega}_R \subset \Omega_R$ as illustrated by figure 4.1. We call this region, hereafter, **the model zone**.

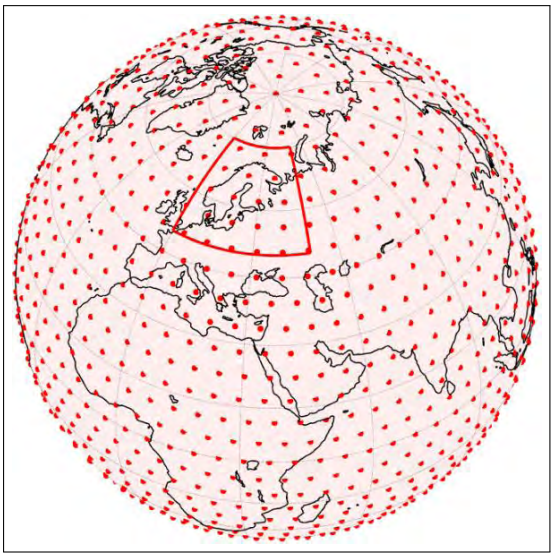

Figure 4.1: From global scale to regional scale; the gravity field is desired on a regional scale within the subsurface $\tilde{\Omega}_R$ shown by blue frame

To explain this in more detail, we start with equation (3.32) for global modelling and split it as

$$\mathbf{A}\mathbf{x} = \mathbf{l} + \mathbf{e} \quad \Longrightarrow \quad \begin{cases} \mathbf{A}_{11}\mathbf{x}_1 + \mathbf{A}_{12}\mathbf{x}_2 = \mathbf{l}_1 + \mathbf{e}_1 \\ \mathbf{A}_{21}\mathbf{x}_1 + \mathbf{A}_{22}\mathbf{x}_2 = \mathbf{l}_2 + \mathbf{e}_2 \end{cases} \tag{4.1}$$

or in matrix form:

$$\underbrace{\begin{bmatrix} \mathbf{A}_{11} & \mathbf{A}_{12} \\ \mathbf{A}_{21} & \mathbf{A}_{22} \end{bmatrix}}_{\mathbf{A}} \underbrace{\begin{bmatrix} \mathbf{x}_1 \\ \mathbf{x}_2 \end{bmatrix}}_{\mathbf{x}} = \underbrace{\begin{bmatrix} \mathbf{l}_1 \\ \mathbf{l}_2 \end{bmatrix}}_{\mathbf{l}} + \underbrace{\begin{bmatrix} \mathbf{e}_1 \\ \mathbf{e}_2 \end{bmatrix}}_{\mathbf{e}}. \tag{4.2}$$

Assume that the upper left part of the design matrix $\mathbf{A}$, i.e. $\mathbf{A}_{11}$, is the 'partial' design matrix, which is set up for the subregion $\tilde{\Omega}_R$ on the sphere. Correspondingly, $\mathbf{x}_1 \subset \mathbf{x}$ and $\mathbf{l}_1 \subset \mathbf{l}$ are the unknown parameters and observation vector within $\tilde{\Omega}_R$. On a regional scale, we attempt to solve the following equation system

$$\mathbf{A}_{11}\mathbf{x}_1 \approx \mathbf{l}_1 + \mathbf{e}_1. \tag{4.3}$$

Equations (3.32) or (4.1) and (4.3) describe the main differences between gravity field modelling using SRBF on the global scale and regional scales. While the former is a complete setting of the design matrix with global observations, the latter ignores some components of (4.1) and therefore suffers from 'cutting' issues. As it can be seen from (4.1) and (4.3) two 'cutting' or truncations exist:

- The second line of equation (4.1), i.e. $\mathbf{A}_{21}\mathbf{x}_1 + \mathbf{A}_{22}\mathbf{x}_2 = \mathbf{l}_2 + \mathbf{e}_2$, is completely removed in (4.3). This equation describes the contribution of $\mathbf{l}_2$ (observations outside the region) to the estimation of scaling coefficients $\mathbf{x}$. Therefore $\mathbf{l}_2$ does have effects on the scaling coefficients $\mathbf{x}_1$ (coefficients inside the region). Without the vector $\mathbf{l}_2$ modelling the global structures of the geopotential is impossible. In other words, only the regional part of the gravitational potential corresponding to the spatial extension of $\tilde{\Omega}_R$ can be modelled and the base functions inside this region can only model the short wavelength (related to the size of $\tilde{\Omega}_R$) of the field. Therefore to solve for $\mathbf{x}_1$, the long wavelengths of the gravity field must be removed from $\mathbf{l}_1$. In addition, the removal of $\mathbf{A}_{21}$ from the row space of the original design matrix $\mathbf{A}$ is equivalent to cutting the base functions from a certain distance. The reason is that the base functions are sampled at data points and since $\mathbf{l}_2$ is removed, there is no sample from the base functions at these locations. This is especially a severe problem in borders of $\tilde{\Omega}_R$ which causes edge effects in the computations. Moreover, those observations which are outside but close to the region $\tilde{\Omega}_R$, can still have a considerable contribution to the estimation of scaling coefficients $\mathbf{x}_1$. Therefore it is reasonable to include more observations beyond the region $\tilde{\Omega}_R$ to reduce the border distortion and effects caused by the sudden *'cut off'* of the observations. This means the data should cover a larger region compared to $\tilde{\Omega}_R$. We call this region, **the data zone** and denote it by $\tilde{\Omega}_R^{data}$.
- Another component which is not considered in (4.3) is $\mathbf{A}_{12}\mathbf{x}_2$. This part models the contribution of the (removed) scaling functions, $\mathbf{x}_2$, which are outside of the region, to model observations inside the region i.e. $\mathbf{l}_1$. Removing $\mathbf{x}_2$ from the equation system causes another kind of border distortion in computations. To overcome this problem, it is logical to bring some of the removed $\mathbf{x}_2$ back to the equations. Those elements of $\mathbf{x}_2$ which are close to the data zone have significant impact and shall be considered in (4.3). Therefore the base functions cover another area which we name **the grid zone** and denote it by $\tilde{\Omega}_R^{grid}$.

Based on the discussions above, there are three zones needed for regional gravity field modelling as

$$\underbrace{\tilde{\Omega}_R^{grid}}_{\text{grid zone}} > \overbrace{\tilde{\Omega}_R^{data}}^{\text{data zone}} > \underbrace{\tilde{\Omega}_R}_{\text{model zone}} \tag{4.4}$$

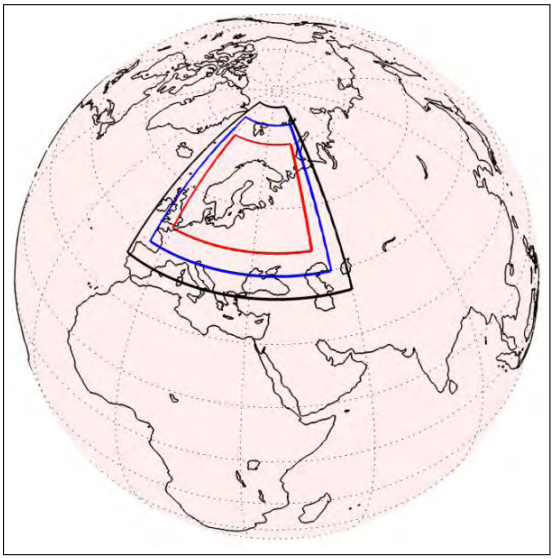

Figure 4.2: Three different zones used in regional gravity field modeling: the model zone (red), the data zone (blue) and the grid zone (black).

which are illustrated in figure 4.2. Except the model zone which is given by the user, the other two zones should be defined according to different aspects of the regional modelling. In addition to these two zones, which should be defined, there are other factors to be predefined for regional gravity field modelling: type of SRBF and their bandwidth, the number and the position of base the functions, the removal of the long wavelengths and finally the method of inversion can be mentioned for instance. Therefore, unlike the global modelling, regional solutions include a collection of different choices to be made. The variety of options in regional gravity field modelling using SRBF, could be considered as an advantage due to the possible flexibility in the model setup. Based on the types of available observations and their coverage in a specific region, the model can be set up for the purpose of the modelling. Most problems mentioned in section 3.1.4 can be handled using appropriate selections in the model setup using SRBF. On the other hand, if the choices are to be made arbitrarily or using trial and error, the regional modelling using SRBF becomes a complicated issue with no clear outcome. In the following section we explain these possible choices in more detail and clarify the way, the model is set up within this thesis.

4.2 Model setup using SRBF

Equation (3.51) describes the most general form of gravity field modelling using SRBF. One can rewrite this equation for regional gravity field modelling as follows:

$$V(r_i,\phi_i,\lambda_i)=\frac{GM}{R}\sum_{k=1}^{K}\alpha_k\sum_{n=N_{min}}^{N_{max}}(\frac{R}{r_i})^{n+1}(2n+1)b_nP_n(<\mathbf{r}_i,\mathbf{r}_k>),\quad i=1,2,...,I \tag{4.5}$$

with the spherical distance $\cos\psi =< \mathbf{r}_i,\mathbf{r}_k >$. From this equation it is clear that the following factors should be defined:

1. Shape of SRBF (non band-limited or band-limited determined by b_n).
2. Maximum degree of expansion N_{max} which is related to the bandwidth of SRBF.
3. Removal of the long wavelengths (defined by N_{min}).
4. Position of SRBF defined by $\mathbf{r}_k=\mathbf{r}_k(r_k,\phi_k,\lambda_k)$.
5. Extension of data zone related to I or the number of observations.

6. Extension of the grid zone related to K or the number of unknowns.

7. Inversion process or choosing a proper regularization approach.

These different possibilities for the regional gravity model using SRBF have made it almost impossible to define a unique way to set up the equation system. It is also not easily possible to speak of the best sequence of choices for all regions and all kinds of data. Due to this diversity, these choices were made arbitrarily using a specific '*recipe*' in almost all previous works on regional modelling.
There are several research studies where the effect of (some of) these options are considered in a comparison manner. For example Tenzer and Klees (2008) investigated the choice of optimal SRBF for local gravity field modelling based on terrestrial data. They concluded that if the depth of SRBF is chosen carefully, different types of SRBF result in more or less the same accuracy for gravity field modelling. In another study Eicker (2008) used spherical splines (as a variant of SRBF) to refine the global gravity field modelling based on satellite data. A main emphasis of her work was to study the impact of different grid types for the distribution of SRBF on the sphere. In a more general work, Wittwer (2009) presented the applicability of several SRBF for regional gravity field modelling based on satellite and terrestrial data. He also investigated some aspects such as bandwidth selection and network design for the position of SRBF. Schachtschneider *et al.* (2010) included the effect of satellite altitude, size of the data zone and the degree of the a priori gravity field model in their research study to investigate the error distribution in regional modelling of the potential and magnetic field.
As an other example, Bentel *et al.* (2013) compared several band-limited and non band-limited SRBF for gravity field modelling based on satellite data in a simulation scenario. They discussed the performance of different SRBF while other choices such as grid type, bandwidth and extension of data and model zones were fixed.
Although such valuable investigations in this field have been carried out, there is yet no reasonable strategy to define the choices rigorously. Therefore the sequence of choices is usually dependent on the focus of analysis and is done in an *Ad-hoc* style. In the followings, we investigate these 7 specifications separately and provide a guideline for these choices. We try to develop a systematic methodology for the choices to be made which also maintains the generality of the model setup.

4.2.1 Shape of the SRBF

The shape of SRBF is determined by the Legendre coefficients b_n in (4.5). These coefficients act as the degree-dependent weighting for the Legendre polynomials P_n and control the spectral behaviour of the base functions. From the signal processing view, the coefficients b_n can be considered as the filtering coefficients of the SRBF and one can tune the **regularity** of the base functions by modifying these coefficients. Therefore, b_n play an important role also in the inversion of regional gravity field models.
There are several kinds of SRBF depending on how the Legendre coefficients b_n are defined. Here we consider some known SRBF which have been used for the regional gravity field modelling.

The Shannon kernel

The simplest set of coefficients is defined by the Shannon kernel where the coefficients are all one up to a certain degree. Shannon Legendre coefficients are given by (e.g. Keller (2004))

$$b_n^{sh} = \begin{cases} 1 & n \in [0, N_{max}) \\ 0 & \text{elsewhere} \end{cases} \tag{4.6}$$

which is an ideal low pass (and band pass) filter in the frequency domain. The advantage of the Shannon kernel is the full control over the frequency content of the base functions since no smoothing is applied.

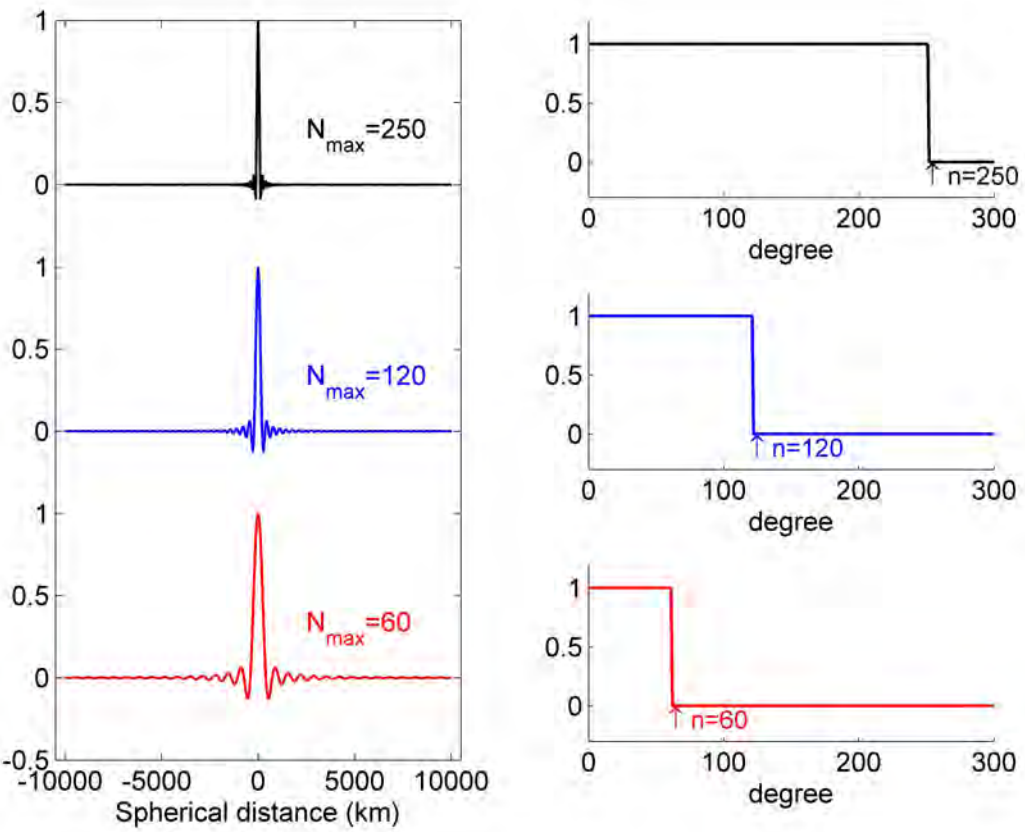

Figure 4.3: Three SRBF with Shannon kernel with $N_{max} = 60, 120$ and 250. The spectral behaviour is shown in the right panel. This kernel acts as an exact low-pass filter with a sudden frequency cut-off.

The drawback is the rippling of the base functions in the spatial domain caused by the truncation in the frequency domain, which is analogous to the Gibbs effect in Fourier analysis. This makes the base functions to have oscillation even in far zones. Nevertheless, as we show in Chapter 6, this shortage can be overcome by means of an appropriate regularization. Figure 4.3 shows the Shannon-type SRBF with different N_{max} as well as their frequency response. The non band-limited version of the Shannon kernel, is the point mass kernel which has been widely used in physical geodesy (Vermeer, 1989). It can also be considered as a variant of the reproducing kernel introduced in equation (3.46).

The Blackman kernel

An alternative to the Shannon Kernel is the Blackman kernel, which was introduced by Schmidt *et al.* (2006). It is based on the Blackman window, widely used in signal processing since the 1950's (Steven, 1997). Blackman coefficients are

$$b_n^{bl} = \begin{cases} 1 & n \in [0, n_1) \\ 0.42 - 0.5\cos\left(\dfrac{2\pi n}{N_{max}}\right) + 0.04\cos\left(\dfrac{4\pi n}{N_{max}}\right) & n \in [n_1, N_{max}) \\ 0 & \text{elsewhere.} \end{cases} \tag{4.7}$$

Figure 4.4 displays several SRBF with the Blackman kernel. As it can be seen, the spectrum has two parts: a Shannon-like segment and a transition band to zero. It oscillates much less compared to the Shannon kernel in far zones. To avoid the smoothing effects of the Blackman kernel in the modelling, n_1 in (4.7) should be

chosen close to the expected resolution of the desired regional gravity field and N_{max} will be rather higher than n_1 (usually twice as n_1). The consequence of choosing a larger N_{max}, will be the need for more base functions in the analysis. For instance, if in a certain regional gravity field using the Shannon kernel with $N_{max} = 120$, 1500 base functions are needed, the number of Blackman base functions would be about 6000 (four times larger). The Blackman kernel has been used by Schmidt *et al.* (2007) for regional gravity field modelling based on CHAMP data. They used $n_1 = 80$ and $N_{max} = 192$ to model geoid heights in the northern part of South America.

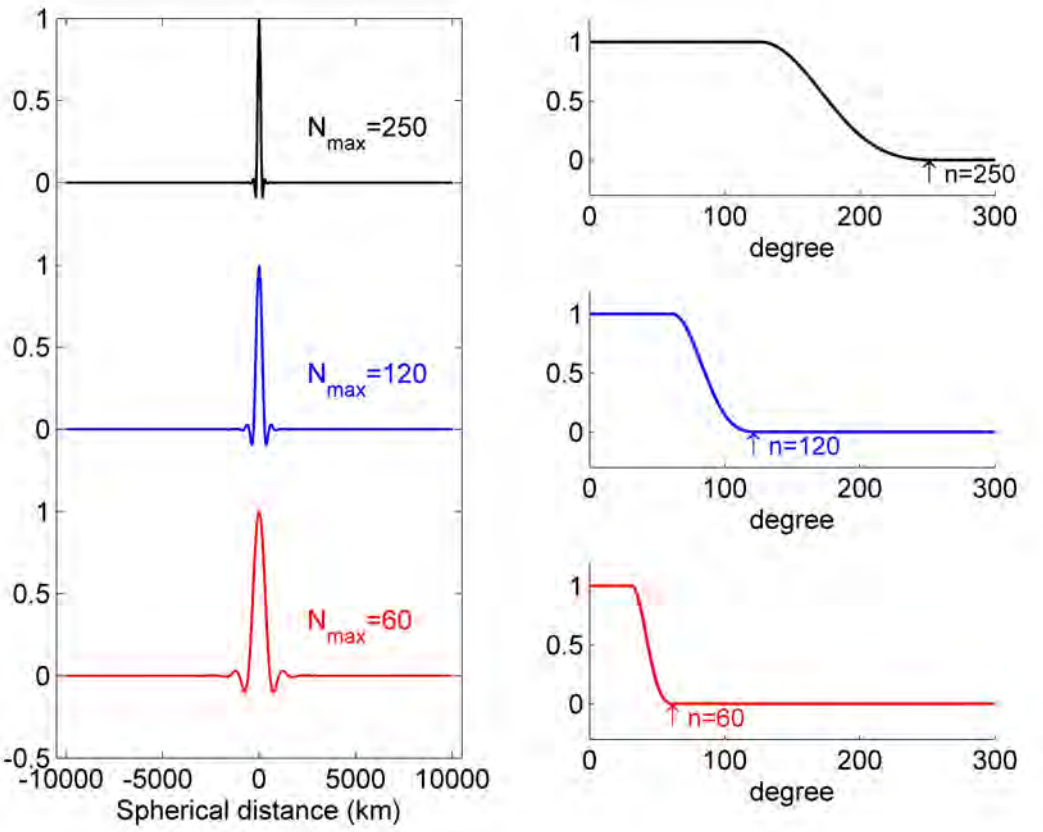

Figure 4.4: Three SRBF with Blackman kernel with $N_{max} = 60, 120$ and 250. The spectral behaviour is shown in the right panel. This kernel has a Shannon-like segment and a transition part for smooth decay to zero.

The CuP kernel

Another kernel is the cubic polynomial or in brief the CuP kernel. It is a polynomial of degree 3 and smoothes the decay of the power spectrum. Unlike the Blackman kernel, the decay of the power spectrum using the CuP kernel starts from the beginning. The CuP coefficients are given by

$$b_n^{cu} = \begin{cases} \left(1 - \frac{n}{N_{max}}\right)^2 \left(1 + \frac{2n}{N_{max}}\right) & n \in [0, N_{max}) \\ 0 & \text{elsewhere.} \end{cases} \tag{4.8}$$

The spatial and spectral behaviour of the CuP kernel is shown in figure 4.5 for different N_{max}. The CuP kernel filters the frequencies from the beginning which results in much less oscillations in the spatial domain. N_{max} in CuP kernel should be chosen with care to avoid unwanted filtering by the base functions. The CuP kernel with $N_{max} = 450$ was used by Bentel *et al.* (2013) along with other types of band and non band-limited SRBF

to assess the performance of each base function. They listed the CuP kernel among the base functions which provide 'very good' results in terms of residuals on the Earth's surface.

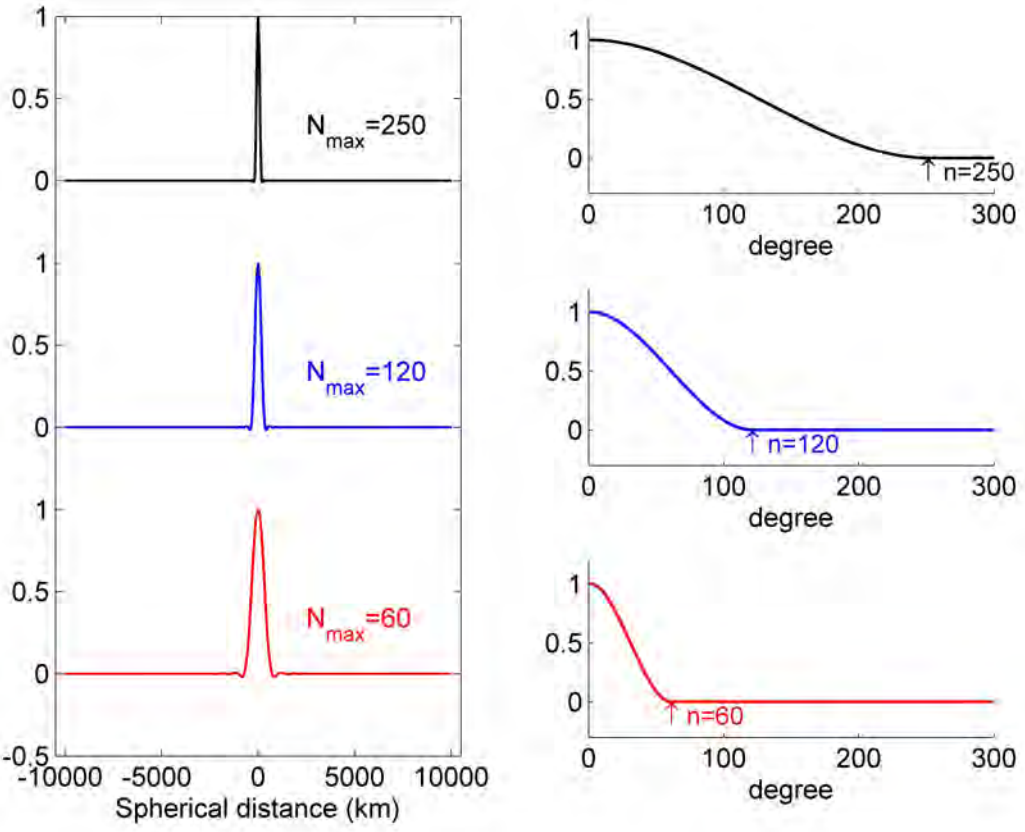

Figure 4.5: Three SRBF with CuP kernel with $N_{max} = 60, 120$ and 250. The spectral behaviour is shown in the right panel. The decay of the spectrum starts from the beginning and thus all frequencies are affected by the kernel.

The Spline kernel

Another way to define the Legendre coefficients b_n is to use the frequency response of the Earth's gravity field. The degree variances given by equation (3.23) are in fact the frequency response of the gravitational potential which can be used as the Legendre coefficients. The resulting SRBF are the harmonic splines with the following kernel

$$b_n^{sp} = \begin{cases} \epsilon(V) & n \in [0, n_1) \\ \dfrac{\sigma_n}{\sqrt{2n+1}} & n \in [n_1, N_{max}) \\ 0 & \text{elsewhere} \end{cases} \tag{4.9}$$

in which, σ_n are the degree standard deviations from a known model. Alternatively, σ_n can be computed using Kaula's rule of thumb. $\epsilon(V)$ can be computed using the error degree variances of a background model or might be set to zero. Figure 4.6 shows the shape of the spline functions in the spatial and spectral domains in which $\epsilon(V) = 0$.

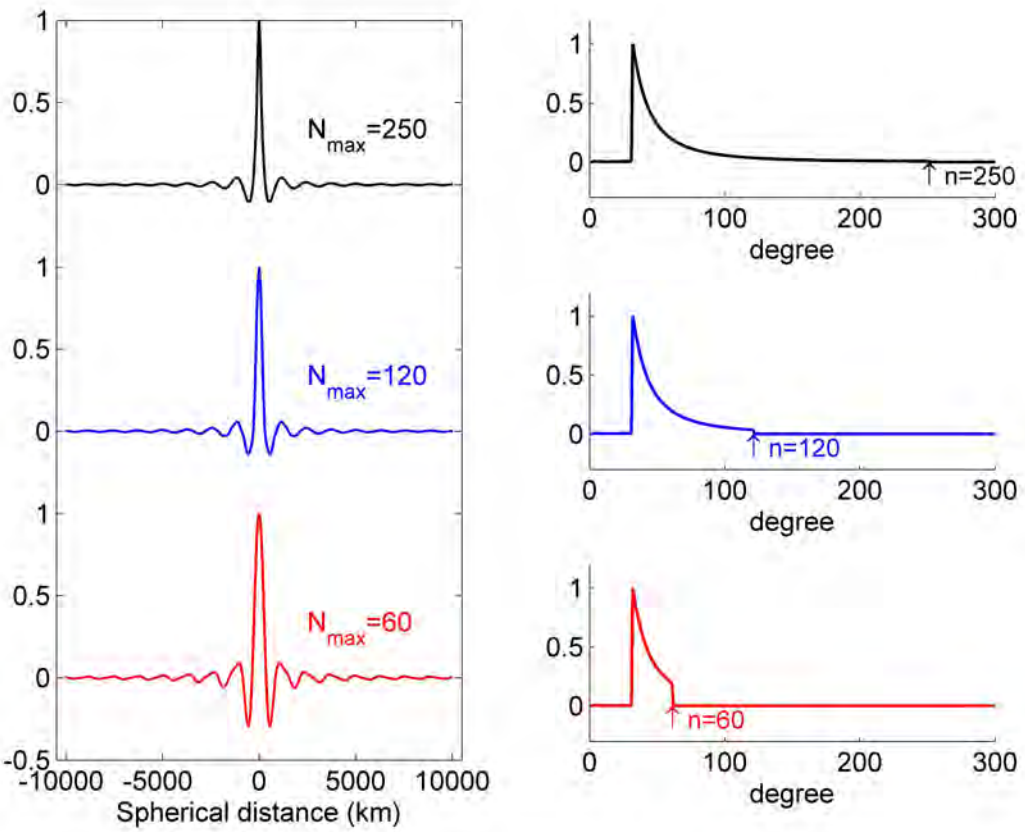

Figure 4.6: Three SRBF with harmonic spline kernel with $N_{max} = 60, 120$ and 250. n_1 is equal to 30 in all cases. The spectral behaviour is also shown in the right panel. This kernel provides a rational decay of the spectrum since the Legendre coefficients are computed using the degree variance of a priori known model or alternatively using the Kaula's rule of thumb.

Compared to the CuP kernel, the Spline kernel has a logical decay in the spectral domain, since it matches the nature of the Earth's gravity field. This approach is proposed by Eicker (2008) for the refinement of globally determined solutions using regional patches, see also Schmidt *et al.* (2007) and Eicker *et al.* (2010). More details on different kinds of spline kernels can be found in Jekeli (2005).

In this thesis, we distinguish two kinds of SRBF depending on the definition of b_n:

- $b_n = 1$ for all n: Such base functions have no measure of regularity since all frequencies have the same weight.
- $0 \leq b_n \leq 1$ for some n: These base functions contain some built-in regularity since some frequency parts (often high frequencies) are damped out by b_n.

Therefore the Shannon kernel with $b_n = 1$ belongs to the first group while other kernels such as Blackman, CuP and spline are in the second group. The difference between these two groups of SRBF and their impact in the regional gravity modelling, can be described in terms of regularization. We will come back to this issue in section 5.8.

4.2.2 Maximum degree of expansion

The issue of choosing the right N_{max} for gravity field analysis is the same for spherical harmonics and SRBF. This is directly related to the fact that spherical harmonics and SRBF given by equation (3.50), belong to the

class of band-limited functions. Band-limitedness of the SRBF implies

$$b_n = 0 \text{ for all } n > N_{max} \tag{4.10}$$

so that the expansion can be restricted to the maximum degree $n = N_{max}$. This assumption is true provided that the signal to be analysed using such base functions, is also band-limited. The observed signals associated with natural phenomena (i.e. gravitational potential) are rarely band-limited and such assumptions are not exactly correct. Nevertheless, due to the presence of noise in observations, the signal to noise ratio (SNR) can be considered as a fair measure to determine the frequency content of a given signal. In case of satellite-based gravimetry, such as GRACE K-band measurements or GOCE gradiometry observations, the data can be fairly assumed to be band-limited not only due to the present observation noise, but also due to the signal attenuation at satellite altitude. Therefore the choice of band-limited SRBF for analysing satellite gravity data is logical and reasonable. As mentioned before, the expected resolutions for GRACE (monthly) and GOCE solutions are about $N_{max} = 120$ and $N_{max} = 250$, respectively. These values are valid provided that $b_n = 1$ for all n up to N_{max}. If kernels such as CuP or Blackman are included in the modelling, the N_{max} should be chosen carefully to avoid filtering of the signal components.
For gravity data with high frequency content such as terrestrial gravity observations or airborne gravimetry, it is still possible to use band-limited SRBF with rather high degree in series expansion. In addition, it is also possible to use another class of SRBF, known as non-band limited SRBF. In principle equation (3.50) describes a non-band limited SRBF in terms of Legendre polynomials where the maximum degree is not bounded. To apply such functions in gravity field analysis, the analytical expressions should be available. Klees *et al.* (2008) summarizes the analytical form of several non-band limited SRBF such as *point mass kernel*, *radial multipole* and *Poisson wavelet*. The point mass kernel has probably the simplest analytical form as it is the reciprocal distance between evaluation points and the location of base functions. Many investigations have been carried out to model gravity fields using point masses. Tenzer and Klees (2008) address a rather complete list of research studies using non-band limited kernels.
In this thesis we restrict our investigation to band-limited SRBF since the goal is to analyse satellite based observations.

4.2.3 Removal of the long wavelengths

The Earth's gravitational potential consists of all frequencies and wavelengths. The long wavelengths correspond to global features of the field and the short wavelengths reveal the regional and local properties. The recovery of all components is only possible on the global scale where global observations are available. This means that on regional scales the long wavelengths, i.e. the global components, cannot be determined. Therefore the expansion (4.5) should be limited to short wavelengths according to the size of the model zone. Hence, while N_{max} is chosen due to the frequency content of the observations, N_{min} is dependent on the size of the region or the model zone. The relation between the spatial wavelengths of the region and corresponding degree of SH or SRBF is given by an approximate rule of thumb:

$$n = \frac{40000}{w} \tag{4.11}$$

in which w is the size of the region in km and the equatorial perimeter of the Earth is approximately set to $40000\,\mathrm{km}$. This equation gives an insight into the right N_{min} in (4.5). For example if the size of the model zone in figure 4.2 is about $1500\,\mathrm{km}$, the wavelengths $n < 26$ cannot be determined correctly and will corrupt the estimation. Hence it is reasonable to set $N_{min} = 26$ or larger.
Restriction of N_{max} and N_{min} to certain values means that the resulting SRBFs act as band-pass filters provided that the scaling coefficients α_k are obtained via convolution. However, since parameter estimation is performed using the least-squares adjustment, the (regional) observation vector $\mathbf{l}_1$ should also be reduced to avoid the leakage of the long wavelengths to the regional solution. In other words, the long wavelengths of the gravitational potential must be removed from the observation vector $\mathbf{l}_1$. This implies that the observations vector $\mathbf{l}_1$ need to be reduced with synthesized pseudo observations based on a prior gravity model up to N_{min}:

$$\delta \mathbf{l}_1 = \mathbf{l}_1 - \mathbf{l}_1^{N_{min}} \tag{4.12}$$

This reduction makes the regional solution being dependent on the prior model used to synthesize $\mathbf{l}_1^{N_{min}}$. One can also consider the regional solution to be a **regional refinement** for this prior model; less refinement is needed for big N_{min} and vice versa more refinement is needed for smaller N_{min}.
As stated before, N_{min} can be obtained from equation (4.11) so that the observations are reduced as little as possible and consequently the final regional model will be less dependent on the prior model. In some research studies, the authors used the maximum reduction of the observation vector. In this case the prior global model plays a central role in the final modelling and the regional solution is responsible for very tiny refinement to the global model. See for example Eicker (2008), Antoni (2012) and Tenzer and Klees (2008). In these studies, the idea is to first model the gravitational potential using spherical harmonics with the maximum possible degree N_{max}. In the next step, the residuals will be 'regionally' re-analysed using space-localizing base functions. This is also a common method in global gravity field modelling. The difference is that, in global gravity field modelling, the corrections to the removed part will also be estimated so that the reference field is updated. In contrast, in regional gravity field modelling, the removed part is considered as the true field which will be added to the regional solution.
In our methodology, we prefer to model the regional gravity in a way, that the SRBF have the maximum contribution. In other words, we reduce the observation using the minimum possible N_{min} so that the final regional solution is less affected by the input global model. In the numerical investigations in Chapter 6, we set $N_{min} = 30$ according to the size of the selected test regions. Choosing a larger N_{min} is unnecessary since no remarkable improvement is seen.

4.2.4 Position of the SRBF

Another important choice to be made for gravity field analysis using SRBF is the location of base functions where they are centred. The position vector of base functions is needed for the evaluation of Legendre polynomials $P_n(\cos\psi)$ as it depends on the location of data (evaluation points) and the base functions, see equation (3.17). There are generally two ways to determine the location of base functions:

Free-positioned base functions
In this method the position of the base functions is to be determined within the parameter estimation along with unknown scaling coefficients. Thus a non-linear problem with three parameters for each base function (two parameters for the position and one as for the scaling coefficient) has to be solved for. This reduces the number of SRBF significantly which is an advantage. The cost, however, is to pose additional unknowns and including non-linear parameters in the equations system which consequently results in more complexity of the gravity field analysis. Antoni (2012) developed a non-linear approach to determine the position of base functions simultaneously with scaling coefficients. Alternative approaches to reduce the number of base functions have been also proposed. Klees *et al.* (2008) and Wittwer (2009) presented a data-adaptive strategy to reduce the number of base functions. Some authors describe the position of base functions in 3D space where the depth of the base functions is also an important choice to be made. For majority of SRBF used in gravity field modelling, the choice of depth is equivalent to bandwidth selection of SRBF (Klees *et al.*, 2008), see also Marchenko (1998), Marchenko *et al.* (2001) and Marchenko (2003) for more optimization algorithms to reduce the number of base functions in a free-position manner.

Fixed-position base functions
A very common way to define the location of base functions is to use fixed positions. In this method a cluster of points, called **grid points**, should be distributed on the surface of the sphere. Since SRBF are symmetric and isotropic base functions, the grid points are also expected to be distributed as homogeneous as possible. The number of grid points, i.e. the number of base functions, must not exceed the total number of observations ($I \geq K$). Moreover, the distance between grid points should be such that the adjacent base functions cover the region in between reasonably. This is directly related to the width and therefore to the highest degree (N_{max}) included in series expansion (for band limited SRBF). The higher the N_{max} is, the narrower the base

function will be and consequently more base functions are needed. Eicker (2008) summarized and presented several kinds of point distribution on the sphere, such as Driscoll-Heal grid, Triangle vertex, Triangle centre and Reuter grid and discussed the characteristics of each in detail. In another study, Gonzalez (2010) introduced a homogeneous point distribution on the surface of the sphere, known as the Fibonacci grid. The goal was to reduce the errors related to the measurement of the Earth coverage of satellite constellations.
Compared to free-positioned base functions, a disadvantage of fixed-position base functions is, that the base functions are more correlated. This causes more ill-posedness in the equation system and the associated design matrix. Nevertheless, the induced ill-posedness is not a serious concern since it can be treated by means of proper regularization.
Our computations show that the choice of grid points does not considerably change the quality of regional gravity field modelling, provided that the grid points are homogeneously distributed. For example, the standard geographical grid with equal angles, does not provide satisfactory homogeneous point distribution on the surface of the sphere. This is due to the convergence of meridians especially in high-latitude regions.
In this thesis we use the fixed-position approach to predefine the location of base functions so that the parameter estimation using least-squares adjustment remains linear. We will compare the performance of two homogeneous grid points: the Reuter grid and the Fibonacci grid. A brief mathematical description of these two grid points is given in the following for the sake of completeness.

The Reuter grid

The concept of the Reuter grid is to distribute the grid points on the surface of the sphere in a way, that the distance between adjacent points is equal. The distance between points as well as the total number of grid points is defined by the control parameter c. This parameter determines the number of points along the meridians. The number of points on each circle of latitude will be computed according to its latitude and the distance to the adjacent circles. Based on the parameter c, the position of the points on the Reuter grid can be obtained as follows:

$$\begin{cases} \phi_j = j\pi/c, \;\; j = 1, 2, ..., c-1 \\ \lambda_{ij} = 0.5\Delta\lambda_j + 2\pi i/c_j, \;\; i = 0, 1, ..., c_j \end{cases} \tag{4.13}$$

where c is the control parameter and c_j and $\Delta\lambda_j$ are computed using:

$$\begin{cases} c_j = \left[\dfrac{2\pi}{\Delta\lambda_j} \right] \\ \Delta\lambda_j = \arccos \dfrac{\cos(\pi/c) - \cos^2\phi_j}{\sin^2\phi_j}. \end{cases} \tag{4.14}$$

It should be mentioned that the two poles are not computed using (4.13) and must be added manually. See also Reuter (1982), Eicker (2008) for a more detailed description on the Reuter grid. The number of grid points, which is controlled by c is directly related to the band width of the base functions of N_{max}. The larger N_{max} is the more base functions are needed for a proper coverage. Figure 4.7 shows the distance between the adjacent base functions on two different Reuter grids corresponding to $c = 30$ and $c = 120$. As it can be seen the base functions get closer as the bandwidth decreases. The global distribution of the Reuter grid points for these two cases is shown in figure 4.8.

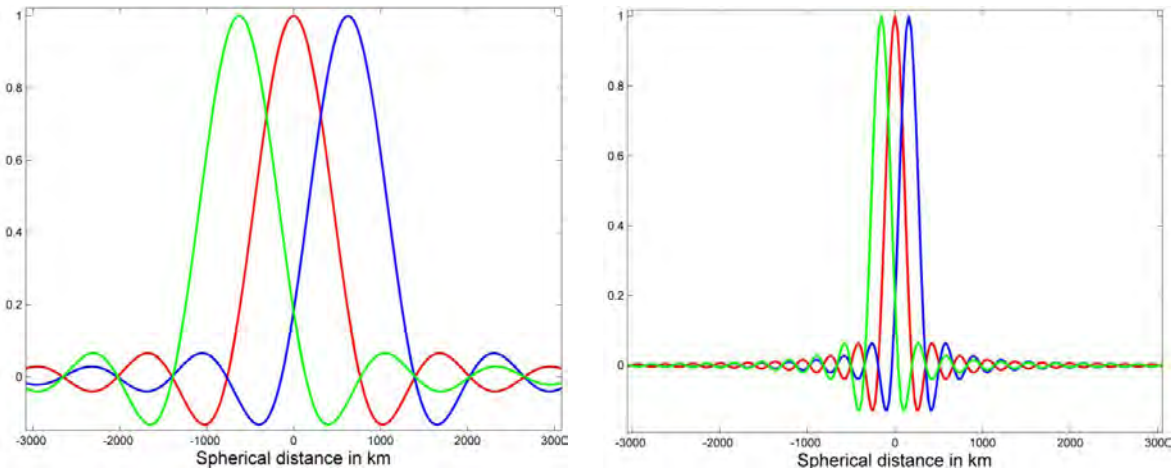

Figure 4.7: **Left**: the distance between adjacent base functions on the Reuter grid corresponding to base functions with $N_{max} = 30$. **Right**: the distance between adjacent base functions on the Reuter grid for base functions with $N_{max} = 120$. As the maximum degree increases, the base functions will be more localized and should get closer.

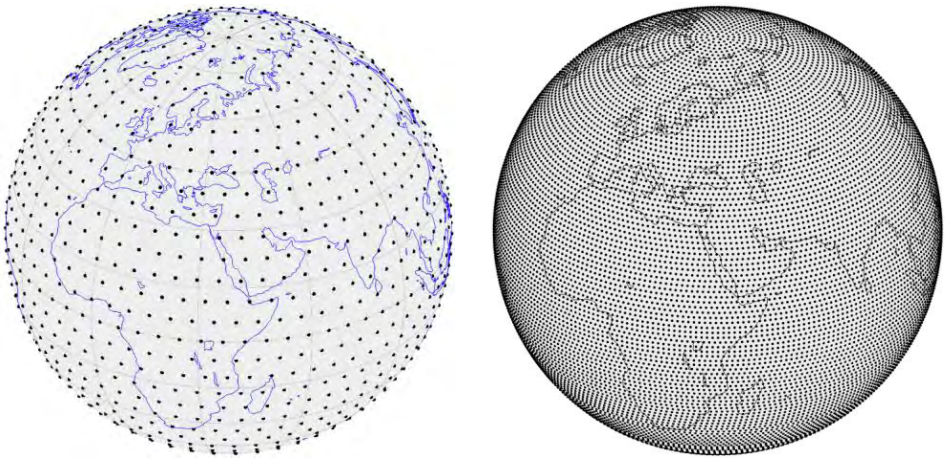

Figure 4.8: The distribution of points on the Reuter grid for $N_{max} = 30$ (left) with a total number of 1290 points and $N_{max} = 120$ (right) with 20798 points.

The Fibonacci grid

The points on the Fibonacci grid approximately provide equal areas on the surface of the sphere. According to Gonzalez (2010), the spherical coordinates of the Fibonacci grid, in radians, are

$$\begin{cases} \phi_i = \arcsin \dfrac{2i}{2N+1} \\ \lambda_i = \dfrac{2\pi i}{(1+\sqrt{5})/2} \end{cases} \tag{4.15}$$

where $i = -N, ..., 0, ..., N$ and N is an integer such that the total number of Fibonacci points is $2N+1$. Every point of this grid is located at a different latitude with the middle point $i = 0$ placed at equator. The interesting fact about the Fibonacci grid is the use of the golden ratio, $\left(\dfrac{1+\sqrt{5}}{2}\right)$, in equation (4.15).

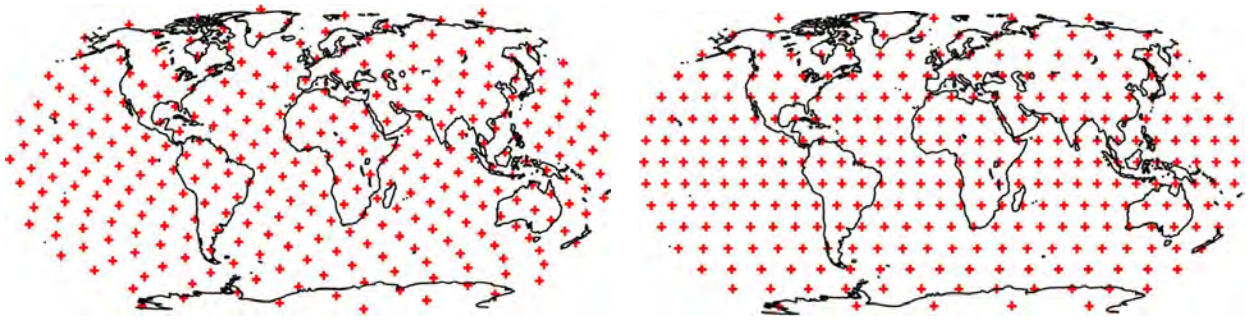

(a) (b)

Figure 4.9: Global and homogeneous point distribution on the surface of the sphere, (a): The Fibonacci grid with equal areas and (b): The Reuter grid with equi-distant intervals. The total number of points in both grids are tuned to be 317. As it can be seen, the points on the Reuter grid are placed on 15 different circles of latitude while the Fibonacci grid has a pseudo-random distribution.

Figure 4.9 shows globally distributed grid points on the Reuter grid with $c = 16$ and a total number of 317 points. In addition, a Fibonacci grid with $N = 158$ is also shown. The total number of Fibonacci points is again 317 which is comparable to the Reuter grid.

4.2.5 Extension of the data zone

As we explained in section 4.1, in regional gravity field modelling, the observations are restricted to a certain region which causes severe border distortions in regional gravity modelling. The reason is obvious due to the fact that the Earth's gravitational potential is a function of mass distribution all over the globe. This means that the potential field in the model zone $\tilde{\Omega}_R$ affects the observations outside this area. As explained in 4.2.3, the removal of the long wavelengths from the observation vector $\mathbf{l}_1$ can overcome this problem considerably. Thus the regional potential field can be determined based on the observations within this region. Nevertheless, those observation which are close to the model zone can still have significant contribution to the estimation of scaling coefficients $\mathbf{x}_1$. Therefore the data zone $\tilde{\Omega}_R^{data}$ is introduced to reduce the edge effects. The data zone cover a broader area beyond the model zone in a way that the adjacent observations to the model zone are also included in the parameter estimation, see figure 4.2.
The extension of the data zone is usually chosen arbitrarily using trial and error and has not been investigated in previous studies. The trial and error is done in a sense that a satisfactory fit in model zone is achieved. Though the extension of the data zone is not a very critical issue in regional gravity field modelling, we consider it here and give a rule of thumb for the size of the data zone.
According to equation (4.12), the observations are reduced based on a reference field. The resulting observation vector $\delta\mathbf{l}_1$ consists of frequencies between $N_{min}+1$ up to the expected maximum degree. The extension of the data zone can be determined based on the longest wavelengths in the observations i.e. $N_{min}+1$. The lowest spatial resolution contained in $\delta\mathbf{l}_1$, can be determined by

$$R_{min} = \frac{20000}{N_{min}} \text{ km} \tag{4.16}$$

or in radians using

$$R_{min} = \frac{2 \times 10^7}{N_{min} \times R \cos\phi_m} \text{ rad} \tag{4.17}$$

where ϕ_m is the average latitude of the region. This gives the minimum spatial resolution at the Earth's surface. For satellite observations at altitude h it can be written as

$$R_{min} = \frac{2 \times 10^7}{N_{min} \times (R+h)\cos\phi_m} \text{ rad.} \tag{4.18}$$

The extension of the data zone beyond the model zone, can be considered as the half of the minimum spatial resolution i.e. $0.5R_{min}$. Therefore the bounds of the data zone is obtained using the model zone extended in all directions by $0.5R_{min}$. For example, for a regional solution using GOCE data with $h = 250$ km over a region with average latitude of 50°, the extension to model zone will be about 4.5°if the long wavelengths are removed up to $N_{min} = 30$.
As it can be understood from equation (4.18), the size of the data zone is dependent on the frequency content of the reduced observations as well as satellite altitude and, of course, on the size of the model zone. Therefore, the data zone is defined based on the features of the observations. It should also be mentioned that equation (4.18) suggests the minimum required extension for the data zone. More extension results in involving more observations in the equation system and consequently better solutions with reduced border effects. The cost will be to deal with a larger equation system and computation time.

4.2.6 Extension of the grid zone

Another area which should be defined is the grid zone. As explained in 4.1, this area is larger than the model and data zones. The grid zone is considered as the extension of the data zone. Similar to the discussion about the data zone, this area has also been selected arbitrarily in previous research studies. Here, we relate the size of the grid zone to the properties of the SRBF. The maximum resolution of the SRBF is dependent on the maximum degree of expansion in equation (4.5). Using (4.17) the maximum resolution of SRBF is

$$R_{max} = \frac{2 \times 10^7}{N_{max} \times R\cos\phi_m} \text{ rad.} \tag{4.19}$$

The base functions outside the data zone which are close to this area have significant contribution in the modelling. Therefore, the grid zone is defined as the extension of the data zone. In our methodology, we define this extension to be equal to the maximum resolution of the base functions used in the analysis. This is illustrated in figure 4.10.

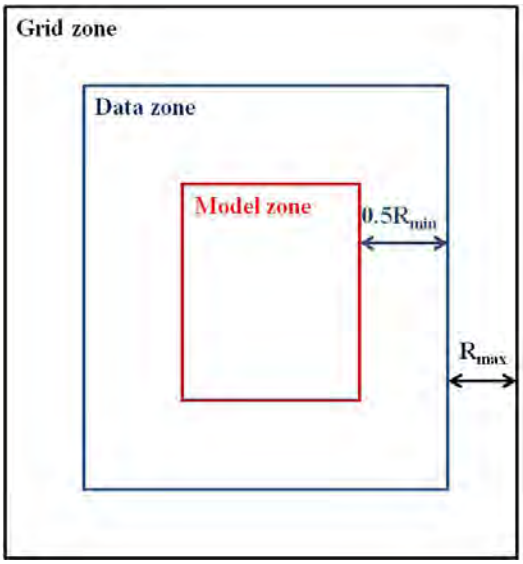

Figure 4.10: The extension of the grid and data zones with respect to the size of the model zone to reduce border distortions. The base functions are distributed within the grid zone where the unknown coefficients are determined. The observations are provided in data zone.

Again it should be noted that equation (4.19) gives the minimum value needed for the extension of the grid zone. Larger extension seems to be unnecessary since the number of unknowns and the size of computations will be increased as the result. Our computations show that a grid extension between 3 and 5 degrees should be satisfactory for gravity field modelling based on satellite data.

4.2.7 Inversion process

When all choices are made, one can set up the observation equation defined by (4.3). According to the presence of errors, the resulting observation equations are strongly inconsistent. The errors in the model can be categorized to three different groups:

- Commission error: The observation noise propagates to the estimated unknown coefficients through the linear model which is called the commission error. This kind of error is present in all types of modelling based on observed values.
- Omission error: This error is due to the restriction of the modelling to the maximum degree of expansion. In principle the gravity field of the Earth is a non band-limited function which contains infinite frequencies. The omission of higher frequencies beyond N_{max} causes the omission error in the final solutions. This type of error exists also in global gravity field modelling since the expansion of spherical harmonics is also restricted to a certain maximum degree.
- Cut-off errors: This error source is the result of regional confinement. According to the discussions in section 4.1 in the context of equations (4.1) and (4.3), the regional gravity models suffer from cutting issues which have to be taken into account.

The last group of errors is a special case for regional gravity field determination which does not exist in global gravity field modelling. Therefore the resulting equation systems in regional gravity field modelling is much more ill-posed compared to global gravity field modelling. This means the estimation of scaling coefficients α_k is not easily possible using the standard least-squares adjustment and should be done by means of special treatments. Additional information should be included to obtain meaningful results. Such special treatments, known as **regularization**, are the most important part of regional gravity field modelling which should be taken into account carefully.
From the view point of signal processing, the regularization process can be compared to the act of averaging and low-pass filtering. Therefore it is possible to consider the regularization procedure, equivalent to applying a low-pass filter to the solution where the goal is to hamper the propagated errors to the solution. The regularization process, which is the central issue of this PhD thesis, will be studied in the following chapter with more detail.

5 Regularization of regional gravity field solutions

5.1 Gravity field modelling: an inverse problem

The gravity field recovery from observed gravity data belongs to the class of **inverse problems**. Inverse problems exist in many fields of applied sciences with the following common concern:

The characteristics of an underlying process (phenomenon) are to be determined from a set of noisy observations.

An inverse problem consists of three components; **input**, **underlying process** and **output**. These components are named in the view of forward modelling. Outputs of a process are always observable and can be measured accordingly. From the underlying process and input, one is usually given and the other is unknown. Figure 5.1 illustrates the forward problem and its associated inverse problem in a general form. In the context of the gravity field modelling, these three components can be defined as follows:

- Process: The gravity field of the Earth, as a continuous function, is the process of the problem. Since this process is not known, we attempt to approximate it using a set of known functions (base functions). Therefore, the approximating model includes a set of known base functions (e.g. spherical harmonics or SRBF) which together with their corresponding coefficients (inputs) construct the output.
- Input: the **coefficients** of a set of known base functions.
- Output: The gravitational potential and/or its functionals, at certain position and time. The output as the realization of the process can always be observed using measurement techniques (e.g. gravimetry, gradiometry, SST, SGG, etc).

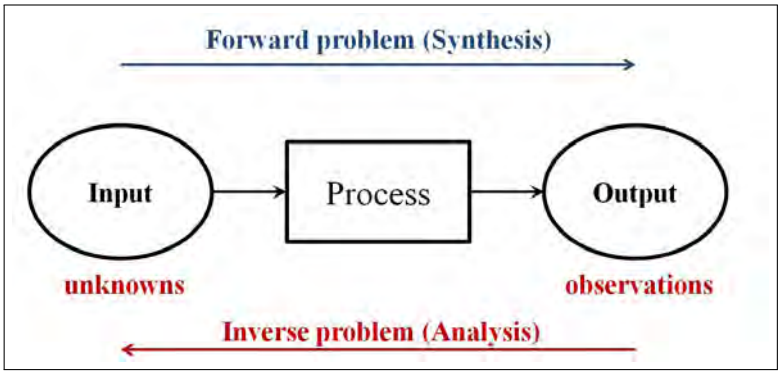

Figure 5.1: The forward and inverse problem and corresponding components. In the context of the gravity field modelling, the process is the gravity field of the Earth, the output are the observations and the input are the unknown coefficients to be estimated.

Many inverse problems take the form of **Fredholm integral equation of the first kind**. Such problems arise in many field of applied sciences such as medical imaging, astronomy, geophysics and in particular geodesy. The general form of this integral equation reads (Hansen, 2010):

$$\int_{\Omega} K(s,t)x(t)dt = l(s) \tag{5.1}$$

in which $K(s,t)$ describes the process and $x(t)$ is the input function at time or position t. The function $l(s)$ at time or position s is the output or the observations of the process. (5.1) describes the inverse problem in the continuous real world. In the discrete numerical computations, this integral equation can be written in terms of matrix notation:

$$\mathbf{A}\mathbf{x} = \mathbf{l} \tag{5.2}$$

which resembles the equation systems for global or regional gravity field modelling given in chapters 3 and 4. The matrix $\mathbf{A} : \mathbb{X} \rightarrow \mathbb{L}$ is a linear operator or a mapping from the unknown space $\mathbb{X}$ to the observation space $\mathbb{L}$. $\mathbf{A}$ describes the process in discrete form. Respectively, the unknown vector $\mathbf{x} \in \mathbb{X}$ and observation vector $\mathbf{l} \in \mathbb{L}$ are the input and output of the process. This is shown in figure 5.2.

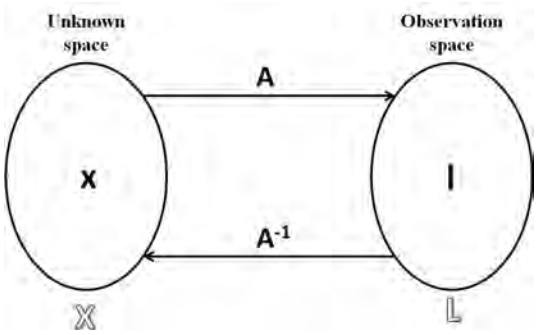

Figure 5.2: The operator $\mathbf{A}$ is a mapping from function space $\mathbb{X}$ of unknowns to the observation space $\mathbb{L}$

The mapping $\mathbf{A}$ is said to be **well-posed** if it has the following properties (Hadamard, 1923):

- $\mathbf{A}$ is **surjective**: the solution $\mathbf{x}$ exists for every right hand side $\mathbf{l}$ (**existence**).
- $\mathbf{A}$ is **injective**: for every right hand side $\mathbf{l}$, there is only one solution $\mathbf{x}$ (**uniqueness**).
- $\mathbf{A}^{-1}$ exists and is continuous (**stability**).

$\mathbf{A}^{-1}$ is the inverse mapping from space $\mathbb{L}$ onto $\mathbb{X}$ such that[1]

$$\mathbf{x} = \mathbf{A}^{-1}\mathbf{l}. \tag{5.3}$$

If one of theses conditions does not hold, the operator $\mathbf{A}$ is said to be **ill-posed** and the solution (5.3) cannot be reliable. In the context of the Earth's gravity field, $\mathbf{A}$ is never surjective in a strict mathematical sense. This implies that there is no exact $\mathbf{x}$ which satisfies equation (5.2). The reason is due to the redundant noisy observations which makes the equation system (5.2) inconsistent. Nevertheless, the existence issue can be resolved by introducing additional requirement for the solution. The least-squares method explained in chapter 3, is a condition that guaranties the existence of a solution for (5.2). According to the least-squares assumption, the approximate solution $\hat{\mathbf{x}}$ (instead of the exact solution $\mathbf{x}$) exists such that $\|\mathbf{A}\hat{\mathbf{x}} - \mathbf{l}\|$ is minimized. Thus, the issue of existence is not a great concern in gravity field modelling since we look for a **good approximation** rather an **exact solution**.

[1]Note that $\mathbf{A}$ is not a matrix here. It denotes a continuous linear operator. Consequently $\mathbf{A}^{-1}$ is not a matrix inverse, rather the inverse projection or inverse mapping in the continuous sense.

Presence of different errors (i.e. observation noise and systematic effects) in the modelling is a limiting factor for the uniqueness of the approximate solution. As a result of the least-squares assumption (or any other requirements to obtain an approximate solution), injectivity of $\mathbf{A}$ and therefore the uniqueness of the solution are vague notions and shall be predefined. The reason is that, there might be several good approximate solutions for a given set of observations depending on how the errors are minimized. Under certain conditions, one can speak of the **best approximation** instead of the unique solution. The best approximation is defined depending on the purpose of modelling and its applications. For example the approximate solution obtained from least-squares method can be considered as the best approximation if minimum variance for the solution is desired. This can be achieved if the weight matrix in the least-squares solution is chosen to be inversely proportional to the covariance matrix of the observations.
For global gravity field modelling, the injectivity of $\mathbf{A}$ is a convenient assumption according to the properties of least-squares solution. In section 3.3.2, the solutions $\hat{\mathbf{x}}_{sh}$ and $\hat{\mathbf{x}}_{srbf}$ (which were shown to be equivalent) are considered as the best approximation. On the contrary, in regional gravity field modelling, $\mathbf{A}$ is not injective even under assumption of the least-squares and several solutions might fulfil the minimum norm condition. We will come back to this issue later in section 5.4, in the explanation of figure 5.5. This is mainly due to the restriction of (globally defined) base functions and observations to a certain region. Hence, additional requirements for the desired solution $\hat{\mathbf{x}}$ are necessary to obtain a measure for the best approximation.
Finally, the inverse problems are instable. Instability implies that the solution $\mathbf{x}$ does not continuously depend on the observation $\mathbf{l}$. The reason is, that the kernel $K(s,t)$ of Fredholm integral equation of the first kind has smoothing effects on the input $f(t)$ so that the output $g(s)$ (observations) are smoother than the input (source). This holds also for the discrete version of this integral equation; the operator $\mathbf{A}$ has smoothing effects on $\mathbf{x}$ so that $\mathbf{l}$ is smoother than $\mathbf{x}$. Smoothing effect in forward modelling causes instability in inverse problem. This phenomenon can be mathematically described by **Riemann-Lebesgue lemma** (Hansen, 2010):
If $f(t)$ is a function defined as:

$$f(t) = sin(2\pi\omega t), \;\; \omega \in [1, \infty) \tag{5.4}$$

it can be shown that

$$g(s) = \int_{\Omega} K(s,t) f(t) dt \to 0 \;\text{ as }\; \omega \to \infty \tag{5.5}$$

for any arbitrary kernel K. This explicitly means that as the frequency of the input (source) increases, the amplitude of the output (observation) will be damped out. Therefore in the inverse problem higher frequencies cannot be determined as precise as lower frequencies, particularly in presence of observation noise. In this case, the inverse operator $\mathbf{A}^{-1}$ (if exists) is not stable so that $\mathbf{x}$ is not continuously dependent on $\mathbf{l}$. This damping effect is even more intensified in gravity field modelling based on satellite data which is known as the **upward continuation**.
To resolve the instability of $\mathbf{A}$, additional information about the unknowns is required to constrain the solution $\hat{\mathbf{x}}$. This procedure is called **regularization** so that the instable operator $\mathbf{A}$ becomes regular.

5.2 Diagnosis of ill-posedness in inverse problems

In previous section we explained that the operator $\mathbf{A}$ is ill-posed and a reliable solution can be obtained only by means of regularization. But before '*curing*' this ill-posedness, the reason and the extent of ill-posedness shall be '*diagnosed*' in a proper way. We often know that the resulting operator $\mathbf{A}$ (design matrix) could be ill-posed due to the characteristics of the modelling but usually the extent to which the design matrix is ill-posed is not known. In practice, there are some tools to check whether an operator is ill-posed and if it is, to which extent. These tools will be explained in the following.

5.2.1 Condition number

An important property of the operator $\mathbf{A}$, which shows the degree of ill-posedness, is the **condition number**. The condition number of $\mathbf{A}$ is defined as (e.g. Cheney and Kincaid (2008), Higham (1987)):

$$cond(\mathbf{A}) = \|\mathbf{A}\|\|\mathbf{A}^{-1}\| \tag{5.6}$$

where $\|\mathbf{A}\|$ and $\|\mathbf{A}^{-1}\|$ denote the norm of $\mathbf{A}$ and its inverse respectively[1]. Condition number is a good measure for the sensitivity of the operator $\mathbf{A}$ to the errors in the observations. If observation error and the solution error are denoted by $\mathbf{e}$ and $\delta\mathbf{x}$ respectively, one can write:

$$\mathbf{A}(\mathbf{x} + \delta\mathbf{x}) = \mathbf{l} + \mathbf{e} \tag{5.8}$$

or in other from:

$$\begin{cases} \mathbf{l} = \mathbf{A}\mathbf{x} \\ \delta\mathbf{x} = \mathbf{A}^{-1}\mathbf{e} \end{cases} \tag{5.9}$$

Taking the norm of both equations and due to the properties of the operator's norm (e.g. Kreyszig (1978) page 92)

$$\begin{cases} \|\mathbf{l}\| = \|\mathbf{A}\mathbf{x}\| \leq \|\mathbf{A}\|\|\mathbf{x}\| \\ \|\delta\mathbf{x}\| = \|\mathbf{A}^{-1}\mathbf{e}\| \leq \|\mathbf{A}^{-1}\|\|\mathbf{e}\| \end{cases} \tag{5.10}$$

Combining these two inequalities yields:

$$\frac{\|\delta\mathbf{x}\|}{\|\mathbf{x}\|} \leq \underbrace{\|\mathbf{A}\|\|\mathbf{A}^{-1}\|}_{cond(\mathbf{A})} \frac{\|\mathbf{e}\|}{\|\mathbf{l}\|} \tag{5.11}$$

Equation (5.11) states that the relative errors $\delta\mathbf{x}$ can be amplified up to level of observation's errors multiplied by $cond(\mathbf{A})$. If $cond(\mathbf{A})$ is close to one or small enough, then the observation errors, $\mathbf{e}$, will not be amplified significantly so the operator and thus the system of equations are said to be well-posed or well-conditioned. A large condition number results in much more error propagation and reveals more ill-posedness in the operator $\mathbf{A}$. Hence more treatment (regularization) is needed to obtain a reasonable solution.

5.2.2 Singular value decomposition

A powerful tool to find out difficulties associated with ill-posed operators, is the Singular Value Decomposition or, hereafter, **SVD**. It is a well-known numerical tool to reveal some characteristics of ill-posed matrices (Gloub and van Loan, 1996, Hansen, 1997, 2010). SVD belongs to the family of matrix factorization and is connected to the spectral theory of linear operators. The SVD of a linear operator $\mathbf{A} \in \mathbb{R}^{I\times K}$ reads:[2]

$$\mathbf{A} = \mathbf{U}\mathbf{S}\mathbf{V}^T = \sum_{k=1}^{K} \mathbf{u}_k s_k \mathbf{v}_k^T \tag{5.12}$$

[1] The L^2-norm of a matrix, in a simple form, is defined as follows:

$$\|A\| = \max\{\|\mathbf{A}\mathbf{x}\| \text{ such that } \|\mathbf{x}\| = 1\} \tag{5.7}$$

Kreyszig (1978) gives a detailed description of the norm of linear operators in general.

[2] $\mathbb{R}^{I\times K}$ is the space of all linear operators whose dimension is $I \times K$.

where $\mathbf{U} \in \mathbb{R}^{I \times I}$ and $\mathbf{V} \in \mathbb{R}^{K \times K}$ are orthonormal matrices with orthonormal column vectors $\mathbf{u}_k$ and $\mathbf{v}_k$ such that:

$$\begin{cases} \|\mathbf{u}_k\| = \|\mathbf{v}_k\| = 1 \\ \mathbf{U}^T = \mathbf{U}^{-1} \\ \mathbf{V}^T = \mathbf{V}^{-1} \\ \mathbf{U}^T\mathbf{U} = \mathbf{U}\mathbf{U}^T = \mathbf{V}^T\mathbf{V} = \mathbf{V}\mathbf{V}^T = \mathbf{I} \end{cases} \tag{5.13}$$

The diagonal matrix $\mathbf{S} \in \mathbb{R}^{I \times K}$ contains non-negative values s_k which are the **singular values** of $\mathbf{A}$ and appear in decreasing order such that:

$$s_1 \geq s_2 \geq s_3 \cdots \geq s_K \geq 0 \tag{5.14}$$

If one or more singular values are equal to zero, the matrix $\mathbf{A}$ is not of full column rank and is said to be **rank deficient**. Using equation (5.12), one can write:

$$\mathbf{A}\mathbf{v}_k = s_k\mathbf{u}_k \tag{5.15}$$

According to the definition of the matrix norm and using (5.15) it can be shown that:

$$\|\mathbf{A}\| = s_1 \tag{5.16}$$

where s_1 is the first and, by definition (5.14), the largest singular value of $\mathbf{A}$. Furthermore, it is straightforward to show that:

$$\mathbf{A}^{-1} = \mathbf{V}\mathbf{S}^{-1}\mathbf{U}^T \tag{5.17}$$

and consequently:

$$\|\mathbf{A}^{-1}\| = s_K^{-1} \tag{5.18}$$

with s_K being the last and smallest singular value of $\mathbf{A}$. Using (5.6), (5.16) and (5.18) the condition number of $\mathbf{A}$ can be obtained as the ratio of the largest singular value to the smallest:

$$cond(\mathbf{A}) = \frac{s_1}{s_K} = \frac{\|\mathbf{A}\|}{\|\mathbf{A}^{-1}\|} \tag{5.19}$$

Since the approximate solution $\hat{\mathbf{x}}$ is to be obtained using least-squares method, it is convenient to write the equation (5.8) in the level of normal equations:

$$\mathbf{N}\mathbf{x} = \mathbf{y} \tag{5.20}$$

in which $\mathbf{N} = \mathbf{A}^T\mathbf{P}\mathbf{A}$ and $\mathbf{y} = \mathbf{A}^T\mathbf{P}\mathbf{l}$ are defined in the context of equation (3.37). In terms of operator equations, $\mathbf{N} : \mathbb{X} \rightarrow \mathbb{Y}$ can be considered as a linear operator which maps the vector $\mathbf{x}$ from unknown space $\mathbb{X}$ onto its dual space $\mathbb{Y}$ (Mohammad-Karim, 1981). Hence, it makes more sense to consider the condition of $\mathbf{N}$ rather than $\mathbf{A}$. Since $\mathbf{N}$ is a symmetric matrix, its SVD is equivalent to eigenvalue decomposition (Strang and Borre, 1997):

$$\mathbf{N} = \underbrace{\tilde{\mathbf{V}}\tilde{\mathbf{S}}\tilde{\mathbf{V}}^T}_{\text{SVD}} = \overbrace{\mathbf{Q}\mathbf{\Lambda}\mathbf{Q}^T}^{\text{eigenvalue decomposition}} \tag{5.21}$$

therein $\tilde{\mathbf{V}}$ is an orthonormal matrix and $\tilde{\mathbf{S}}$ is a diagonal matrix with singular values $\tilde{s}^2$ on its diagonal. $\mathbf{Q}$ contains the eigenvectors of $\mathbf{N}$ and $\mathbf{\Lambda}$ is a diagonal matrix with eigenvalues λ on its diagonal.
A special case (as often occurs in practice) is when $\mathbf{P} = \sigma^2\mathbf{I}$ and thus $\mathbf{N} = \sigma^2\mathbf{A}^T\mathbf{A}$. Then using (5.12) and (5.13) one can write:

$$\mathbf{N} = \sigma^2\mathbf{A}^T\mathbf{A} = \sigma^2\mathbf{V}\mathbf{S}\underbrace{\mathbf{U}^T\mathbf{U}}_{\mathbf{I}}\mathbf{S}\mathbf{V}^T = \sigma^2\mathbf{V}\mathbf{S}^2\mathbf{V}^T \tag{5.22}$$

which gives the singular value decomposition of the normal matrix $\mathbf{N}$ in terms of SVD components of $\mathbf{A}$. It also follows that in this case ($\mathbf{P} = \sigma^2\mathbf{I}$) the singular values of $\mathbf{A}$ are the squared root of the eigenvalues of the corresponding normal matrix. In the following we assume that $\mathbf{P} = \sigma^2\mathbf{I}$ and therefore use (5.22) as SVD of $\mathbf{N}$ unless otherwise stated.
With the same line of reasoning for the condition number of $\mathbf{A}$ (equation 5.19), the condition number of $\mathbf{N}$ can be estimated by means of its singular values or equivalently by its eigenvalues:

$$cond(\mathbf{N}) = \frac{\|\mathbf{N}\|}{\|\mathbf{N}^{-1}\|} = \frac{s_1^2}{s_K^2} = \frac{\lambda_{max}}{\lambda_{min}} \tag{5.23}$$

According to (5.22) and using (3.36), it is straightforward to show that the least-squares solution $\hat{\mathbf{x}}$, in terms of SVD components reads:

$$\hat{\mathbf{x}} = \mathbf{V}\mathbf{S}^{-2}\mathbf{V}^T\mathbf{y} \tag{5.24}$$

which replaces the inversion of $\mathbf{N}$ by inversion of a diagonal matrix $\mathbf{S}^2$ i.e. inverting the singular values s^2.
The singular value decomposition is analogous to the Fourier transform in a sense that it reveals the spectral properties of the linear operators (or matrices) (Hansen, 2010); Large singular values correspond to long wavelengths (low frequencies) and small singular values represent the high frequency characteristic of the operator. The SVD enables us to determine the significance of different frequencies for the mapping.
From viewpoint of functional analysis, the column vectors of $\mathbf{A}$ and similarly $\mathbf{N}$, constitute a base (say a K-dimensional coordinate system for simplicity) for the function space $\mathbb{X}$. The unknown vector $\mathbf{x}$ is to be measured in this coordinate system. This base is chosen by the user according to the nature of the problem and desired application.

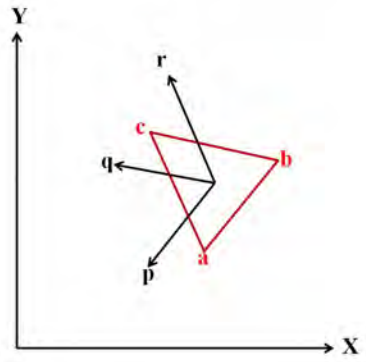

Figure 5.3: Two coordinate systems for studying the object abc. The coordinate system pqr is defined locally according to properties of abc.

As in gravity field modelling, we chose SRBF due to its benefits explained in chapters 3 and 4. Nevertheless, as the choice of base functions is mostly **physically reasonable**, it might not be always **computationally efficient**. An abstract and simple example is illustrated in figure 5.3. If the object abc is to be investigated on a $2D$ plane, it is common to use the Cartesian coordinate system XY which enjoys the features of orthogonality. Yet, for studying some properties of this object (e.g. the slope of its sides), it is perhaps preferred to define a local coordinate system such as pqr which fits better to the geometry of abc since its axes are defined parallel to abc's sides. The slopes of ab, bc and ac are now zero with respect to the localized axes p, q and r respectively. While this can be regarded as an advantage of this localized coordinate system, the drawback is the loss of orthogonality of axes (bases) and consequently the Euclidean geometry is not valid any more. In addition, three axes are linearly dependent on a $2D$ plane which cause dependency and rank-deficiency in the operator which describes the base pqr. This example mimics how spherical harmonics as XY and SRBF as pqr look like in gravity field analysis.
SVD can be considered as a coordinate transformation in the function space $\mathbb{X}$ from system defined by column vectors of $\mathbf{A}$ or $\mathbf{N}$ to an orthonormal base defined by column vectors of $\mathbf{V}$. In other words, SVD is a transition to an interim orthogonal coordinate system for efficient computations.
The magnitude of singular values exhibits the significance of $\mathbf{v_k}$ as the axes of this orthonormal base. This is how SVD together with condition number can be worthwhile to detect the ill-posedness of operators and give insight into the proper treatment. In section 5.4.3 this issue will be considered with more details.

5.2.3 Discrete Picard condition

Another tool to detect the ill-posedness of the equations is the discrete picard condition which is closely connected to SVD. This condition also describes the effect of observation errors on the solution. Equation (5.24) which describes the least-squares solution based on SVD components, can also be written as the linear combination of orthonormal vectors $\mathbf{v}_k$:

$$\hat{\mathbf{x}} = \sum_{k=1}^{K} \frac{\mathbf{v}_k^T \mathbf{y}}{s_k^2} \mathbf{v}_k \tag{5.25}$$

As it is clear from this equation, the solution $\hat{\mathbf{x}}$ converges if the ratio $\mathbf{v}_k^T\mathbf{y}/s_k^2$ is convergent. This requires that the coefficients $\mathbf{v}_k^T\mathbf{y}$ in the nominator are smaller than the singular values s_k^2 on average. If this condition is violated, the ratio $\mathbf{v}_k^T\mathbf{y}/s_k^2$ diverges so does the solution $\hat{\mathbf{x}}$. Hansen (1990a) described this condition as the **discrete Picard condition** which states that the coefficients $\mathbf{v}_k^T\mathbf{y}$ decay on the average to zero faster than the singular values s_k^2. See also Hansen (1997, 2010) for more details on the discrete Picard condition.

5.3 Ill-posedness of gravity field determination

To see how SVD and condition number can reveal the ill-posedness of normal equations in gravity field analysis, we consider the normal matrices used in section 3.3.2, for global gravity field solutions.
Figure 5.4 shows the singular values of the normal matrices computed from $\mathbf{N}_{sh}$ and $\mathbf{N}_{srbf}$. The solutions obtained from these two normal equations were shown to be equivalent in section 3.3.2. Now a closer look at the corresponding singular values shows this clearly. There are 5038 and 6200 singular values for $\mathbf{N}_{sh}$ and $\mathbf{N}_{srbf}$ corresponding to the number of unknowns in each case. As it can be seen from figure 5.4, the singular values s_{srbf}^2 show the same behaviour to s_{sh}^2 up to the 5038^{th} singular value. A sudden jump after this point exhibits the dependency of column vector and thus the rank deficiency in $\mathbf{N}_{srbf}$ as discussed in section 3.3.2. Ignoring the singular values after sudden jump, the condition number of $\mathbf{N}_{sh}$ and $\mathbf{N}_{srbf}$ will be the same:

$$cond(\mathbf{N}_{sh}) = cond(\mathbf{N}_{srbf}) = 1.376 \times 10^5 \tag{5.26}$$

A condition number in the order of 10^5, is not a real problem for today's computers so that the the normal matrices with such condition numbers can be inverted without difficulties.

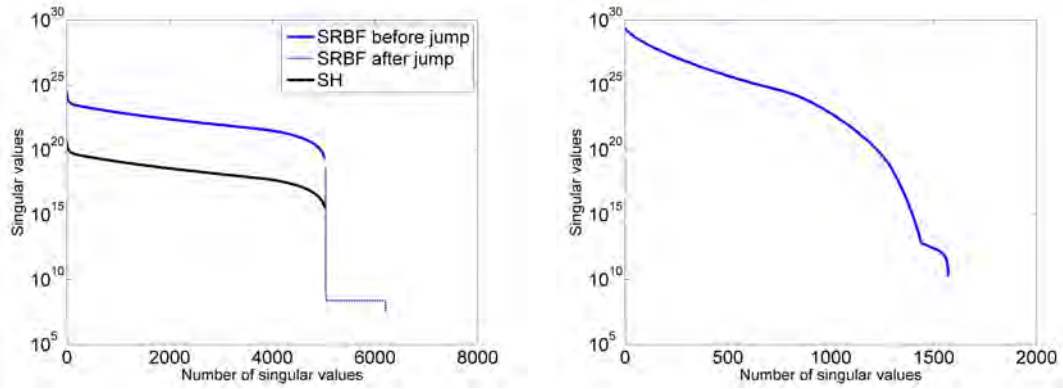

(a) (b)

Figure 5.4: (a) Singular values of the normal matrices $\mathbf{N}_{sh}$ (black) and $\mathbf{N}_{srbf}$ (blue) described in 3.3.2 for global gravity field modelling; the sudden jump between 5038^{th} and 5039^{th} singular values reveals the rank deficiency of $\mathbf{N}_{srbf}$ and is the truncation point for TSVD solution. The singular values before sudden jump span approximately 5 orders of magnitude and have the same behaviour as the singular values of $\mathbf{N}_{sh}$. (b) Singular values for the ill-posed problem resulting from regional gravity field determination described in section 6.2.2; these singular values with rapid decay, span about 18 orders of magnitude.

To judge whether the condition number of a matrix is normal or large (i.e. whether regularization is necessary or not), it is good to know a measure of this number. For gravity field analysis the expected condition number can be approximately estimated based on Kaula's rule of thumb explained before. This is used in many gravity field solutions as a pre-conditioning of the normal matrix to stabilize the solution. Figure 5.4 also shows the singular values of the normal matrix $\mathbf{N}_{11}$ obtained from a high-resolution regional solution ($n_j = 255$) using SEBF. The condition number is now in the order of 10^{18} which shows a strong ill-posedness of the normal matrix. The reasons of such ill-posedness are not only those coming from observations and downward continuation (as in global case) but also due to the incompleteness of the mathematical model, discussed in chapter 4. A reliable solution for such regional models can be obtained only by means of a proper regularization method. Hence, the regularization for regional gravity field solutions should resolve the following problems simultaneously:

- the non-stability of the inverse operator $\mathbf{N}_{11}^{-1}$ due to presence of errors and issues such as the downward continuation and
- the non-injectivity of $\mathbf{N}_{11}$ according to discussions in chapter 4.

See also the discussions concerning different sources of errors in section 4.2.7.

5.4 Regularization of ill-posed problems

Due to equation (5.25) which gives the least-squares solution in terms of SVD components, singular values equal to zero or very small singular values are the source of instabilities in the solution and shall be filtered out. Therefore, once the SVD components are computed, it is necessary to evaluate which singular values are significant and which ones cause instability (due to their small values). Small singular values will have a large contribution in the inversion process using equation (5.25). This means the column vectors of $\mathbf{v}_k$ which correspond to small singular values, can artificially contribute to the solution $\hat{\mathbf{x}}$ so that not only the magnitude of $\hat{x}_k$ changes, but even their signs. Therefore the trivial (small) singular values shall be either removed or filtered out so that their contribution smoothly decay. To do so, there must be a measure to determine the significance of singular values. This is key point and indeed the crux of regularization of ill-posed problems. Since there are no rigorous criteria for that, there are several regularization methods in practice. Xu (1998) gives an overview of several truncated SVD methods for discrete linear ill-posed problems and compared them

for a regional gravity field determination using Stokes' kernel. Regularization of ill-posed problems can also be performed without using SVD or any other decomposition tools. Such regularization approaches belong to the class of Tikhonov regularization (Tikhonov and Arsenin, 1977) and can be considered as direct regularization methods. Nevertheless, the Tikhonov-type regularizations can also be expressed in terms of SVD components and introducing filter factors (Hansen, 1997). In this PhD thesis, we categorize two types of regularization:

- Truncated SVD (TSVD)
- Tikhonov regularization (weighted SVD)

In the following we investigate these two classes of regularizations for ill-posed problems and put emphasis on the regional gravity field solutions using SRBF. We also propose a heuristic approach to regularize regional gravity field solutions using SRBF.

5.4.1 Truncated singular value decomposition

The least-squares solution $\hat{\mathbf{x}}$ using SVD is given by (5.25) which takes all singular values of $\mathbf{N}$ into account. Since very small singular values cause instability in the solution, it is common to filter the singular values to obtain a stable or regular solution. This filtering can be performed using filter factors f_k^2:

$$\hat{\mathbf{x}} = \sum_{k=1}^{K} f_k^2 \frac{\mathbf{v}_k^T \mathbf{y}}{s_k^2} \mathbf{v}_k. \tag{5.27}$$

The idea of truncated SVD is to discard some singular values to obtain a regularized solution. Hence, the filter factor for TSVD solution reads:

$$f_k^2 = \begin{cases} 1 \text{ for } k \leq k' \\ 0 \text{ for } k > k' \end{cases} \tag{5.28}$$

or equivalently using:

$$\hat{\mathbf{x}}_{tsvd} = \sum_{k=1}^{k'} \frac{\mathbf{v}_k^T \mathbf{y}}{s_k^2} \mathbf{v}_k. \tag{5.29}$$

This equation states that the truncated SVD solution is obtained from the first k' singular values and the rest are ignored. Due to the lack of enough theoretical foundation, k' is usually chosen arbitrarily. The first obvious way is to find k' such that the solution $\mathbf{A}\hat{\mathbf{x}}_{tsvd}$ fits well to the observations $\mathbf{l}$ (Scales, 1996). Some authors proposed to use statistical criteria to define a significance level for small singular values to be discarded. See for instance Lawless and Wang (1976) and Dempster *et al.* (1977). This method can also be considered as selective singular value decomposition or in brief SSVD. The solution for SSVD reads:

$$\hat{\mathbf{x}}_{ssvd} = \sum_{|\mathbf{v}_k^T \mathbf{y}| \geq \tau} \frac{\mathbf{v}_k^T \mathbf{y}}{s_k^2} \mathbf{v}_k \tag{5.30}$$

where τ determines the significance of Fourier coefficients $|\mathbf{v}_k^T \mathbf{y}|$. Thus the SSVD method is dependent on the choice of τ. See also Hansen (2010), Xu (1998) and Rust (1998) for more details on SSVD. As another variant for TSVD solution, Xu (1998) proposed a quality-based TSVD method by minimizing the mean squared error. The mean squared error of TSDV is defined as the sum of estimated error of $\hat{\mathbf{x}}_{tsvd}$ and the bias caused by truncation.

The TSVD method is an attractive method in the sense that it eases the computation of a regularized solution once the SVD components are computed. The only shortage of SVD technique could be its high computational

burden for large scale problems. However, due to the capability of current computers this issue is not a great concern as before. Moreover, there are some mathematical techniques for the decomposition of large matrices which reduces the computational costs. See for example Martinsson *et al.* (2006) and Martinsson *et al.* (2010) for the randomized decomposition of matrices. For regional gravity field solutions based on satellite data, this problem becomes even less important since the size of normal matrices on regional scales are significantly reduced. For instance, with $N_{max} = 300$, the size of the normal matrix will be about 6000×6000 for a region as big as Central Africa (c.f. table 6.8).
An alternative to the TSVD, i.e. truncating the singular values, is to weight them properly. In other words, the truncation can be replaced by smoothing the singular values. This can be done by either SVD techniques or direct regularization of ill-posed problems. Direct regularization methods can improve the condition of ill-posed normal matrices without the need for performing SVD analysis. Nevertheless, this class of regularizations can be still described by SVD analysis with the advantage of proper weighting of SVD instead of truncation.

5.4.2 Tikhonov regularization

The most well-known direct regularization of ill-posed problems is the Tikhonov regularization which is perhaps the most successful regularization method so far (Hansen, 2010). The key idea of regularization, in general, is to assume a priori condition about the size and smoothness of the solution. This assumption can be described by adding an additional model to the main equation system. To describe this, we consider the equation (5.2) once more and this time together with its stochastic components:

$$\mathbf{A}\mathbf{x} = \mathbf{l} + \mathbf{e} \quad \text{with} \quad \mathbf{C}_\mathbf{l} = \sigma_0^2 \mathbf{P}_\mathbf{l}^{-1} \tag{5.31}$$

therein $\mathbf{C}_\mathbf{l}$ is the covariance matrix of observations. $\mathbf{P}_\mathbf{l}$ and σ_0^2 are the weight matrix and its corresponding unknown variance factor. Even though the design matrix $\mathbf{A}$ is ill-posed, the least-squares assumption minimizes the norm of residuals $\|\mathbf{A}\hat{\mathbf{x}} - \mathbf{l}\|$. However, the solution $\hat{\mathbf{x}}$ will be unreliable according to instability of the inversion. Therefore a trusted solution needs additional information about the unknowns. Now we suppose that this information is given by a **refining model**:

$$\mathbf{L}\mathbf{x} = \boldsymbol{\mu} \quad \text{with} \quad \mathbf{C}_{\boldsymbol{\mu}} = \sigma_{\boldsymbol{\mu}}^2 \mathbf{P}_{\boldsymbol{\mu}}^{-1} \tag{5.32}$$

in which, $\mathbf{L}$ describes the refining model which is known as the **regularization matrix**. $\boldsymbol{\mu}$ is a functional of unknown parameters $\mathbf{x}$, which can also be regarded as the pseudo observation vector containing prior knowledge about the unknown parameters. $\sigma_{\boldsymbol{\mu}}^2$ and $\mathbf{P}_{\boldsymbol{\mu}}$ are variance factor and the weight matrix of the pseudo observations $\boldsymbol{\mu}$. Equation (5.32), together with observation equation (5.31) yields:

$$\begin{bmatrix} \mathbf{A} \\ \mathbf{L} \end{bmatrix} \mathbf{x} = \begin{bmatrix} \mathbf{l} \\ \boldsymbol{\mu} \end{bmatrix}. \tag{5.33}$$

The normal equation system for (5.33) reads:

$$(\sigma_0^{-2}\mathbf{A}^T\mathbf{P}_\mathbf{l}\mathbf{A} + \sigma_{\boldsymbol{\mu}}^{-2}\mathbf{L}^T\mathbf{P}_{\boldsymbol{\mu}}\mathbf{L})\mathbf{x} = \sigma_0^{-2}\mathbf{A}^T\mathbf{P}_\mathbf{l}\mathbf{l} + \sigma_{\boldsymbol{\mu}}^{-2}\mathbf{L}^T\mathbf{P}_{\boldsymbol{\mu}}\boldsymbol{\mu} \tag{5.34}$$

or in brief:

$$(\mathbf{N} + \mathbf{R})\mathbf{x} = \mathbf{y} + \mathbf{u} \tag{5.35}$$

where $\mathbf{R} = \sigma_{\boldsymbol{\mu}}^{-2}\mathbf{L}^T\mathbf{P}_{\boldsymbol{\mu}}\mathbf{L}$ and $\mathbf{u} = \sigma_{\boldsymbol{\mu}}^{-2}\mathbf{L}^T\mathbf{P}_{\boldsymbol{\mu}}\boldsymbol{\mu}$. Introducing the **regularization parameter**:

$$\gamma^2 = \frac{\sigma_0^2}{\sigma_{\boldsymbol{\mu}}^2}. \tag{5.36}$$

Equation (5.34) can be reformulated as:

$$(\mathbf{A}^T\mathbf{P}_\mathbf{l}\mathbf{A} + \gamma^2\mathbf{L}^T\mathbf{P}_{\boldsymbol{\mu}}\mathbf{L})\mathbf{x} = \mathbf{A}^T\mathbf{P}_\mathbf{l}\mathbf{l} + \gamma^2\mathbf{L}^T\mathbf{P}_{\boldsymbol{\mu}}\boldsymbol{\mu} \tag{5.37}$$

which is equivalent to the minimization process:

$$\min\{\|\mathbf{A}\mathbf{x} - \mathbf{l}\|^2_{\mathbf{P}_\mathbf{l}} + \gamma^2\|\mathbf{L}\mathbf{x} - \boldsymbol{\mu}\|^2_{\mathbf{P}_{\boldsymbol{\mu}}}\}. \tag{5.38}$$

Relations (5.33) and (5.38) give the general form of regularization process for ill-posed problems. According to this equation, the regularization components $\mathbf{L}$, γ^2 and $\boldsymbol{\mu}$ along with its weight matrix $\mathbf{P}_{\boldsymbol{\mu}}$ have to be predefined in a proper way. Therefore, depending on how these components are determined and applied to equation (5.37), there are several regularization methods. Among these methods, Tikhonov regularization (Tikhonov and Arsenin, 1977) is, perhaps, the most well-known method for ill-posed problems. The key idea of Tikhonov regularization is to find a solution with a priori assumption about the covariance matrix of unknown parameters which is given by $\mathbf{R}$. If $\boldsymbol{\mu} = \mathbf{0}$ and $\mathbf{P}_{\boldsymbol{\mu}} = \mathbf{I}$ in equation (5.37), the Tikhonov regularization will be:

$$(\mathbf{A}^T\mathbf{P}_\mathbf{l}\mathbf{A} + \gamma^2\mathbf{L}^T\mathbf{L})\mathbf{x} = \mathbf{A}^T\mathbf{P}_\mathbf{l}\mathbf{l} \tag{5.39}$$

in which $\mathbf{L}$ has to be defined depending on the particular application and γ^2 should be chosen carefully. $\mathbf{L}$ is a linear operator with certain smoothness constraints. The influence of $\mathbf{L}$ is addressed in details in Hansen (1997). Ilk (1993) showed that Tikhonov regularization for gravity field modelling based on satellite data is insensitive to the choice of $\mathbf{L}$ and it can be well approximated by a unit matrix. Setting $\mathbf{L} = \mathbf{I}$ means the prior information is available for the unknown vector $\mathbf{x}$ and not for its functional such as first or second derivatives. This also guarantees the existence of a solution $\hat{\mathbf{x}}$ which is close to its exact value $\hat{\mathbf{x}}_{\mathbf{ex}}$, so that $\|\hat{\mathbf{x}} - \hat{\mathbf{x}}_{\mathbf{ex}}\|$ is minimized (MacLeod, 1988). In this case the Tikhonov regularization is called standard Tikhonov regularization and is also known as ridge regression in statistics. In this PhD thesis we also set $\mathbf{L} = \mathbf{I}$ and confine ourselves to the proper choice of the regulariuation parameter γ^2. In this case, the (standard) Tikhonov regularization (5.39) reads:[1]

$$(\mathbf{A}^T\mathbf{P}_\mathbf{l}\mathbf{A} + \gamma^2\mathbf{I})\mathbf{x} = \mathbf{A}^T\mathbf{P}_\mathbf{l}\mathbf{l} \tag{5.40}$$

with the minimization procedure:

$$\min\{\|\mathbf{A}\mathbf{x} - \mathbf{l}\|^2_{\mathbf{P}_\mathbf{l}} + \gamma^2\|\mathbf{x}\|^2_{\mathbf{I}}\}. \tag{5.41}$$

The Tikhonov-regularized solution, $\hat{\mathbf{x}}_\gamma$, will be obtained using:

$$\hat{\mathbf{x}}_\gamma = (\mathbf{A}^T\mathbf{P}_\mathbf{l}\mathbf{A} + \gamma^2\mathbf{I})^{-1}\mathbf{A}^T\mathbf{P}_\mathbf{l}\mathbf{l}. \tag{5.42}$$

According to (5.41), not only the norm of residuals $\|\mathbf{A}\mathbf{x} - \mathbf{l}\|$ will be minimized, but also the solution norm $\|\mathbf{x}\|$ is enforced to be minimum which implies a smoothness or regularity for the solution. Without a proper regularization, the estimated coefficients $\hat{\mathbf{x}}$ can be physically meaningless tough they satisfy the condition min $\|\mathbf{A}\hat{\mathbf{x}} - \mathbf{l}\|^2_{\mathbf{P}_\mathbf{l}}$. Figure 5.5 illustrates this clearly. The estimated coefficients for regional gravity field solution based on simulated GRACE data (see section 6.2.2) are shown in this figure. The first plot on the top, shows the estimated coefficients without any regularization and the second plot displays the estimated coefficients by means of a proper regularization method.

[1] It should be mentioned that even if $\mathbf{L} \neq \mathbf{I}$, it is still possible to transform the problem to the standard case. To do so, it is enough to multiply both sides of (5.39) by $\mathbf{R}^{-1}$ so that the corresponding normal equations reads:

$$(\hat{\mathbf{N}} + \gamma^2\mathbf{I})\mathbf{x} = \hat{\mathbf{y}}$$

in which, $\hat{\mathbf{N}} = \mathbf{R}^{-1}\mathbf{N}$ and $\hat{\mathbf{y}} = \mathbf{R}^{-1}\mathbf{y}$. Hence the discussions concerning the standard Tikhonov regularization, can be generalized to the case with $\mathbf{L} \neq \mathbf{I}$.

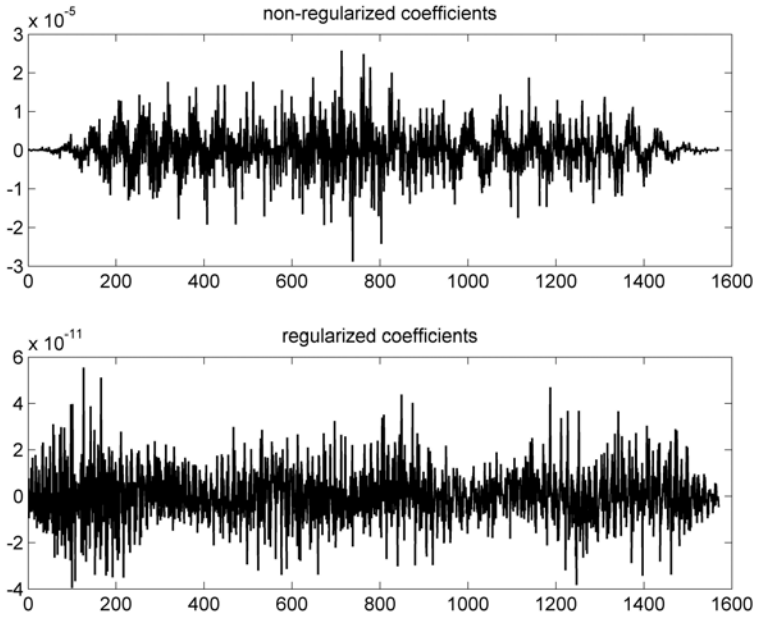

Figure 5.5: The estimated coefficients for the regional gravity field solution in section 6.2.2. **top**: No regularization is applied and the solution is simply obtained based on least-squares method. **bottom**: the solution using a proper regularization method. The non-regularized solution is undesirably oscillatory. The values of these coefficients are about 6 orders of magnitude larger then the regularized solution. Note that these two figures have different vertical scales.

The norm of residuals i.e. $\|\mathbf{A}\hat{\mathbf{x}} - \mathbf{l}\|$ is almost the same for both sets of coefficients. In contrast, the norm of the non-regularized solution i.e. $\|\hat{\mathbf{x}}\|$, is about 6 orders of magnitude larger than the norm of the regularized solution. As it can be seen in the figure 5.5, the standard least-squares solution contains undesirably large oscillations especially in the tails of the unknown vector. This makes the solution to be a physically meaningless estimation even though it mathematically satisfies $\mathbf{A}\hat{\mathbf{x}} = \hat{\mathbf{l}}$. Therefore the condition (5.41) will also control the smoothness of the solution based on the given weight or regularization parameter γ^2. The choice of the regularization parameter is a trade-off between the norm of the residuals and the smoothness of the estimated coefficients. Too large γ^2 values lead to over-smoothing of the solution i.e. to loose some information contained in the observation. On the other hand, choosing too small regularization parameter results in a physically meaningless solution.
The regularization parameter should be usually chosen from a set of numbers which span several orders of magnitude. This implies a high computational burden to find the right number if it is done empirically. Using SVD in the regularization process, gives an insight into the approximate value of regularization parameter and helps to find the proper parameter very fast.

5.4.3 Tikhonov regularization in terms of SVD

As we explained before, it is possible to describe the Tikhonov regularization in terms of singular value decomposition. To do this, we can rewrite (5.40) as:

$$\underbrace{(\mathbf{N} + \gamma^2\mathbf{I})}_{\tilde{\mathbf{N}}}\mathbf{x} = \mathbf{A}^T\mathbf{P}_\mathbf{l}\mathbf{l}. \tag{5.43}$$

The regularized normal matrix $\tilde{\mathbf{N}}$ can be decomposed using SVD:

$$\tilde{\mathbf{N}} = \mathbf{N} + \gamma^2\mathbf{I} = \mathbf{V}\mathbf{S}^2\mathbf{V}^T + \gamma^2\mathbf{I}. \tag{5.44}$$

Since $\mathbf{V}$ is an orthonormal matrix with $\mathbf{V}\mathbf{V}^T = \mathbf{I}$, we can write:

$$\tilde{\mathbf{N}} = \mathbf{V}\mathbf{S}^2\mathbf{V}^T + \gamma^2\mathbf{V}\mathbf{V}^T \tag{5.45}$$

or simply:

$$\tilde{\mathbf{N}} = \mathbf{V}(\mathbf{S}^2 + \gamma^2\mathbf{I})\mathbf{V}^T = \mathbf{V}\tilde{\mathbf{S}}\mathbf{V}^T. \tag{5.46}$$

We consider $\tilde{\mathbf{S}}$ as the regularized matrix of singular values. Equation (5.46) indicates that only the singular values of the normal matrix $\mathbf{N}$ (or equivalently its eigenvalues) will be different as a result of standard Tikhonov regularization.
Using (5.46) and (5.43), the Tikhonov-regularized solution (5.42) can be obtained in terms of singular value decomposition of $\mathbf{N}$ and the regularization parameter γ^2:

$$\hat{\mathbf{x}}_\gamma = \tilde{\mathbf{N}}^{-1}\mathbf{y} = \mathbf{V}\tilde{\mathbf{S}}^{-1}\mathbf{V}^T\mathbf{y}. \tag{5.47}$$

Furthermore the singular values of $\tilde{\mathbf{N}}$ will be:

$$\tilde{s}_k^2 = s_k^2 + \gamma^2 \tag{5.48}$$

therefore analogous to (5.25) one can obtain:

$$\hat{\mathbf{x}}_\gamma = \sum_{k=1}^{K} \frac{\mathbf{v}_k^T\mathbf{y}}{\tilde{s}_k^2}\mathbf{v}_k \tag{5.49}$$

or equivalently using (5.27), in terms of filter factors f_k^2 defined by:

$$f_k^2 = \frac{s_k^2}{s_k^2 + \gamma^2}. \tag{5.50}$$

See also Hansen (1997) and Hansen (2010) for more details. The filter factors f_k^2 determine the contribution of the singular values to the solution. Therefore the Tikhonov regularization can be considered as the weighted or filtered SVD solution or WSVD. From signal processing view, f_k^2 can also be interpreted as the coefficients of a low-pass filter. The difference between truncated SVD and Tikhonov regularization (or WSVD) lies in the difference between their corresponding filter factors. Comparing the filter factors for truncated SVD given by (5.28) and filter factors for the Tikhonov regularization in (5.50), demonstrates that TSVD is an exact low-pass filter while Tikhonov regularization is a smooth one. Figure 5.6 shows the TSVD and Tikhonov filter factors for the ill-posed singular values shown in figure 5.4 (right). For TSVD the truncation point is assumed to be at 850^{th} singular value i.e. $k' = 850$ in (5.28).

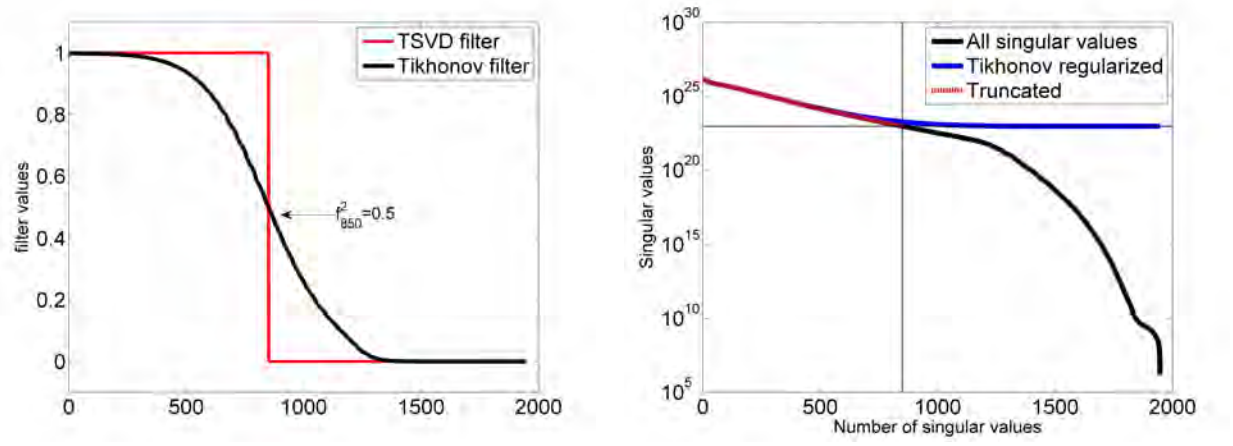

(a) (b)

Figure 5.6: (a): the filter factors for truncated SVD (red) as well as Tikhonov regularization (black). The former is an exact low-pass filter while the latter exhibits a smooth low-pass filter. (b): singular values of an ill-posed problem (black), truncated singular values at $k' = 850$ (red) and the Tikhonov regularized singular values (blue). The intersection of horizontal and vertical lines has the coordinate $(850, s^2_{850})$. $k' = 850$ shows where truncated singular values end and s^2_{850} is the regularization parameter for Tikhonov regularization and is the number to which the regularized singular values (blue) settle down.

The corresponding Tikhonov filter factors for the assumption $k' = 850$ can be obtained if $\gamma^2 = s^2_{850}$ so that the value of 850^{th} filter factor reaches half of its maximum i.e. $f^2_{850} = 0.5$. Figure 5.6 also illustrates the corresponding truncated singular values as well as the Tikhonov regularized singular values. Evidently the value to which the Tikhonov-regularized singular values settle down, is the chosen regularization parameter. This number is also where the truncated singular values end. This is shown by the intersection of the vertical and horizontal line in figure 5.6.
From figure 5.6 it also follows that a mathematically meaningful regularization parameter lies between the smallest and the largest singular values of $\mathbf{N}$. If γ^2 is chosen less than the smallest singular value, it does have no effect on the solution. Respectively if a γ^2 bigger than the largest singular value is to be used, the linear operator $\mathbf{N}$ looses its effect on the solution. This leads to the following proposition for the bounds of the regularization parameter:
Proposition: In the standard Tikhonov regularization, the regularization parameter γ^2 is bounded by the smallest and the largest singular values of the associated normal matrix, i.e.

$$s^2_K < \gamma^2 < s^2_1 \text{ or similarly } \|\mathbf{N}^{-1}\| < \gamma^2 < \|\mathbf{N}\|. \tag{5.51}$$

Although the bounds of γ^2 in this relation gives a theoretical insight into the value of regularization parameter, it, numerically, introduces a very large domain for the regularization parameter. According to figure 5.4 (b) the singular values (for this specific problem) span 20 orders of magnitude and the regularization parameter will be a number between 10^6 and 10^{26} with a condition number about 10^{21}.
Therefore the selection criteria for γ^2 is the main and the most critical task in all regularization methods. In the following some well-known methods will be considered in detail.
To end this section and similar to equation (3.40), for global gravity field modelling, it is also necessary to estimate the covariance matrix of estimated parameters for regional solutions from (5.42) or (5.47). The regularized covariance matrix $\tilde{\mathbf{C}}_{\hat{\mathbf{x}}}$ can be obtained by applying the covariance law to (5.42):

$$\tilde{\mathbf{C}}_{\hat{\mathbf{x}}} = (\frac{\partial \hat{\mathbf{x}}}{\partial \mathbf{l}})\mathbf{P}_\mathbf{l}^{-1}(\frac{\partial \hat{\mathbf{x}}}{\partial \mathbf{l}})^T = (\mathbf{A}^T\mathbf{P}_\mathbf{l}\mathbf{A} + \gamma^2\mathbf{I})^{-1}\mathbf{A}^T\mathbf{P}_\mathbf{l}\mathbf{P}_\mathbf{l}^{-1}\mathbf{P}_\mathbf{l}\mathbf{A}(\mathbf{A}^T\mathbf{P}_\mathbf{l}\mathbf{A} + \gamma^2\mathbf{I})^{-1} \tag{5.52}$$

or briefly:

$$\tilde{\mathbf{C}}_{\hat{\mathbf{x}}} = \tilde{\mathbf{N}}^{-1}\mathbf{N}\tilde{\mathbf{N}}^{-1} \tag{5.53}$$

which gives the formal covariance matrix for the estimated coefficients. The calibrated covariance matrix will be computed using the a posteriori variance factor given by (3.41).
(5.53) can also be rewritten by means of singular value decomposition of $\mathbf{N}$ and $\tilde{\mathbf{N}}$:

$$\tilde{\mathbf{C}}_{\hat{\mathbf{x}}} = \mathbf{V}\tilde{\mathbf{S}}^{-2}\mathbf{V}^T\mathbf{V}\mathbf{S}^2\mathbf{V}^T\mathbf{V}\tilde{\mathbf{S}}^{-2}\mathbf{V}^T \tag{5.54}$$

and since $\mathbf{V}^T\mathbf{V} = \mathbf{I}$:

$$\tilde{\mathbf{C}}_{\hat{\mathbf{x}}} = \mathbf{V}\tilde{\mathbf{S}}^{-2}\mathbf{S}^2\tilde{\mathbf{S}}^{-2}\mathbf{V}^T \tag{5.55}$$

which shows the impact of the regularization on the variance and covariances of the estimated parameters.

5.5 The choice of the regularization parameter

The regularization parameter γ^2 is the most important regularization component and plays a significant role in regularization. It sets a balance between the contribution of the normal matrix $\mathbf{N}$ and the prior information $\mathbf{R}$ to the solution $\hat{\mathbf{x}}_\gamma$. If $\gamma^2 = 0$ it implies that the reliable solution can be obtained without any regularization and thus $\hat{\mathbf{x}}_\gamma = \hat{\mathbf{x}}$. A larger γ^2 means more ill-posedness and consequently more prior information needed for the solution. This trade-off between the norm of the solution and the norm of residuals, makes the choice of regularization parameter a sensitive task. In practice, there are several criteria used to select a proper γ^2, each of them may suite better for some specific problems. Discrepancy principle, Normalized cumulative periodogram (NCP analysis), L-curve criterion, Generalized cross validation and variance component estimation are some known methods for the choice of regularization parameter. The first two methods are given in Hansen (1997, 2010) and will not be considered here. The rest will be given in the following with more details. Furthermore, we introduce our proposed criterion for the choice of γ^2 which suits better for the regional gravity field modelling using SRBF. In chapter 6, we use these methods for regional gravity field modelling based on satellite data.

5.5.1 Generalized cross validation

The idea of Generalized Cross Validation (GCV) is to minimize the norm of residuals using the leave-out-one approach. This is a well-known method in geodetic literature for statistical tests. According to Golub *et al.* (1979), a good regularization parameter γ^2 is a minimizer of the function $G(\gamma^2)$ defined by:

$$G(\gamma^2) = \frac{I\|\mathbf{A}\hat{\mathbf{x}}_\gamma - \mathbf{l}\|^2}{[trace(\mathbf{I} - \mathbf{Q}_{\gamma^2})]^2} \tag{5.56}$$

where I is the number of observations and $\mathbf{Q}_{\gamma^2}$ is the so-called influence matrix and is defined by:

$$\mathbf{Q}_{\gamma^2} = \mathbf{A}\tilde{\mathbf{N}}^{-1}\mathbf{A}^T \tag{5.57}$$

where $\hat{\mathbf{N}}$ is the regularized normal matrix as given in (5.44). Therefore the chosen regularization parameter should minimize the function $G(\gamma^2)$. A key difficulty concerning (5.56) is the calculation of the trace in the denominator. The size of influence matrix is $I \times I$ and for large scale problems, computations of trace is rather expensive. Hutchinson (1990) proposed a statistical trace estimator to overcome this problem. Another way to

ease the calculation of the trace is to use the SVD of the normal matrix. For this purpose, we can rewrite the denominator as follows:

$$trace(\mathbf{I} - \mathbf{Q}_{\gamma^2}) = trace(\mathbf{I}) - trace(\mathbf{Q}_{\gamma^2}) = I - trace(\mathbf{Q}_{\gamma^2}) \tag{5.58}$$

since $trace(pq) = trace(qp)$ one can assume $p = \mathbf{A}\tilde{\mathbf{N}}^{-1}$ and $q = \mathbf{A}^T$ which yields:

$$trace(\mathbf{Q}_{\gamma^2}) = trace(\mathbf{A}\tilde{\mathbf{N}}^{-1}\mathbf{A}^T) = trace(\mathbf{A}^T\mathbf{A}\tilde{\mathbf{N}}^{-1}) = trace(\mathbf{N}\tilde{\mathbf{N}}^{-1}) \tag{5.59}$$

and taking SVD of $\mathbf{N}$ and $\mathbf{N}^{-1}$:

$$trace(\mathbf{N}\tilde{\mathbf{N}}^{-1}) = trace(\mathbf{V}\mathbf{S}^2\mathbf{V}^T\mathbf{V}\tilde{\mathbf{S}}^{-2}\mathbf{V}^T) = trace(\mathbf{V}\mathbf{S}^2\tilde{\mathbf{S}}^{-2}\mathbf{V}^T) \tag{5.60}$$

and finally:

$$trace(\mathbf{Q}_{\gamma^2}) = trace(\mathbf{V}\mathbf{S}^2\tilde{\mathbf{S}}^{-2}\mathbf{V}^T) = \sum_{k=1}^{K} \frac{s_k^2}{s_k^2 + \gamma^2} \tag{5.61}$$

Therefore (5.56) can be written as:

$$G(\gamma^2) = \frac{I\|\mathbf{A}\hat{\mathbf{x}}_\gamma - \mathbf{l}\|^2}{(I - \sum_{k=1}^{K} \frac{s_k^2}{s_k^2 + \gamma^2})^2}. \tag{5.62}$$

This equation gives a convenient way of computing the GCV function in terms of the regularized singular values. See also Chung *et al.* (2008) and Save (2009).
The generalized cross validation function G given by (5.56) or (5.62) is related to the a posteriori variance factor for the covariance matrix of observation as given by (3.41). It has been used in geodetic literature for the calibration of covariance matrices as well as in the statistical tests after least-squares adjustment. See, e.g. Vanicek and Krakiwsky (1982) or Koch (1999). The difference is that the denominator which is the degree of freedom, df, is a function of the regularization parameter and is not constant. Therefore the generalized cross validation can be seen as a method to minimize the a posteriori variance factor $\hat{\sigma}_0^2$, using a proper regularization method.

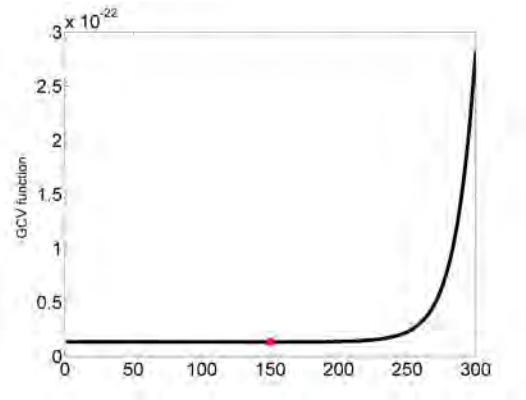

Figure 5.7: The generalized cross validation function for the choice of regularization parameter

Figure 5.7 displays the GCV function associated with the regional gravity field solution described in section 6.2.2, for a set of regularization parameters. The point where G is minimum is marked in this figure. The

generalized cross validation has been used in many research studies. Alberts (2009), Bouman (2000), Lio (2008), van Loon (2008) and Xu (2009) used GCV for the choice of regularization parameters in their analyses. GCV can be used for other optimization issues as well. See for instance Tenzer and Klees (2008) where they used GCV to choose an optimal depth of SRBF.
A remarkable benefit of GCV is that it works based on the residuals' norm and is a data-dependent method. This is especially desired for global gravity field modelling where data are globally available. For regional gravity field determination based on satellite data the criterion may not suit well. Because even though the observations at satellite altitude are well represented using the solution (so that the GCV function is minimized), a satisfactory representation on the Earth's surface is not necessarily guaranteed due to additional ill-posedness caused by the downward continuation. This issue will be discussed more in chapter 6 where the GCV will be used for the regularization of regional gravity field solutions based on satellite data.

5.5.2 Variance component estimation

The method of variance (and covariance) component estimation or VCE is the estimation of an unknown variance factor for the known symmetric positive-definite covariance matrix of observations. It is a useful method when several data sets have to be combined in a parameter estimation procedure. See e.g. Koch (1999) and Amiri-Simkooei (2007).
One can consider the pseudo observations $\boldsymbol{\mu}$ given in the refining model (5.32) as an additional data set to be combined with the observations $\mathbf{l}$ in model (5.31). According to equations (5.31) and (5.32), two variance components σ_0^2 and $\sigma_{\boldsymbol{\mu}}^2$ are unknown and shall be estimated using variance component estimation. Therefore the variance component estimation can be used for choosing γ^2 in Tikhonov regularization since it is the ratio of σ_0^2 and $\sigma_{\boldsymbol{\mu}}^2$ as given by (5.36). The variance components σ_0^2 and $\sigma_{\boldsymbol{\mu}}^2$ can be estimated using:

$$\begin{cases} \sigma_0^2 = (\hat{\mathbf{e}}^T \mathbf{P}_{\mathbf{l}} \hat{\mathbf{e}})/df_{\mathbf{l}} \,, \;\; \hat{\mathbf{e}} = \mathbf{A}\hat{\mathbf{x}}_\gamma - \mathbf{l} \\ \sigma_{\boldsymbol{\mu}}^2 = (\delta\hat{\mathbf{x}}^T \mathbf{P}_{\boldsymbol{\mu}} \delta\hat{\mathbf{x}})/df_{\boldsymbol{\mu}} \,, \;\; \delta\hat{\mathbf{x}} = \mathbf{L}\hat{\mathbf{x}}_\gamma - \boldsymbol{\mu} \end{cases} . \tag{5.63}$$

Since in standard Tikhonov regularization (5.40), $\mathbf{L} = \mathbf{P}_{\boldsymbol{\mu}} = \mathbf{I}$, $\boldsymbol{\mu} = \mathbf{0}$ and furthermore we assumed that $\mathbf{P}_{\mathbf{l}} = \mathbf{I}$, equations (5.63) can be rewritten as:

$$\begin{cases} \sigma_0^2 = (\hat{\mathbf{e}}^T \hat{\mathbf{e}})/df_{\mathbf{l}} \\ \sigma_{\boldsymbol{\mu}}^2 = (\hat{\mathbf{x}}_\gamma^T \hat{\mathbf{x}}_\gamma/df_{\boldsymbol{\mu}} \end{cases} . \tag{5.64}$$

The partial redundancies $df_{\mathbf{l}}$ and $df_{\boldsymbol{\mu}}$ can also be obtained by (Koch and Kusche, 2002):

$$\begin{cases} df_{\mathbf{l}} = I - \dfrac{1}{\sigma_0^2} trace(\mathbf{N}\tilde{\mathbf{N}}^{-1}) \\ df_{\boldsymbol{\mu}} = K - \dfrac{1}{\sigma_{\boldsymbol{\mu}}^2} trace(\tilde{\mathbf{N}}^{-1}) \end{cases} . \tag{5.65}$$

Using SVD of $\mathbf{N}$ and $\tilde{\mathbf{N}}$ and according to (5.61), the redundancy numbers can be evaluated using singular values s_k^2:

$$\begin{cases} df_{\mathbf{l}} = I - \dfrac{1}{\sigma_0^2} \sum\limits_{k=1}^{K} \dfrac{s_k^2}{s_k^2 + \gamma^2} \\ df_{\boldsymbol{\mu}} = K - \dfrac{1}{\sigma_{\boldsymbol{\mu}}^2} \sum\limits_{k=1}^{K} (s_k^2 + \gamma^2) \end{cases} . \tag{5.66}$$

Due to the fact, that the variance components and the redundancy numbers are dependent, the variance component estimation is an iterative process where a first initial guess for σ_0^2 and $\sigma_{\boldsymbol{\mu}}^2$ is necessary.

Variance component estimation has been shown to be a successful method of data combination and regularization in many applications. There are several examples in the context of gravity field modelling where VCE has been used as a method for regularization and weight estimation. Kusche (2003) used the VCE method for the optimal weight determination in gravity field recovery based on GOCE data. Kusche and van Loon (2005), van Loon and Kusche (2005) employed the VCE to assess the stochastic model of CHAMP data using the energy balance approach. For a rather complete list of research studies, where VCE is used for analysing geodetic data such as GPS data processing or gravity field modelling, see Amiri-Simkooei (2007).

5.5.3 L-curve analysis

The L-curve analysis is a graphical tool for regularization of discrete ill-posed problems. The idea was proposed by Hansen (1990b) and Hansen and OLeary (1993) and soon attracted very much attention in the solution of discrete ill-posed problems.
The L-curve is a logarithmic plot of the residuals' norm, $\|\mathbf{A}\hat{\mathbf{x}}_\gamma - \mathbf{l}\|$ versus the solution norm $\|\hat{\mathbf{x}}_\gamma\|$. This curve is obtained based on a set of regularization parameters γ^2, and their corresponding solutions $\hat{\mathbf{x}}_\gamma$. The parametric equation of the L-curve is:

$$\begin{cases} x_L = \log \|\mathbf{A}\hat{\mathbf{x}}_\gamma - \mathbf{l}\| \\ y_L = \log \|\hat{\mathbf{x}}_\gamma\| \end{cases} . \tag{5.67}$$

Figure 5.8 (a) illustrates a typical L-curve plot. The idea of using this curve, for the choice of regularization parameter, is directly connected to minimum norm condition given by (5.41).

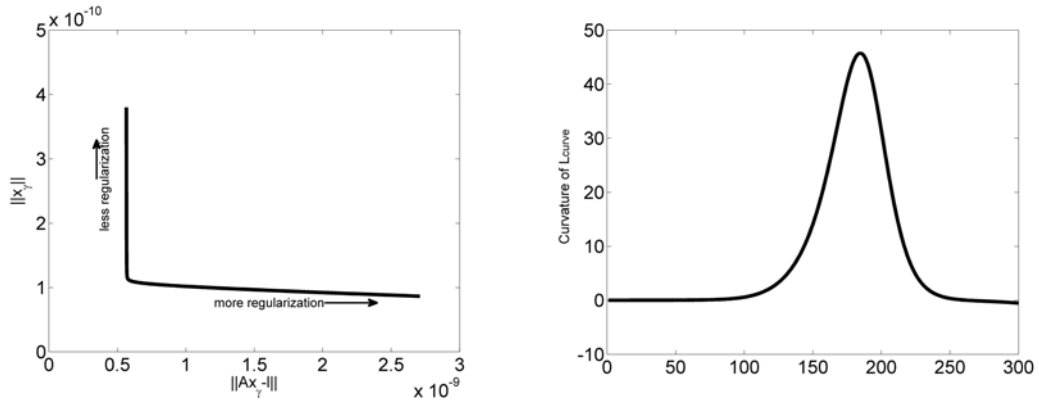

(a) (b)

Figure 5.8: (a): the L-curve function and its corner point where the norm of the solution and the norm of residuals compromise a minimum. (b): the curvature of the L-curve. The maximum curvature refers to the corner point of the L-curve.

As it can be seen from figure 5.8 (a), the name 'L-curve' refers to the fact, that this curve visually appears like an 'L' shape with a vertical and horizontal part. The corner point of the 'L' shape is the point where the norm of residuals and the solution norm compromise their minima. To find the regularization parameter corresponding to the corner point of the L-curve, (Hansen, 1997) suggested to find the point on the L-curve which has the maximum curvature. To do this, one can fit a function to the L-curve which is at least two times differentiable. Thus the curvature of L-curve can be calculated as follows:

$$k(x_L, y_L) = \frac{x'_L y''_L - y'_L x''_L}{\sqrt{(x'^2_L + y'^2_L)^3}}. \tag{5.68}$$

The maximum value of $k(x_L, y_L)$ corresponds to the corner point and is, consequently, assigned to the desired regularization parameter. Figure 5.8 (b) shows the curvature of the L-curve in 5.8 (a).
Xu (1998) proposed another way to find the corner of the L-curve. Since the corner point is the closest point of L-curve to the origin, it is enough to minimize the distance of the L-curve coordinates (x_L, y_L) from origin.
Reginska (1996) tried to describe the mathematical features of the L-curve. She gave a theoretical justification for choosing regularization parameter assigned to the corner point. Later Hansen (2000) extended Reginska's work into more details. Clavetti and co-authors investigated the L-curve and its curvature for Tikhonov regularization in a series of papers. They estimated the L-curve and the bounds of its curvature using Lanczos bidiagonalization. See more details in Calvetti *et al.* (1999), Calvetti *et al.* (2002) and Calvetti *et al.* (2004).
The L-curve analysis has been used in numerous research studies for variety of different applications. It has also been used for ill-posed problems in gravity field determination. In a simulation study Kusche and Klees (2002) compared the performance of the L-curve analysis to generalized cross validation for Tikhonov regularization of gravity field modelling based on SGG data. They concluded that L-curve yields over-smooth solutions in their analyses and suggested to use L-curve with cares. In contrast, Save (2009) used the L-curve criterion for regularization of global solutions using real GRACE data to reduce errors in monthly GRACE solutions and reported the success of the method. Later, Save and Bettadpur (2012) showed that use of L-curve and applying Lanczos bidiagonalization results in remarkably reduced stripe errors compared to CSR GRACE unconstrained solutions RL04. The L-curve method has been also used by Ramillien *et al.* (2011) for the inversion of surface water mass anomalies from GRACE data. They computed the maximum curvature of the L-curve using (5.68) and used the benefits of fast computations using SVD-based Tikhonov regularization.

5.6 Signal-adaptive parameter choice: The parameter-signal correlation (PSC)

In section 3.3, it was shown that the estimated scaling coefficients α_k resemble the shape of the gravitational potential or geoid, see figure 3.7. The cross correlation function for the estimated coefficients and geoid heights at the same locations were also computed which shows a high correlation between the estimated coefficients and the signal to be modelled using SRBF (figure 3.7). The reason is the space-localizing property of SRBF; the energy of a SRBF is concentrated around its centre and consequently the corresponding coefficients are significantly determined by observations around it. This fact can be seen if we consider the general form of the gravity field synthesis using SRBF as (see also 3.3)

$$V(\mathbf{r}_i) = \sum_{k=1}^{K} \alpha_k B(\mathbf{r}_k, \mathbf{r}_i) \tag{5.69}$$

which can be written in terms of the inner product

$$V(\mathbf{r}_i) = < \mathbf{x}, B(\mathbf{r}_k, \mathbf{r}_i) > \tag{5.70}$$

where $\mathbf{x} = [\alpha_1, \alpha_2, ..., \alpha_k]^T$ is the vector of unknown coefficients. These relations can be approximately expressed by means of the convolution of the functions α_k and $B(\mathbf{r}_k, \mathbf{r}_i)$:

$$V(\mathbf{r}_i) = \mathbf{x} * B(\mathbf{r}_k, \mathbf{r}_i). \tag{5.71}$$

The SRBF defined by (3.50) have two properties which can be used for the regularization purposes. Firstly, $B(\mathbf{r}_k, \mathbf{r}_i)$ is a (spherically) symmetric function. This implies that the convolution given by (5.71) can be equivalently expressed by the cross-correlation function [1]. Therefore the synthesized values V_i are nothing

[1] According to the definition of the convolution and the cross-correlation, if the kernel function $g(\tau)$ is symmetric i.e. $g(\tau) = g(-\tau)$, the convolution and the cross correlation of g with any other function are equivalent. See e.g. Yarlagadda (2010) and Steven (1997).

but the cross correlation of α_k and the symmetric base function B at different positions. Secondly, the base functions B have their maximum value at their centre, i.e. at $\mathbf{r}_i = \mathbf{r}_k$. In other words, B does have the space-localization feature as explained in the previous chapters. If B were an ideal space-localizing function i.e. the Dirac function, V_i and α_k would be identical. Nevertheless, the coefficients α_k should correspond to the synthesized values V_i around the position $\mathbf{r}_k$ since the base functions B are space-localizing.
These features can be considered as prior knowledge about the unknown coefficients and one can make use of this for the regularization purposes. The idea of the signal-adaptive parameter choice is, therefore, based on this property: **A good regularization parameter provides a solution where the estimated scaling coefficients have maximum correlation with the (residual) gravitational potential.**
The mathematical description of this method can be expressed as follows:
Let the scaling coefficients at locations ϕ_k and λ_k be denoted by $\alpha_k(\gamma^2, \phi_k, \lambda_k)$ where γ^2 is the corresponding regularization parameter. Furthermore the function dV[1], which is to be modelled using SRBF, is available at grid points ϕ_k and λ_k. The desired regularization parameter γ^2 is chosen such that the scaling coefficients α_k and the signal dV have the maximum correlation. In other words, α_k and dV should be as (much) *similar* as possible. To measure the similarity, one can use the normalized cross correlation function $\Gamma_{xy}(\tau)$ defined by

$$\Gamma_{xy}(\tau) = \frac{E[x(t)y(t+\tau)]}{\sqrt{E[x(t)]E[y(t)]}} \tag{5.72}$$

where E is the expectation operator and x and y are two arbitrary functions. τ defines the lag of the cross correlation function (Orfanidis, 1996). Since we are interested in the correlation of dV_k and α_k at the same positions, the cross correlation function is needed only at zero lag, i.e. $\tau = 0$:

$$\Gamma_{xy}(0) = \frac{E[x(t)y(t)]}{\sqrt{E[x(t)]E[y(t)]}} \tag{5.73}$$

which can be equivalently expressed by the inner product:

$$\Gamma_{xy}(0) =< \frac{x}{\|x\|}, \frac{y}{\|y\|} > . \tag{5.74}$$

Therefore the similarity between dV_k and α_k can be measured using

$$\Gamma_{dV_k,\alpha_k}(0) =< \frac{dV}{\|dV\|}, \frac{\alpha_k}{\|\alpha_k\|} > . \tag{5.75}$$

The correlation function $\Gamma_{dV_k,\alpha_k}(0)$ determines the linear dependency between α_k and dV_k which is expected to be significantly high. Thus using (5.75), the regularization parameter γ^2 can be obtained by the following criterion:

The desired regularization parameter γ^2 is the maximizer of the function $\Gamma_{dV_k,\alpha_k}(0)$ given by (5.75).

We call this parameter choice method as the **parameter-signal correlation** or briefly the PSC method.
Figure 5.9 shows the function $\Gamma_{dV_k,\alpha_k}(0)$, associated with a set of regularization parameters used to determine the regional gravity field in Central Africa based on the simulated GRACE data (see 6.2.2). As it can be seen, the function does have a maximum which corresponds to the desired regularization parameter.

The key point of using (5.75) is to obtain a priori value for dV at grid locations ϕ_k and λ_k. It can be computed using either regional gravity field models (if available) or existing global models. This implies

[1] dV refers to the residual potential since for regional gravity field modelling the long wavelengths should be removed.

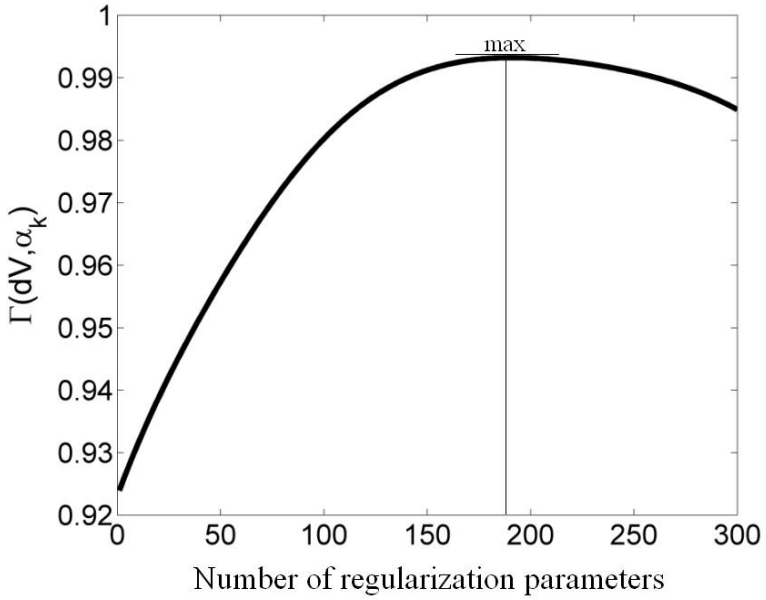

Figure 5.9: The PSC function for a set of regularization parameters. The maximum correlation is assigned to the desired regularization parameter. In this figure the 187^{th} selected parameter is the desired regularization parameter.

that a high-resolution gravity field model should be available to obtain dV_k. According to (5.75), it is necessary to evaluate the residual potential dV on grid locations ϕ_k and λ_k using:

$$dV(\phi_k, \lambda_k) = V(\phi_k, \lambda_k) - V_0(\phi_k, \lambda_k) \tag{5.76}$$

where $V(\phi_k, \lambda_k)$ is the gravitational potential and $V_0(\phi_k, \lambda_k)$ refers to the long wavelengths of the potential field which should be removed. V_0 is computed and subtracted according to discussions given in 4.2.3. To assess the effect of using different models to obtain dV_k, we used several geopotential models listed in table 5.1 for the regional gravity field model in Section 6.3.3. Our computation indicate that by using different reference models to compute dV_k, the maximum value of the function $\Gamma_{dV_k,\alpha_k}(0)$ does not change significantly. Consequently the resulting regularization parameter does not change remarkably as shown in table 5.1. It can be seen that if the geopotential models EGM2008 and EGM1996 are employed to compute dV_k, the resulting regularization parameters will be 1.65×10^{24} and 1.89×10^{24}, respectively. The difference between these values is rather small especially if we compare it with the regularization parameters obtained using the VCE, GCV or L-curve (see table 6.9). Using these two regularization parameters we estimated two sets of scaling coefficients, and then the geoid heights in this region were synthesized. Figure 5.10 shows the regional geoid differences between two models obtained using the above regularization parameters. As it can be seen, the total regional RMS is about 1.1 cm with the maximum value of about 6 cm in a few specific locations. Again, such deviations are not remarkable if they are compared to the results obtained using other methods of regularization (see Figure 6.18). Nevertheless one can try to refine the results to still eliminate the residuals by modifying the PSC method and reducing the impact of the reference geopotential model. Overall, we concluded that almost all models provide rather the same regularization parameter at the current accuracy level for satellite-derived gravity fields. Therefore there is no preference given to a specific geopotential model for the PSC approach. This means that the prior model used for the PSC method does not have to be the state-of-the-art. Only an approximate model which can show the geometry of the field, fulfils the purpose of the PSC method.
Using (5.75) to find the regularization parameter gives an insight into easy and straightforward computations. It provides satisfactory and even better results compared to other parameter choice methods such as L-curve or variance component estimation. In chapter 6, we will use this method and compare it to other parameter choice methods introduced in this chapter.

Reference model	data used	N_{max}	year	resulting γ^2
GOCO03s	GRACE, GOCE	250	2011	1.31×10^{24}
GGM03c	GRACE, Terrestrial	360	2009	1.48×10^{24}
EGM2008	GRACE, Altimetry, Terrestrial	2190	2008	1.65×10^{24}
PGM2000	Altimetry, TOPEX,ERS1, Terrestrial	360	2000	1.90×10^{24}
EGM1996	Altimetry, TOPEX,ERS1, Terrestrial	360	1996	1.89×10^{24}

Table 5.1: Different geopotential models used to compute dV_k for the PSC method. The second column shows the data used to determine the gravity field model. See GFZ (2013) for more details about these models. The resulting regularization parameter is also shown in the table for the regional gravity field model in Section 6.3.3. As it can be seen, all models give approximately the same regularization parameter.

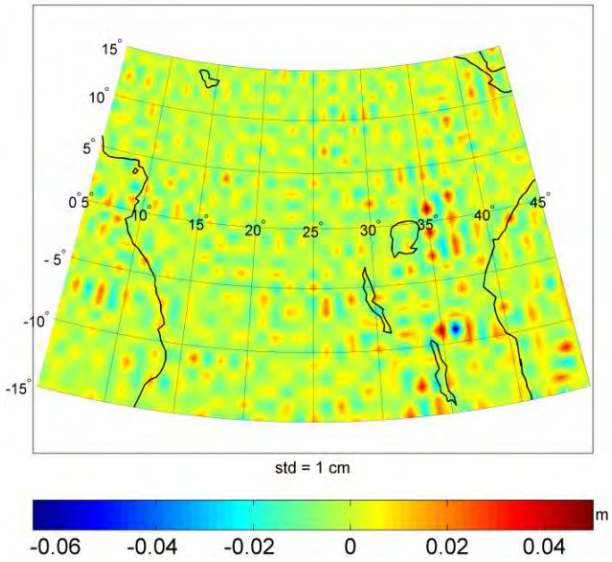

Figure 5.10: Geoid differences between two regional models obtained using the PSC regularization method but with different reference geopotential models; the EGM2008 and the EGM1996. The total geoid RMS is about 1 cm with maximum deviation of about 6 cm. See Section 6.3.3. for more details about regional solution in this region.

5.7 Initial value for the regularization parameter

A good first guess for the regularization parameter is necessary for all parameter choice methods. Existence of such an approximate value reduces the computational costs and leads to a faster convergence. Once the initial guess for the regularization parameter is obtained, it can be improved by means of iteration in the variance component estimation or criteria such as the L-curve analysis, the generalized cross validation or the the PSC method. The final regularization parameter is expected to be close to the initial guess. Therefore it is possible to define a search band for the regularization parameter in the neighbourhood of the initial guess as shown in figure 5.11. Our computations indicate, that this approach considerably helps to decrease computational costs and provides a rapid convergence in the iterations.
In this section, we propose two different ways to obtain a first realistic guess for the regularization parameter. The basic tool for these two methods are the singular values of the normal matrix. In addition, in both cases we

benefit from the fact that the spherical harmonics and SRBF span the same function space on the global scale. Figure 5.6 (b) shows the singular values of an ill-posed normal matrix. In addition, the Tikhonov-regularized

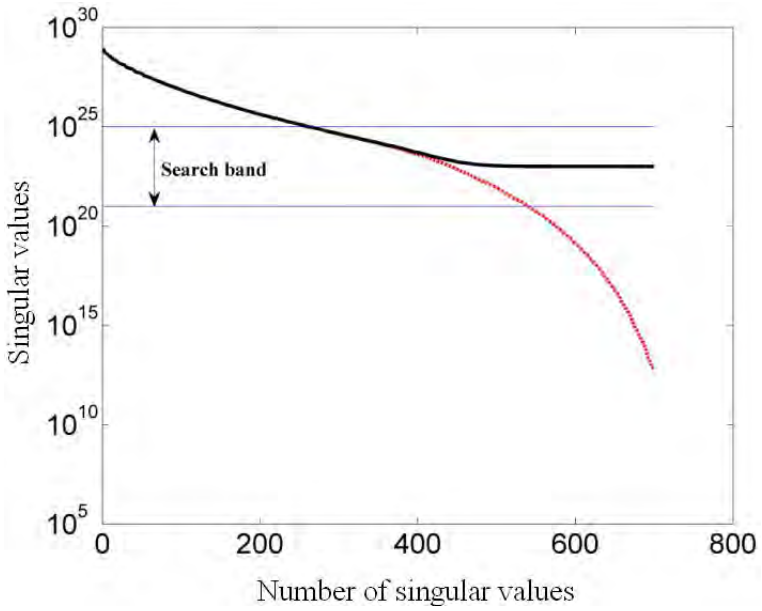

Figure 5.11: The regularized singular values (black) using initial guess for the regularization parameter and the original non-regularized singular values (red). The regularized singular values are now stable and level out at value $\gamma^2 = 10^{23}$. The search band displays the area where the final regularization parameter is located.

singular values as well as truncated singular values are also shown. As we discussed in the context of this figure, the number to which the Tikhonov-regularized singular values level off, is the truncation point for truncated singular values. This point has the coordinates (n, s_n^2). The horizontal component or n, gives an insight into the number of significant singular values, needed to obtain a good solution. On the other hand, the vertical component or s_n^2 refers to the amount of regularization needed for the solution. A good initial guess can be found if either n or s_n^2 are approximately known. Therefore, we propose two ways to find an initial first guess for the regularization parameter:

- using information about n which is based on the size of the region
- using information about s_n^2 which is based on the 'desired' condition number

In the following we discuss these two methods.

5.7.1 Initial guess based on the size of the region

Figure 5.4 (a) displays the singular values related to global gravity field modelling using SH as well as SRBF up to max degree $N_{max} = 70$ (i.e. the number of SH functions are 5038). The sudden jump in singular values related to SRBF at $n = 5038$ explicitly shows that only the first 5038 singular values are necessary to obtain an equivalent solution to SH. This is due to the fact that spherical harmonics and SRBF span the same function space on the global scale (see section 3.3).
One can use this equivalence between SH and SRBF to (approximately) find the number of significant singular values for regional solutions. Since the number of significant singular values on the global scale is $(N_{max} + 1)^2$, the number of significant singular values on regional scales can be approximately estimated by a simple proportion based on the area of the region using

$$k' = \frac{A_\Omega}{4\pi}(N_{max} + 1)^2 \tag{5.77}$$

where A_Ω denotes the size of the region on the unit sphere and is given by:

$$A_\Omega = \int_{\lambda_1}^{\lambda_2} \int_{\phi_1}^{\phi_2} cos\phi d\phi d\lambda = (\lambda_2 - \lambda_1)(\sin\phi_2 - \sin\phi_1). \tag{5.78}$$

The boundaries of the region are defined by λ_1, λ_2, ϕ_1 and ϕ_2. Therefore, the initial guess for the regularization parameter is equal to the k'^{th} singular value of the associated normal matrix. For instance if the regional gravity field is desired in the region defined by $\lambda_1 = 0$, $\lambda_2 = 50$, $\phi_1 = 50$ and $\phi_2 = 75$, using SRBF with $N_{max} = 250$, the number of significant singular values is approximately equal to 870. Thus, the initial guess for the regularization parameter is the 870^{th} singular value i.e. s^2_{870}.

5.7.2 Initial guess based on the condition number

Another method to obtain a realistic initial value for the regularization parameter is to use the condition number. To do this, we consider the condition number of the normal matrix given by

$$cond(\mathbf{N}) = \frac{s_1^2}{s_K^2} = \frac{\|\mathbf{N}\|}{s_K^2} \tag{5.79}$$

in which s_1^2 and s_K^2 are the first and last singular values of $\mathbf{N}$ (see also 5.23). The same holds for the regularized normal matrix $\tilde{\mathbf{N}}$:

$$cond(\tilde{\mathbf{N}}) = \frac{\tilde{s}_1^2}{\tilde{s}_K^2} = \frac{\|\tilde{\mathbf{N}}\|}{\tilde{s}_K^2}. \tag{5.80}$$

From (5.48) it follows that

$$\begin{cases} \tilde{s}_1^2 = s_1^2 + \gamma^2 = \|\mathbf{N}\| + \gamma^2 \\ \tilde{s}_K^2 = s_K^2 + \gamma^2. \end{cases} \tag{5.81}$$

Therefore (5.80) becomes

$$cond(\tilde{\mathbf{N}}) = \frac{\tilde{s}_1^2}{\tilde{s}_K^2} = \frac{\|\mathbf{N}\| + \gamma^2}{s_K^2 + \gamma^2}. \tag{5.82}$$

Due to the fact that $\|\mathbf{N}\| \gg \gamma^2$ and $\gamma^2 \gg s_K^2$, (5.82) can be well approximated by

$$cond(\tilde{\mathbf{N}}) \cong \frac{\|\mathbf{N}\|}{\gamma^2} \tag{5.83}$$

which results in a rather explicit relation for the regularization parameter:

$$\gamma^2 \cong \frac{\|\mathbf{N}\|}{cond(\tilde{\mathbf{N}})}. \tag{5.84}$$

This means that if prior information about the condition number of the 'desired' regularized normal matrix $\tilde{\mathbf{N}}$ is available, the regularization parameter γ^2 can be determined directly.
According to the discussions concerning equations (4.2) and (4.3), the ill-posed regional normal matrix $\mathbf{N}$ is in fact extracted from the global normal matrix $\mathbf{N}_{srbf}$. The strong ill-posedness of $\mathbf{N}$ is due to the horizontal and vertical truncation of $\mathbf{N}_{srbf}$ (see 4.1). Therefore, by means of regularization, we try to repair these 'cutting' effects such that the regularized normal matrix $\tilde{\mathbf{N}}$ be as stable as $\mathbf{N}_{srbf}$.
Based on this argument, we postulate the following assumption to obtain an initial value for γ^2

$$cond(\tilde{\mathbf{N}}) = cond(\mathbf{N}_{srbf}) \tag{5.85}$$

where $\mathbf{N}_{srbf}$ is the normal matrix associated with the global gravity field modelling using SRBF. Since SRBF and SH span the same space function

$$cond(\mathbf{N}_{srbf}) = cond(\mathbf{N}_{SH}) \tag{5.86}$$

and the condition number of $\mathbf{N}_{SH}$ can be approximately estimated using Kaula's rule of thumb (Kaula, 1966, Knudsen, 1987)

$$cond(\mathbf{N}_{SH}) = \frac{N_{max}^3}{8} \tag{5.87}$$

where N_{max} is the maximum degree of expansion. Putting (5.85), (5.86) and (5.87) together, the initial value for γ^2 can be obtained from

$$\gamma^2 = \frac{8\|\mathbf{N}\|}{N_{max}^3} \tag{5.88}$$

which evaluates the initial regularization parameter using the norm of the normal matrix and the maximum degree of expansion. In the following chapter, we use these two approaches to estimate an initial γ^2. This will also be shown that both methods give rather close initial values.

5.8 Different types of SRBF and their impact on the regularization

In section 4.2.1 we explained, that different kinds of SRBF can have different effects on the regularization process. The reason is the smoothing properties of some SRBF defined by the Legendre coefficients b_n. In this section we discuss this issue in more detail.
In principle, the goal of regularization for regional gravity field modelling is the suppression of the model errors (omission, commission and cut-off errors) to obtain a solution with the least possible error. If we note equation (5.11) once more

$$\frac{\|\delta\mathbf{x}\|}{\|\mathbf{x}\|} \leq cond(\mathbf{A})\frac{\|\mathbf{e}\|}{\|\mathbf{l}\|}$$

it is evident that the solution error is dependent on the condition number of the design matrix (and the normal matrix) as well as the observation errors. Therefore, to reduce the solution's error one should either reduce the condition number or the observation error or both. The aim of regularization procedure is to improve the condition number by modifying the normal matrix $\mathbf{N}$. The regularized normal matrix $\tilde{\mathbf{N}} = \mathbf{N} + \gamma^2\mathbf{I}$, has a condition number which is considerably smaller than the condition number of $\mathbf{N}$. As the result, the solution's error in (5.11) will be drastically reduced. Our investigations show that the use of different SRBF does not noticeably improve the ill-posedness of the design and normal matrices. The reason is that the rapid decay of the singular values of the normal matrix $\mathbf{N}$ and its rather large condition number are mainly dependent on the size of the region which does not remarkably change by using different SRBF.
The main difference between different types of SRBF is their impact on the vector of observations $\mathbf{l}$. To explain this, we reconsider the regularized solution (5.42) from another perspective:

$$\hat{\mathbf{x}}_\gamma = (\underbrace{\mathbf{A}^T\mathbf{P}_\mathbf{l}\mathbf{A} + \gamma^2\mathbf{I}}_{\tilde{\mathbf{N}}})^{-1}\underbrace{\mathbf{A}^T\mathbf{P}_\mathbf{l}\mathbf{l}}_{\mathbf{y}}. \tag{5.89}$$

According to (5.89), the regularized solution $\hat{\mathbf{x}}_\gamma$ is obtained from the observation vector $\mathbf{l}$ via a sequence of linear operations. In the first step, the observation vector $\mathbf{l}$ is projected from the observation space $\mathbb{L}$ to its dual space $\mathbb{L}'$ using the weight matrix $\mathbf{P}_\mathbf{l}$. The result is the vector $\mathbf{P}_\mathbf{l}\mathbf{l}$ in the space $\mathbb{L}'$. In this step, the observations

are normalized according to their variances. If only one type of observation is used, the vector $\mathbf{P_l l}$ is just a scaled version of $\mathbf{l}$.
Then the vector $\mathbf{P_l l}$ will be projected onto another function space using $\mathbf{A}^T$. This function space denoted by $\mathbb{X}'$ is the dual space of the unknown function space $\mathbb{X}$. The result of this projection, is the vector $\mathbf{y} = \mathbf{A}^T\mathbf{P_l l}$ in the function space $\mathbb{X}'$. In this projection, the observation vector $\mathbf{l}$ will be filtered due to the smoothing effects of the SRBF as the row vectors of $\mathbf{A}^T$.
In the last step the vector $\mathbf{y}$ is projected onto the function space $\mathbb{X}$ using the operator $\mathbf{N}^{-1}$ to obtain the final solution. Since $\mathbf{N}^{-1}$ is an unstable operator, $(\mathbf{N} + \gamma^2\mathbf{I})^{-1}$ shall be used to obtain the regularized solution. The whole operation sequence is diagrammatically shown in figure 5.12.
The shape of SRBF, affects the second projection and consequently the vector $\mathbf{y}$. If SRBF have no smoothing effects, the vector $\mathbf{y}$ includes all frequencies of $\mathbf{l}$. Otherwise, the observation vector $\mathbf{l}$ will be filtered in the second step. A result of this filtering is the reduction of the observation noise and according to (5.11), the solution's error will be reduced. If the observation noise is reduced in the second operation, less regularization will be needed in the inversion process (third operation). From this point of view, it may seem logical to use some sort of SRBF which contain built-in filters. The CuP, Blackman and Spline kernels are examples of these functions which reduce the observation's noise before the inversion process by filtering the high frequency components of $\mathbf{l}$.
Nevertheless, applying any kind of filtering to the observation vector leads to the loss of some signal components, particularly the higher frequencies. This is a contradiction of the main goal of regional modelling which is, to extract more local features (high frequencies) out of the data. To avoid this problem, one should be aware of the filtering properties of the employed SRBF.
In our methodology, we always use the SRBF with the Shannon kernel with no filtering features. Thus, the observation vector $\mathbf{l}$ and its noise will remain untouched and the solution error will be minimized via a proper regularization process in the final stage. In addition, we set the maximum degree of expansion, i.e. N_{max}, to be slightly higher than the expected value. For example, if the expected resolution of solutions based on GOCE observations is about $n = 250$, we set $N_{max} = 300$. This makes the Shannon kernel to be an exact low-pass filter where the cut-off frequency is far beyond the expected frequency content of the signal. Therefore it is guaranteed that the observation vector is not filtered out in the second operation.

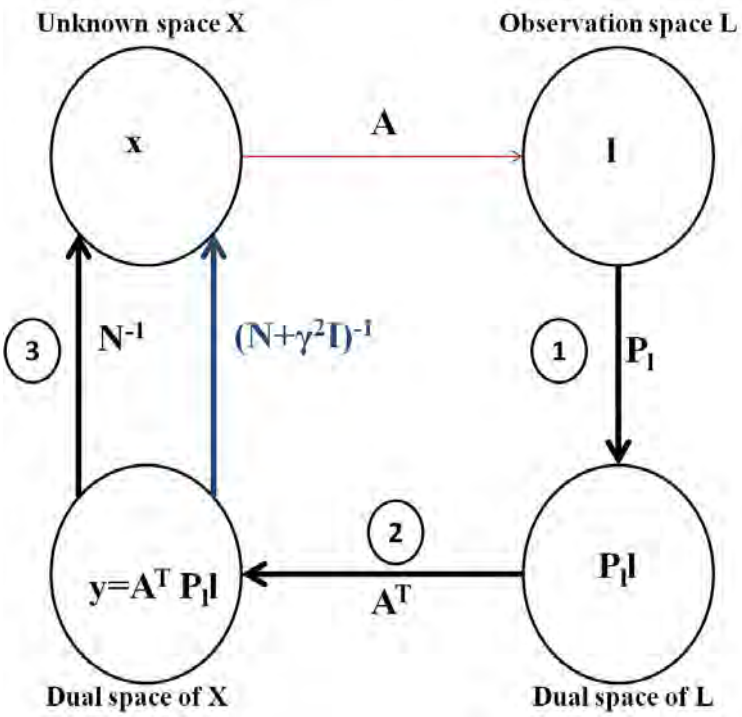

Figure 5.12: The sequence of matrix operations to obtain the regularized solution from the observation vector. In the first operation, the observations are projected onto an interim function space called the dual space of $\mathbb{L}$. The second step, is the projection onto the dual space $\mathbb{X}$. In this step, the observations might be filtered out if the base functions have the smoothing property. Finally, the last projection is the inversion process which gives the final solution. The diagrammatic view of the standard least-squares solution (without regularization) is described by Mohammad-Karim (1981).

The choice of the Shannon kernel for the shape of the SRBF makes the choice of base functions very simple. There is no more efforts needed to define the Legendre coefficients b_n as they are all equal to 1. The use of other SRBF for regional gravity field modelling such as Blackman and CuP is also possible provided that the bandwidth of these functions are selected properly to avoid filtering of the signal parts. As a result, the number of base functions increases remarkably which seems to be unnecessary. The discussions concerning the number of base functions is given in Section 4.2.1.

5.9 Assessment of regional solutions

Having obtained the solution for the unknown vector $\hat{\mathbf{x}}$, we have to assess the quality of the estimated parameters. In global gravity field modelling based on satellite data, there are some measures used to check the quality of the solution. Bouman (2000) introduces several quality measures used to assess the quality of satellite-based gravity models. These measures can be classified into three groups: statistical assessment, external validation and model-dependent evidences.

5.9.1 Statistical assessment

This group of quality measures consists of information obtained from observations and their given covariance matrices. The statistical assessment has roots in the parametric statistics. The emphasis of the statistical tests are mainly on the vector of post-fit residuals. The normal test of a single observation, test of a residual outlier and test of the quadratic form of the residuals can be mentioned as examples of statistical assessments. The latter is in fact the test of a posteriori variance factor given by equation (3.41) and is also a base for the generalized cross validation (c.f. section 5.5.1). Vanicek and Krakiwsky (1982), (chapter 13), give a rather complete overview of

statistical tests used to assess the results of least-squares adjustment for geodetic applications.
This type of quality measures are indications for the capability of the solution to reconstruct the observations. For gravity field determination from satellite data, it is not sufficient. The reason is, that even if the observations at satellite altitude are well represented by the solution, it does not guaranty an acceptable representation on the Earth's surface. This issue is not trivial especially for regional gravity field solutions. Therefore, a regional gravity field solution should be obtained in a way, that not only it passes statistical tests, but also other external validations.

5.9.2 External validation

The quality of gravity field models should be tested against other sets of observations. As it is common in practice, new gravity field solutions will be checked using other independent data sets such as GPS levelling, absolute and relative gravimetry data and gravity anomalies as well as satellite altimetry data. In addition, the new model can be checked using a previously known model which is accepted as a high-quality model. Here the residuals are desired to be minimum on the Earth's surface rather in the observation level. Gruber (2004) gives more details on the concepts of validation strategies for satellite-based gravity field solutions. Gruber *et al.* (2011) used orbit residuals as well as GPS-levelling to validate three global gravity field solutions based on GOCE data. See also Gruber (2009), Tapley *et al.* (2005) and Ihde *et al.* (2010). In another study, Voigt (2012) used astro-geodetic vertical deflections in Germany to validate GOCE gravity field models.
In the following chapter, we use the global geo-potential models GOCO03s and EGM2008 for the validation of regional solutions.

5.9.3 Model-dependent evidences

No matter based on which data sets a gravity field is determined, the parameters should have the essential characteristics of the model or the base functions used in the analysis step. For example, spherical harmonic coefficients should fit the Kaula's degree variances. Almost in all degree variance plots, the Kaula's degree variances are shown as an indication of agreement between the model and the expected behaviour (figure 3.5). This expected compromise is even used for the regularization of global solutions known as Kauls's stabilization. While Kaula's rule gives an insight into the expected spectral properties of SH coefficients, one should look for spatial behaviours of scaling coefficients for SRBF. As we showed in figure 3.7, the scaling coefficients α_k should represent the spatial pattern of the gravitational potential or geoid according to the space-localizing feature of SRBF. This is the idea of the PSC method explained in section 5.6. Bentel *et al.* (2013) also used this fact as a measure of validation for their regional solutions using different SRBF.
Based on the discussions above, the regularization process for a **reliable regional solution** should satisfy the following criteria:

- The observations' residuals (e.g. the potential difference or the gravity gradients in the case of GRACE and GOCE respectively) along the orbit of the satellite, i.e. $\|\mathbf{A}_{11}\hat{\mathbf{x}}_1 - \mathbf{l}_1\|$, should be minimum.
- The synthesized geoid on the Earth's surface should have minimum regional RMS with respect to a high-resolution global gravity field model (say GOCO03s) or available terrestrial data sets.
- The estimated coefficients α_k at grid point (ϕ_k, λ_k) should have high correlation to the synthesized geoid at these positions. In other words, α_k should represent the shape of residual potential or geoid as much as possible.

We will use these three measures to judge the quality of regional solutions and consequently the performance of different regularization methods.

6 Numerical results

This chapter is devoted to the numerical implementation of the regional gravity field analysis using SRBF. The main goal is to compare the performance of different regularization approaches, explained in the previous chapter. In particular, the applicability of the proposed parameter-signal correlation (PSC) method is to be assessed. To achieve this goal, we investigate the regional modelling in several test regions under different conditions. Therefore the following questions are to be answered:

- What is the impact of different regularization methods on the regional solution?
- Does the quality of solutions significantly depend on the choice of grid points?
- Are regional solutions better than (or at least equivalent to) global solutions using SH (we use the geoid RMS on the Earth's surface as a measure for comparison)?

In the following section the specifications for regional gravity field modelling, such as test regions and grid points will be defined. In section 6.2 gravity field modelling based on the data for a GRACE-type mission will be addressed in a closed-loop simulation. Moreover, the regional solutions will be compared to a global spherical harmonic solution based on the same data and imposed noise. Since it is beyond the scope of this PhD thesis to discuss the technical details of dealing with real GRACE data, simulated GRACE data are used in this section. However, to check the regional solutions based on real data, the regional gravity field modelling based on real GOCE observations will be considered in 6.3. According to the drag-free system used on board the GOCE satellite, much less data reduction and preparation are required compared to GRACE data. Moreover, temporal corrections such as direct and indirect tide, polar tide and non-tidal variations are provided for GOCE data which eliminate most of pre-processing efforts (Gruber *et al.*, 2010).

6.1 Specifications of regional solutions

As we discussed in chapter 4, regional gravity field modelling using space localizing base functions includes a collection of several choices which have to be made. Therefore it is not possible to define a unique way for regional gravity field modelling. In the following computations, the emphasis is put on the choice of the regularization parameter to compare the methods presented in chapter 5. The reason is the key role of regularization in regional gravity field modelling. The job of regularization is to adjust different model components to achieve the best possible approximation. Hence if the model is regularized appropriately, other choices are not of great concern and can be kept rather simple. The regional gravity field modelling using SRBF will be investigated in several test regions. The model specifications are defined in the following.

6.1.1 Test regions

The regional gravity field modelling will be considered in three test regions: **Scandinavia**, **Central Africa** and **South America**. The main reason for choosing Scandinavia and Central Africa is the different coverage of satellite data; while in regions with high latitude such as Scandinavia, satellite data are fairly dense, the coverage is less dense in equatorial regions like Central Africa. This is due to the polar and near polar orbits of GRACE and GOCE satellites. In addition, we also consider the regional modelling in South America due to its rough gravity field along the Andes. It is an interesting region for geologists and geophysicists since the world's highest volcanoes are in the Andes. Thus, from the viewpoint of the signal content, it is a good region to challenge the regional gravity field modelling.
Figure 6.1 displays the geographical extension of these regions on the global scale. In addition, the residual geoid is also shown where the long wavelengths up to degree $n = 30$ are subtracted. The geographical extensions of these regions are as follows:

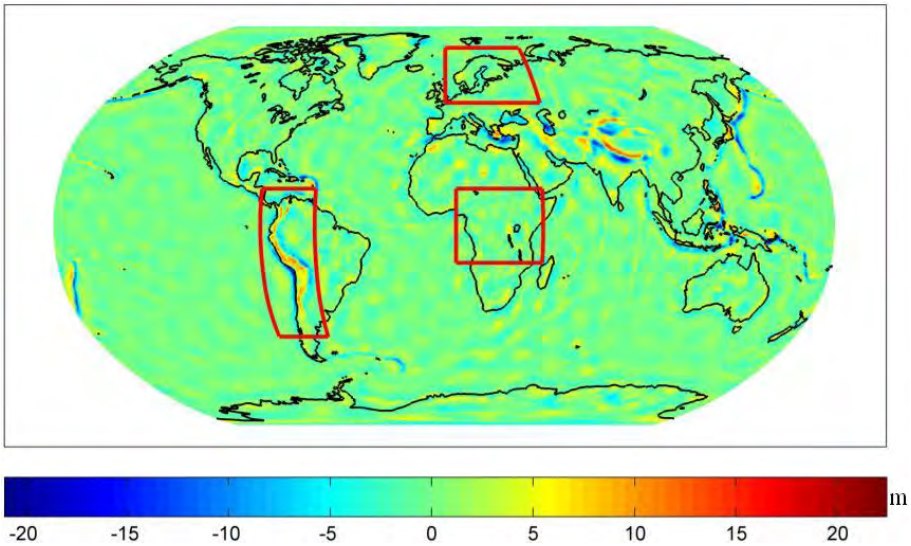

Figure 6.1: The test areas for regional gravity field modelling based on satellite data: Scandinavia as a high latitude region and Central Africa as an equatorial region. South America along the Andes will also be considered due to its rough gravity field.

- Central Africa : $-15^\circ \leq \phi \leq 15^\circ$ and $5^\circ \leq \lambda \leq 45^\circ$,
- Scandinavia : $50^\circ \leq \phi \leq 75^\circ$ and $0^\circ \leq \lambda \leq 50^\circ$,
- South America : $-45^\circ \leq \phi \leq 15^\circ$ and $-85^\circ \leq \lambda \leq -60^\circ$.

These limits will be considered as the model zone. The data and grid zones will be defined for each region specifically.

6.1.2 Type of SRBF

According to the discussions in section 5.8, we confine ourselves to the Shannon kernel in the following and show that it gives promising results using the proposed PSC method for the choice of the regularization parameter. The maximum degree of expansion for the SRBF with the Shannon kernel will be $N_{max} = 130$ and $N_{max} = 300$ for regional gravity field modelling based on simulated GRACE data and real GOCE observations, respectively.

6.1.3 Type of grid points

The position of SRBF, i.e. $(\phi_k, \lambda_k, k = 1, ..., K)$, is a remarkable issue to be considered. This can be determined along with other unknowns which results in non-linear parametrization. An alternative way is to assume a set of fixed positions for the base functions. As mentioned in section 4.2.4, we follow the latter method to maintain the linearity of the observation equations. Therefore a set of predefined grid points will be used to locate the base functions. Our calculations show, that the use of different grid points does not affect the quality of the regional solutions, provided that the grid points are distributed homogeneously (see 6.2.2). It only affects the regularization process and the resulting regularization parameter. Therefore if the regularization is performed correctly, the type of grid points is not a big concern in regional gravity field modelling. To show this numerically, we use two different homogeneous point distributions on the sphere; the Reuter grid and the Fibonacci grid. While the former gives equal-distant spacing, the latter results in equal areas on the surface of the sphere. The mathematical formulation of these two grid points are given in section 4.2.4. Since the regional modelling using these two grids are almost the same, the Fibonacci grid will be discussed only in section 6.2.2 to avoid repetition.

6.2 Regional gravity field modelling based on GRACE-type simulation

In this section, the performance of regional gravity field modelling will be checked based on the data from a GRACE-like satellite mission. To have enough control over observation and model errors, the modelling is done in a (pseudo) closed-loop simulation. In the first step, the potential differences between a pair of satellites along GRACE-type orbits are synthesized using a global gravity field model. Furthermore, a realistic noise model (white and coloured) is generated and added to the potential differences along the orbit.
Regional solutions are determined in the test regions using several regularization methods. The results will be then compared to the input gravity field in the test regions. We assess the quality of the regional solutions based on the RMS values of the reconstructed gravity fields on the Earth's surface with respect to the input field. In addition, a global gravity field solution using spherical harmonics is determined based on the same simulated potential differences. Therefore the regional solutions can be directly compared to a global solution of the same resolution. Figure 6.2 shows the simulation scheme used in this section.

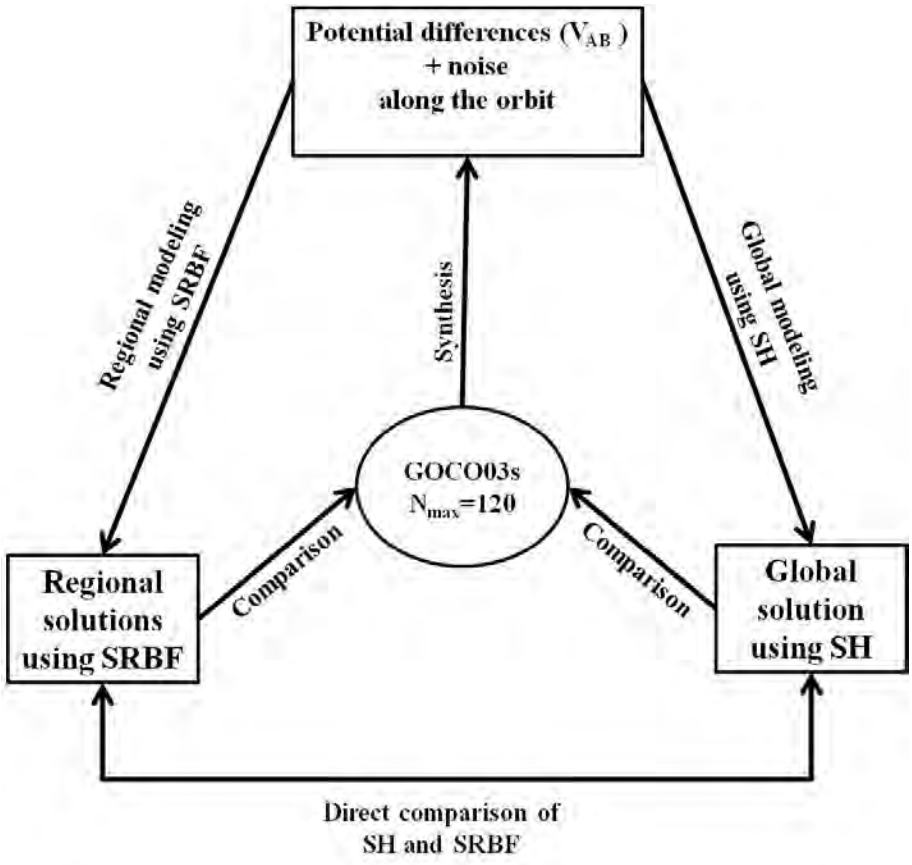

Figure 6.2: Simulation scenario used to assess the performance of regional gravity field solution based on satellite data. Several regional solutions in the test areas will be determined using SRBF to compare different choices for the regularization. Furthermore, a global gravity field using spherical harmonics will also be determined which makes it possible to directly compare the regional solutions to the global solution.

6.2.1 Simulated data and noise

The simulated observations consist of synthesized potential differences V_{AB} between satellites A and B. The simulation scenario is the same as described in 3.3.2. The only difference is that here the maximum degree of expansion in the synthesis is equal to $N_{max} = 120$. This value matches the expected baseline resolution of GRACE monthly solutions.

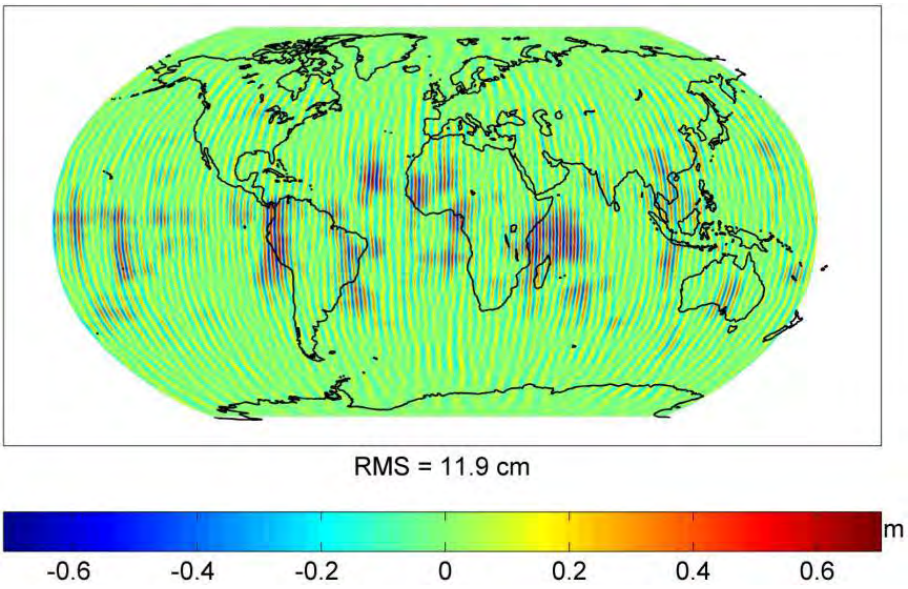

Figure 6.3: The geoid differences between the estimated global model using SH and the model GOCO03s which is considered as the truth. The global RMS value is about $12\,\mathrm{cm}$ with the largest values near equatorial areas. The test regions Scandinavia, Central Africa and South America along the Andes are also shown in the map. The regional RMS values in these regions are 5.8, 21.7 and $22.7\,\mathrm{cm}$, respectively.

Based on this data set, a global gravity field model, using spherical harmonics is determined up to degree and order $N_{max} = 120$. Using this model, the gravity field will be synthesized in the test regions and the RMS values will be calculated with respect to the true model GOCO03s. This gives an insight into the error budget in each region when spherical harmonics are used in modelling. Therefore, the regional solutions using SRBF can be directly compared to the spherical harmonic solution of an equivalent resolution. The number of unknown SH coefficients is $K = (120+1)^2 - 3$ or 14638 since the harmonics of degree zero and one are excluded. The normal matrix therefore, has the size of 14638×14638 with the condition number of about 4.8×10^7. The covariance matrix of observations is assumed to be diagonal as if no information about the coloured noise is available. The solution is estimated using equation (3.36) with no regularization.
Figure 6.3 shows the geoid differences between the estimated global model and GOCO03s which is considered as the truth. As it can be seen, the largest deviations occur near equator where the satellite data are rather sparse. The global RMS value for the geoid differences is $11.9\,\mathrm{cm}$. The geoid differences in the test regions, Scandinavia, Central Africa and South America along the Andes, which are displayed in the figure, are 5.8, 21.7 and $22.7\,\mathrm{cm}$, respectively. In the following section, the regional solutions in the test regions shall be obtained using SRBF with confinement of the data and base functions to the region boundaries. Compared to the global spherical harmonic analysis, the number of data and base functions used in these test regions will be approximately reduced by about 90%. Yet, equivalent or better solutions are expected on the regional scales using SRBF. It should also be mentioned that the coloured noise generated for the global data set will be used for regional solutions as well. Thus, the global solution and the following regional solutions are affected by the same realization of coloured noise.

6.2.2 Regional solutions in Central Africa

The model zone in Central Africa is shown in figures 6.1 and 6.3. It is extended symmetrically around the equator where the sampling of satellite data is less dense. The scope of gravity field modelling in this area is to investigate the performance of SRBF in equatorial regions. The noisy data used for gravity field modelling in this region are taken from the simulated global data, described in section 6.2.1. The potential differences up to degree and order 30 are synthesized and subtracted from the simulated data, since the long wavelengths

of the gravitational potential cannot be modelled on regional scales. Therefore the observations contain the frequencies between degree 30 and 120, in terms of spherical harmonics. Figure 6.4 shows the geoid heights between degree 30 and 120 in Central Africa synthesized using the true model GOCO03s. Therefore, the goal is to model this field using SRBF as precise as possible. The difference between the model GOCO03s and the global SH model described in previous section, is also shown in figure 6.4 in terms of geoid heights. The geoid RMS in this region is about $22\,\mathrm{cm}$ with sharp stripes in the edges of the region.

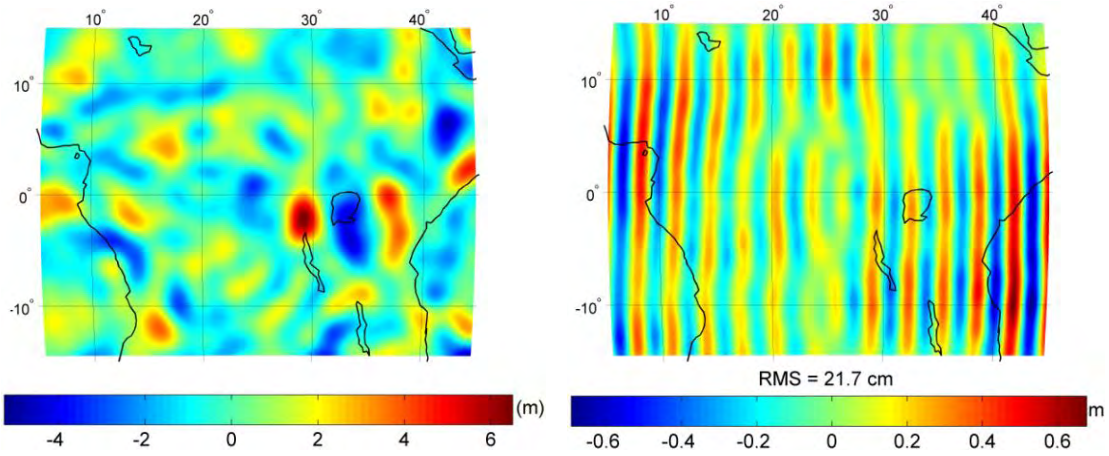

Figure 6.4: **Left**: Geoid heights in Central Africa, between degrees 30 and 120, synthesized using the global model GOCO03s. The maximum and minimum values within this region are about 6.5 and $-5.2\,\mathrm{m}$ respectively. **Right**: The geoid difference, in Central Africa, between GOCO03s and the spherical harmonic model based on the simulated data explained in section 6.2.1. The geoid RMS is $21.7\,\mathrm{cm}$ in this region.

As explained in chapter 4, the bounds of the data and grid zones should be defined appropriately. This is due to the edge effects caused by confinement of data and base functions to a region. For the extension of the data zone, equations (4.18) is used with $N_{min} = 30$, $\phi_m = 0^\circ$ and $h = 500$ km. Therefore the data zone for Central Africa will be extended 6° beyond the model zone. The total number of observations within the data zone will be about 16700 which is 3% of the total observations on the global scale. Furthermore, the grid extension is set to be 5°. The number of unknowns inside the grid zone depends on the type of grid points used for the distribution of the base functions. Since we use the Reuter and Fibonacci grids which are homogeneous grids the number of base functions differ very slightly and is around 1400. Compared to about 14000 SH on the global scale, the number of unknowns is reduced by 90%. Finally, the SRBF with $N_{max} = 130$ and with the Shannon kernel are used for the inversion of the simulated data. Figure 6.5 shows the boundaries of the model, the data and the grid zones for regional modelling in Central Africa.

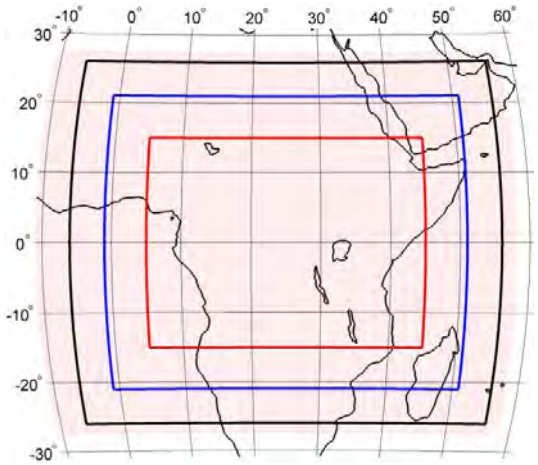

Figure 6.5: The model zone (red) ,the data zone (blue) and the grid zone (black) for the regional gravity field solution in Central Africa. The data zone is extended 6° beyond the model zone and the grid zone is extended 5° beyond the data zone.

Based on this setup, the corresponding design and normal matrices are computed. The condition number of the normal matrix is about 9.9×10^{18} which reveals a strong ill-posedness as expected. As proposed in section 5.7, one can use equations (5.77) or (5.88) to evaluate an initial value for the regularization parameter. For this region, these values will be about 3×10^{23} and 1.3×10^{23} using (5.77) and (5.88), respectively. This shows that these two methods lead, more or less, to the same values. We set the initial value equal to 2×10^{23} and search for the optimal regularization parameter in the neighbourhood of this value with radius of 10^2. The summary of the model setup for regional gravity field modelling in this region is given in table 6.1.
According to the set-up mentioned in the table 6.1, two groups of solutions are obtained using the Reuter and Fibonacci grids. Each group consists of four different solutions based on four different parameter choice methods for regularization. All solutions are obtained using the following relation:

$$\hat{\mathbf{x}} = (\mathbf{A}^T\mathbf{P}_\mathbf{l}\mathbf{A} + \gamma^2\mathbf{I})^{-1}\mathbf{A}^T\mathbf{P}_\mathbf{l}\delta\mathbf{l}. \tag{6.1}$$

The only difference between the solutions is the criterion used to choose γ^2. These criteria (explained in section 5.5) are: The variance component estimation (VCE), the generalized cross validation (GCV), the L-curve analysis and the proposed parameter-signal correlation (PSC). The weight matrix $\mathbf{P}_\mathbf{l}$ is assumed to be a diagonal matrix. In other words, we assume that the observation noise is white because there is no information available about the colour of noise in real-life experiments. The reduced observation vector $\delta\mathbf{l}$ is obtained using (4.12) where the long wavelengths up to degree 30 are subtracted. Therefore the solution $\hat{\mathbf{x}}$ shall be used to represent the gravitational potential (and other functionals) between frequencies 30 and 120. To compare the solutions and judge their quality, we use the three conditions explained at the end of section 5.9. Thus, the residuals at orbit altitude, the residuals on the Earth's surface and the correlation between the estimated coefficients and a reference field shall be considered.
The summary of the results for the regional solutions in Central Africa using the Reuter grid is given in table 6.2. The results for the same solutions but using Fibonacci grid is given in table 6.3. As it can be seen, in all cases, the RMS values at orbit level are closely the same. The statistical test on the a posteriori variance factor $\hat{\sigma_0^2}$ are also passed in all cases. This means that all parameter choice methods can provide good results when no downward continuation is included. Nevertheless, the results are very different when the solutions are to be compared on ground level. The proposed PSC method, gives the best results compared to other regularization methods. The L-curve analysis provides rather the same results as the PSC with slightly larger RMS values for the reconstructed fields on the Earth's surface. On the other hand, the VCE and GCV approaches result in significantly different RMS values on the Earth's surface. This is also clear by comparing the regularization parameters. While VCE and GCV methods give parameters in the order of 10^{21}, the regularization parameters

Model specification	Remarks
Geographical limits	the model zone: $-15^\circ \leq \phi \leq 15^\circ,\ 5^\circ \leq \lambda \leq 45^\circ$
	the data zone: $-21^\circ \leq \phi \leq 21^\circ,\ -1^\circ \leq \lambda \leq 51^\circ$
	the grid zone: $-26^\circ \leq \phi \leq 26^\circ,\ -6^\circ \leq \lambda \leq 56^\circ$
Observations	observation type: potential difference at orbit altitude
	frequency content: above 30 (SH)
	number of observations: $I = 16728$
	standard deviation: $2 \times 10^{-3}\,\mathrm{m^2/s^2}$
	weight matrix: $\mathbf{P_l} = (2 \times 10^{-3}\,\mathrm{m^2/s^2})^{-2} \times \mathbf{I}$
	the a priori variance factor: $\sigma_0^2 = 1$
The base functions	type of SRBF: Shannon ($N_{max} = 130$)
	number of base functions: $K = 1389$
The normal matrix $\mathbf{N}$	size: 1389×1389
	condition number: 9.9×10^{18}
	largest singular value: $s_1^2 = \|\mathbf{N}\| = 2.9 \times 10^{28}$
Initial regularization parameter	using (5.77): $\gamma^2 = 3.2 \times 10^{23}$
	using (5.88): $\gamma^2 = 1.3 \times 10^{23}$

Table 6.1: Specifications of the regional modelling in Central Africa. The number of unknowns is in fact the number of grid points. In this table, 1389 refers to the number of points on the Reuter grid. For the Fibonacci grid, this number is 1380.

for the L-curve and the PSC methods are one and two orders of magnitude larger. Obviously the VCE and GCV methods do not provide sufficient regularization for regional gravity field modelling based on satellite data. If the regional modelling based on terrestrial or airborne data (with no considerable downward continuation) were desired, these methods could be satisfactory. The L-curve method requires a compromise between the minimization of the post-fit residuals and the norm of the solution. Similarly, the PSC method enforces the solution to have the expected geometry by correlating the coefficients with a background model[1]. That is why the correlation between the coefficients and the signal is maximum (97.7%) in case of the PSC method and is nearly followed by the L-curve analysis with (97.3%). This correlation for the VCE and GCV methods is about 10% less and amounts to 91% and 87% respectively.
Figure 6.6 shows the estimated coefficients obtained from the PSC regularization approach[2]. It can be compared to the regional geoid shown in figure 6.4. As it can be seen, the coefficients reveal the general shape of the geoid (between frequencies 30 and 120).

[1]For the numerical computations in this chapter, we used the model EGM2008 to evaluate the potential values dV_k at grid locations. See Table 5.1 for more details.

[2]For a better visualization, the coefficients are interpolated to a dense regular grid with cell size of $0.1^\circ \times 0.1^\circ$

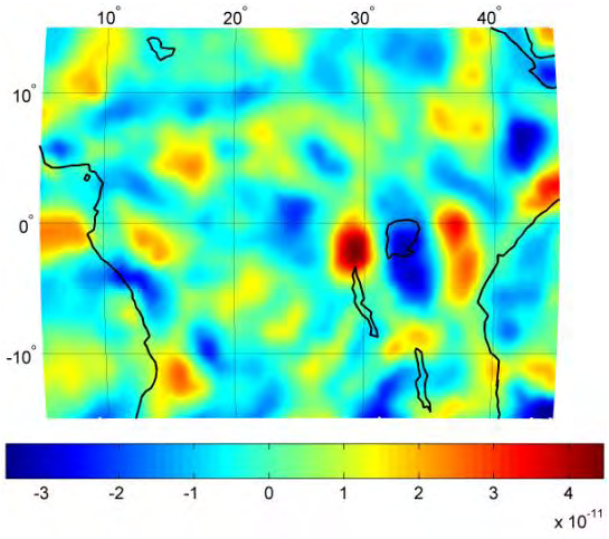

Figure 6.6: The dimensionless estimated coefficients obtained from the PSC regularization approach. For better illustration, the coefficients are interpolated on a dense regular grid with cell size of $0.1^\circ \times 0.1^\circ$. The coefficients show the general shape of geoid shown in figure 6.4. The correlation coefficient is about 97.7%.

To assess the quality of the solutions in terms of residuals on the Earth's surface, the geoid heights are synthesized using the estimated coefficients and a set of SRBF with the Shannon kernel. Figure 6.7 illustrates the geoid differences between the regional solutions and the geopotential model GOCO03s. The solutions obtained using the Reuter grid and from four different approaches for the choice of the regularization parameter. The same group of solutions but using the Fibonacci grid is shown in figure 6.8.

Summary and concluding remarks for regional solutions in Central Africa

Eight regional solutions were determined in Central Africa using four different regularization methods and two types of grid points. The results of the solutions and the conclusion after comparisons can be summarized as follows:

- Among the four solutions using different parameter choice methods for each grid type, the PSC gives the best results with the least geoid RMS. The L-curve analysis also provides a rather promising solution with a geoid RMS slightly more than the PSC. The VCE and GCV methods, have RMS values about 3 times larger than PSC and L-curve.

- The results obtained from the Fibonacci grid are almost the same as the Reuter grid. No significant differences are seen when the two grids are compared. Hence these two grid points (and other grid types with homogeneous point distribution) can be used alternatively. In the following sections, the Fibonacci grid will not be considered for brevity.

- All solutions can be compared to the global spherical harmonic solution shown in figure 6.4 (left). The SH solution gives a geoid RMS of about $21.7\,\mathrm{cm}$ in Central Africa which is comparable to the regional solutions obtained from the VCE and GCV methods. On the other hand, the L-curve with geoid RMS of $13\,\mathrm{cm}$ and, in particular, the PSC methods with geoid RMS of $10\,\mathrm{cm}$ provide much better results with much less stripes compared to the global SH solution. The results also indicate that the north-south GRACE stripes are significantly reduced as a result of using the PSC method.

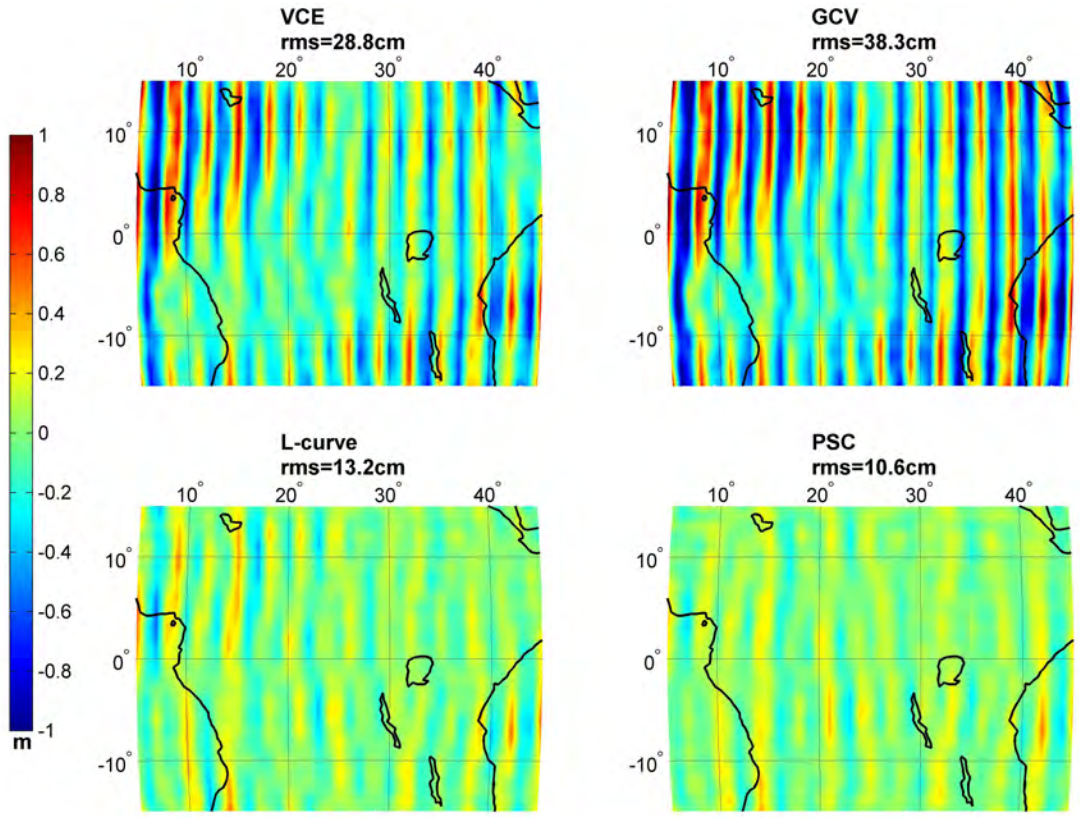

Figure 6.7: Geoid differences between the global model GOCO03s and regional solutions in Central Africa using four different regularization methods: the variance component estimation (top-left), the generalized cross validation (top-right), the L-curve analysis (bottom-left) and the proposed PSC (bottom-right). The best regional geoid RMS is obtained using PSC. The L-curve analysis gives slightly more RMS. The VCE and GCV methods yield significantly larger geoid RMS. These solutions are obtained using the Reuter grid.

Regularization method	γ^2	RMS (orbit, $\mathrm{m}^2/\mathrm{s}^2$)	RMS (Earth's surface, cm)	test on $\hat{\sigma}_0^2(95\%)$	correlation of signal and parameters
VCE	2.417×10^{21}	0.0016	28.8	passed	91.9%
GCV	7.948×10^{20}	0.0016	38.8	passed	87.5%
L-curve	5.084×10^{22}	0.0017	13.2	passed	97.3%
PSC	2.129×10^{23}	0.0018	10.6	passed	97.7%

Table 6.2: Summary of the regional solutions in Central Africa and their quality measures. The solutions are obtained using the Reuter grid. The best results are obtained using the proposed parameter-signal correlation method where all three quality measures are satisfactory. The L-curve method provides also satisfactory results which are only slightly different from the PSC method.

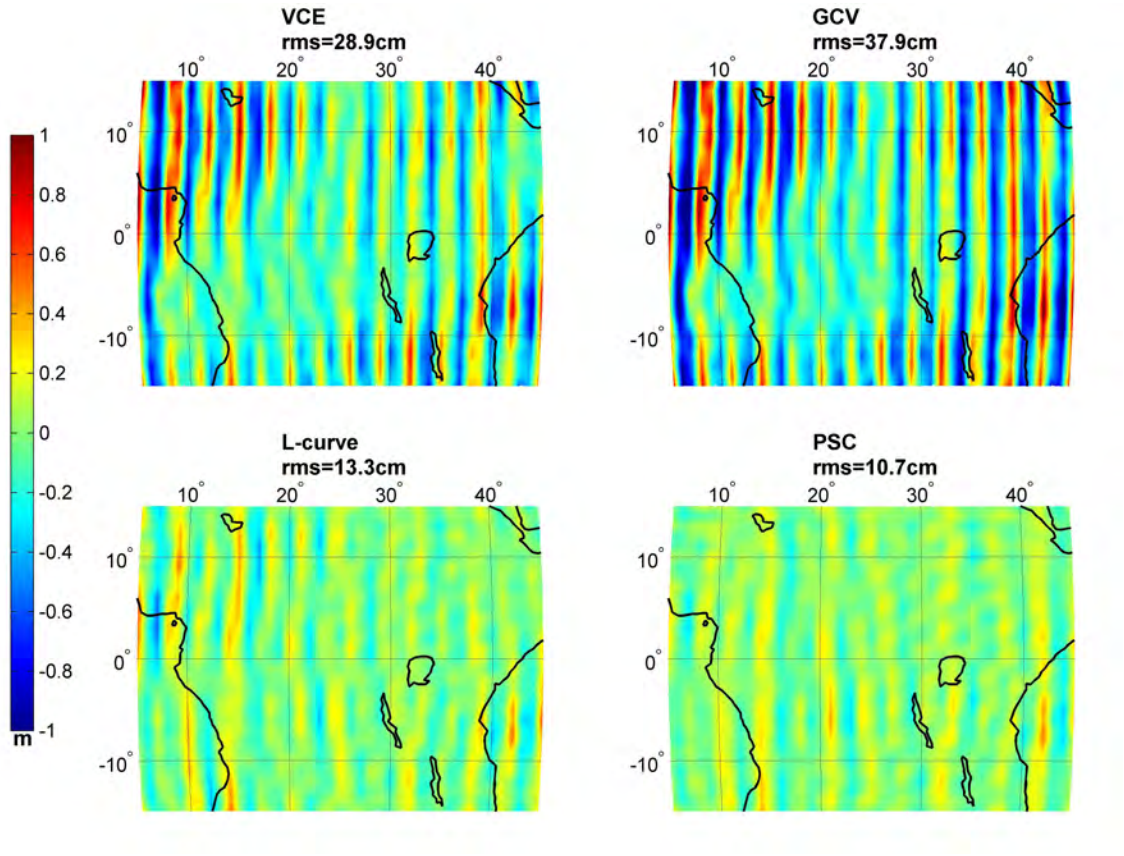

Figure 6.8: The geoid differences between the global model GOCO03s and the regional solutions in Central Africa using four different regularization methods: the variance component estimation (top-left), the generalized cross validation (top-right), the L-curve analysis (bottom-left) and the proposed PSC (bottom-right). The best regional geoid RMS is obtained using PSC method. The L-curve analysis gives slightly more geoid RMS. The VCE and GCV methods yield significantly larger geoid RMS. These solutions are obtained using the Fibonacci grid.

Regularization method	γ^2	RMS (orbit, $\mathrm{m}^2/\mathrm{s}^2$)	RMS (Earth's surface, cm)	test on $\hat{\sigma}_0^2(95\%)$	correlation of signal and parameters
VCE	2.354×10^{21}	0.0016	28.9	passed	91.6%
GCV	7.937×10^{20}	0.0016	37.9	passed	87.2%
L-curve	5.078×10^{22}	0.0017	13.3	passed	97.1%
PSC	2.558×10^{23}	0.0018	10.7	passed	97.5%

Table 6.3: Summary of the solutions in Central Africa and their quality measures. The solutions are obtained using the Fibonacci grid. The best results are obtained using the proposed PSC method where all three quality measures are satisfactory.

6.2.3 Regional solutions in Scandinavia

To consider the performance of regional gravity field modelling as well as different regularization methods, the regional modelling should be checked under different conditions and test areas. In this section, the procedure explained in the previous section for Central Africa will be repeated for Scandinavia. The main reason to choose this area is its high latitude. In such areas, the satellite missions such as GRACE, GOCE and GRACE Follow-on collect more observation so that the sampling is rather dense.
The desired model zone in Scandinavia is shown in figures 6.1 and 6.3 with geographical bounds $50^\circ \leq \phi \leq 75^\circ$ and $0^\circ \leq \lambda \leq 50^\circ$. The description of the simulated data set and imposed noise is the same as explained in previous section. The geoid in Scandinavia between frequencies 30 and 120, in terms of spherical harmonics, is the target field to be modelled using SRBF. This field is shown in figure 6.9 (left) which is synthesized using the global model GOCO03s. In this region the geoid varies approximately from -4 to 5 m (the frequencies less than $n = 30$ are subtracted). Furthermore, the geoid difference between GOCO03s and the SH model determined in section 6.2.1 is also shown in this figure. The total RMS is about $6\,\mathrm{cm}$ with large stripes in the southern part of the area.

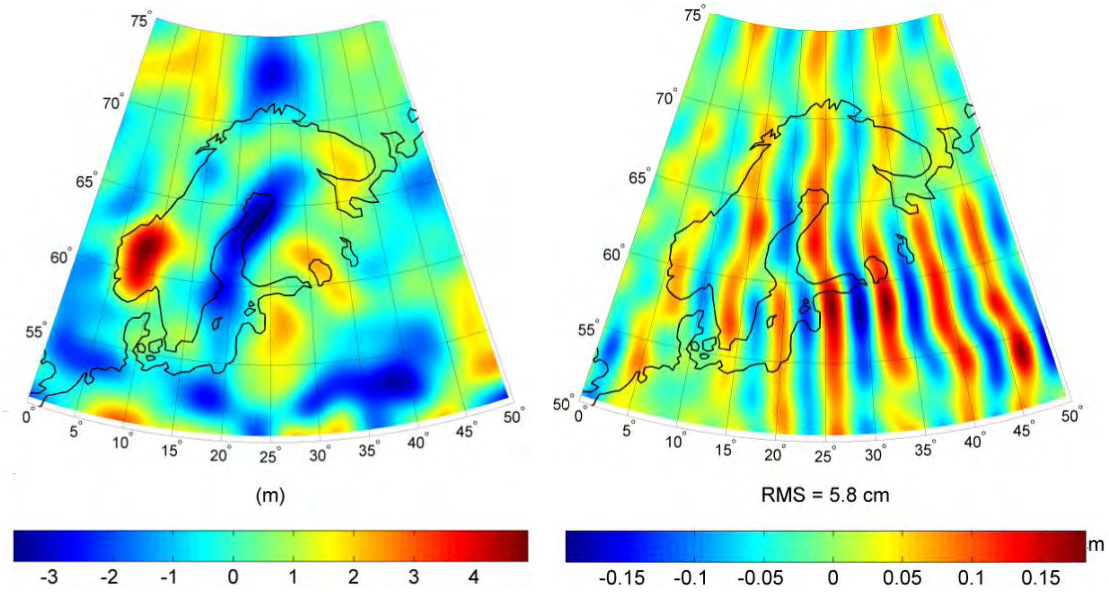

Figure 6.9: **Left**: Geoid heights in Scandinavia, between degrees 30 and 120 synthesized using the global model GOCO03s. The maximum and minimum values within this region are about $4.8\,\mathrm{m}$ and $-3.6\,\mathrm{m}$, respectively. **Right**: The geoid differences in Scandinavia between GOCO03s and the spherical harmonic model based on the simulated data explained in section 6.2.1. The geoid RMS is about $6\,\mathrm{cm}$ in this region. The north-south GRACE stripes are also visible especially in the southern part of the region.

To model this regional field based on the simulated data and using SRBF, the boundaries of the data and the grid zone have to be defined. Similar to the definition of these zones in Central Africa, the extension of data and grid zones are equal to 6° and 5°, respectively. These three zones in Scandinavia are illustrated in figure 6.10.

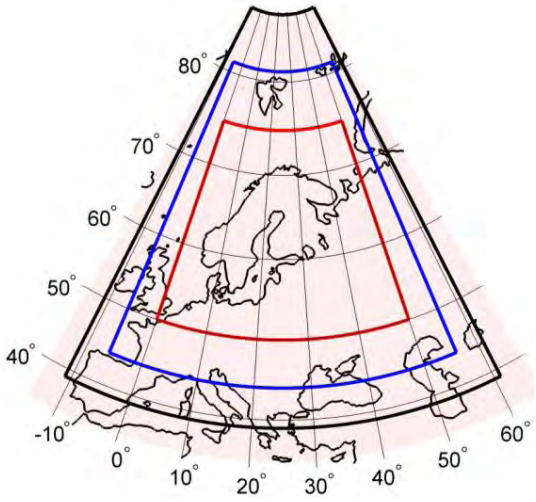

Figure 6.10: The model zone (red), the data zone (blue) and the grid zone (red) for regional modelling in Scandinavia. The grid and data zones are extended by 6° and 5° beyond the model and data zones, respectively.

The number of observations inside the data zone is about 25800 with a total number of over 1130 base functions (grid points). The summary of the observation equations as well as the model characteristics is given in table 6.4.

Model specification	Remarks
Geographical limits	the model zone: $50^\circ \leq \phi \leq 75^\circ,\ \ 0^\circ \leq \lambda \leq 50^\circ$
	the data zone: $44^\circ \leq \phi \leq 81^\circ,\ \ -6^\circ \leq \lambda \leq 56^\circ$
	the grid zone: $39^\circ \leq \phi \leq 86^\circ,\ \ -11^\circ \leq \lambda \leq 61^\circ$
Observations	observation type: potential differences at orbit altitude
	frequency content: above 30 (SH)
	number of observations: $I = 25830$
	standard deviation: $2 \times 10^{-3}\,\mathrm{m^2/s^2}$
	weight matrix: $\mathbf{P_l} = (2 \times 10^{-3}\,\mathrm{m^2/s^2})^{-2} \times \mathbf{I}$
	the a priori variance factor: $\sigma_0^2 = 1$
The base functions	type of SRBF: Shannon ($N_{max} = 130$)
	number of base functions: $K = 1136$
The normal matrix $\mathbf{N}$	size: 1136×1136
	condition number: 1.5×10^{19}
	largest singular value: $s_1^2 = \|\mathbf{N}\| = 9.8 \times 10^{28}$
Initial regularization parameter	using (5.77): $\gamma^2 = 1.1 \times 10^{25}$
	using (5.88): $\gamma^2 = 4.4 \times 10^{23}$

Table 6.4: Specifications of the regional modelling in Scandinavia. The number of unknowns which is in fact the number of grid points is 1136 in this table. This number refers to the number of points on the Reuter grid.

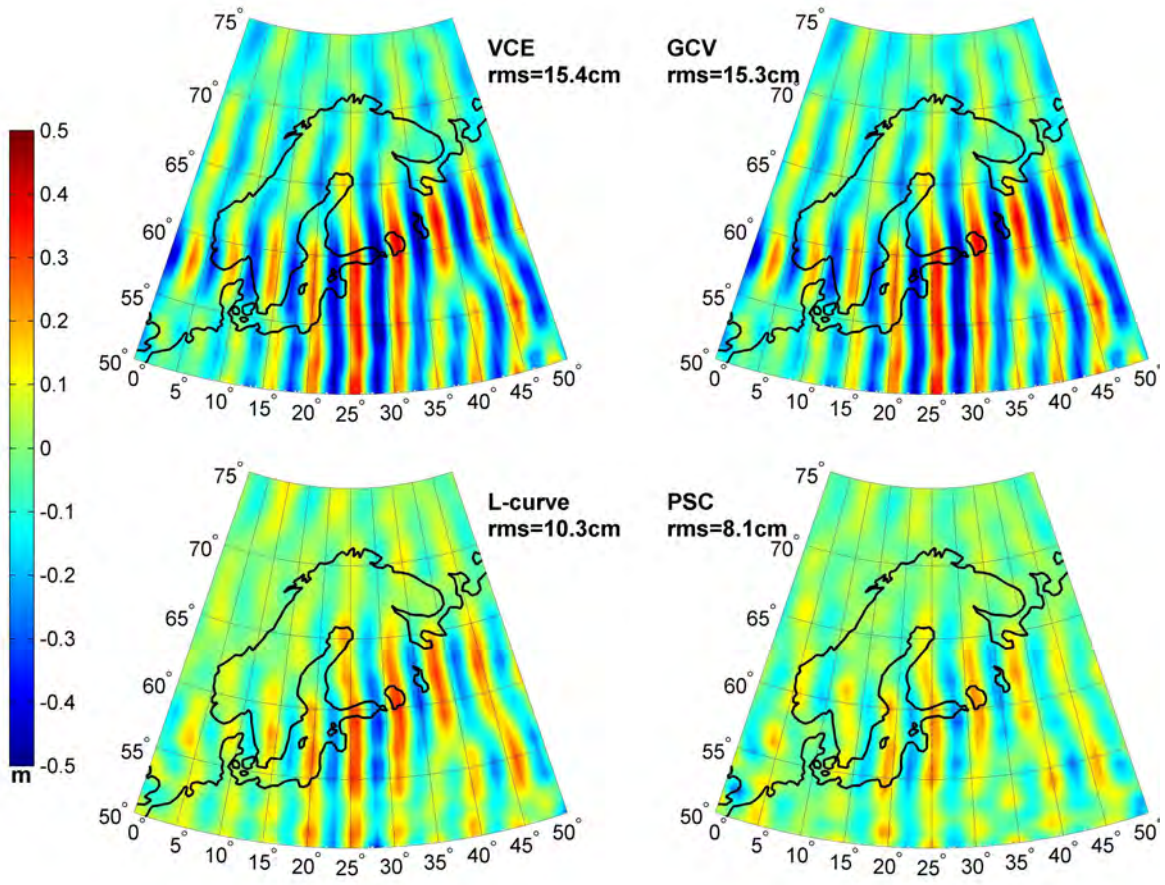

Figure 6.11: The geoid differences between the global model GOCO03s and the regional solutions in Scandinavia using four different regularization methods: the variance component estimation (top-left), the generalized cross validation (top-right), the L-curve analysis (bottom-left) and the proposed PSC (bottom-right). The best regional RMS is obtained using the PSC method. The L-curve gives slightly more geoid RMS. The VCE and GCV methods yield significantly larger RMS. These solutions are obtained using the Reuter grid.

Regularization method	γ^2	RMS (orbit, $\mathrm{m}^2/\mathrm{s}^2$)	RMS (Earth's surface, cm)	test on $\hat{\sigma}_0^2(95\%)$	correlation of signal and parameters
VCE	2.426×10^{21}	1.8×10^{-3}	15.4	passed	95.2%
GCV	2.606×10^{21}	1.8×10^{-3}	15.3	passed	95.2%
L-curve	1.003×10^{23}	1.8×10^{-3}	10.3	passed	96.0%
PSC	4.608×10^{23}	2×10^{-3}	8.1	passed	96.2%

Table 6.5: Summary of the regional solutions in Scandinavia with their quality measures. The solutions are obtained using the Reuter grid. The best results are obtained using the proposed parameter-signal correlation method where all three quality measures are satisfactory. The L-curve method provides also satisfactory results which are just slightly different from the PSC method.

Finally, the solutions are obtained using equation (6.1) and four methods for the choice of the regularization parameter. The results of the solutions for the Reuter grid are given in table 6.5. It can be evidently seen that all solutions pass the statistical tests at the observation level. That is, the test on the a posteriori variance factor is

passed in all cases and the post fit residuals at orbit level have more or less the same RMS values. On the other hand, the geoid RMS on ground level are different. The VCE and GCV methods provide almost the same geoid RMS values. It is about $15\,\mathrm{cm}$ which, for these two methods, is significantly improved compared to the regional solutions in Central Africa. The reason is the availability of more observations in high-latitude regions such as Scandinavia. The L-curve analysis and the PSC methods result in less geoid RMS on ground level which is about $10\,\mathrm{cm}$ and $8\,\mathrm{cm}$, respectively. The geoid differences on the Earth's surface using different regularization approaches are shown in figures 6.11. Due to the similarity of the results obtained from the Reuter and the Fibonacci grids, the results of the Fibonacci grid are not shown anymore.
The estimated scaling coefficients are displayed in figure 6.12. The estimated coefficients explicitly reveal the shape of geoid heights above $n = 30$ (c.f. figure 6.9).

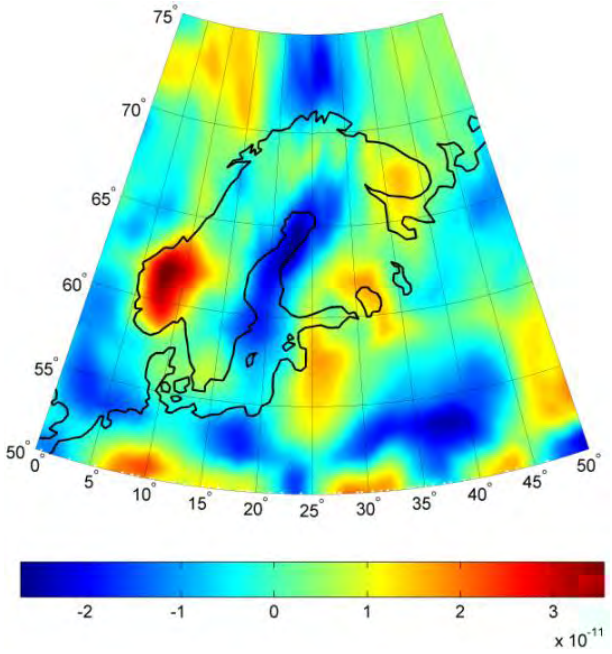

Figure 6.12: The dimensionless estimated coefficients obtained from the PSC regularization approach. For better illustration, the coefficients are interpolated on a dense regular grid with a cell size of $0.1^\circ \times 0.1^\circ$. The coefficients reveal the general shape of the geoid shown in figure 6.9. The correlation coefficient is about 96.2%.

Summary and concluding remarks for the regional solutions in Scandinavia

In Scandinavia, four regional solutions were determined based on simulated GRACE-type observations using SRBF. The solutions are obtained using four different methods for the choice of the regularization parameter. The results of modelling and comparisons can be summarized as follows:

- Among the regularization methods, the PSC method results in the least geoid RMS values and give the most promising solution. The L-curve analysis leads to nearly the same results compared to the PSC method. The VCE and GCV give rather the same geoid RMS values but considerably larger than the first two methods.
- Compared to the regional solutions in Central Africa, the solutions in Scandinavia have less geoid RMS values. This is due to the fact that more observations are available in this region according to its high latitude.
- All regional solutions give larger geoid RMS compared to the global SH solution. Only the PSC method provides approximately the same geoid RMS ($8\,\mathrm{cm}$) compared to the global solution using spherical harmonics ($6\,\mathrm{cm}$).

- It can be concluded that in high-latitude regions, spherical harmonics perform optimally. Nevertheless, the regional solution which is regularized using the PSC method can provide a comparable accuracy with much less computational burden. This is a great advantage especially if more data than a month are included.

6.2.4 Regional solutions in South America

The last test area for the investigation of the regional gravity field solution, is South America along the Andes. In this area, the gravity field is very rough and has significant spatial changes across the mountain chains in east-west direction. The maximum and minimum values of the geoid are about -14 and $11\,\mathrm{m}$, respectively (between SH frequencies 30 and 120). This rather big changes occur within a few hundred kilometres. In addition, the world's largest volcanoes are in this region which makes it an interesting area for geophysical and geological studies. Thus, this region can be considered as a challenging test area for regional gravity field modelling from satellite data.

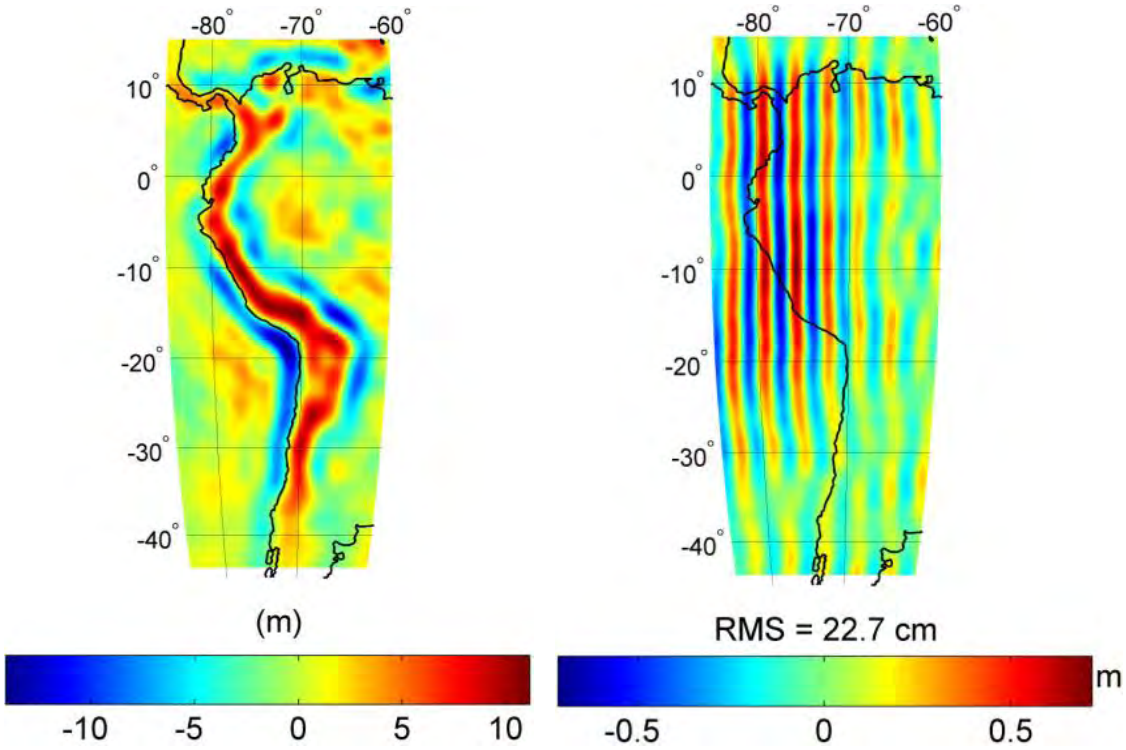

Figure 6.13: **Left**: Geoid heights in South America along the Andes, between degrees 30 and 120, synthesized using the global model GOCO03s. The maximum and minimum values within this region are about 11.1 and $-14.1\,\mathrm{m}$ respectively. **Right**: The geoid difference, in South America, between the model GOCO03s and the spherical harmonic model based on the simulated data explained in section 6.2.1. The geoid RMS is about $23\,\mathrm{cm}$ in this region. The north-south GRACE stripes are also visible especially in the west part of the region.

The model zone in this region is shown in figures 6.1 and 6.3 with geographical bounds $-45^\circ \leq \phi \leq 15^\circ$ and $-85^\circ \leq \lambda \leq -60^\circ$. The description of the simulated data set and imposed noise is the same as explained in previous sections. The geoid in the Andes, between frequencies 30 and 120, is to be modelled in this region using SRBF. This field is shown in figure 6.13 (left) which is synthesized using the global model GOCO03s. Furthermore, the geoid difference between GOCO03s and the SH model determined in section 6.2.1 is also shown in this figure. The total RMS in this region is about $23\,\mathrm{cm}$ with large stripes in the west of the area. The boundaries of the data and grid zones are defined similar to the definition of these zones in Central Africa and Scandinavia with the extension of 6° and 5°. These three zones in the Andes are illustrated in figure 6.14.

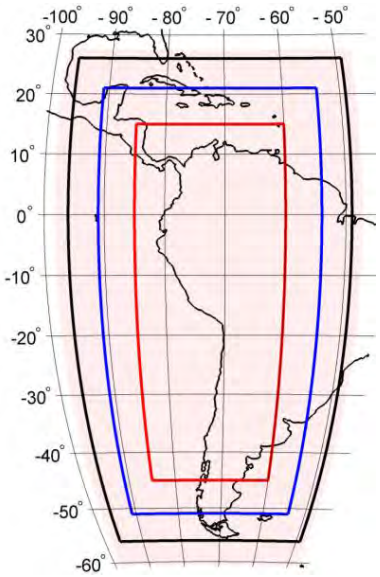

Figure 6.14: The model zone (red), the data zone (blue) and the grid zone (red) for regional modelling in South America along the Andes. The grid and data zones are extended 6° and 5° beyond the model and data zones, respectively.

The description of observation equations and the model setup is given in table 6.6.

Model specification	Remarks
Geographical limits	the model zone: $-45^\circ \leq \phi \leq 15^\circ, \quad -85^\circ \leq \lambda \leq -60^\circ$
	the data zone: $-51^\circ \leq \phi \leq 21^\circ, \quad -91^\circ \leq \lambda \leq -54^\circ$
	the grid zone: $-56^\circ \leq \phi \leq 26^\circ, \quad -96^\circ \leq \lambda \leq -49^\circ$
Observations	observation type: potential differences at orbit altitude
	frequency content: above 30 (SH)
	number of observations: $I = 20532$
	standard deviation: $2 \times 10^{-3}\,\mathrm{m^2/s^2}$
	weight matrix: $\mathbf{P_l} = (2 \times 10^{-3}\,\mathrm{m^2/s^2})^{-2} \times \mathbf{I}$
	the a priori variance factor: $\sigma_0^2 = 1$
The base functions	type of SRBF: Shannon ($N_{max} = 130$)
	number of base functions: $K = 1520$
The normal matrix $\mathbf{N}$	size: 1520×1520
	condition number: 8.9×10^{18}
	largest singular value: $s_1^2 = \|\mathbf{N}\| = 3.4 \times 10^{28}$
Initial regularization parameter	using (5.77): $\gamma^2 = 4.3 \times 10^{23}$
	using (5.88): $\gamma^2 = 1.5 \times 10^{23}$

Table 6.6: Specifications of the regional modelling in South America along the Andes. The number of unknowns or the number of grid points is 1520 in this table. This number refers to the number of points on the Reuter grid.

The solutions are obtained using equation (6.1) and four different regularization parameters. The results are very similar to those obtained in Central Africa. The proposed PSC method results in the most promising solution compared to other approaches for the choice of the regularization parameters. Figure 6.15 shows the estimated coefficients obtained from the PSC regularization approach. It can be compared to the regional geoid shown in figure 6.13. As it can be seen, the coefficients reveal the general shape of the geoid (between frequencies 30 and 120).

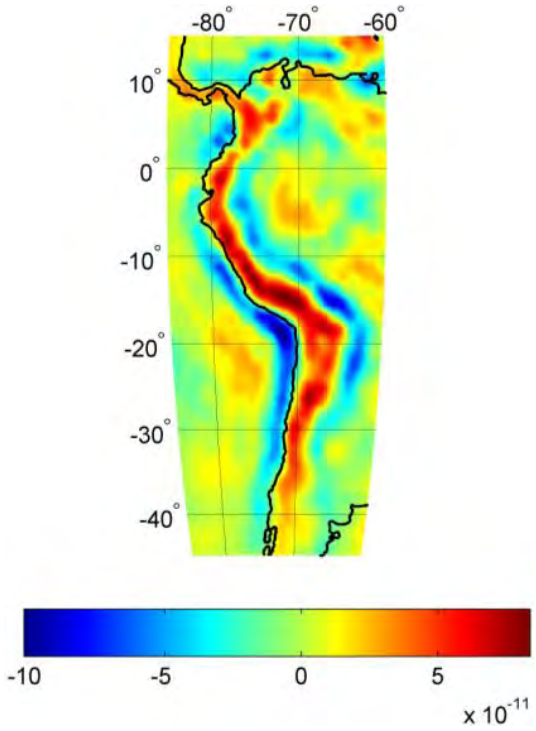

Figure 6.15: The dimensionless estimated coefficients obtained from the PSC regularization approach. For better illustration, the coefficients are interpolated on a dense regular grid with cell size of $0.1^\circ \times 0.1^\circ$. The coefficients reveal the general shape of the geoid shown in figure 6.13. The correlation coefficient is about 96.9%.

The results of regional modelling in South America along the Andes on the Reuter grid is given in table 6.7. The same calculations were performed using the Fibonacci grid (results not shown here) which led to the same numerical results with no statistically significant differences. This indicates that as long as the distribution of grid points is homogeneous enough, the type of grid is not a great concern and does not affect the quality of regional solutions. Furthermore, the geoid differences between the regional solutions and the global model GOCO03s are shown in figures 6.16 for the Reuter grid. As it can be seen, the best results are obtained using the PSC method followed by the L-curve analysis. The geoid RMS values for the GCV and the VCE are nearly the same but still far from the results obtained using the PSC and L-curve analysis.

Regularization method	γ^2	RMS (orbit, $\mathrm{m}^2/\mathrm{s}^2$)	RMS (Earth's surface, cm)	test on $\hat{\sigma}_0^2(95\%)$	correlation of signal and parameters
VCE	9.945×10^{20}	0.0016	45.3	passed	94.6%
GCV	9.152×10^{20}	0.0016	46	passed	94.5%
L-curve	1.844×10^{22}	0.0016	25.4	passed	96.6%
PSC	8.875×10^{22}	0.0017	19.7	passed	96.9%

Table 6.7: Summary of the regional solutions in the Andes with their quality measures. The solutions are obtained using the Reuter grid. The best results are obtained using the proposed parameter-signal correlation method where all three quality measures are satisfactory. The L-curve method provides also satisfactory results which are slightly different from the PSC method.

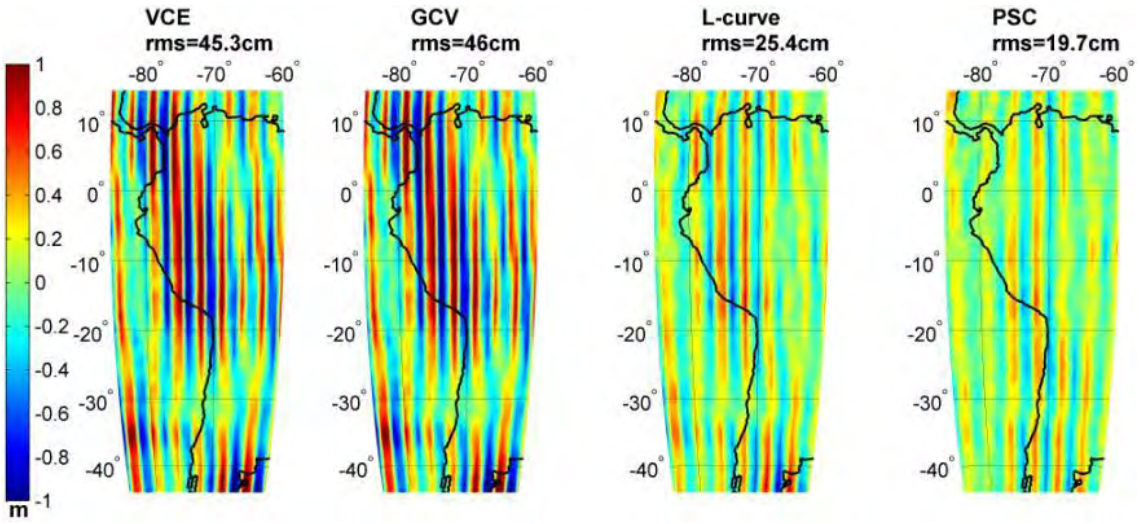

Figure 6.16: The geoid differences between the global model GOCO03s and the regional solutions in South America using four different regularization methods. From left to right: the variance component estimation, the generalized cross validation, the L-curve analysis and the proposed PSC method. The best regional RMS is obtained using the PSC. The L-curve analysis gives slightly more RMS. The VCE and GCV methods yield significantly larger RMS. Results are for the case of Reuter grid.

Summary and concluding remarks for the regional solutions in South America along the Andes

In the area of the Andes, four regional solutions were determined based on simulated GRACE-type observations using SRBF. The solutions are obtained using the Reuter grid and four different methods for the choice of the regularization parameter. The results of modelling and comparisons can be summarized as follows:

- Among the regularization methods, the PSC method results in the least geoid RMS values and give the most promising solution. The L-curve analysis leads to nearly the same results compared to the PSC method. The VCE and GCV give rather the same geoid RMS values but considerably larger than the first two methods.
- Compared to the regional solutions in Central Africa and Scandinavia, the solutions in the Andes have larger geoid RMS values. This is due to the fact that less observations are available in this region compared to Scandinavia.

- The regional solutions using the PSC and L-curve methods provide better geoid RMS compared to the global solution using spherical harmonics. For the VCE and GCV methods, the largest deviations between the regional solutions and the model GOCO03s are visible in the western part of the region around the equator. These RMS values are much larger than the global solution shown in figure 6.13 (right). Thus the VCE and GCV methods cannot provide sufficient regularity for the regional solutions based on satellite data when the base functions have no measure of regularity (c.f. section 5.8).

6.3 Regional gravity field modelling based on GOCE gravity gradients

In the previous section, the performance of different methods for the choice of the regularization parameter for regional gravity field modelling was investigated based on simulated GRACE-type data. Results indicate that the proposed PSC method gives promising solutions compared to other methods. Although the simulated data were corrupted with a realistic coloured noise, it is however desired to check the applicability of the method when real data are included. For this purpose, the real GOCE gravity gradients will be used in this section. In addition, GOCE data are more appropriate to be used for regional modelling than GRACE-type observations. The long wavelengths of the gravity field, i.e. global features ($n < 30$), cannot be accurately determined using GOCE gravity gradients. The reason is the poor quality of GOCE gravity gradients in low-degree parts of the field. As a result, the long wavelengths of GOCE-only solutions are not comparable to those of GRACE-only solutions. Instead, GOCE data are very sensitive in the measurement bandwidth (approximately between degrees 30 and 250 in terms of spherical harmonics). This means, GOCE gradiometry is very useful for the determination of medium and short wavelengths of the gravity field ($30 < n < 250$). In the spatial domain, this is equivalent to regional areas from about $1000\,\mathrm{km}$ to local features down to almost $200\,\mathrm{km}$.

6.3.1 GOCE data and functional model

The real GOCE data used in this thesis are gravity gradients observed by the GOCE gradiometer. These data cover a time span of two months (October and November 2010) and are part of GOCE level-2 data product. In addition, GOCE kinematic orbit data are used to locate gravity gradients along the orbit. For a complete description of GOCE level-2 product see GOCE Level 2 Product Data Handbook (Gruber *et al.*, 2010). Two months of data, are the minimum amount of data for high-resolution gravity field recovery based on GOCE data. The use of more data will improve the quality of the final solution. Nevertheless, we confined our calculations to two months of GOCE data only which are sufficient to fulfil the aims of this thesis.
In order to use GOCE observations, it is necessary to note the following issues:

- From six components of gradient tensor, only four components can be measured with high sensitivity. These components are: V_{xx}, V_{yy}, V_{zz} and V_{xz}. Other components, i.e. V_{xy} and V_{yz}, are of less quality (Bouman *et al.*, 2011, Stummer *et al.*, 2008). According to equation (2.31), all gravity gradient components in LNOF are linear combinations of gravity gradients in GRF (c.f. figure 2.3). Direct rotation of gravity gradients from GRF into LNOF without additional processing would project the larger error of the less accurate gravity gradients into the accurate components in the LNOF. In other words, high accurate components are *mixed* with less accurate ones to provide the gravity gradient tensor in the LNOF. A way out of this problem is, to compute V_{xy} and V_{yz} based on an a prior gravity field model and use the computed values instead of observed values (Gruber *et al.*, 2010). An alternative way is to set up the observation equations in the GRF, instead of the LNOF. This means that the equations are rotated rather than the observations. Therefore it will be possible to use the original GOCE measurements in the observation vector. Hence, one can employ (2.34) instead of (2.31) to avoid the undesired mixture of accurate measurements with less sensitive ones. See Bouman (2007) for more details on this issue.

- The high sensitivity of GOCE measurements is achievable in a specific frequency band which is known as measurements bandwidth (MBW). This bandwidth includes the frequencies from about 0.005 to $0.04\,\mathrm{Hz}$ which approximately corresponds to the spherical harmonic degree $n = 30$ up to $n = 220$[1]. This implies that the lower degrees or long wavelengths of the gravitational potential cannot be precisely measured based on GOCE gradiometer data. Therefore it is necessary to calibrate GOCE observations using a state-of-the-art gravity field model. The algorithm is described in Gruber *et al.* (2010) for EGG-TRF-2 product. See also Brieden and Müller (2011) for more details.

We use equation (2.34) as the observation equation, i.e. the equations are rotated rather than the observations. Moreover, we use filtered GOCE measurements provided in the GRF, that is, the observations are externally

[1] According to Gruber *et al.* (2010), the official measurement bandwidth ranges from 0.005 to $0.1\,\mathrm{Hz}$. However the usable part is limited to approximately $0.04\,\mathrm{Hz}$ in the upper bound.

calibrated using a global gravity field model. Brieden and Müller (2011) give more details on the concepts used for GOCE data validation.
In section 2.3, the relation between gravity gradients in the Earth fixed frame and the LNOF were given using (2.35). It was also mentioned, that the first and second derivatives of the gravitational potential V change with the type of base functions used for the representation. Here in this section, we determine these derivatives, i.e. V_r, V_ϕ and V_λ as well as V_{rr}, $V_{r\phi}$, $V_{\phi\phi}$, $V_{\phi\lambda}$ and $V_{\lambda\lambda}$ in terms of SRBF. The general form of gravity field representation using SRBF is given by

$$V(r_i,\phi_i,\lambda_i) = \frac{GM}{R}\sum_{k=1}^{K}\alpha_k\sum_{n=0}^{\infty}(\frac{R}{r_i})^{n+1}(2n+1)b_nP_n(s) \tag{6.2}$$

where s is the spherical distance defined as:

$$s = \sin\phi\sin\phi_k + \cos\phi\cos\phi_k\cos(\lambda-\lambda_k). \tag{6.3}$$

The first derivatives can be expressed using the following

$$\begin{cases} V_r(r_i,\phi_i,\lambda_i) = -\dfrac{GM}{R^2}\sum\limits_{k=1}^{K}\alpha_k\sum\limits_{n=0}^{\infty}(\dfrac{R}{r_i})^{n+2}(2n+1)(n+1)b_nP_n(s) \\ V_\phi(r_i,\phi_i,\lambda_i) = \dfrac{GM}{R}\sum\limits_{k=1}^{K}\alpha_k\sum\limits_{n=0}^{\infty}(\dfrac{R}{r_i})^{n+1}(2n+1)b_ns_\phi P_n'(s) \\ V_\lambda(r_i,\phi_i,\lambda_i) = \dfrac{GM}{R}\sum\limits_{k=1}^{K}\alpha_k\sum\limits_{n=0}^{\infty}(\dfrac{R}{r_i})^{n+1}(2n+1)b_ns_\lambda P_n'(s) \end{cases} \tag{6.4}$$

in which s_ϕ and s_λ are the directional derivatives of the spherical distance s given by

$$\begin{cases} s_\phi = \dfrac{ds}{d\phi} = \cos\phi\sin\phi_k - \sin\phi\cos\phi_k\cos(\lambda-\lambda_k) \\ s_\lambda = \dfrac{ds}{d\lambda} = -\cos\phi\cos\phi_k\sin(\lambda-\lambda_k). \end{cases} \tag{6.5}$$

The components of the gradient tensor can be obtained by taking the derivatives of (6.4). Thus, the second derivatives are

$$\begin{cases} V_{rr}(r_i,\phi_i,\lambda_i) = \dfrac{GM}{R^3}\sum\limits_{k=1}^{K}\alpha_k\sum\limits_{n=0}^{\infty}(\dfrac{R}{r_i})^{n+3}(2n+1)(n+1)(n+2)b_nP_n(s) \\ V_{\phi\phi}(r_i,\phi_i,\lambda_i) = \dfrac{GM}{R}\sum\limits_{k=1}^{K}\alpha_k\sum\limits_{n=0}^{\infty}(\dfrac{R}{r_i})^{n+1}(2n+1)b_n[s_{\phi\phi}P_n'(s)+s_\phi^2P_n''(s)] \\ V_{\lambda\lambda}(r_i,\phi_i,\lambda_i) = \dfrac{GM}{R}\sum\limits_{k=1}^{K}\alpha_k\sum\limits_{n=0}^{\infty}(\dfrac{R}{r_i})^{n+1}(2n+1)b_n[s_{\lambda\lambda}P_n'(s)+s_\lambda^2P_n''(s)] \\ V_{r\phi}(r_i,\phi_i,\lambda_i) = -\dfrac{GM}{R^2}\sum\limits_{k=1}^{K}\alpha_k\sum\limits_{n=0}^{\infty}(\dfrac{R}{r_i})^{n+2}(2n+1)(n+1)b_ns_\phi P_n'(s) \\ V_{r\lambda}(r_i,\phi_i,\lambda_i) = -\dfrac{GM}{R^2}\sum\limits_{k=1}^{K}\alpha_k\sum\limits_{n=0}^{\infty}(\dfrac{R}{r_i})^{n+2}(2n+1)(n+1)b_ns_\lambda P_n'(s) \\ V_{\phi\lambda}(r_i,\phi_i,\lambda_i) = \dfrac{GM}{R}\sum\limits_{k=1}^{K}\alpha_k\sum\limits_{n=0}^{\infty}(\dfrac{R}{r_i})^{n+1}(2n+1)b_n[s_{\phi\lambda}P_n'(s)+s_\phi s_\lambda P_n''(s)] \end{cases} \tag{6.6}$$

and noting that $V_{r\lambda} = V_{\lambda r}$, $V_{r\phi} = V_{\phi r}$ and $V_{\phi\lambda} = V_{\lambda\phi}$ due to the fact that the gradient tensor is symmetric. The second derivatives of the spherical distance s, i.e. $s_{\phi\phi}$, $s_{\phi\lambda}$ and $s_{\lambda\lambda}$ are obtained by taking the directional derivatives of (6.5)

$$\begin{cases} s_{\phi\phi} = \dfrac{d^2 s}{d\phi^2} = -[\sin\phi \sin\phi_k + \cos\phi \cos\phi_k \cos(\lambda - \lambda_k)] = -s \\ s_{\phi\lambda} = \dfrac{d^2 s}{d\phi d\lambda} = \sin\phi \cos\phi_k \sin(\lambda - \lambda_k)] = s_{\lambda\phi} \\ s_{\lambda\lambda} = \dfrac{d^2 s}{d\lambda^2} = -\cos\phi \cos\phi_k \cos(\lambda - \lambda_k). \end{cases} \tag{6.7}$$

$P'_n(s)$ and $P''_n(s)$ are the first and second derivatives of the Legendre polynomials $P_n(s)$ with respect to s. Having obtained the gravity gradients using equation (6.6), the equations can now be rotated into the GRF frame using (2.34). Finally the design matrix will be set up by differentiating (2.34) with respect to the unknown coefficients α_k:

$$\frac{\partial \mathbf{V}_{jk}^{GRF}}{\partial \alpha_k} = \hat{\mathbf{R}} \frac{\partial \mathbf{V}_{jk}^{LNOF}}{\partial \alpha_k} \hat{\mathbf{R}}^T \tag{6.8}$$

where $\hat{\mathbf{R}}$ is the rotation matrix which is defined in section 2.3.2.

6.3.2 Setting up the regional models

Regional gravity field modelling based on GOCE data will be investigated in the same test regions explained in section 6.1. The limits of the model zone are exactly the same as before. The extension of the data and grid zones is 3° beyond the model and data zone respectively. The Shannon kernel with $N_{max} = 300$ is used for the analysis of the regional solutions. The maximum degree of expansion is chosen to be above the expected resolution of the GOCE gravity field models to reduce aliasing effects. Nevertheless, the synthesis of the regional solutions will be restricted to $N_{max} = 240$ since the solutions for the higher degrees are too noisy. As it is shown in the previous section, the type of grid points does not noticeably change the quality of the regional solutions. Therefore we only use the Reuter grid and the Fibonacci grid is not considered anymore.
The observations are the V_{zz} component measured by the GOCE gradiometers in the GRF. The data span a time period of two months with sampling rate of 1 s. A moving average filter is applied to down sample the observations to the sampling rate of 5 s. The averaging filter reduces the size of the design matrix and decreases the cost of computation. In addition, the observation noise will also be reduced due to the low-pass features of the averaging filter. To set the weight matrix, the standard deviation of observations are assumed to be about 2×10^{-12} E. The long wavelengths of V_{zz} up to degree $n = 30$ are computed using the geopotential model GOCO03s and subtracted from the observations. Therefore the data contain the frequencies above degree 30. Finally, the four methods for the choice of regularization parameters (VCE, GCV, L-curev and PSC) will be used for the inversion of the regional solutions. The regional solutions will be compared to two existing global gravity field models, the EGM2008 and the GOCO03s. The former contain no information from GOCE mission and its high frequency parts are mainly dependent on terrestrial data. The latter, on the other hand, is a combined model based on GRACE and GOCE observations with no terrestrial data included.

6.3.3 Regional solutions based on GOCE data

Regional solutions in Central Africa

The specifications of the regional setup for Central Africa are given in table 6.8. The total number of the gravity gradients V_{zz} is about 27000 inside the data zone. With the total number of almost 6000 unknown parameters, the size of the design matrix is about 27000×6000.
The condition number of the normal matrix is around 4×10^{19} revealing the strong ill-posedness of the regional model. Table 6.9 summarizes the characteristics of the solutions.

Model specification	Remarks
Geographical limits	the model zone: $-15^\circ \leq \phi \leq 15^\circ,\ 5^\circ \leq \lambda \leq 45^\circ$
	the data zone: $-18^\circ \leq \phi \leq 18^\circ,\ 2^\circ \leq \lambda \leq 48^\circ$
	the grid zone: $-21^\circ \leq \phi \leq 21^\circ,\ -1^\circ \leq \lambda \leq 51^\circ$
Observations	observation type: V_{zz} at orbit altitude
	frequency content: above 30 (SH)
	number of observations: $I = 27121$
	standard deviation: $2 \times 10^{-12}\,\mathrm{Etvs}$
	weight matrix: $\mathbf{P_l} = (2 \times 10^{-12}\,\mathrm{Etvs})^{-2} \times \mathbf{I}$
	the a priori variance factor: $\sigma_0^2 = 1$
The base functions	type of SRBF: Shannon ($N_{max} = 300$)
	number of base functions: $K = 6015$
The normal matrix $\mathbf{N}$	size: 6015×6015
	condition number: 4.2×10^{19}
	largest singular value: $s_1^2 = \|\mathbf{N}\| = 9.7 \times 10^{26}$
Initial regularization parameter	using (5.77): $\gamma^2 = 2.5 \times 10^{21}$
	using (5.88): $\gamma^2 = 2.8 \times 10^{20}$

Table 6.8: Specifications of the regional modelling in Central Africa.

Regularization method	γ^2	orbit RMS (Etvs)	surface RMS (EGM2008, cm)	surface RMS (GOCO03s, cm)	correlation of signal and parameters
VCE	5.519×10^{22}	2.3×10^{-12}	46.5	37.0	90.0%
GCV	4.523×10^{23}	2.4×10^{-12}	36.4	22.6	96.6%
L-curve	3.273×10^{23}	2.4×10^{-12}	37.6	24.6	96.3%
PSC	1.649×10^{24}	2.4×10^{-12}	34.1	19.4	97.1%

Table 6.9: Summary of the regional solutions in Central Africa and their quality measures. The solutions are obtained using the Reuter grid. The RMS values on the Earth's surface are obtained with respect to two global models EGM2008 and GOCO03s

The PSC method gives the largest regularization parameter with the minimum surface RMS values. The correlation of the PSC-derived coefficients with geoid heights is maximum. The L-curve analysis and the GCV methods result in more or less the same results. The GCV method gives closely the same results as the L-curve and the PSC. The VCE leads to the largest value of surface RMS showing that the amount of regularization by this method, compared to others, is not sufficient. The interesting fact is that all methods provide nearly the same RMS values at orbit altitude. The RMS values on the Earth's surface are given with respect to two global models EGM2008 and GOCO03s. In all cases, the RMS values with respect to the global model GOCO03s, are smaller than those with respect to EGM2008. The reason is the absence of GOCE data in the EGM2008.

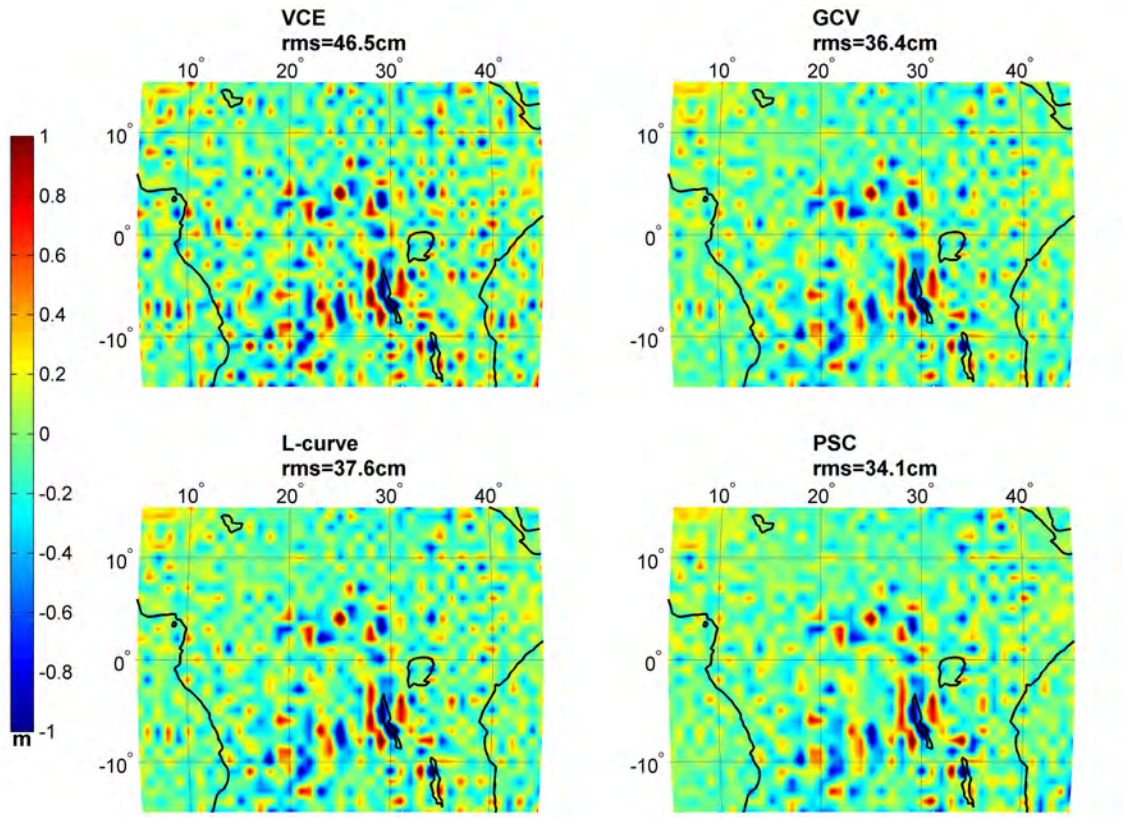

Figure 6.17: The differences between regional solutions in Central Africa and the global model EGM2008. The comparison is limited to the maximum degree $N_{max} = 240$. The solutions are based on the GOCE data and obtained using four different regularization methods: the variance component estimation (top-left), the generalized cross validation (top-right), the L-curve analysis (bottom-left) and the proposed PSC method (bottom-right)

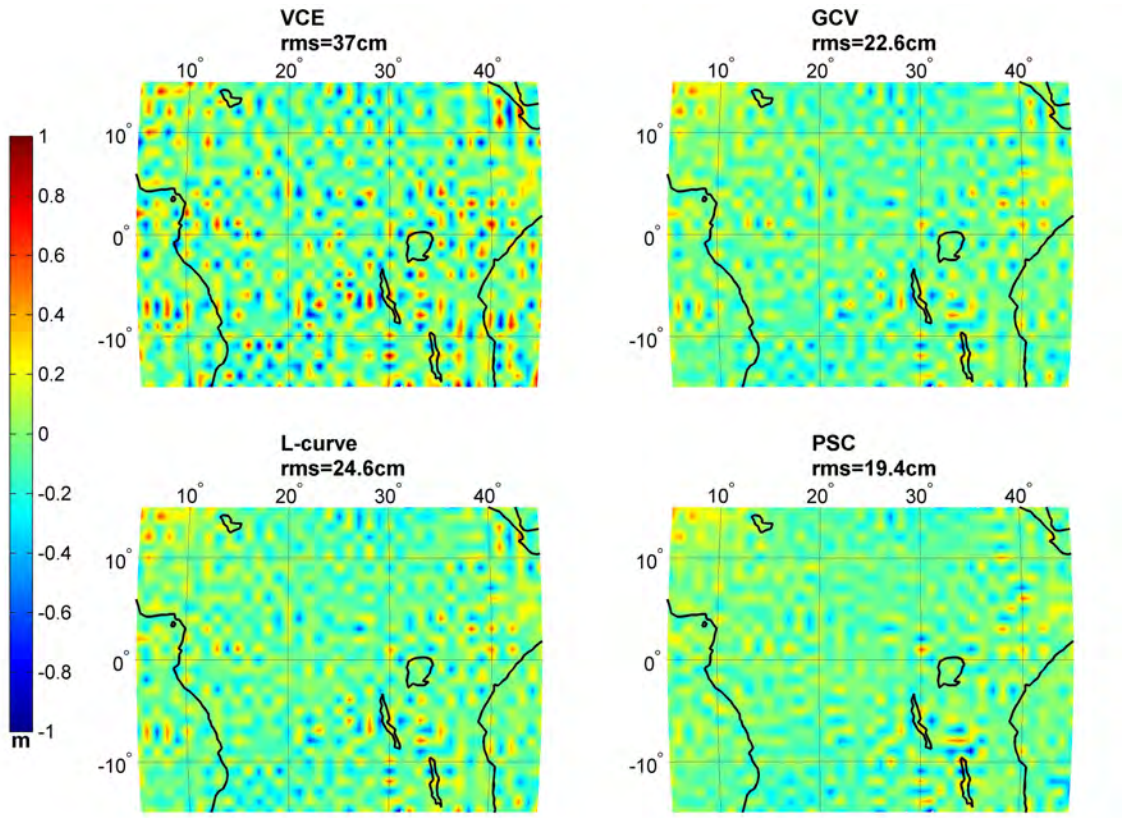

Figure 6.18: The differences between regional solutions in Central Africa and the global model GOCO03s. The comparison is limited to the maximum degree $N_{max} = 240$. The solutions are based on GOCE data and obtained using four different regularization methods: the variance component estimation (top-left), the generalized cross validation (top-right), the L-curve analysis (bottom-left) and the proposed PSC method (bottom-right)

The quality of the EGM2008 beyond the resolution of the GRACE-only models (say above $n = 100$) is highly dependent on the available terrestrial data. In Central Africa with poor availability of terrestrial data the EGM2008 cannot provide as good results as the GOCE data can. Therefore the deviations between the regional solutions with the GOCE data and the EGM2008 are expected. The smaller differences between regional solutions and the global model GOCO03s (a GRACE-GOCE combined model) indicate this explicitly. Figures 6.17 and 6.18 illustrate the differences between regional solutions and the global models EGM2008 and GOCO03s respectively.
The differences between the regional solutions and the model GOCO03s are due to the fact that the regional solutions are based on the GOCE data of only two months. In addition, only the V_{zz} components were used. In contrast, the GOCO03s model is based on the combination of 7 years of GRACE KBR measurements as well as 18 months of GOCE gravity gradiometry. In addition, 8 years of CHAMP orbit data and 5 years of SLR data are also involved in the determination of this model. A fair comparison would be possible if the same data sets were used to obtain the regional solution using SRBF.

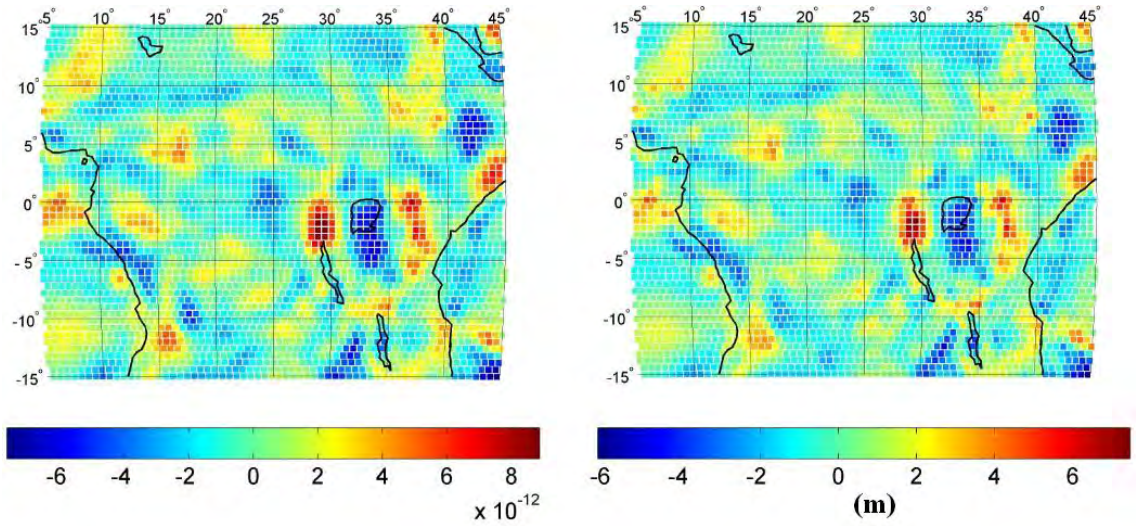

Figure 6.19: **Left**: the dimensionless estimated coefficients using the PSC method on the Reuter grid points in Central Africa. **Right**: the geoid heights synthesized using GOCO03s from degree $n = 30$ up to degree $n = 250$ on the points of the Reuter grid. The coefficients reveal the shape of the geoid in the corresponding frequency band.

Finally, figure 6.19 shows the value of the estimated coefficients using the PSC method on the Reuter grid points. In addition, the synthesized geoid heights are given on the same locations. The synthesis is done using the global model GOCO03s between spherical harmonic degrees 30 and 250. As it can be seen the general shape of the geoid heights is shown by the coefficients which is an indication for the quality of the solution.

Regional solutions in Scandinavia

The description of the setup for regional gravity field recovery in Scandinavia is given in table 6.10. The total number of gravity gradients (V_{zz}) is about 29000 inside the data zone. With the total number of almost 2880 unknown parameters, the size of the design matrix is about 29000×2880.

Model specification	Remarks
Geographical limits	the model zone: $50^\circ \leq \phi \leq 75^\circ,\ 0^\circ \leq \lambda \leq 50^\circ$
	the data zone: $47^\circ \leq \phi \leq 78^\circ,\ -3^\circ \leq \lambda \leq 53^\circ$
	the grid zone: $44^\circ \leq \phi \leq 81^\circ,\ -6^\circ \leq \lambda \leq 56^\circ$
Observations	observation type: V_zz at orbit altitude
	frequency content: above 30 (SH)
	number of observations: $I = 29600$
	standard deviation: $2 \times 10^{-12}\,\mathrm{Etvs}$
	weight matrix: $\mathbf{P_l} = (2 \times 10^{-12}\,\mathrm{Etvs})^{-2} \times \mathbf{I}$
	the a priori variance factor: $\sigma_0^2 = 1$
The base functions	type of SRBF: Shannon ($N_{max} = 300$)
	number of base functions: $K = 2880$
The normal matrix $\mathbf{N}$	size: 2880×2880
	condition number: 2.6×10^{19}
	largest singular value: $s_1^2 = \|\mathbf{N}\| = 4.6 \times 10^{27}$
Initial regularization parameter	using (5.77): $\gamma^2 = 1.7 \times 10^{22}$
	using (5.88): $\gamma^2 = 1.3 \times 10^{21}$

Table 6.10: Specifications of the regional modelling in Scandinavia.

The condition number of the normal matrix is around 2×10^{19} revealing the strong ill-posedness of the regional model. Table 6.11 summarizes the characteristics of the solutions.

Regularization method	γ^2	orbit RMS (Etvs)	surface RMS (EGM2008, cm)	surface RMS (GOCO03s, cm)	correlation of signal and parameters
VCE	7.316×10^{22}	2.4×10^{-12}	21.2	21.1	92.7%
GCV	8.638×10^{23}	2.5×10^{-12}	14.9	14.7	98.4%
L-curve	8.248×10^{23}	2.5×10^{-12}	15.0	14.8	98.4%
PSC	7.578×10^{24}	2.7×10^{-12}	11.3	11.3	98.8%

Table 6.11: Summary of the regional solutions in Scandinavia and their quality measures. The solutions are obtained using the Reuter grid. The RMS values on the Earth's surface are obtained with respect to the two global models; EGM2008 and GOCO03s.

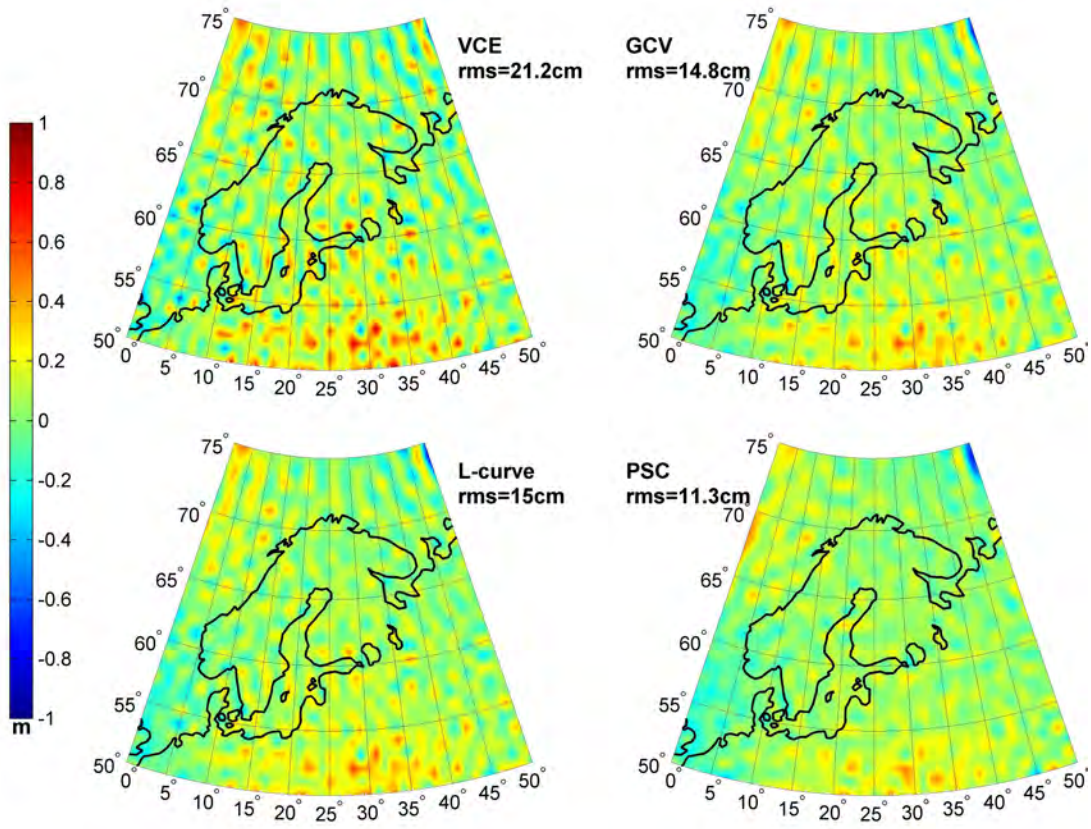

Figure 6.20: The differences between regional solutions in Scandinavia and the global model EGM2008. The comparison is limited to the maximum degree $N_{max} = 240$. The solutions are based on GOCE data and obtained using four different regularization methods: the variance component estimation (top-left), the generalized cross validation (top-right), the L-curve analysis (bottom-left) and the proposed PSC method (bottom-right).

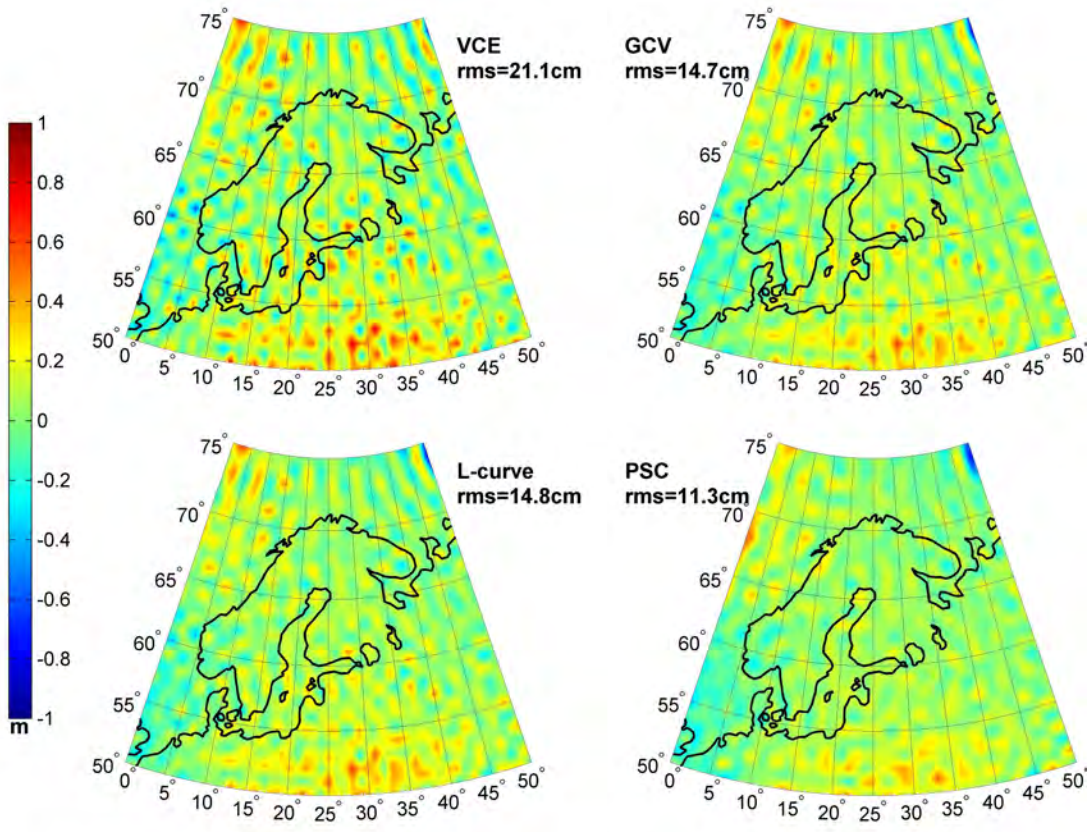

Figure 6.21: The differences between regional solutions in Scandinavia and the global model GOCO03s. The comparison is limited to the maximum degree $N_{max} = 240$. The solutions are based on GOCE data and obtained using four different regularization methods: the variance component estimation (top-left), the generalized cross validation (top-right), the L-curve analysis (bottom-left) and the proposed PSC method (bottom-right)

According to the results given in table 6.11, the PSC method gives again the most promising results compared to other approaches for the choice of regularization parameter. The L-curve and the GCV result in more or less the same RMS values on the Earth's surface. The VCE provides an insufficient amount of regularization leading to the largest RMS value on the Earth's surface.
The interesting fact in the case of Scandinavia is that the differences with respect to both EGM2008 and GOCO03s models, are almost the same for each regularization approach. The reason is the availability of enough terrestrial gravity observation used to determine the EGM2008 model. Therefore, the high frequencies of the EGM2008 (regional spatial structures) are well determined and can be therefore compared to those models obtained based on GOCE precise observations. Figures 6.20 and 6.21 display the differences between the regionally derived geoids and the two global models EGM2008 and GOCO03s, respectively.

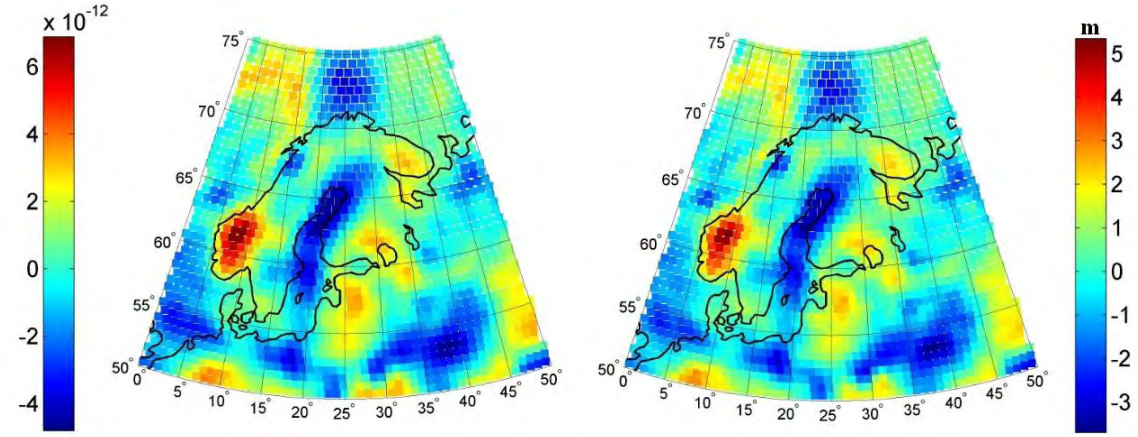

Figure 6.22: **Left**: the dimensionless estimated coefficients using the PSC method on the Reuter grid points in Scandinavia. **Right**: the geoid heights synthesized using GOCO03s from degree $n = 30$ up to degree $n = 250$ on the points of the Reuter grid. The coefficients reveal the shape of the geoid in the corresponding frequency band.

Figure 6.22 shows the value of the estimated coefficients using the PSC method on the Reuter grid points. The synthesized geoid heights are given on the same locations in Scandinavia. In the synthesis, the coefficients of the global model GOCO03s above the spherical harmonic degrees 30 have been used. As it can be seen, the general shape of the geoid heights is shown by the coefficients which is an indication for the quality of the solution.

Regional solutions in South America along the Andes

As the last test region, the regional gravity field modelling will be considered in South America in the area of the Andes. The description of the model setup is given in table 6.12.

Model specification	Remarks
Geographical limits	the model zone: $-45^\circ \leq \phi \leq 15^\circ, \quad -85^\circ \leq \lambda \leq -60^\circ$
	the data zone: $-48^\circ \leq \phi \leq 18^\circ, \quad -88^\circ \leq \lambda \leq -57^\circ$
	the grid zone: $-51^\circ \leq \phi \leq 21^\circ, \quad -91^\circ \leq \lambda \leq -54^\circ$
Observations	observation type: $V_z z$ at orbit altitude
	frequency content: above 30 (SH)
	number of observations: $I = 33353$
	standard deviation: $2 \times 10^{-12}\,\mathrm{Etvs}$
	weight matrix: $\mathbf{P_l} = (2 \times 10^{-12}\,\mathrm{Etvs})^{-2} \times \mathbf{I}$
	the a priori variance factor: $\sigma_0^2 = 1$
The base functions	type of SRBF: Shannon ($N_{max} = 300$)
	number of base functions: $K = 6743$
The normal matrix $\mathbf{N}$	size: 6743×6743
	condition number: 1.7×10^{20}
	largest singular value: $s_1^2 = \|\mathbf{N}\| = 1.1 \times 10^{27}$
Initial regularization parameter	using (5.77): $\gamma^2 = 2.4 \times 10^{21}$
	using (5.88): $\gamma^2 = 3.3 \times 10^{20}$

Table 6.12: Specifications of the regional modelling in the area of the Andes.

The condition number of the normal matrix is around 1×10^{20} showing the strong ill-posedness of the regional model. The solutions are obtained using four regularization methods and table 6.13 summarizes the characteristics of the solutions.

Regularization method	γ^2	orbit RMS (Etvs)	surface RMS (EGM2008, cm)	surface RMS (GOCO03s, cm)	correlation of signal and parameters
VCE	2.015×10^{22}	2.4×10^{-12}	54.0	45.9	95.3%
GCV	2.850×10^{23}	2.5×10^{-12}	42.3	29.2	98.6%
L-curve	9.847×10^{22}	2.5×10^{-12}	47.1	37.0	98.1%
PSC	5.969×10^{23}	2.6×10^{-12}	41.0	25.9	98.6%

Table 6.13: Summary of the regional solutions in the area of Andes and their quality measures. The solutions are obtained using the Reuter grid. The RMS values on the Earth's surface are obtained with respect to the two global models; EGM2008 and GOCO03s

Again, the best results are obtained using the PSC method with the least RMS values on the Earth's surface. The GCV also provides rather satisfactory results with a slightly bigger RMS values than the PSC. The L-curve analysis and the VCE methods are at the 3rd and 4th places among the methods.

The RMS values with respect to the EGM2008 are again larger compared to GOCO03s model. The reason is the same as explained in the case of Central Africa. Figures 6.23 and 6.24 show the geoid differences between the regional solutions and the models EGM2008 and GOCO03s in terms of geoid heights.

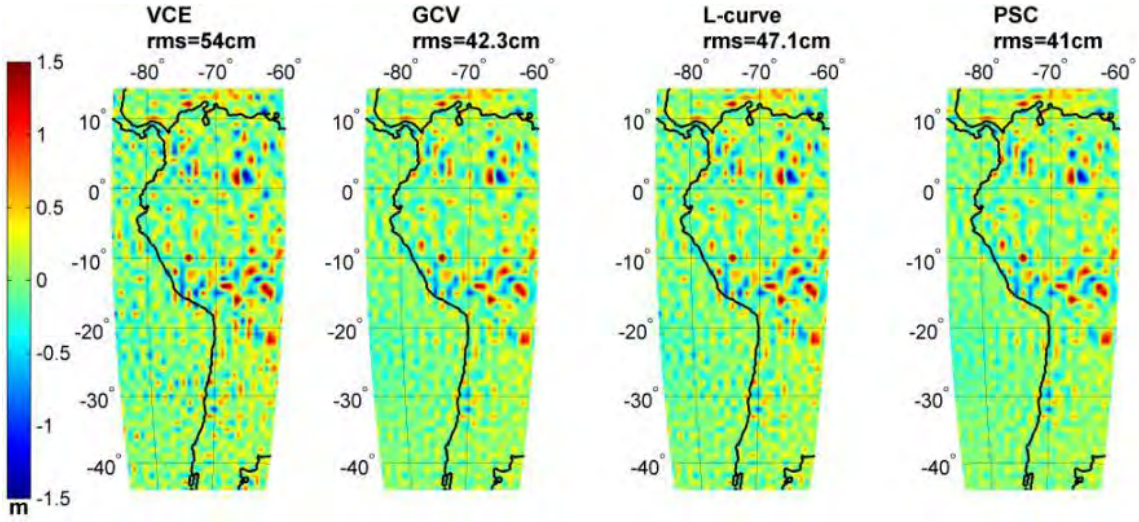

Figure 6.23: The differences between regional solutions in the area of the Andes and the global model EGM2008. The comparison is limited to the maximum degree $N_{max} = 240$. The solutions are based on GOCE data and obtained using four different regularization methods. From left to right: the variance component estimation, the generalized cross validation, the L-curve analysis and the proposed PSC method.

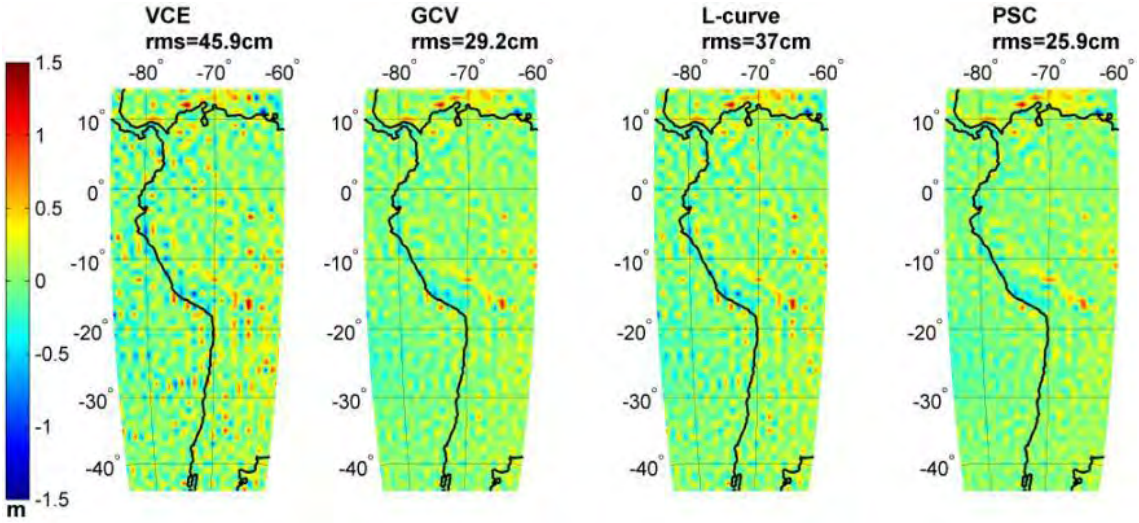

Figure 6.24: The differences between regional solutions in the area of the Andes and the global model GOCO03s. The comparison is limited to the maximum degree $N_{max} = 240$. The solutions are based on GOCE data and obtained using four different regularization methods. From left to right: the variance component estimation, the generalized cross validation, the L-curve analysis and the proposed PSC method.

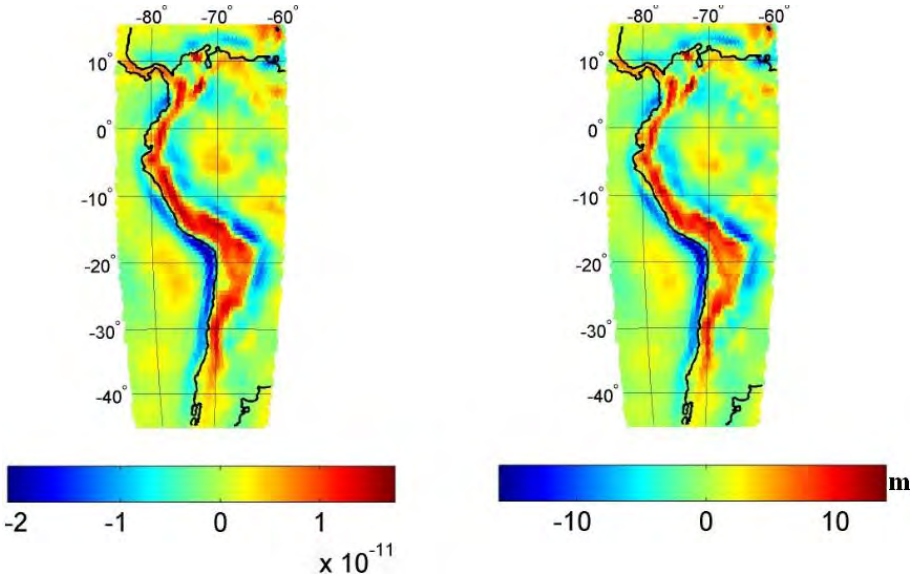

Figure 6.25: **Left**: the dimensionless estimated coefficients using the PSC method on the Reuter grid points in the area of Andes. **Right**: the geoid heights synthesized using GOCO03s from degree $n = 30$ up to degree $n = 250$ on the points of the Reuter grid. The coefficients reveal the shape of the geoid in the corresponding frequency band.

Similar to the other two test regions, the values of the estimated coefficients using the PSC method on the Reuter grid points is shown in Figure 6.25. The synthesized geoid heights on the same locations are also given in this figure. The general shape of the geoid heights is can be illustrated by the coefficients which is an indication for the quality of the solution.

6.3.4 Summary of regional solutions based on real GOCE data

In this section, the regional gravity field modelling was considered using SRBF based on the GOCE gravity gradients. Two months of GOCE gravity gradients were used with a sampling rate of 1 second. The data are down sampled to 5 seconds using a moving average filter. Only the V_{zz} component is used and other components of the gravity tensor are not considered. The long wavelengths of the V_{zz} up to degree $n = 30$ are synthesized using the global model GOCO03s and subtracted from the observations. The Shannon kernel with $N_{max} = 300$ is employed as the base function distributed on the points of the Reuter grid corresponding to $N_{max} = 300$.
The regional solutions are determined in three test regions Central Africa, Scandinavia and the area of the Andes. Four different parameter choice methods for the regularization parameter were applied to investigate their performance in the regional inversion. These methods are: the variance component estimation (VCE), the generalized cross validation (GCV), the L-curve analysis and our proposed parameter-signal correlation (PSC). The solutions were compared then to the two global models EGM2008 and GOCO03s. The results of the regional modelling are summarized as follows:

- At orbit level, all methods for the choice of regularization parameter lead to the same results. The RMS values of the post-fit residuals along the orbit are the same. When the solutions are to be compared on the Earth's surface, the results are very different. Among the four methods for the choice of regularization parameters, the proposed PSC method provides the best results with the least RMS values on the Earth's surface. The GCV, The L-curve analysis and the VCE methods provide larger RMS values on ground level.

- The surface RMS values for different regularization methods are smaller in Scandinavia compared to the other two regions. According to figure 6.21, the RMS value for the PSC and VCE methods are 11

and $21\,\mathrm{cm}$ respectively. The reason is the redundancy of observations which is rather big in this region compared to the others.

- The geoid differences with respect to the global model EGM2008 are rather big in South America and Central Africa. When the solutions are compared to the global model GOCO03s, the differences are fairly smaller than EGM2008. This shows that our regionally derived geoids are noticeably better than the EGM2008 (as a pre-GOCE model) in those regions with insufficient available terrestrial data. This improvement is not seen in regions like Scandinavia where the coverage of terrestrial gravity data is rather good.

- The differences between our regional solutions and the geoid from the model GOCO03s are due to the fact that GOCO03s is a combined gravity field model. GOCO03s is based on several years of the GRACE and nearly one year of the GOCE observations. On the other hand, our regional solutions are based on only two months of the GOCE V_{zz} observations. Nevertheless, the differences are in the range of current accumulated geoid errors (c.f. figure 2.5) which indicates the success of regional gravity field modelling as well as our proposed regularization method.

7 Summary and conclusions

We investigated the regional gravity field modelling based on satellite observations. The base functions used for the regional gravity field modelling are **band-limited SRBF**. The objective was to develop a simple and clear guideline for the regional gravity field modelling based on satellite data. The investigations were carried out using simulated data of a GRACE-like mission as well as the real GOCE observations.

The spherical harmonics and SRBF were compared, first, on the global scale. It was numerically shown that these two base functions span the same function space and result in the same accuracy for the representation of the global gravity field. In addition, we showed that the spatial pattern of the scaling coefficients associated with the SRBF are highly correlated with the gravitational potential difference or geoid heights. This is due to the space-localizing property of the SRBF. This high correlation is considered as a prior information about the unknown scaling coefficients in regional gravity field modelling. Such valuable prior information gave an insight into the proper regularization of regional gravity modelling and led to the development of the parameter-signal-correlation (PSC) method.

Model setup using SRBF

The regional gravity field modelling was studied in detail from different perspectives. First, the mathematical explanation of regional modelling using SRBF and its connection to the global modelling were given. The truncation of the data and base functions which cause severe instabilities in the inversion step were explained where we partitioned the global observation equations to sub-regions. We showed how the observation equation for the regional gravity field modelling is extracted from the global observation and discussed the contribution of the missing components.
The procedure of model setup for regional gravity field modelling was considered in detail. The crux of the regional gravity field modelling using SRBF is the variety of different choices for model setup as well as the inversion process. We divided these choices into seven groups and discussed each specifically. These choices are the shape of the SRBF, the maximum degree of expansion, the removal of the long wavelengths, the position of the SRBF, the size of the data zone, the size of the grid zone and finally the inversion process. According to our investigations and numerical results given in chapter 6, the following concluding remarks can be made for these choices.

1. **Shape of the SRBF**: We classified the band-limited SRBF into smoothing and non-smoothing base functions. Examples for the smoothing SRBF are CuP, Blackman and Spline kernels which include built-in low-pass filters. The Shannon kernel (as a special case of the point mass kernel) belongs to the class of non-smoothing SRBF if N_{max} is chosen sufficiently beyond the expected frequency content of the signal. As a result of using smoothing kernels, the severe observation's noise in high frequency components of the signal will be considerably reduced. On the other hand, the use of smoothing SRBF causes the filtering of high-frequency parts of the signal as well. Increasing the bandwidth of these functions by choosing a larger N_{max} to cover the expected spectrum of the signal imposes much more base functions to the model which is unnecessary. Therefore, we confined our investigations to the Shannon kernel as a non-smoothing kernel. This kernel leaves the observations unchanged. Therefore, for the satellite data, the use of the SRBF with Shannon kernel is recommended provided that the solution is obtained by means of a proper regularization method.

2. **Maximum degree of the expansion**: the maximum degree of the expansion, N_{max} is directly dependent on the expected frequency content of the signal. For instance, N_{max} for the GRACE monthly solutions and the GOCE observations are nominally 120 and 250, respectively. We recommend to set this number

slightly bigger than these values so that it is guaranteed that the signal is not undesirably filtered. We chose 130 and 300 as the maximum degree of the expansion for GRACE and GOCE observations which are beyond the expected resolution of the GRACE monthly solutions and the the GOCE static field.

3. **Removal of the long wavelengths**: Since it is not possible to model the long wavelengths of the gravity field on regional scales, these parts must be excluded from the observations. The extent to which the long wavelengths are removed is dependent on the size of the region. The smaller the region is the more removal is needed. In our computations, we synthesized and subtracted the long wavelengths up to degree $n = 30$. This number was obtained using a rule of thumb based on the size of the target region. Our investigations show that the removal of long wavelengths more than necessary does not improve the accuracy of the regional solutions considerably.

4. **Position of the SRBF**: There are several kinds of grids which can be used to define the location of base functions. Using different kinds of grids does not change the quality of the solutions provided that the grid offers a homogeneous point distribution. The slight differences between various grids can be refined by means of regularization in the inversion step. Examples of homogeneous point distribution are the Reuter grid and the Fibonacci grid which can be alternatively used with no preference.

5. **Size of the data zone**: To obtain a useful regional solution, the size of the data zone must be larger than the size of the model zone, where the representation is desired. The extension of the data zone depends on the type of observations and the frequency content of the reduced signal. We related the size of the data zone to the frequency content of the reduced signal and the satellite altitude and proposed a rule of thumb given by equations (4.16) and (4.17) to compute the minimum required extension. More data extension seems to be unnecessary since no significant improvement is achieved.

6. **Size of the grid zone**: The base functions which are outside, but close to the borders of the data zone can still have significant contribution to the solution. Thus the grid zone should be still larger than the data zone. We also proposed a rough rule to determine the extension of the grid zone. This estimation is dependent on the bandwidth of the the SRBF which is connected to the maximum degree of expansion N_{max}.

7. **Inversion process**: The modelling of the regional gravity field using SRBF is strongly ill-posed even though the above 6 choices are made reasonably. The reason is the regional confinement of the data as well as the base functions which are, in principle, globally defined. Thus, additional information is required to provide sufficient regularity for the solution. A useful solution must be achieved only by means of a proper regularization method.

Inversion and regularization

The Tikhonov regularization as a successful regularization method for many inverse problems gives sufficient regularity provided that the regularization parameter is chosen correctly. There are several well-known parameter choice methods which can be used for Tikhonov regularization. The variance component estimation (VCE), the generalized cross validation (GCV) and the L-curve analysis are examples of such methods. Nevertheless, the use of existing methods for the choice of regularization parameter cannot solely regularize the regional solutions. If these methods are used, other measures of regularity (such as using smoothing SRBF) should be incorporated in the model setup. An important achievement of this research study is the development of a new method for the choice of the regularization parameter which provides adequate regularization for the regional inversions. The proposed parameter-signal correlation (PSC) method is a new approach to choose the right (Tikhonov) regularization parameter. The method works based on the fact, that the scaling coefficients α_k represent the geometry of the residual gravitational potential or geoid heights. Thus, the desired unknown coefficients α_k should be highly correlated to the target residual potential on the Earth's surface.
The regularization parameter is a number between the smallest and the largest singular values of the ill-posed normal matrix. Since it is a vast range of numbers (over 18 orders of magnitude for regional gravity field solutions), having an initial guess for the regularization parameter is very essential for reducing the computational

burden. Two methods were also proposed to obtain a realistic guess for the regularization parameter which result in more or less the same numbers. Using these initial values, the final regularization parameter can be rapidly found using the PSC method. The proposed methods for the initial regularization parameter is not restricted to the PSC method and can be used with other parameter choice methods to reduce the computational costs.

Summary of the numerical results

The performance of the proposed PSC method was assessed in comparison with VCE, GCV and the L-curve methods. To compare the methods reasonably, several regional solutions were determined in different test areas. In addition, the solutions are obtained, separately, based on simulated GRACE data and real the GOCE observations. The following conclusions can be made accordingly:

1 Based on the simulated GRACE data, a global solution using spherical harmonics and several regional solutions using SRBF have been determined. As quality measure, the differences between solutions and the input gravity field model have been computed and their RMS values were determined. The RMS of the differences contain the total error (model error and the observation noise) and is a good measure for the quality assessment. The regional solutions obtained using VCE, GCV and L-curve analysis have larger RMS values compared to the global spherical harmonics. On the contrary, the PSC method gives equivalent results to the spherical harmonic solutions in high-latitude regions and better results with less RMS values in equatorial areas. The GRACE north-south stripes seen in GRACE monthly solutions are remarkably reduced in regional solutions using the PSC regularization method.

2 Among VCE, GCV, L-curve and the PSC methods, the PSC gives the most promising results with less RMS values. The L-curve also provides satisfactory results with slightly larger RMS values compared to the PSC. The other two methods, i.e. VCE and GCV, cannot regularize the regional solutions sufficiently and result in rather large geoid RMS. The use of the VCE and GCV methods (for regional gravity field modelling) should be made with other kernels such as the Blackman, CuP and Spline which have built-in regularity defined by their Legendre coefficients b_n. This fact has not been addressed in previous studies. **The advantage of the PSC method is that it provides adequate regularization so that the base functions remain simple with no further efforts to define the Legendre coefficients b_n.**

3 To assess the regional solutions based on other data sets, we also employed two months of GOCE gravity gradients (V_{zz}). Three regional solutions were determined in South America along the Andes, in Central Africa and in Scandinavia. They were compared to the high-resolution global gravity field model EGM2008 and the recent satellite based global model GOCO03s. The EGM2008 is chosen because it is a pre-GOCE gravity field model and can show the improvements achieved by GOCE data. The reason for choosing the GOCO03s is that this model is a combined model based on the GRACE and GOCE data and can be considered as the state-of-the-art gravity field model.

   Again, the PSC method gives the least geoid RMS compared to the other methods. This is another indication for the success of the PSC regularization method. Moreover, the results reveal that in the area of Andes as well as the Central Africa, regional solutions are considerably better than the global model EGM2008. This is evident from figures 6.17 and 6.23. The reason is that in these areas, there have not been enough terrestrial data to be incorporated in the determination of EGM2008. In contrast, in Scandinavia where terrestrial data have been available, there is no significant difference between EGM2008 and the solutions including GOCE observations. The improvement achieved for the quality of regional solutions in comparison with the model EGM2008 does have two clear messages: first, even two months of GOCE observations can improve the quality of the gravity field in medium and short wavelengths compared to pre-GOCE models. Second, the regional gravity field modelling using the SRBF provide promising results and can compete (and outperforms) the global models.

4 The differences between our regional solutions and the global model GOCO03s can be seen from different perspectives. First, the differences are almost in the range of accumulated geoid errors shown in figure

2.6 which shows the accumulated geoid errors of some recent global models. This is more evident for the case of the regional solution in Scandinavia where a better solution is obtained according to the dense GOCE orbit tracks. Secondly, it should be noted that the regional solutions are obtained based on two months of GOCE data only which in addition, were limited to the V_{zz} components. Finally, the GOCO03s is a combined model based on the data from several satellite missions. A fair comparison would be possible if the regional solutions were also obtained based on the same data sets. Incorporating more GOCE observations as well as combination with other satellite data will increase the accuracy of regional solutions considerably and is left for further works.

Further works

1. The proposed PSC method gives an insight into a data-adaptive choice for the regularization parameter. It requires a prior gravity field model. The prior gravity field model does not have to be a state-of-the-art model and an approximate model also suffices for the PSC method. Nevertheless, it is desired to get the PSC method working even without the need for an input gravity field model. The method can be modified by means of iteration so that no prior gravity field model might be needed.

2. The stochastic relations of the satellite observations can also help to provide prior information about the variance and covariance of the desired solution. In particular one can try to describe the stochastic effects of the observations outside the data zone on the final solution. This should be taken into account in connection with the equations (4.1), (4.2) and (4.3) which describe the deterministic effects of the observations outside the target region.

3. Incorporating other components of GOCE gravity gradient tensor will improve the quality of the regional solutions. This is not only due to the use of much more observations, but also due to the fact that other components such as V_{xx} and V_{xy} are more accurate than the V_{zz} and contain additional information about the features of the Earth's gravity field. This is to be done in further regional gravity field modelling with the PSC method.

4. For regional gravity field determination based on the GRACE (and the GRACE follow-on) mission, it is recommended to use the modified acceleration approach proposed at the technical University of Delft or the integral equation approach (c.f. section 2.2). The advantage of these methods for regional gravity field modelling is the reduced observation noise according to their observation equations. As we discussed in section 5.8, less observation noise requires less regularization in regional gravity field modelling and leads to better solutions.

5. Finally, the PSC method shall be adopted for data combination in regional gravity determination. An idea is to combine the PSC, as a regularization parameter choice method, and the VCE as a weighting approach for different data sets. This could be a possible subject for further works.

Bibliography

Alberts, B. (2009). *Regional gravity field modeling using airborne gravimetry data*. Publications on geodesy 70, Technical University of Delft. ISBN: 978 90 6132 312 9.

Amiri-Simkooei, A. (2007). *Least-Squares Variance Component Estimation, Theory and GPS Applications*. Publications on geodesy 64, Technical University of Delft. ISBN: 978 90 6132 301 3.

Antoni, M. (2012). *Nichtlineare Optimierung regionaler Gravitationsfeldmodelle aus SST-Daten*. PhD thesis, Institute of Geodesy, University of Stuttgart. ISBN 978-3-7696-5082-2.

Austen, G. and Grafarend, E. (2004). Gravitational field recovery from GRACE data of type high-low and low-low SST. In *The conference proceedings of the Joint CHAMP/GRACE Science Meeting, Potsdam, Germany*.

Bentel, K., Schmidt, M., and Gerlach, C. (2013). Different Radial Basis Functions and their Applicability for Regional Gravity Field Representation on the Sphere. *GEM - International Journal on Geomathematics*, 4, Pages 67–96.

Beutler, G., Jäggi, A., Mervart, L., and Meyer, U. (2010). The celestial mechanics approach: theoretical foundations. *Journal of Geodesy*, 84, Pages 605–624.

Biancale, R., Balmino, G., Lemoine, J., Marty, J., Moynot, B., Barlier, F., Exertier, P., Laurain, O., Gegout, P., Schwintzer, P., Reigber, C., Bode, A., König, R., Massmann, F., Raimondo, J., Schmidt, R., and Zhu, S. (2000). A new global Earth's gravity field model from satellite orbit perturbations: GRIM5-S1. *Geophysical Research Letters*, 27, Pages 3611–3614.

Bisnath, S. (2004). Precise orbit determination of low Earth orbiters with a single GPS receiver based, geometric strategy. Technical Report, Department of Geodesy and Geomatics Engineering, University of New Brunswick.

Bjerhammer, E. (1975). Discrete approaches to the solution of boundary value problem in phyiscal geodesy. *Bollettino Di Geodesia E Scienze Affini*, 34.

Bjerhammer, E. (1985). On a relativistic geodesy. *Bollettino Di Geodesia E Scienze Affini*, 59, Pages 207–220.

Bosch, W. (2002). Geodetic Applications of Satellite Altimetry, a review. IAG Workshop on Satellite Altimetry, Wuhan, 08-13 September. http://space.cv.nctu.edu.tw/altimetryworkshop/Lecture/keynote-bosch.pdf.

Bouman, J. (2000). *Quality assessment of satellite-based global gravity field models*. Publications on geodesy 48, Technical University of Delft. ISBN 9061322707.

Bouman, J. (2007). *Alternative method for rotation to TRF*. The European GOCE Gravity Consortium, 1 Edition. GO-TN-HPF-GS-0193.

Bouman, J., Fiorot, S., Martin, F., Gruber, T., Schrama, E., Tscherning, C., Veicherts, M., and Visser, P. (2011). GOCE gravitational gradients along the orbit. *Journal of Geodesy*, 85, Pages 791–805.

Brieden, P. and Müller, J. (2011). Current results of GOCE in-orbit validation via the cross-over approach. In L. Ouwehand (Ed.), *Proceedings of 4th International GOCE User Workshop*. European Space Agency.

Calvetti, D., Golub, G., and Reichel, L. (1999). Estimation of the L-curve via Lanczos bidiagonalization. *BIT Numerical Mathematics*, 39, Pages 603–619.

Calvetti, D., Hansen, P., and Reichel, L. (2002). L-curve curvature bounds via Lanczos bidiagonalization. *Electronic Transactions on Numerical Analysis*, 14, Pages 20–35.

Calvetti, D., Reichel, L., and Shuibi, A. (2004). L-curve and curvature bounds for Tikhonov regularization. *Numerical Algorithms*, 35, Pages 301–314.

Case, K., Kruizinga, G., and Wu, S. (2010). *GRACE Level 1B Data Product User Handbook*. Jet Propulsion Laboratory California Institute of Technology JPL. D-22027.

Cheney, W. and Kincaid, D. (2008). *Numerical Mathematics and computing, sixth edition*. Brooks/Cole Publishing Company. ISBN-13: 978-0-495-11475-8.

Chung, J., Nagy, J., and OLeary, D. (2008). A weighted-GCV method for Lanczos-Hybrid regularization. *Electronic Transactions on Numerical Analysis*, 28, Pages 149–167.

Colombo, O. (1981). Numerical methods for harmonic analysis on the sphere. Technical Report 310, Department of Geodetic Science and Surveying, The Ohio State University, Columbus, Ohio. 139pp.

Dempster, A., Schatzoff, M., and Wermuth, N. (1977). A simulation study of alternatives to ordinary least-squares. *Journal of the American Statistical Association*, 72, Pages 77–106.

Ditmar, P. and Klees, R. (2002). *A method to compute the Earth's gravity field from SGG/SST data to be acquired by GOCE satellite*. Delft University press.

Edmonds, A. (1957). *Angular Momentum in Quantum Mechanics*. Princeton University Press. ISBN: 9780691025896.

Eicker, A. (2008). *Gravity Field Refinement by Radial Base Functions from In-situ Satellite Data*. PhD thesis, Institute of geodesy and geo-information, University of Bonn. ISBN 978-3-7696-5088-4.

Eicker, A., Mayer-Gürr, T., Ilk, K., and Kurtenbach, E. (2010). Regionally refined gravity field models from in-situ satellite data. In F. Flechtner, T. Gruber, A. Güntner, M. Mandea, M. Rothacher, T.Schöne, and J. Wickert (Ed.), *System Earth via Geodetic-Geophysical Space Technologies*, Pages 255–264. Springer.

Fengler, M., Freeden, W., and Kusche, J. (2005). Multiscale geopotential solutions from CHAMP orbits and accelerometry. In C. Reigber, H. Lühr, P. Schwintzer, and J. Wickert (Ed.), *Earth observation with CHAMP, results from three years in orbit.*, Pages 139–144. Springer.

Flury, J. and Rummel, R. (2005). *Future satellite gravimetry and earth dynamics*. Springer, Dordrecht, The Netherlands.

Freeden, W. (1999). *Multiscale modelling of spcaeborne geodata*. Teubner, Stuttgart.

Freeden, W., Gervens, T., and Schreiner, M. (1998). *Constructive approximation on the sphere (with applications to geomathematics)*. Clarendon Press, Oxford.

Gerlach, C., Földvary, L., Svehla, D., Gruber, T., Wermuth, M., Sneeuw, N., Frommknecht, B., Oberndorfer, H., Peters, T., Rothacher, M., Rummel, R., and Steigenberger, P. (2003). A CHAMP-only gravity field model from kinematic orbits using the energy integral. *Geophysical Research Letters*, 30, Page 2037.

GFZ (2013). ICGEM - Table of Global Gravity Field Models. `http://icgem.gfz-potsdam.de/ICGEM/ICGEM.html`.

Gloub, G. and van Loan, C. (1996). *Matrix computations, third edition*. John Hopkins University Press, Baltimore, MD.

Golub, G., Heath, M., and Vahba, G. (1979). Generalized Cross-Validation as a method for choosing a Good Ridge parameter. *Technometrics*, 21, Pages 215–223.

Gonzalez, A. (2010). Measurement of areas on a sphere using Fibonacci and latitude-longitude lattices. *Mathematical Geosciences*, 42, Pages 49–64.

Grafarend, E. and Vanicek, P. (1980). On the Weight Estimation in Leveling. Technical Report, NOAA Technical Report NOS 86, NGS 17.

Gruber, T. (2004). Validation concepts for gravity field models from new satellite missions. In H. Lacoste (Ed.), *Proceedings of the 2nd International GOCE User Workshop: GOCE, The Geoid and Oceanography*, ESA SP-569. ESA.

Gruber, T. (2009). Evaluation of EGM2008 gravity field by means of GPS-levelling and sea surface topography solutions. *Newton's Bulletin, Bureau Gravimetrique International (BGI)*, 4, Pages 3–17.

Gruber, T., Brockmann, J., Schuh, W., and l. Krasbutter (2010). *GOCE Level 2 Product Data Handbook*. The European GOCE Gravity Consortium EGG-C, issue 4, revision 3 Edition.

Gruber, T., Visser, P., and Ackermann, C. (2011). Validation of GOCE gravity field models by means of orbit residuals and geoid comparisons. *Journal of Geodesy*, 85, Pages 845–860.

Hadamard, J. (1923). *Lectures on the Cauchy Problem in Linear Partial Differential Equations*. Yale University Press, Haven.

Han, S., Jekeli, C., and Shum, C. (2002). Efficient Gravity Field Recovery Using in situ Disturbing Potential Observables from CHAMP. *Geophysical Research Letters*, 29, Pages 36/1–36/4.

Han, S., Jekeli, C., and Shum, C. (2003). Static and temporal gravity field recovery using GRACE potential difference observables. *Advances in Geosciences*, 1, Pages 19–26.

Han, S., Shum, C., Jekeli, C., and Alsdorf, D. (2005). Improved estimation of terrestrial water storage changes from GRACE. *Geophysical Research Letters*, 32, Page L07302.

Han, S., Shum, C., and Jekeli, C. (2006). Precise estimation of in situ geopotential difference from GRACE low-low satellite-tosatellite tracking and accelerometry data. *Journal of Geophysical Research*, 111, Page B04411.

Hansen, P. (1990a). The discrete picard condition for discrete ill-posed problems. *BIT Numerical Mathematics*, 30, Issue 4, Pages 658–672.

Hansen, P. (1990b). Truncated singular value decomposition solutions to discrete ill-posed problems with ill-determined numerical rank. *SIAM Journal on Scientific and Statistical Computing*, 11, Pages 503–518.

Hansen, P. (1997). *Rank Deficient and Discrete Ill-Posed Problems*. SIAM, Philadelphia.

Hansen, P. (2000). The L-Curve and its Use in the Numerical Treatment of Inverse Problems. In *in Computational Inverse Problems in Electrocardiology, ed. P. Johnston, Advances in Computational Bioengineering*, Pages 119–142. WIT Press.

Hansen, P. (2010). *Discrete Inverse Problems, Insight and Algorithms*. SIAM, Philadelphia.

Hansen, P. and OLeary, D. (1993). The Use of the L-Curve in the Regularization of Discrete Ill-Posed Problems. *SIAM Journal on Scientific Computing*, 14, Pages 1487–1503.

Hashemi, F., Ditmar, P., Klees, R., Liu, X., Zhao, Q., and Guo, J. (2012). The Earth's static gravity field model DGM-1S from an optimal combination of GRACE and GOCE data: computation and validation aspects. *Journal of Geodesy*, in review.

Heiskanen, W. and Moritz, H. (1967). *Physical geodesy*. Freeman, San Francisco.

Higham, N. (1987). A Survey of condition number estimation for triangular matrices. *Society for Industrial and Applied Mathematics*, 29, Pages 575–596.

Hirt, C., Bürki, B., Somieski, A., and Seeber, G. (2010). Modern Determination of vertical deflections using digital zenith cameras. *Journal Surveying Engineering*, 136, Pages 1–12.

Hofmann, B. and Moritz, H. (2005). *Physical Geodesy*. SpringerWienNewYork.

Hutchinson, M. (1990). A stochastic estimator of the trace of the influence matrix for laplacian smoothing splines. *Communications in Statistics, Simulation and Computation*, 19, Pages 433–450.

Ihde, J., Wilmes, H., Müller, J., Denker, H., Voigt, C., and Hosse, M. (2010). Validation of Satellite Gravity Field Models by Regional Terrestrial Data Sets. In F. Flechtner, T. Gruber, A. Güntner, M. Mandea, M. Rothacher, T. Schöne, and J. Wickert (Ed.), *System Earth via Geodetic-Geophysical Space Techniques*, Advanced Technologies in Earth Sciences, Pages 227–296. Springer.

Ilk, K. (1993). Regularization for high resolution gravity field recovery by future satellite techniques. In G. Anger, R. Gorenflo, H. Jochmann, H. Moritz, and W. Webers (Ed.), *Inverse problems: principles and applications in geophysics, technology, and medicine*. AkademieVerlag, Berlin.

Jekeli, C. (1999). The determination of gravitational potential differences from satellite-to-satellite tracking. *Celestial Mechanics and Dynamical Astronomy*, 75, Pages 85–101.

Jekeli, C. (2005). Spline representation of functions on a sphere for geopotential modeling. Technical Report 475, Department of Geodetic Science, The Ohio State University.

Jäggi, A., Hugentobler, U., Bock, H., and Beutler, G. (2007). Precise orbit determination for GRACE using undifferenced or doubly differenced GPS data. *Advances in Space Research*, 39, Pages 1612–1619.

Kang, Z., Tapley, B., Bettadpur, S., Ries, J., Nagel, O., and Pastor, R. (2006). Precise orbit determination for the GRACE mission using only GPS data. *Journal of Geodesy*, 80, Pages 322–331.

Kaula, W. (1966). *Theory of Satellite Geodesy, Applications of Satellites to Geodesy*. Dover Publications, INC. Mineola, New York.

Keller, W. (2004). *Wavelets in Geodesy and Geodynamics*. Walter de Gruyter. Berlin. New York.

Klees, R., Tenzer, R., Prutkin, I., and Wittwer, T. (2008). A data-driven approach to local gravity field modelling using spherical radial basis functions. *Journal of Geodesy*, 82, Pages 457–471.

Knudsen, P. (1987). Estimation and Modelling of the Local Empirical Covariance Function Using Gravity and Satellite Altimeter Data. *The Journal of the international association of Geodesy*, 61, N2, Pages 145–160.

Koch, K. (1999). *Parameter Estimation and Hypothesis Testing in Linear Models*. Springer-Verlag Berlin Heidelberg NewYork.

Koch, K. and Kusche, J. (2002). Regularization of geopotential determination from satellite data by variance components. *Journal of Geodesy*, 76, Pages 259–268.

Koop, R. (1993). *Gloabal gravity field modelling using satellite gravity gradiometry*. PhD thesis, Technical University of Delft.

Kreyszig, E. (1978). *Introductory Functional Analysis with Applications*. John Wiley & Sons, USA.

Kroes, R. (2006). *Precise relative positioning of formation flying spacecraft using GPS*. PhD thesis, Technical University of Delft.

Kusche, J. (2003). Noise variance estimation and optimal weight determination for GOCE gravity recovery. *Advances in Geosciences*, 1, Pages 81–85.

Kusche, J. and Klees, R. (2002). Regularization of gravitay field estimation from satellite gravity gradients. *Journal of Geodesy*, 76, Pages 359–368.

Kusche, J. and van Loon, J. (2005). Statistical Assessment of CHAMP Data and Models Using the Energy Balance Approach. In C. Reigber, H. Lühr, P.Schwintzer, and J. Wickert (Ed.), *Earth Observation with CHAMP, Results from Three Years in Orbit*. Springer.

Lawless, J. and Wang, P. (1976). A simulation study of ridge and other regression estimators. *Communications in Statistics - Theory and Methods*, A5, Pages 307–323.

Lee-Lueng, F. and Cazenave, A. (2000). *Satellite Altimetery and Earth Sciences - A Handbook of Techniques and Applications*. International Geophysics series.

Lemoine, F., Luthcke, S., Rowlands, D., Chinn, D., Klosko, M., and Cox, C. (2007). *The use of mascons to resolve time-variable gravity from GRACE*, Volume 130, Pages 231–236. International Association of Geodesy Symposia.

Lio, X. (2008). *Global gravity field recovery from satellite-to-satellite tracking data with acceleration approach*. PhD thesis, Technical University of Delft.

MacLeod, A. (1988). Finite-dimensional regularizations with nonidentity smoothing matrices. *Linear Algebra and its Applications*, 111, Pages 191–207.

Marchenko, A. (1998). *Parametrization of the Earth's gravity field:point and line singularities*. Lviv Astronomical and Geodetic Society, Lviv, Ukraine.

Marchenko, A. (2003). Regional gravity field model from satellite altimetry, gravimetry and GPS-levelling data in Black Sea area. *Bollettino Di Geodesia E Scienze Affini*, 1XII, Pages 245–259.

Marchenko, A., Barthelmes, F., Mayer, U., and Schweintzer, P. (2001). Regional geoid determination: an application to airborne gravity data in the Skagerrak. Technical Report STR01/07, GeoForschungsZentrum, Potsdam.

Martinsson, P.-G., Rokhlin, V., and Tygert, M. (2006). A randomized algorithm for the approximation of matrices. Technical Report, Yale University Department of Computer Science.

Martinsson, P.-G., Rokhlinb, V., and Tygert, M. (2010). A randomized algorithm for the decomposition of matrices. *Applied and Computational Harmonic Analysis*, 30, Pages 47–68.

Mayer-Gürr, T. (2006). *Gravitationsfeldbestimmung aus der Analyse Kurzer Bahnbögen am Beispiel der Satellitenmissionen CHAMP und GRACE*. PhD thesis, University of Bonn.

Mayer-Gürr, T. (2012). The new combined satellite only model GOCO03s. *International Symposium on Gravity, Geoid and Height Systems, Venice (Poster)*.

Mayer-Gürr, T., Ilk, K., Eicker, A., and Feuchtinger, M. (2005). ITG-CHAMP01: a CHAMP gravity field model from short kinematic arcs over a one-year observation period. *Journal of Geodesy*, 78, Pages 462–480.

Müller, C. (1966). *Spherical harmonics, Lecture notes in mathematics*, Volume 17. Springer Verlag, Berlin.

Mohammad-Karim, M. (1981). Diagramatic approach to solve least-squares adjustment and collocation problems. Technical Report 83, Department of geodesy and geomatics engineering, University of New Brunswick.

Montenbruck, O. and Gill, E. (2000). *Satellite orbits: models, methods and aoolications*. Springer Verlag, Heidelberg.

Moritz, H. (1980). *Advanced Physical Geodesy*. Herbert Wichmann Verlag Karlsruhe, Abacus Press Tunbridge Wells Kent.

Moritz, H. and Sünkel, H. (1978). *Approximation methods in Geodesy*. Herbert Wichmann Verlag Karlsruhe.

Neumann, J. (1968). *Mathematische Grundlagen der Quantenmechanik*. Grundlagen der Mathematuschen Wissenschaften, Band 38, Springer-Verlag, Heidelberg.

Orfanidis, S. (1996). *Optimum Signal Processing. An Introduction*. Prentice-Hall, Englewood Cliffs, NJ.

Pail, R., Fecher, T., Murböck, M., Rexer, M., Stetter, M., Gruber, T., and Stummer, C. (2013). Impact of GOCE Level 1b data reprocessing on GOCE-only and combined gravity field models. *Studia Geophysica et Geodaetica*, 57, Pages 155–173.

Panet, I., Flury, J., Biancale, R., Gruber, T., Johannessen, J., den Broeke, M. V., Van-Dam, T., Gegout, P., Hughes, C., Ramillien, G., Sasgen, I., Seoane, L., and Thomas, M. (2012). Earth System Mass Transport Mission (e.motion): A Concept for Future Earth Gravity Field Measurements from Space. *Surveys in Geophysics*, 34, Pages 141–163.

Payne, M. (1971). *Truncation effects in geopotential modelling*. Analytical Mechanics Associates, Seabrook, Maryland.

Petit, G. and Luzum, B. (2010). *IERS Conventions 2010*. International Earth Rotation and Reference Systems Service. ADA535671.

Ramillien, G., Biancale, R., Gratton, S., Vasseur, X., and Bourgogne, S. (2011). GRACE-derived surface water mass anomalies by energy integral approach: application to continental hydrology. *Journal of Geodesy*, 85, Pages 313–328.

Reginska, T. (1996). A regularization parameter in discrete ill-posed problems. *SIAM Journal on Scientific Computing*, 17, Pages 740–749.

Reigber, C. (1989). Gravity field recovery from satellite tracking data. In Sanso.F and Rummel.R (Ed.), *Theory of satellite geodesy and gravity fild determination*, Volume 25, Pages 197–234. Springer.

Reubelt, T., Austen, G., and Grafarend, W. (2003). Harmonic analysis of the earht's gravitational field by means of semi-continuous ephemerides of a low Earth orbiting GPS-tracked satellite. Case study: CHAMP. *Journal of Geodesy*, 77, Pages 257–278.

Reubelt, T., Götzelmann, M., and Grafarend, W. (2006). Harmonic analysis of the earht's gravitational field from kinematic CHAMP orbits based on numerically derived satellite accelerations. In J. Flury, R. Rummel, C. Reigber, M. Rothacher, G. Boedecker, and U. Schreiber (Ed.), *Observation of the Earth from space*, Pages 27–42. Springer.

Reuter, R. (1982). Über Integralformeln der Einheitssphäre und harmonische Splinefunktionen. Technical Report, Veröffentlichungen des Geodätischen Instituts der Rheinisch-Westfälischen Technischen Hochschule Aachen.

Rummel, R. (1979). Determination of short-wavelength components of the gravity field from satellite-to-satellite tracking or satellite gradiometry. *Manuscripta geodaetica*, 4/2, Pages 107–148.

Rummel, R., Reigber, C., and Ilk, K. (1978). The use of satellite-to-satellite tracking for gravity parameter recovery. In S. Heiber and T. Guyenne (Ed.), *Proceedings of the European Workshop on Space Oceanography, Navigation and Geodynamics (SONG)*, Pages 153–161. esa SP-137.

Rummel, R., Balmino, G., Johannessen, J., Visser, P., and Woodworth, P. (2002). Dedicated gravity field missions-principles and aims. *Journal of Geodynamics*, 33, Pages 3–20.

Rummel, R., Gruber, T., Yi, W., and Albertella, A. (2012). GOCE: Its Principles and Science. In H. Schuh, J. Böhm, T. Nilsson, and N. Capitaine (Ed.), *Proceedings of the Journées 2011 "Systèmes de référence spatio-temporels"*, Volume 2012. Vienna University of Technology.

Rust, B. (1998). Truncating the Singular Value Decomposition for Ill-Posed Problems. Technical Report NISTIR 6131, Mathematical and Computational Sciences Division.

Save, H. (2009). *Using regularization for error reduction in GRACE gravity estimation*. PhD thesis, The university of Texas at Austin.

Save, H. and Bettadpur, S. (2012). Reducing errors in the GRACE gravity solutions using regularization. *Journal of Geodesy*, 86, Pages 695–711.

Scales, J. (1996). Uncertainties in seismic inverse calculations. In B. Jacobsen, K. Mosegaard, and P. Sibani (Ed.), *Inverse Methods*, Volume 63, *Lecture Notes in Earth Sciences*, Pages 79–97. Springer Verlag, Berlin.

Schachtschneider, R., Holschneider, M., and Mandea, M. (2010). Error distribution in regional inversion of potential field data. *Geophsical Journal International*, 181, Pages 1428–1440.

Schmidt, M., Han, S.-C., Kusche, J., Sanchez, L., and Shum, C. K. (2006). Regional high-resolution spatiotemporal gravity modeling from GRACE data using spherical wavelets. *Geophysical Research Letters*, 33, Page L08403.

Schmidt, M., Fengler, M., Mayer-Gürr, T., Eicker, A., Kusche, J., Sanchez, L., and Han, S.-C. (2007). Regional gravity field modeling in terms of spherical base functions. *Journal of Geodesy*, 81, Pages 17–38.

Schneider, M. (1968). A general method of orbit determination. Technical Report, Royal Aircraft Translation no. 1279, Ministry of Technology, Farnborough, UK.

Sheard, B., Heinzel, G., Danzmann, K., Shaddock, D., Klipstein, W., and Folkner, W. (2012). Intersatellite laser ranging instrument for the GRACE follow-on mission. *Journal of Geodesy*, 86, Pages 1083–1095.

Souza and César, R. (2010). Kernel Functions for Machine Learning Applications. http://crsouza.blogspot.com/2010/03/kernel-functions-for-machine-learning.html.

Steven, W. (1997). *The Scientist and Engineer's Guide to Digital Signal Processing*. California Technical Publishing, San Diego, California.

Strang, G. and Borre, K. (1997). *Linear Algebra, Geodesy, and GPS*. Wellesley-Cambridge Press.

Stummer, C., Gruber, T., Bouman, J., and s. Rispens (2008). GOCE gradiometry - A Guide for users. IAG, international symposium, Gravity, geoid and Earth observations. 23-27 June 2008, China.

Tapley, B., Bettadpur, S., Watkins, M., and Reigber, C. (2004). The gravity recovery and climate experiment: Mission overview and early results. *Geophysical Research Letters*, 31, Page L09607.

Tapley, B., Ries, J., Bettadpur, S., Chambers, D., Cheng, M., Condi, F., Gunter, B., Kang, Z., Nagel, P., Pastor, R., Pekker, T., Poole, S., and Wang, F. (2005). GGM02: An improved Earth gravity field model from GRACE. *Journal of Geodesy*, 79, Pages 467–478.

Tenzer, R. and Klees, R. (2008). The choice of the spherical radial basis functions in local gravity field modelling. *Studia Geophysica et Geodaetica*, 52, Pages 287–304.

Tikhonov, A. and Arsenin, V. (1977). *Solutions of Ill-posed Problems*. John Wiley & Sons, New York.

Torge, W. and Müller, J. (2012). *Geodesy*. Walter de Gruyter. Berlin/Boston.

van Loon, J. (2008). *Functional and stochastic modelling of satellite gravity data*. PhD thesis, Technical Universtiy of Delft.

van Loon, J. and Kusche, J. (2005). Stochastic model validation of satellite gravity data: A test with CHAMP pseudo-observations. In C. Jekeli, L.-M. Bastos, and J. Fernandes (Ed.), *Gravity, Geoid and Space Missions, IAG proceedings*, Volume 129, Pages 24–29. Springer.

Vanicek, P. and Krakiwsky, E. (1982). *Geodesy;the concepts*. North-Holland Publishing Company.

Vermeer, M. (1989). FGI studies on satellite gravity gradiometry. 1. Experiments with a 5-degree buried masses grid representation. Technical Report, Finish Geodetic Institute.

Voigt, C. (2012). *Astrogeodätische Lotabweichungen zur Validierung von Schwerefeldmodellen*. PhD thesis, Faculty of civil eingineering and geodesy, University of Hanover.

Weightman, J. (1965). Gravity, geodesy and artificial satellites, A unified analytical approach. G. Veis (Ed.), *The Use of Artificial Satellites for Geodesy, Proceedings of the International Symposium, Athens, Greece, April 27-May 1, 1965*, Volume 2.

Wittwer, T. (2009). *Regional gravity field modelling with radial basis functions*. PhD thesis, Technical University of Delft.

Wolff, M. (1969). Direct measurements of the Earth's gravity potential using a satellite pair. *Journal of Geophysical Research*, 74, Pages 5295–5300.

Xu, G. (2010). *Sciences of Geodesy - I, Advances and Future Directions*. Springer.

Xu, P. (1998). Truncated SVD methods for discrete ill-posed problems. *Geophysical Journal International*, 135, Pages 505–514.

Xu, P. (2009). Iterative generalized cross-validation for fusing heteroscedastic data of inverse ill-posed problems. *Geophysical Journal International*, 179, Pages 182–200.

Yarlagadda, R. (2010). *Analog and Digital Signals and Systems*. Springer.

Zaho, Q. (2004). *Research on precise orbit determination theory and software of both GPS navigation constellation and LEO satellites*. PhD thesis, School of geodesy and geomatics of Wuhan University.

Zhu, S., Reigber, C., and König, R. (2004). Integrated adjustment of CHAMP, GRACE, and GPS data. *Journal of Geodesy*, 78, Pages 103–108.

Acknowledgement

First of all, I would like to express my gratitude to Jakob Flury for his decent supervision and helpful advices during my PhD studies. Without his many ideas, steady support and incentives, this work would not have been possible. I also appreciate the freedom he gave me for choosing the topic and following my research interests. Especial thanks go to Jürgen Müller for providing me the opportunity to do my research studies in the Institut für Erdmessung and supporting me in the whole PhD period.

I am also indebted to Michael Schmidt for hosting me several times in Deutsches Geodätisches Forschungsinstitut (DGFI) in Munich as well as for a series of technical discussions within his research group. His willingness to review and correct my thesis is highly appreciated. Furthermore, I would like to thank Gerhard Heinzel and Ingo Neumann for accepting to be in the exam committee and for giving me constructive feedback and comments in the exam and in their reviews on my thesis. Appreciation is extended to Phillip Brieden for providing the real GOCE orbit and calibrated GOCE gravity gradients as well as for providing the German version of the Summary. Many thanks go to my colleagues at Institut für Erdmessung for their help and encouragements.

This work has been carried out in the framework of the fellowship program of the Centre for Quantum Engineering and Space-Time research (QUEST). QUEST is a cluster of excellence funded by the Deutsche ForschungsGemeinschaft (DFG). It is a joint venture of the Leibniz Univeristät Hannover, the Max Plank Institute for Gravitational Physics, the Physikalisch-Technische Bundesanstalt (PTB) and several other research institutes. The outstanding support by the QUEST office in all administrative matters, especially by Birgit Ohlendorf, is gratefully acknowledged.

Last but not least, I would like to thank my parents for their generous and devotional supports in all periods of my life. I especially thank my wife, Mina, for her understanding, patience and support during the preparation of this thesis.

Curriculum Vitae

- Since May 2013: Academic staff, Institute of geodesy, University of Hanover, Germany
- November 2008-April 2013: PhD scholarship holder, Centre for Quantum Engineering and Space-Time Research (QUEST), University of Hanover, Germany
- September 2004-January 2007: Master of Science in geodesy, K.N.T University of technology, Tehran, Iran
- September 1999-May 2004: Bachelor of Science in surveying engineering, K.N.T University of technology, Tehran, Iran
- September 1995-January 1999: High school diploma in physics and mathematics, Towhid high school, Tehran, Iran
- September 1987-May 1995: Primary and guidance school, Dorood/Tehran, Iran
- August 1981: Born in Tehran, Iran

I, Majid Naeimi, hereby certify that this thesis, has been written by me and contains no material that has been submitted previously, in whole or in part, for the award of any other academic degree or diploma. Except where otherwise indicated, this thesis is my own work.